

Coherence and control of a single electron spin in a quantum dot

Proefschrift

ter verkrijging van de graad van doctor
aan de Technische Universiteit Delft,
op gezag van de Rector Magnificus prof.dr.ir. J.T. Fokkema,
voorzitter van het College voor Promoties,
in het openbaar te verdedigen op maandag 8 oktober 2007 om 15:00 uur

door

Frank Henricus Louis KOPPENS

natuurkundig ingenieur
geboren te Deurne.

Dit proefschrift is goedgekeurd door de promotor:

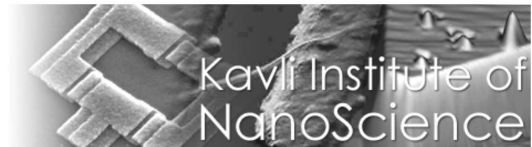
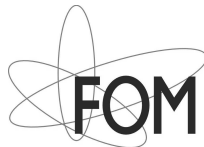
Prof.dr.ir. L.P. Kouwenhoven

Toegevoegd promotor:

Dr.ir. L.M.K. Vandersypen

Samenstelling van de promotiecommissie:

Rector Magnificus	voorzitter
Prof.dr.ir. L.P. Kouwenhoven	Technische Universiteit Delft, promotor
Dr.ir. L.M.K. Vandersypen	Technische Universiteit Delft, toegevoegd promotor
Prof.dr.ir. G.E.W. Bauer	Technische Universiteit Delft
Prof.dr. J.J. Finley	Walter Schottky Institute, München, Duitsland
Prof.dr. L.S. Levitov	MIT, Cambridge, Verenigde Staten
Prof.dr. D. Bouwmeester	University of California, Santa Barbara, Verenigde Staten
Prof.dr. J.A. Folk	University of British Columbia, Vancouver, Canada



Keywords: quantum dots, electron spin, quantum computation,
quantum coherence

Published by: Frank Koppens

Coverimage: A measurement of the spin-states of two electrons
getting disrupted by the nuclear-spin environment
(see chapter 5 and Fig. 5.5)

Cover design by: Judith Steijvers (www.youdidit.nl)

Printed by: PrintPartners Ipskamp

An electronic version of this thesis, including color figures, is available at:
<http://www.library.tudelft.nl/dissertations>

Casimir PhD Series, Delft-Leiden, 2007-13

ISBN: 978-90-8593-037-2

Copyright © 2007 by Frank H.L. Koppens

Voor mijn vader

Preface

After getting my physics masters degree in Eindhoven, I started to work in the energy business for a company called Nuon. About two years later, I realized that I found single electrons more fascinating than billions of electrons moving through thick copper wires. My eye fell on a group called Quantum Transport (QT), and the research on quantum phenomena sounded exciting to me. It was a big change to move back to a lab, but the last four years were the fastest in my life and there was no single moment I regretted my choice. QT is besides the good atmosphere also characterized by people with a wide variation of personalities, all with different interests and approaches. Without this mix of skills and knowledge, the work described in this thesis would not have been possible. I'm very grateful to all who have contributed.

First of all, I want to thank Hans and Leo for making QT a scientific Walhalla. Leo, thanks for sharing your physics knowledge, and for showing me how to distinguish in physics the most important from side issues. Hans, I hope you keep on inventing qubits after your retirement: the perfect qubit is still waiting for the invention by you.

The work described in this thesis is about manipulating single electron spins, with the long-term goal to make spin-qubits. All the spin-qubit work in Delft is carried out in a team of about seven people. When I came to QT, Ronald, Jeroen, Laurens and Lieven were already working in this team for a few years and succeeded in making the Delft spin-qubit a rising star. In the first months, I asked thousands of questions to all of them and there was always time for answers and discussions. Laurens made the fabrication of quantum dots possible in Delft; this work was crucial for all the future spin-qubit work, thanks. Jeroen, thank you for always being there (except in the morning), even during Christmas when you helped me with cooling down a fridge; also, I appreciated your hospitality in Zurich. Ronald, I enjoyed very much our heavy physics debates; it's funny that we discussed more often while you were in Santa Barbara than in Delft. Thanks for this and for teaching me some scientific politics. Lieven, thanks for giving me all the freedom in the lab, for teaching me how to convey a message in papers

and presentations, and for the endless discussions about physics, papers, data or instruments. During my first project, I worked closely together with Joshua Folk, a temporary postdoc in the spin-qubit team. In the beginning, I was surprised that Josh enjoyed fixing a leak in the middle of the night. But soon, I got infected as well which resulted in innumerable measurement sessions in the middle of the night. Josh, thanks for teaching me lots of techniques and tricks, and for sharing your passion for physics with me. Ivo, the guy who wants to make everything faster, thanks for creating a special atmosphere in the lab. I will certainly miss our yells! Katja, you came in the spin-qubit team as a theorist, but it's amazing how fast you learned all the experimental skills. It was a lot of fun working with you and you didn't even get bothered by the way we speak German in the lab. Tristan, thanks for your scepticism (which I even sometimes believed), for bringing quantum optics knowledge to QT and for ALL the discussions.

I enjoyed working with undergraduate students and their contributions are invaluable. Christo, you were always able to give a creative twist to a project. I don't know how you did it, but suddenly it was there: the famous and mysterious "modified picoprobe". Klaas, physics is a lot more fun with your sense of humor, even if you fall asleep when I give you an EBPB introduction at 8am in the morning. Wouter Naber, thanks for being always happy, even after tuning gates voltages for three months. Rutger, thanks for decorating the blackboard with funny characters instead of boring equations. Paul, thanks for being so brave to choose a project about (seemingly boring) noise. Han, I enjoyed your stories about the giraffe. Tjitte, I never saw a student using a 12.000 € oscilloscope for playing a video clip with Katja Schuurman and collecting measurement data at the same time. It was fun to have you in the lab!

Collaborations are crucial for our work, and it is also much more enjoyable to share knowledge, discussions and materials with different groups from all over the world. Werner Wegscheider and Peter Stano from Regensburg, thanks for growing the famous Wegscheider6 heterostructure. It has made our life much more pleasant and stable. Daniel Loss, it was great to have you in our group during your sabbaticals, and thank you for being easily accessible for questions, discussions or just a chat. Your famous "Loss-lectures" have impressed many of us because after a talk of 3 hours, there were still 75 powerpoint slides left. Bill Coish and Daniel Klauser are the nuclear-spin specialists from Basel; thank you for always answering in great detail my endless number of e-mails. I always found it inspiring to discuss with Leonid Levitov and Mark Rudner from MIT; I hope we can continue our (almost) weekly conference calls. David DiVincenzo spent some time in our group; thanks for sharing your very deep and broad knowledge about quantum information. We are lucky to have a number geniuses on the

fourth floor that helped greatly with theoretical insight and understanding our experimental data: Oleg Jouravlev, Jeroen Danon, Miriam Blaauboer and Yuli Nazarov. I never knew whether I should be happy or depressed after sharing new experimental data with Yuli, but that I learned a lot from the discussions is a fact! Together with Omar Usmani, I helped Jos Thijssen with teaching the quantum mechanics course. Jos, it was an honor to get my first teaching experience with someone who wins so often a teaching prize.

If you hear someone whistling in the hall and shouting at French postdocs, it must be Bram; thank you for bringing atmosphere in QT. Remco and Bram, thanks for all your help with fixing, designing and making basically everything that we need for the experimental setups. To see why Raymond was crucial for this thesis work, go to page 92 and look at the vertical axis of the figure. Raymond, thank you for having noise reduction as a hobby. Mascha, thank you for your patience when bonding our dirty samples, and Leo Dam for making cold fingers. Willem den Braver, Willem schot, and Leo Dam: the past four years would have been very depressing without liquid helium supply. Yuki, Ria and Angele, thank you for all kinds of arrangements and paper work.

Besides the lab, the most important place at QT for relaxing and some entertainment is the FFF-lounge. Floor and Floris, we should definitely stick to our yearly gourmet parties. I'm very grateful to all the members of the flux-qubit team who were always willing to share their high-frequency knowledge and instruments. Thank you Kees, Ad, Pol, Patrice, Irinel, Adrian, Thomas, Pieter and Jelle. In particular, I want to thank Pieter for dealing with all the IT miseries of QT. Jelle, writing my thesis at the same time as you did doubled the fun; cool that you realized the CNOT-gate [1] and thanks for providing some additional material to all the work-related mails. Stevan, Juriaan, Georg, Marc, good luck making (double) dots in nanowires and Umberto, Maarten with getting light out of them. Val, amazing how fast you set up the optics lab, good luck with building the futuristic device. Lan, I'm sure you will make the perfect qubit in graphene. We have had two in-house theorists at QT: Bjorn Trauzettel and Patrick Recher, thanks for discussions and for translating our experiments into Hamiltonians. Gary, I will miss your physics encyclopedia (in your head). Some former QT-members will always be remembered. Hubert and Jorden, I will miss our adventures with nitrogen in B013. Pablo, I'm looking forward to the next ICPS; good luck at MIT. Alex, thanks for preventing an explosion of the helium bath. Sami, for helping setting up the Caro fridge. Franck Balestro, Eugen Onac, Patrice Bertet, Jonathan Eroms, Elisabeth Reiger, Adrian Lupascu, Ethan Minot and Yong-joo Doh, thanks for help and discussions.

Friends and family made me realize there is also a different world than a lab

with electron spins and helium. The coffee-conglomeraat guys, Niels, Marcel, Uko and (aspirant-member) Michel: the moments of “onthaasting” were very rare during the last few years, but we should definitely plan our golf surfing trip. Thank you Tom, for pointing out (a long time ago) that a university is not a scary place. I’m the only physicist left of the “Fysisch Dispuut Thales”, but it’s still great to be part of this group of very good friends. The fun of physics can never beat my passion for climbing. I enjoyed weekly indoor-climbing with friends: Remi, Adam, Iris, Idwine, and the bouldering-clan in the globe. I thank my two brothers for accepting that I’m fascinated more by electron spins than cucumbers. Pap, je hebt me laten zien wat doorzetten en hard werken is. Mam, het doet me goed dat je altijd voor me klaar staat. Ik weet dat je zo zal genieten als je dit boekje in handen hebt. Finally, but most important: Heske, some words here are not enough to thank you for your endless support, love and belief in me. I’m happy that you have more patience than I do.

Frank Koppens
August 2007

Contents

1	Introduction	13
1.1	Physical implementations of a qubit	15
1.2	Exploring single electron spins	16
1.3	Outline of this thesis	18
2	Device and measurement techniques	21
2.1	Device fabrication	21
2.2	Device stability	27
2.3	Measurement setup	29
2.3.1	Dilution refrigerator and device cooling	29
2.3.2	Measurement electronics and grounding	29
2.3.3	Wires and filtering	35
2.3.4	High frequency signals	36
3	Interaction of a confined electron spin with its environment	39
3.1	Relaxation and decoherence	40
3.2	Spin-orbit interaction	43
3.3	Interaction with the nuclear spin bath	46
3.3.1	Hyperfine interaction	46
3.3.2	Spin dephasing due to the nuclear field	47
3.3.3	Spin decoherence due to nuclear dynamics	49
4	Electron spin state detection in a double quantum dot	53
4.1	Introduction	54
4.2	Double dot spin states and Pauli spin blockade	55
4.3	Singlet-triplet mixing by the nuclear spins	57
4.4	Oscillating magnetic field and rate equations	61
4.5	Simulation results and physical picture	64

5	Control and detection of singlet-triplet mixing in a random nuclear field	69
5.1	Introduction	70
5.2	Spin blockade	71
5.3	Lifting of spin blockade due to the nuclear field	71
5.4	Singlet-triplet splitting	73
5.5	Competition between exchange interaction and nuclear field	75
5.6	Competition between exchange interaction, nuclear field and external field	78
5.7	Current fluctuations	78
5.8	Conclusions	80
5.9	Additional material	81
5.9.1	Other processes that lead to leakage currents	81
5.9.2	Bistability of the nuclear polarization	81
6	Driven coherent oscillations of a single electron spin in a quantum dot	83
6.1	Introduction	84
6.2	Device and ESR detection concept	85
6.3	Role of the nuclear spin bath for ESR detection	87
6.4	ESR spectroscopy	88
6.5	Coherent Rabi oscillations	90
6.6	Theoretical model	91
6.7	Time evolution of the spin states during RF bursts	93
6.8	Quantum gate fidelity	94
6.9	Additional material	95
6.9.1	Photon assisted tunnelling due to electric fields	95
6.9.2	Additional figures: lifting of spin blockade by nuclear spins or ESR.	98
7	Universal phase shift and non-exponential decay of driven single-spin oscillations	101
7.1	Introduction	102
7.2	Theoretical model	102
7.3	Power-law decay	105
7.4	Phase shift	107
7.5	Additional information	109
7.5.1	Fit procedure	109
7.5.2	Asymptotic expansion	111

Contents

8	Spin-echo of a single electron spin in a quantum dot	115
8.1	Introduction	116
8.2	Free-evolution decay	117
8.3	Spin-echo	120
8.4	Decoherence mechanism	123
8.5	Conclusion	123
9	Coherent control of a single spin with electric fields	125
9.1	Introduction	126
9.2	Device and measurement technique	126
9.3	Spin spectroscopy	128
9.4	Rabi oscillations	129
9.5	Mechanism	131
9.6	Conclusions	134
9.7	Additional material	135
9.7.1	Estimate of the electric field strength at the dot	135
9.7.2	Upper bound on the ac magnetic field strength at the dot	137
10	Conclusions and outlook	139
10.1	Current status	140
10.2	Outlook	141
10.2.1	Longer decoherence times	141
10.2.2	Improving single spin rotations (one-qubit gate)	143
10.2.3	Improving the $\sqrt{\text{SWAP}}$ -gate (two-qubit gate)	144
10.2.4	Improving spin read-out	145
10.2.5	Scaling	145
10.2.6	Long-distance communication	146
10.3	Conclusion	147
	Bibliography	149
	Summary	169
	Samenvatting	173
	Curriculum Vitae	177

Chapter 1

Introduction

Scientific researchers are continuously searching for new technological tools to comprehend and manipulate the basic elements available in nature. They develop experiments and theories that seem at first sight highly abstract, virtually useless and far from meaning anything to our society. Strikingly, it is precisely this attitude of exploring the “extremes of what is possible” which has induced the most significant technological breakthroughs that have seriously affected our society. An important example is the discovery of a means to record the magnetic properties of atomic nuclei, which is now widely applied as an imaging tool in hospitals. Second, the rapid developments in computer industry are based on the invention of the transistor that was a result of fundamental interest in the nature of electrons at the interface between a metal and a semiconductor. Finally, the boost in data storage of the last decade, induced by the discovery of a phenomenon called giant magnetoresistance, was based on research on magnetic layers which are only one nanometer thick.

The realization of these techniques has relied heavily on the knowledge about the most fundamental laws of physics, called quantum mechanics, of which the theory was developed during the last century. Quantum mechanics predicts how electrons move in materials, what processes lead to light emission, what is the source of magnetism et cetera. First, these laws were used to understand *macroscopic* properties of devices and materials, but this has changed since small structures could be made at a scale where we can study and control nature at the *microscopic* scale, at the scale of nanometers. Nanotechnology has made it possible to observe electron tunneling in real-time, one by one [2], or even more striking, to controllable displace atoms, one by one [3]!

At this small scale, the laws of nature exhibit some peculiar properties that contradict our physical intuition. Examples are particles that start behaving like waves, and the striking manifestation of superposition states, where a particle can

exist at multiple positions at the same time. Even more surprising, two particles can share a connection, called entanglement, even if they are separated over a very long distance.

The current status of experiments allow not only for the observation, but also make it possible to *control* these counterintuitive manifestations in very small systems like a single atom or electron. This level of control makes it possible to address important questions about the stability of quantum superpositions and entangled states and how these are affected by measurements or interactions with the environment. It is still a big open question to what extent macroscopic systems can be in superposition states, and if not, where and why the transition to the “macroscopic” world occurs. Currently, experiments are being developed to study these phenomena. Examples are the observation of interference of large molecules with themselves [4], coupling a small well-defined quantum system with a macroscopic system like a tiny mirror [5], and the preparation of large numbers of photons in a superposition state [6].

In parallel to addressing these fundamental issues, we can raise the question whether this high level of control over small quantum objects can form a useful basis for technological applications. It is too early to say whether applications will indeed fully exploit the fundamental resources available in nature, but major conceptual breakthroughs have already been realized. For example, entangled states have proven a valuable resource for novel quantum communication protocols, such as quantum cryptography [7], which is fundamentally unbreakable. Implementations of these protocols are already commercially available! Another development is a result of the dramatic developments in the computer industry, where logic gates and wires become a factor of two smaller every two years and soon might consist of only a few atoms. This is the scale where the laws of quantum mechanics will be encountered. Remarkably, instead of dealing with the quantum properties, it is also possible to exploit the quantum properties. This makes a new and much more powerful type of information processing possible, based on the existence of superposition states and entanglement [8, 9].

A so-called quantum computer would, rather than classical bits which are either 1 or 0, use qubits, which can be in a superposition of both 1 and 0 simultaneously. The idea is that if a quantum computer has N such qubits, these can then be entangled to represent 2^N values at the same time. By processing each of these values simultaneously, a quantum computer could, in principle, operate exponentially faster than its classical counterpart. Quantum algorithms can turn certain classes of hard mathematical problems into easy ones; the factoring of large numbers is an important example [8]. In fact, the first proposal to develop a quantum computer [10] was inspired by the prospect that quantum computers

1.1 Physical implementations of a qubit

can efficiently simulate complex quantum systems [11] like high temperature superconductors, quantum magnets or chemical compounds and reactions. These simulations would take a classical computer longer than the age of the universe.

1.1 Physical implementations of a qubit

An implementation of a qubit, useful as a basis for a quantum computer, should meet a number of requirements [12]. First of all, we need a quantum-mechanical two-state system with very precise and fast control of its quantum state. The second ingredient is a universal two-qubit gate, based on the interaction between two qubits. This interaction, which causes entanglement, should ideally be switchable but a fixed interaction is in some cases sufficient. The last, but most stringent criterium is related to a general problem with the fragile superposition and entangled states. Namely, quantum information is easily lost into the environment, causing errors in the computation. This process is called decoherence. Fortunately, if errors induced by decoherence are small enough, it is possible to correct them faster than they propagate. The requirements for the implementation of error correction are hard but not impossible to meet. The exact error-threshold (error allowed per operation) depends on the type of decoherence and the architecture, but currently it is believed to be around 10^{-4} . This implies that at least 10^4 operations within the coherence time of the qubit should be performed.

Since the invention of quantum error correction, a large number of physical qubit implementations have been proposed and a part of these are under experimental investigation. Among these are atomic systems such as:

- cavity quantum electrodynamics systems [13]
- atoms in an optical lattice [14]
- ions in electrostatic traps [15]
- ensembles of nuclear spins in a liquid [16]

and solid state systems such as:

- superconducting circuits containing Josephson junctions [17]
- electrons floating on helium [18]
- nuclei of implanted phosphorous in silicon [19]

- single electron spins trapped in quantum dots [20], (implanted) impurities in silicon [21] or nitrogen-defects in diamond [22].

With nuclear magnetic resonance techniques, a quantum algorithm has already been demonstrated, using seven quantum bits [23]. However, this system cannot be scaled up to a large number of qubits. In trapped ion systems, impressive experiments with up to eight qubits have been performed, for example demonstrating error-correction [24], multi-qubit entanglement [25] and quantum teleportation [26]. Although atom systems are generally difficult to scale, efforts towards a scalable ion trap system have so far been made, such as shuttling ions between different zones [27] or fabrication of ion traps on a solid state device [28]. In solid-state systems, scaling is in principle easier to realize because the fabrication technique for one qubit is the same as for a large number of qubits. However, with these systems it is more difficult to combine long coherence times with a sufficiently high level of control.

In summary, it is not yet clear which system will meet the scalability condition and the necessary requirements mentioned above. In any case, exploring these systems has so far been extremely helpful in gaining more knowledge about different techniques and coherence properties of a wide variety of quantum systems. This has triggered the development of new, improved or hybrid qubit implementations. Likely, the perfect qubit is still waiting for its invention.

1.2 Exploring single electron spins

The magnetic moment of the electron, called spin, is a property that has been used in a variety of applications like memory devices. More recently, a large number of potential advantages of the spin degree of freedom were recognized, such as increased data processing speed, low-dissipation and nonvolatility [29, 30]. This has spawned in a new research field called spintronics aiming at controlling electron spins in metals or semiconductors, and developing devices like spin transistors, spin LED's or magneto-optical elements. In parallel, advances in nanotechnology has made it possible to fabricate devices in which only a small number electrons can be confined electrically, so-called quantum dots. Many parameters of these "artificial atoms" are in-situ tunable, simply by tuning the voltages on the gates, and this has delivered very interesting studies on fundamental quantum mechanical properties. These rapid developments triggered the idea that confined electron spins could represent a quantum bit where spin-up and spin-down states in a magnetic field represent the qubit states [20]. This was supported by the expectation that an electron spin is well protected against

1.2 Exploring single electron spins

decoherence because most fluctuations in the environment couple directly only to the electron charge.

Since the two earliest spin-qubit proposals were launched [20, 31], several systems have been developed to isolate and manipulate single electron spins:

- nitrogen-vacancy (N-V) centers in diamond
- strain-induced (self-assembled) quantum dots
- phosphorus donor impurities in silicon
- quantum dots defined in one-dimensional carbon nanotubes or semiconductor nanowires
- quantum dots defined in a two-dimensional electron gas with metallic gates
- surface acoustic waves

In most of these systems, coupling of the qubits is possible via the Heisenberg interaction, which is based on the exchange symmetry and electrostatic interaction between electrons. This interaction requires some overlap between the electron wavefunctions, but if the spins cannot be brought close together, the electron spin interaction can be mediated by a cavity photon [31]. This requires optical access of the spin, as is the case for N-V centers and self-assembled dots.

Single-qubit operations can be performed via electron spin resonance induced magnetically, or electrically when the electron orbital is coupled to its spin state. This coupling is possible, for example via a magnetic field gradient [32], varying g-tensor [33] or through the spin-orbit interaction [34]. For optically accessible spin systems, single-qubit operations are in principle also possible via the optical stark effect [35] or Raman-resonance [31].

The experiments presented in this thesis are performed on spins in quantum dots that are defined in a two-dimensional GaAs/AlGaAs electron gas with metallic gates. Since the spin-qubit proposal for gated quantum dots published about nine years ago, there has been enormous research efforts by a large number of groups in realizing the basic spin-qubit elements. First, specific gate designs were developed to isolate a single electron in each of two coupled quantum dots. Next, the development of fast gate pulsing [36] and charge sensing techniques [37] allowed for the observation of single electron tunneling events [2, 38] and measurements of the spin relaxation time [36, 39, 40]. In combination with spin-dependent tunneling events, this enabled single-shot read-out of a single electron spin [41, 40]. The foundation of the two-qubit gate was laid by performing fast switching of the exchange interaction between two electron spins, which resulted

in the observation of the coherent evolution of two-electron spin states [42]. In combination with driven coherent rotations of a single spin, this forms the required set of universal quantum operations.

In this thesis, we demonstrate the coherent manipulation of a single electron spin, and we study the coherence properties of one and two-electron spin states. The goal is to prove experimentally the ability to rotate the electron spin to any arbitrary superposition state, using both magnetically and electrically induced spin resonance. The purpose of the coherence measurements is to resolve the most important microscopic decoherence processes and to explore ways to suppress these. Together with the research efforts from other groups, the presented results form the basis for the implementation of simple quantum algorithms using electron spins. Furthermore, the existing techniques can be combined to make experiments possible that reveal the exciting properties of quantum mechanics, like the effects of weak measurements or the demonstration of entanglement via the violation of Bell's inequalities.

1.3 Outline of this thesis

The content of this thesis is as follows. In **chapter 2**, we start with a description of the fabrication process of few-electron lateral quantum dot devices. We will discuss the fabrication and functionality of an on-chip coplanar stripline to guide high-frequency signals, fabricated on top of the quantum dot device, separated by a dielectric layer. Next, we will address the charge stability of the quantum dots, and techniques to improve this. Finally, we give a detailed description of the measurement set-up and techniques. **Chapter 3** provides a theoretical description of the most important interactions of the electron spin with its environment. These are the electron-phonon interaction together with the spin-orbit coupling, and the hyperfine interaction with the nuclear spins in the host semiconductor lattice. **Chapter 4** summarizes the theory of two-electron spin states in a double quantum dot and the detection of spin dynamics via spin-dependent transport through the dots. This forms the most important detection tool for the work in this thesis.

We show in **chapter 5** that the spins in the quantum dots experience a random background field caused by the nuclear spins in the substrate, leading to the hybridization of two-electron singlet and triplet states. We demonstrate that the hybridization between these spin states can be suppressed by increasing the double dot singlet-triplet splitting. In **chapter 6**, we demonstrate the coherent manipulation of a single electron spin confined in a quantum dot. By generating

1.3 Outline of this thesis

bursts of an oscillating magnetic field at the location of the quantum dot, we observe Rabi oscillations of the electron spin. Two unusual features in these Rabi oscillations are analyzed in more detail in **chapter 7**. Due to the long correlation time of the nuclear spin bath, the decay follows a power law, and the oscillations are shifted in phase by a universal value of $\sim \pi/4$. These properties are well understood from a theoretical expression that we derive in the static limit for the nuclear bath.

In **chapter 8**, we present measurements of the coherence properties of the electron spin. Via sequences of bursts, we measure the free evolution coherence decay time, which is well-understood as dephasing due to the interaction with the nuclear spins. We reverse this dephasing to a large extent via spin-echo, and find a lower bound on the spin coherence time of $0.5 \mu\text{s}$. We demonstrate in **chapter 9** that coherent control of the electron spin can also be achieved with AC *electric* fields. Our analysis and measurements of the magnetic field dependence suggest that the driven spin transitions are mediated by the spin-orbit interaction. The conclusions, outlook and some ideas for future directions will be presented in **chapter 10**.

Chapter 2

Device and measurement techniques

2.1 Device fabrication

Fabrication of lateral gated quantum dots starts with a semiconductor heterostructure, a sandwich of different layers of semiconducting material (see Fig. 2.1a). These layers, in our case GaAs and AlGaAs, are grown on top of each other using molecular beam epitaxy (MBE), resulting in very clean crystals. By doping the n-AlGaAs layer with Si, free electrons are introduced. These accumulate at the interface between GaAs and AlGaAs, typically 100 nm below the surface, forming a two-dimensional electron gas (2DEG) – a thin (~ 10 nm) sheet of electrons that can only move along the interface. The 2DEG can have a high mobility and relatively low electron density (typically $10^5 - 10^6$ cm²/Vs and $\sim 3 \times 10^{15}$ m⁻², respectively). The low electron density results in a large Fermi wavelength (~ 40 nm) and a large screening length, which allows us to locally deplete the 2DEG with an electric field. This electric field is created by applying (negative) voltages to metal gate electrodes on top of the heterostructure (Fig. 2.1b,c). When choosing the gate structure properly, these electric fields lead to the formation of one or more small islands that are isolated from the large 2DEG reservoirs. These islands are the quantum dots.

Electron-beam lithography, which defines the gate pattern (Fig. 2.1d), consists in general of the following steps. First, we spin a layer of organic resist (poly-methyl-methacrylate, PMMA) on the heterostructure surface (Fig. 2.2a). Then the pattern is defined by writing with a focused electron-beam in the electron-sensitive resist. This locally breaks up the polymer chains, so that the exposed parts can be removed by a developer (solution of methyl isobutyl ketone, MIBK, and iso-propyl alcohol, IPA), see Fig. 2.2b. In the next step (Fig. 2.2c), metal is evaporated, which only makes contact to the heterostructure at the places where the resist has been exposed and removed. The last step is the removal of the

2. Device and measurement techniques

remaining resist by acetone (Fig. 2.2d). In this process, the metal on top of the resist is removed as well, the so-called ‘lift-off’. The lift-off process is facilitated by the undercut in the resist layer. Now metal electrodes are left at the places that were exposed to the electron-beam.

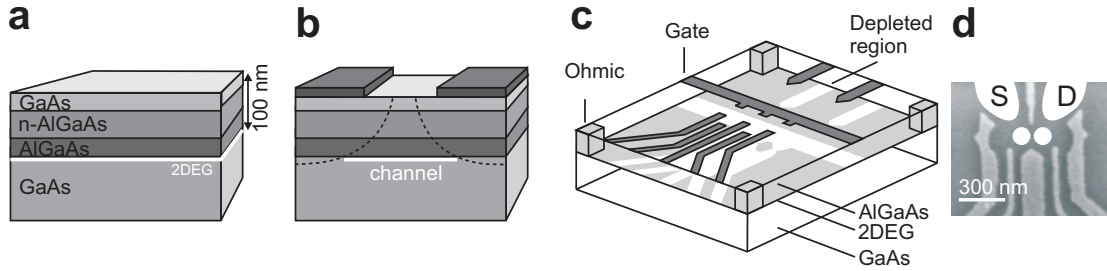


Figure 2.1: Confining electrons in a semiconductor. **(a)** Semiconductor heterostructure containing a 2DEG (indicated in white) approximately 100 nm below the surface, at the interface between GaAs and AlGaAs. The electrons in the 2DEG result from Si donors in the n-AlGaAs layer. (The thickness of the different layers is not to scale.) **(b)** By applying negative voltages to the metal electrodes on the surface of the heterostructure, the underlying 2DEG can be locally depleted. In this way, electrons can be confined to one or even zero dimensions. **(c)** Schematic view of a lateral quantum dotdevice. Negative voltages applied to metal gate electrodes (dark gray) lead to depleted regions (white) in the 2DEG (light gray). Ohmic contacts (light gray columns) enable bonding wires (not shown) to make electrical contact to the 2DEG reservoirs. **(d)** Scanning electron microscope image of an actual device, showing the gate electrodes (light gray) on top of the surface (dark gray). The two white dots indicate two quantum dots, connected via tunable tunnel barriers to a source (S) and drain (D) reservoir, indicated in white.

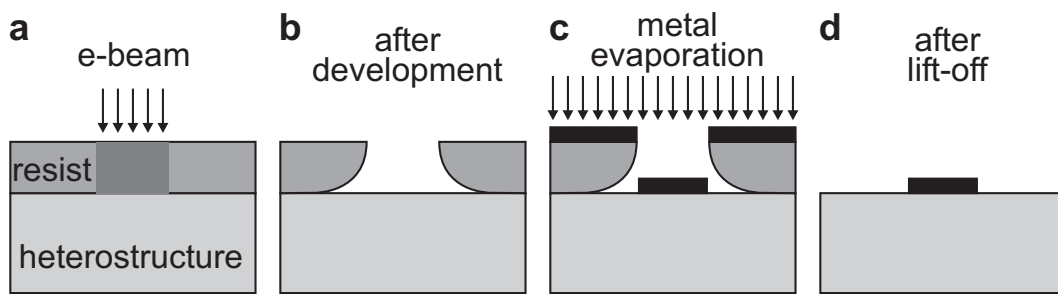


Figure 2.2: Fabrication of metal electrodes on the surface of the heterostructure. **(a)** Writing a pattern in the resist layer with an electronbeam. **(b)** After developing, the resist has been locally removed. **(c)** Evaporating metal. **(d)** After lift-off, a metal electrode remains.

2.1 Device fabrication

The fabrication of a gate-defined quantum dot device consists of a series of steps (Fig. 2.3) [43]:

1. The definition of the **alignment** markers, which are $20\ \mu\text{m} \times 20\ \mu\text{m}$ squares of 50/150 nm Ti/Au. These structures are made using electron-beam lithography. We note that the alignment of the coplanar stripline and the finegates has to be very accurate (within 50 nm), and therefore, we use two times four alignment markers per chip. The other fabrication steps are aligned by using four markers for a large number of chips (in our case 52).
2. The second step is the etching of the **mesa** which is performed to electrically isolate conducting regions on the chip. We write an inverted pattern with the electron beam in a single layer of PMMA resist. We etch about 120-150 nm (about 30-60 nm more than the 2DEG depth) at a temperature of 10° in a solution of $\text{H}_2\text{O}_2 : \text{H}_2\text{SO}_4 : \text{H}_2\text{O}$ mixed in a ratio of 1:5:25.
3. The **ohmic contacts** make electrical contact between the reservoirs and metal bonding pads on the surface (see step 5). We make them by rapid thermal annealing (at 400°C for 60 sec) of an evaporated sandwich of Ni/AuGeNi (5/150/25 nm). The pattern is defined by electron-beam lithography and we use a bi-layer of organic resist to improve the undercut. This facilitates the lift-off. The ohmic contacts have a resistance of about 1 kOhm. Metal wires bonded to these pads run toward the current or voltage probes, enabling us to perform transport measurements.
4. The **finegates** define the quantum dot pattern which has the smallest dimensions of only about 20 nm. This makes the definition of the finegate pattern the most crucial electron-beam lithography step. Because the thickness of the 10/20 Ti/Au finegates is also very small, we use a single layer resist and clean the structure before evaporation with diluted sulphuric acid (1:5 $\text{H}_2\text{SO}_4/\text{H}_2$). The thin (10 nm) layer of titanium is used as a ‘sticking’ layer for the gold. The electron beam can accurately write with a resolution of about 5 nm, but in practice the minimal width of a gate electrode is about 20 nm, limited by the development and the lift-off step.
5. The **large gate** pattern connects the finegates to the large pads on the outside of the chip, used for wire bonding. The pattern is defined by electron beam lithography and we use a bi-layer of organic resist to improve the undercut. A rather thick layer of metal (50/150 nm Ti/Au) is evaporated in order to overcome the transition from unetched to etched mesa.

2. Device and measurement techniques

6. As a **dielectric**, we used calixarene [44], which is an organic material and can be dissolved in chlorobenzene. The solution is spin coated on the device and electron-beam lithography is used for writing the pattern. The high degree of electrical isolation of the calixarene and its apparent small contribution to charge noise (see section 2.2) makes it very suitable for the realization of an on-chip CPS. Furthermore, this type of dielectric allows for the development of devices with increasing flexibility via extra layers of gates.
7. In order to generate a strong AC magnetic field at the location of the quantum dot, we fabricated an on-chip **coplanar stripline** (CPS) on top of the surface gates and dielectric (see Fig. 2.4). A CPS consists of two parallel sheets of metal on the surface of a dielectric layer and is designed to carry electromagnetic fields in a large bandwidth over long distances. The two sheets of metal confine the electromagnetic field similarly as in the case of a coax cable. By shorting the two sheets of the CPS close to the quantum dot, a local source of magnetic flux is created. The CPS itself is designed to match the 50Ω impedance of the coax line in the dilution refrigerator to minimize power loss due to reflections. The connection from coax cable to the CPS is made by a modified picoprobe to the two sheets of metal on the chip. We fabricate the shorted CPS similar as the large gate pattern.

2.1 Device fabrication

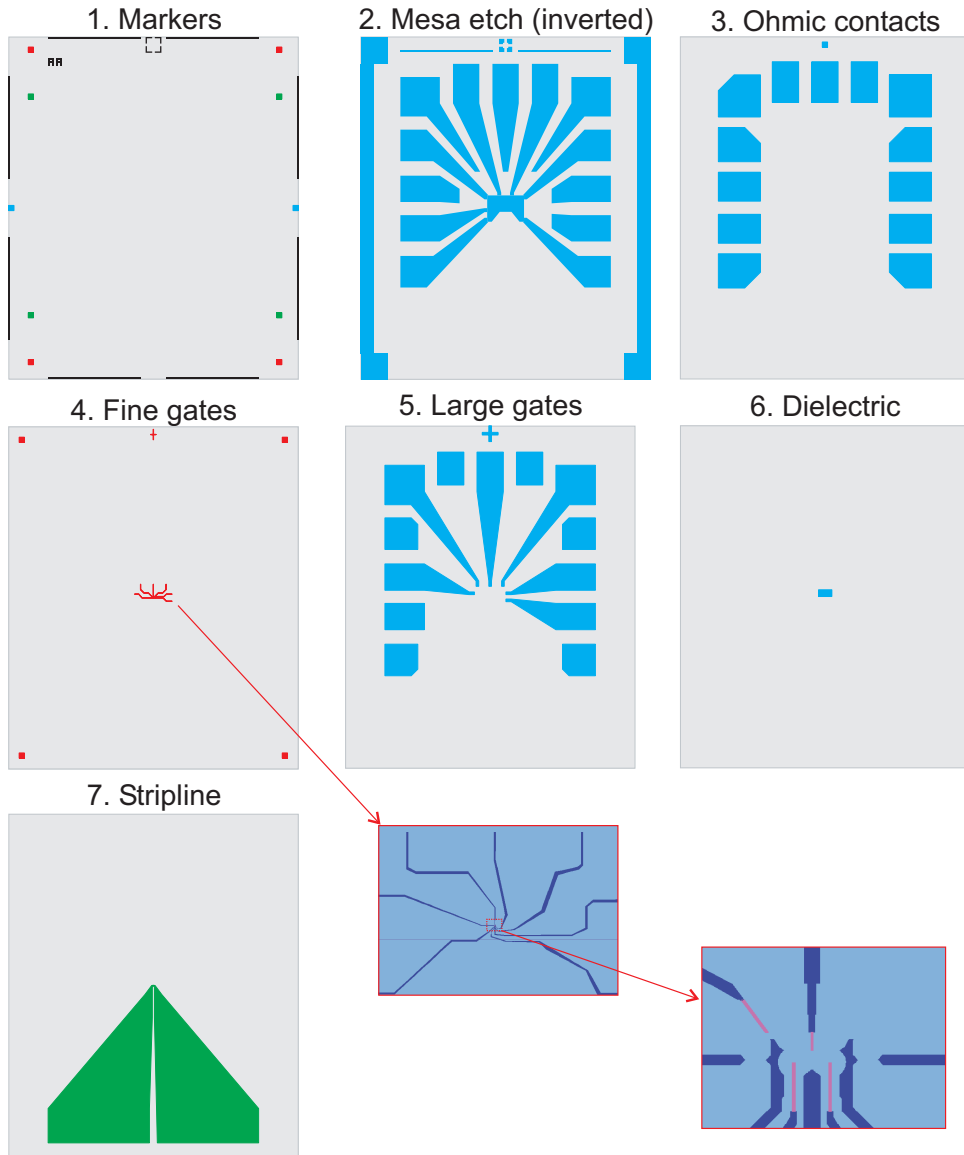


Figure 2.3: Fabrication steps for lateral quantum dot device with coplanar stripline on top of the gates. The color of the structures is associated with the color of the respective alignment markers.

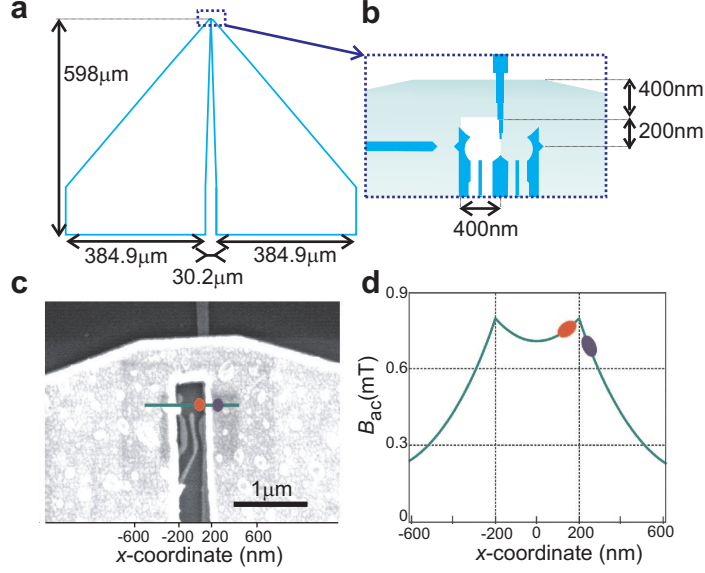


Figure 2.4: (a) Schematic diagram of the on-chip coplanar stripline. The CPS is terminated by a narrow wire that shorts the two planes. The wire effectively acts as a shorted termination of the $50\ \Omega$ transmission line and therefore the current will exhibit an anti-node at the wire. (b) Schematic diagram showing the termination of the stripline and the position of the surface gates that define the double quantum dot. The design is optimized to maximize B_{ac} at the location of the dots. (c) SEM image of a device similar to the one used in the experiment of chapter 6. The termination of the CPS is visible as well as part of the surface gates that define the dots. The estimated locations of the two quantum dots are indicated in red and blue. (d) Amplitude of the oscillating magnetic field perpendicular to the plane, 200 nm below the CPS, along the green line in (c) ($P=-22\ \text{dBm}$, $f=200\ \text{MHz}$), computed numerically using CST Microwave Studio. This program solves the integral form of Maxwell's equations with the finite difference time domain method for a discretised spatial domain. In the simulation, an ideal waveguide source is connected to the CPS, through which a quasi-TEM wave will propagate. The approximate x-coordinates of the dots are indicated in blue and red. Based on these simulation results, we expect a field of $B_{ac} \sim 0.7\ \text{mT}$ for a $-22\ \text{dBm}$ excitation (corresponding to $I_{cps} \sim 1\ \text{mA}$) at 200 MHz. Furthermore, we expect the fields in the two dots to differ from each other by no more than 20%.

2.2 Device stability

Lateral gated quantum dots are extremely sensitive to fluctuations in their local electrostatic environment. These random fluctuations provide one of the most important obstacles when operating such devices as spin qubits. Although the origin of switching noise observed in GaAs/AlGaAs 2DEG devices is not yet fully understood, the switching events are attributed to changes in the charge states of electronic traps.

It has been experimentally found that charge noise in quantum dot devices can be reduced by applying a positive voltage to the surface gates during cool down of the device. Due to the electric field, the conduction band edge at the donor sites will be lowered relative to the Fermi level, leading to a higher population of DX states (donor related defects [45]) under the gates. After removal of the bias voltage, this enhanced DX population is frozen in, and the sample behaves as if there was a built-in gate voltage. Therefore, less negative voltages have to be applied to the gates to form the quantum dot. Apparently, this reduces the charge noise.

To show that indeed the DX states are populated with charges, we have studied the response to bias cooling as a function of the Al-concentration x in the AlGaAs-layer. We found that for $x = 0.1$, bias cooling had no effect on the built-in gate voltage, whereas we found a strong effect for $x = 0.3$. The reason is that the energy of the DX-states depends on x . For $x > 0.22$, the DX-state is located in energy below the conduction band, and therefore, it will be very effective in capturing electrons. On the other hand, if the DX states are located above the conduction band, the response will be negligible as the DX-centers are not effective in capturing electrons.

The reason why a lower gate voltage reduces charge noise is not yet fully understood, but in [46] it is proposed that the origin of charge noise is due to temporary trapping of electrons leaking through the Schottky barrier. It is suggested that this leakage can be reduced by bias cooling, requiring less negative gate voltages when forming the quantum dot. We have found additional evidence for this hypothesis by using the coplanar stripline on top of a dielectric as a depletion gate as well. Whereas surface gates can induce electron leakage through the Schottky barrier, no leakage is expected from the stripline through the dielectric to the semiconductor. We observed a dramatic reduction of the noise level in a quantum point contact when making the voltage difference between stripline and 2DEG more negative (Fig. 2.5). Again, the voltages needed on the local gates were less negative than otherwise. Applying this method as well when forming a quantum dot allowed us to reduce the charge noise level much further than what

2. Device and measurement techniques

would have been possible with bias cooling only. Namely, bias cooling is limited by the maximum positive voltage that can be applied during cool down (~ 700 mV \sim Schottky barrier height). In contrast, stabilizing with a gate on top of a dielectric is possible with voltages until the dielectric breaks down, which are in general higher ($\sim 2 - 3$ V for our devices), although the capacitive coupling of the stripline to the 2DEG is smaller than for a normal gate. Furthermore, we can enhance the stabilization effect by applying a positive voltage to the stripline during cool down.

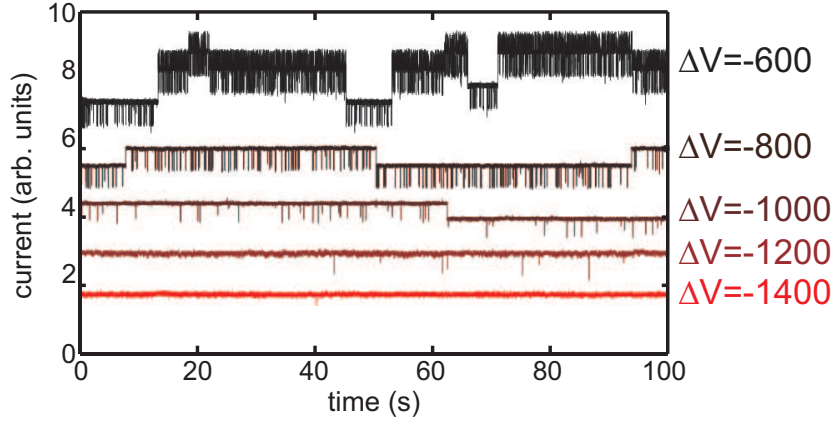


Figure 2.5: Current through a quantum point contact (QPC) as a function of voltage difference ΔV between the stripline and 2DEG. The Schottky gates defining the QPC are retuned for each ΔV such that the average QPC-conductance remains constant. Because one side of the stripline is connected to ground, it is not possible to apply a voltage directly to the stripline. Still, an equivalent -2 V bias of both branches of the stripline can be realized by biasing the reference of the voltage sources and I/V converter (connected to the gates and the 2DEG) by +2 V.

2.3 Measurement setup

2.3.1 Dilution refrigerator and device cooling

In order to isolate an electron spin in a quantum dot well enough from the electrons in the reservoirs (of the 2DEG), the device temperature should be well below 1K. We use a Kelvinox 400 dilution refrigerator to cool down the device to a temperature of about 10-40 mK (with a cooling power of $400 \mu W$ at 100 mK). Although phonons in the semiconductor lattice will have a similar temperature as the base temperature of the refrigerator, the electron temperature of the 2DEG is higher, around 100 mK, which has two reasons. First, due to weak electron-phonon coupling, electrons are cooled mostly via DC wires which are connected to the source/drain contacts. Furthermore, they are susceptible to radiation or noise in the DC wires which are connected to source/drain contacts. In order to suppress radiation, the device is in a copper can which is cooled as well to base temperature, protecting the device from the 4 K radiation of the inner vacuum chamber (IVC). In order to suppress the noise in the DC wires, we use different filtering stages at different temperatures and covering different frequency ranges. This will be discussed in section 2.3.3. The cold finger, which connects the device to the dilution stage of the refrigerator, together with the different filtering stages is shown in Fig. 2.6.

2.3.2 Measurement electronics and grounding

Typical measurements on the device involve electron transport through the quantum dots as a function of source-drain voltage and the applied voltages to the gates. The implementation of this circuit in the dilution fridge is shown in Fig. 2.8. The measurement electronics that are connected to the device, i.e. I-V converter, voltage source and digital-to-analog converters, contain isolation amplifiers. This isolates the device from external measurement devices (containing switching elements creating input spikes) and from the GPIB-bus that creates charge injections at the input terminals. In addition, all the circuitry at the sample side is analog (no clock frequencies) and battery-powered (does not contain 50 Hz noise).

For the experiments discussed in this thesis, we use a low bandwidth I-V converter with a noise floor of $5 \text{ fA}/\sqrt{Hz}$. The amplifier gain A can be chosen to be 10000 or 1000 respectively for lower input resistance (and thus higher bandwidth)

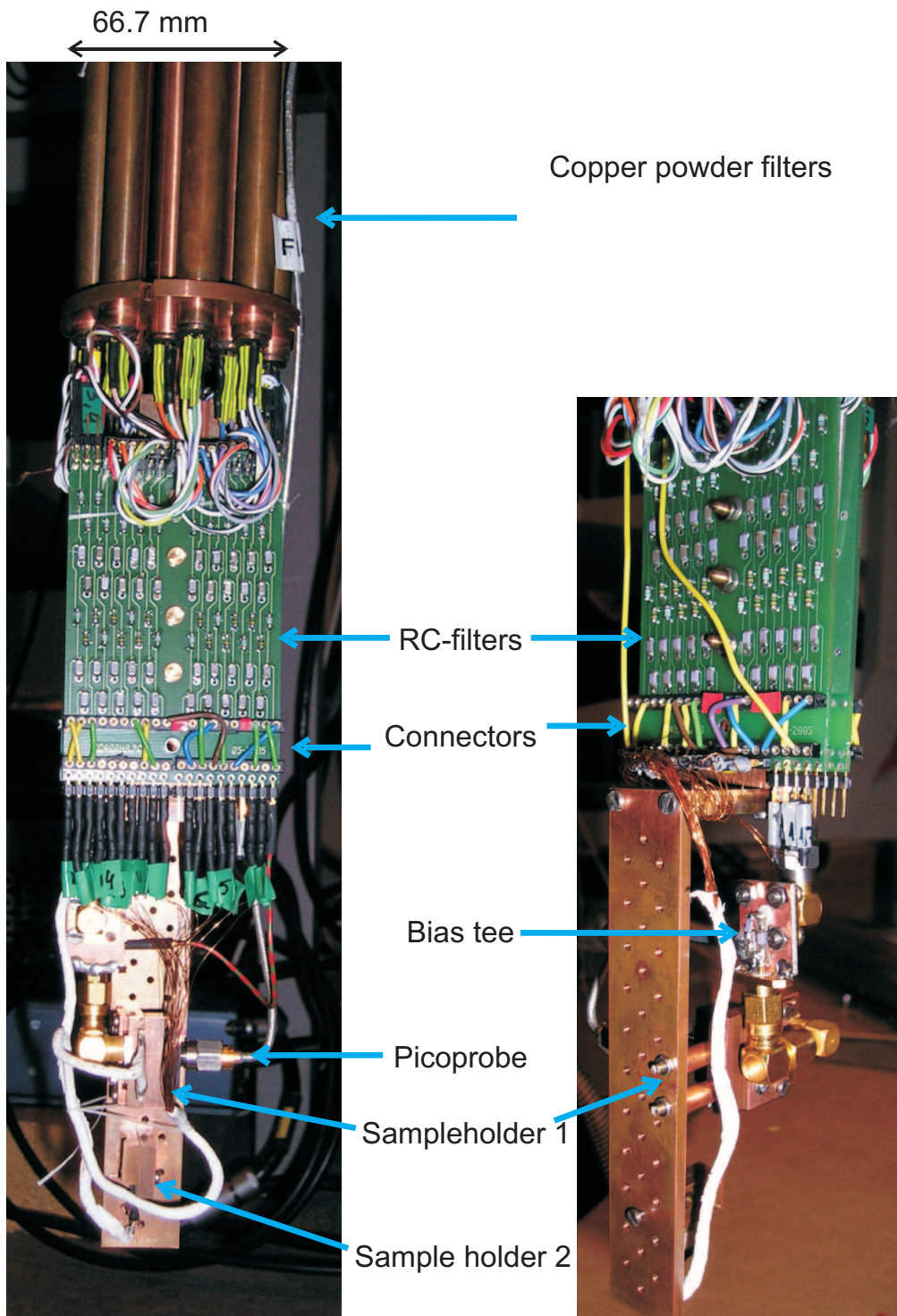
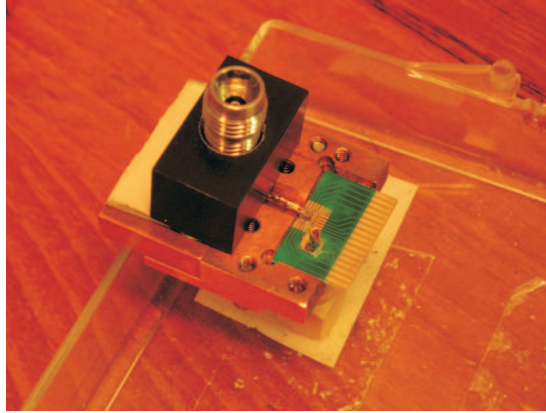


Figure 2.6: Coldfinger with device, RF-filters and copper powder filters.

2.3 Measurement setup

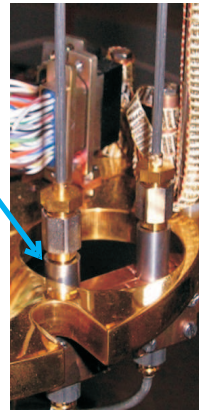
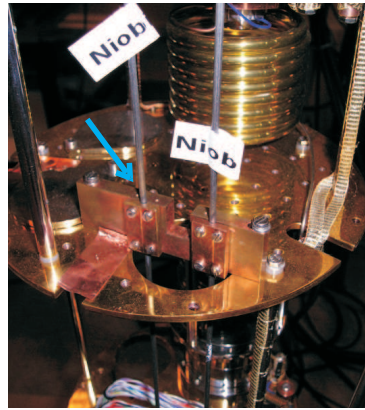
a Picoprobe



b Coax anchoring

Outer conductor

Inner conductor



c Bias tee

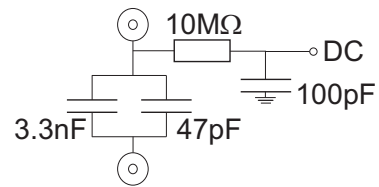
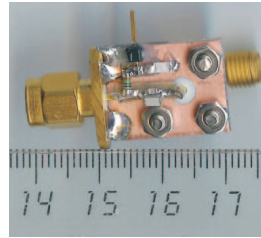
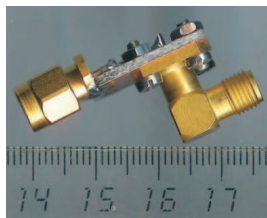


Figure 2.7: (a) Modified picoprobe contacting the coplanar stripline. (b) Thermal anchoring of the coax lines. (c) Home-made bias tee.

2. Device and measurement techniques

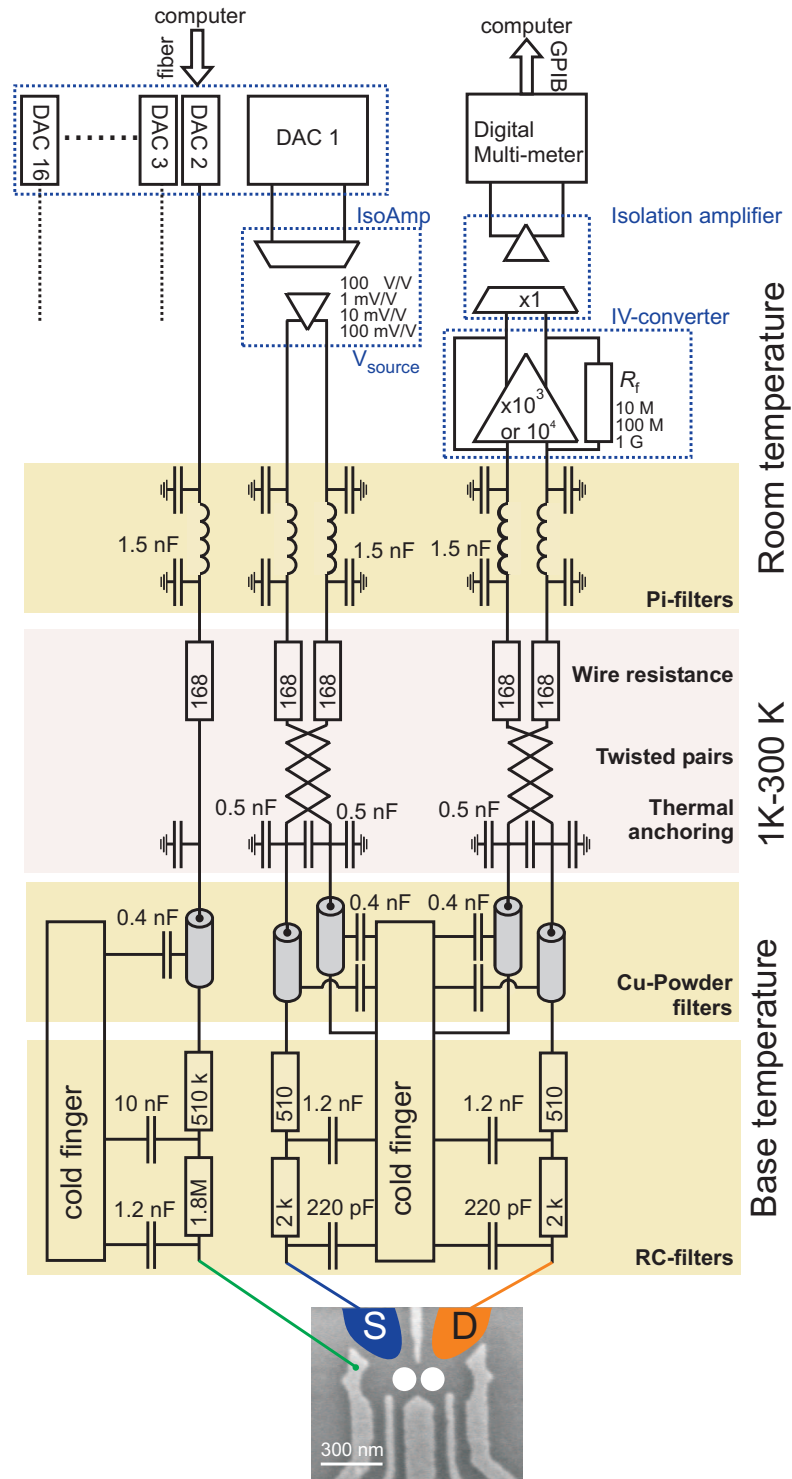


Figure 2.8: Electrical circuit for applying voltages to the gate electrodes, and for performing a voltage-biased current measurement

2.3 Measurement setup

or lower noise¹. Because the amplifier is at room temperature, the absolute noise floor of the IV-converter is limited by the Johnson noise V_J of the feedback resistor, which is given by $V_J\sqrt{\frac{4kT}{R_f}} = 4fA/\sqrt{Hz}$ for $R_f = 1\text{ G}\Omega$ (see Fig. 2.9b for a measured spectrum of this noise floor).

In order to achieve this noise floor, other noise sources need to be suppressed. An important second noise source is the noise generated within the amplifier. This can be considered as an equivalent voltage (V_n) and current noise (I_n) source at the two inputs of the amplifier, as illustrated in Fig. 2.9a. Compared to the Johnson noise of R_f , we can neglect I_n , but the contribution from V_n (of order 5-100 nV/ \sqrt{Hz}) to the output noise can be relatively large, depending on the impedance Z_s at the inverting input of the amplifier (consisting of R_s and C_s). This can be seen directly from the relation $V_0 = V_n\frac{A}{1+AK} + V_J$, with $K = \frac{Z_s}{Z_s+Z_f}$. We consider first the case when $Z_s \gg Z_f$ (open IV-converter). Then, $V_0 \sim V_n + V_J$, where V_n does hardly contribute to V_0 because $V_n \ll V_J$.

In contrast, if Z_s is small compared to R_f , a current will flow through Z_s and R_f and we find an increasing amplifier noise contribution for decreasing Z_s : $V_0 \sim V_n Z_f/Z_s$ for $1 \ll Z_f/Z_s \ll A$ and $V_0 \sim AV_n$ for $Z_f/Z_s \gg A$. Therefore, due to the capacitive coupling of the DC-wires to the dilution refrigerator and the capacitors in the filters (Pi-filters and RC-filters, see Fig. 2.8) the contribution from this noise source becomes more important at higher frequencies. For example, if $C_s=3\text{ nF}$, $f=10\text{ Hz}$ and $R_f=1\text{ G}\Omega$, we find $Z_f/Z_s = 200$, implying a significant amplification of the amplifier noise by a factor of 200. A measurement of the amplifier noise V_n is shown in Fig. 2.9c (obtained by shorting the input and using the relation $V_0 = AV_n$). Together with the Johnson noise of the feedback resistor, we obtain a noise spectrum which is representative for our set-up (Fig. 2.9d). We find a noise floor of $5fA/\sqrt{Hz}$ at zero Hz and a linear increase for increasing frequencies, which is due to the amplifier noise and the wire/filter capacitances. In our set-up, we have chosen the highest RC-filter capacitance such that we have a good compromise between low-pass filtering and mitigation of the amplifier noise, provided that we measure with a bandwidth less than 10 Hz. We remark that other noise sources can be ignored or were eliminated. Examples are the Johnson noise from the DC wires ($168\text{ }\Omega$ gives at room temperature $1.6\text{ nV}/\sqrt{Hz} < V_n$) or magnetic fields coupling to a wire loop via induction. The latter is reduced dramatically by using twisted pairs (see Fig. 2.8).

Another important noise source, which occurs predominantly at 50 Hz or

¹Via the feedback loop, the voltage noise of the amplifier is sent back to the device. This so-called “kickback” drops partially over R_f/A , and therefore, lower noise is achieved with smaller amplification. To prevent “kickback” over a large bandwidth, A is frequency dependent with a cutoff around 85 Hz.

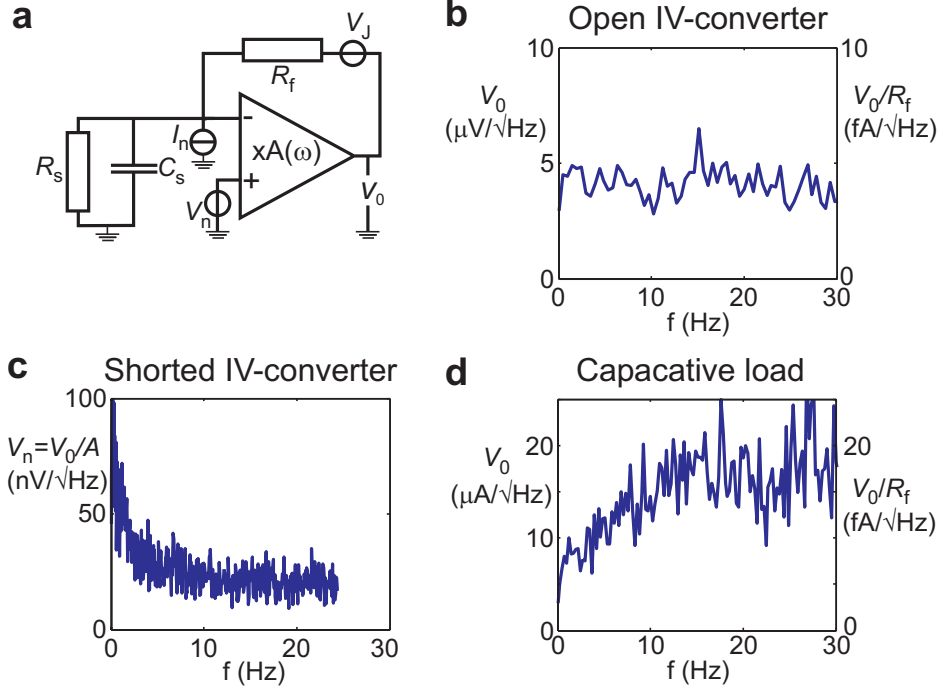


Figure 2.9: (a) Schematic of the IV-converter. R_f is the feedback resistor, and R_s, C_s are the resistance and capacitance of the wires, filters and sample. The voltage and current noise (V_n and I_n) of the amplifier are shown as equivalent voltage and current sources. (b) Output noise voltage V_0 when the input of the IV-converter is open. In this case, only the Johnson noise V_J from the feedback resistor $R_f = 1 \text{ G}\Omega$ contributes to the noise at the input. The amplifier voltage noise V_n at the non-inverting input is exactly the same as the inverting input and therefore, does not contribute to V_0 . (c) Spectrum of the amplifier voltage noise V_n , measured via the output noise voltage $V_0 = VA$ (here, $A=1000$) when the input of the IV-converter is connected to ground. The measurement corresponds reasonably well with the specifications of the most important amplifier in the circuit (CMOS operational amplifier, type TLC2201). (d) Output voltage noise V_0 when the input of the IV-converter is connected to a DC-wire in the dilution fridge including the Pi-filter and RC-filter. At 25 Hz the signal saturates which is due to the cutoff of A .

multiples of this, are the ground loops which are currents that flow through the circuit if different parts of the circuit have different ground definitions. To minimize ground loops, we define only one ground and connect all the instruments (including the magnet) and the main bath of the dilution refrigerator to the socket corresponding to this ground. Also, the ground shield of the output of the isolation amplifier (IsoAmp), as well as the box of the matrix rack should be connected to this ground. It is important to prevent that the dilution refrigerator is in any other way electrically connected to another possible ground definition.

2.3 Measurement setup

To achieve this, we use plastic pump line connections. Also, the measurement electronics are isolated from other possible ground definitions via plastic screws or rubber.

From the noise characterization it is clear that high bandwidth measurements in a dilution fridge are tedious due to the capacitances of the DC-wires. One way to improve the bandwidth is to use a JFET amplifier, which has a smaller amplifier noise ($\sim 1 \text{ nV}/\sqrt{\text{Hz}}$; note that here the Johnson noise of the DC wires becomes relevant!). However, most ideally, one would like to be able to eliminate the contribution from the capacitances, which can be achieved with a low-temperature amplifier [47] or by using the technique of radio frequency reflectometry [48].

2.3.3 Wires and filtering

In order to connect the source/drain contacts and the gates of the device to the room temperature electronics, 2 times 12 twisted pairs of wires run from room temperature down to the plate at the mixing chamber of the dilution refrigerator. The diameter of the wires is very small ($\sim 100 \mu\text{m}$), and the material (manganine) is chosen such that the heat conduction of the wires is small (resulting in a relative high electrical resistance of 168Ω). Four wires are made of copper which perform worse regarding heat conductivity, but have a much lower resistance and will therefore be more appropriate for high bandwidth measurements. For the electrical circuits that carry a current, like the connection to the source/drain contacts of the device, two twisted pairs are used like depicted in Fig. 2.8. One side of a twisted pair is connected to the differential output of the voltage source. At the other side of the pair, one wire is connected to the cold finger (defining a “cold-ground”), and the other wire is connected to the source contact of the device. Another twisted pair is connected at one side to the differential input of the IV-converter, and one wire at the other side is connected to the cold finger and one to the drain contact of the device. In this way, the surface of the loop that carries a current is very small, and therefore also the noise that couples to the wires via magnetic induction. No current flows through the wires that connect to a gate and therefore, both wires from a pair are separately used to connect to two different gates. All the wires are thermally anchored to the fridge by wrapping them around copper posts at several temperature stages (4 K, 1K and $\sim 10 \text{ mK}$). This anchoring is causing a parasitic capacitance to ground of about 0.5 nF .

The wires connecting the device to the measurement electronics have to be filtered carefully to reduce electron heating and uncontrolled excitations of the

device disturbing the measured signal. We use three types of filters, which cover together the required frequency range. At room temperature, so-called Pi-filters (combination of two capacitors and an inductor) filter noise in the middle frequency range, which is above 10 MHz (attenuation is 5 dB at 10 MHz, and 45 dB at 100 MHz), but they perform less well above 1 GHz. Therefore, at base temperature, the signal wires run through copper tubes filled with copper powder in which about 2 meters of wire is wound. Via eddy currents, the high-frequency noise is absorbed in the powder very effectively (attenuation of more than 60 dB from 1 GHz up to more than 50 GHz). The remaining low-frequency noise is removed by two types of two-stage RC-filters with a cut-off at 20 Hz for the wires connecting the gates, and a cut-off at 150 kHz for wires connecting ohmic contacts (more appropriate for high bandwidth measurements). The ground plane of the filter-board is carefully designed to minimize leaking of high frequency signals through the resistors.

2.3.4 High frequency signals

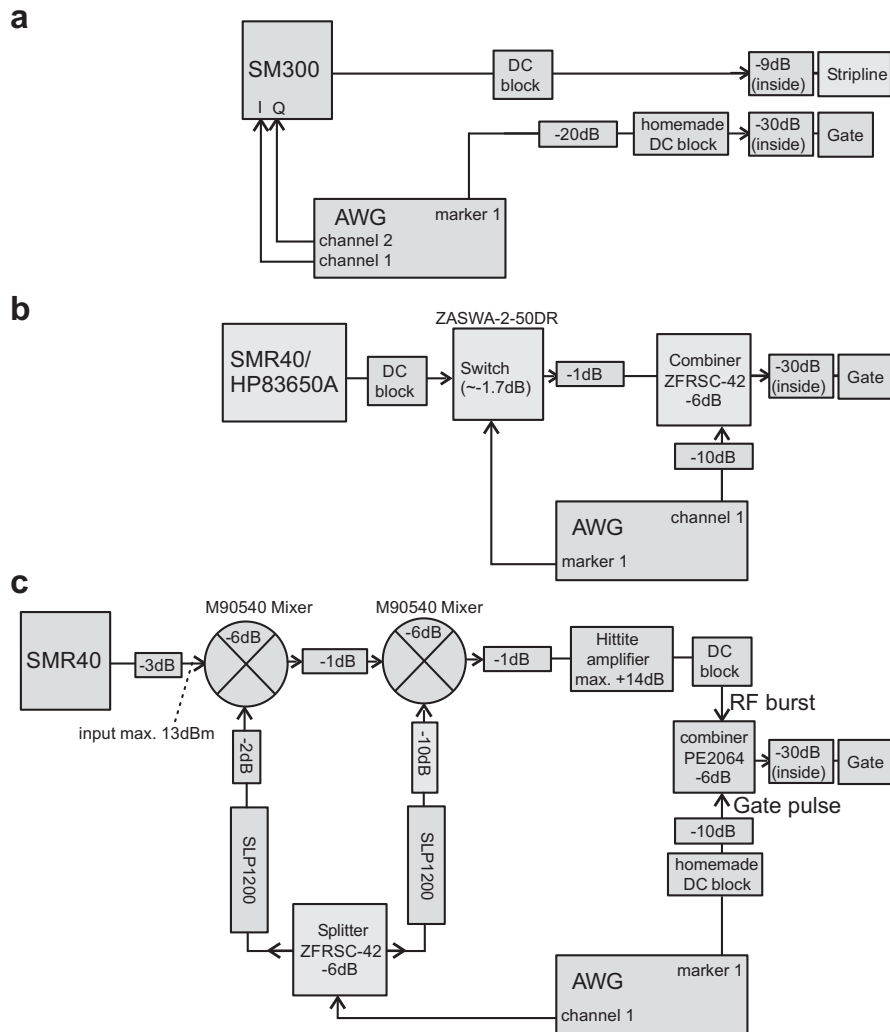
High frequency lines are needed in order to apply fast voltage pulses to one of the gates, or microwave signals to the coplanar stripline. We have two coaxial lines which consist of three parts, connected via 2.4 mm Hewlett Packard connectors which are specified up to 50 GHz, and a SMA feedthrough at room temperature, which is specified up to 18 GHz. From room temperature to 1 Kelvin, we use a silver-plated brass coaxial cable (Keycom ULT-05). This type of coax is optimized for performance at low temperature, high frequency transmission (up to 40 GHz) together with relatively low heat conductivity. From 1 Kelvin to the mixing chamber, we use semi-rigid coax lines with both inner and outer conductor made of Nb (Keycom 085A). The coax is superconducting at these temperatures, which fully suppresses heat conduction. From the mixing chamber to the sample holder, we use tin plated Cu coaxial cables which are flexible and therefore convenient in use. The outer conductors of the coaxial lines are thermally anchored to the dilution unit at 4K, 1K, ~ 800 mK and ~ 40 mK (see Fig. 2.7b). In order to anchor the inner conductor of the coaxial lines as well, we use attenuators which are anchored at 1 K (Agilent, -10 dB and -6 dB) and at the mixing chamber (Weinschel, -20 dB and -3 dB). The attenuation of the coax line used for excitation of the stripline is only 9 dB (compared to 30 dB for the coax line to the gate) because high power excitation is required and the mixing chamber cooling power is limited. Finally, we use a home-made and commercially available DC block (Picosecond model:5505) which intersects both inner and outer conductor of the coaxial lines with capacitors. This prevents that low-frequency noise couples from

2.3 Measurement setup

the high frequency generators into the electrical circuit of the device.

The phase-controlled RF burst sequences used for magnetic ESR are generated with a vector source (Rohde&Schwarz SM300, 9 kHz to 3 GHz) with RF modulator, controlled by two channels of a Tektronix arbitrary waveform generator (see Fig. 2.10a for a block diagram). Voltage pulses are applied to the right side gate through a bias-tee, so that the gate can remain biased with a DC voltage as well. The bias-tee was home-made (see Fig. 2.7c), with a rise time of 150 ps and a RC charging time of 10ms at 77K ($R=10\text{ M}\Omega$, $C=3.3\text{ nF}$). For generation of RF bursts at higher frequencies (see Fig. 2.10b), we use a HP 83650A source (10 MHz to 50 GHz) or Rohde&Schwarz SMR40 source (1-40 GHz). The bursts are created by sending this signal through a high isolation GaAs RF switch (Minicircuits ZASWA-2-50DR, typical rise time 3 ns), gated by rectangular pulses from an arbitrary waveform generator (Tektronix AWG520, channel rise time $\leq 2.5\text{ ns}$, marker rise time 0.5-2 ns). The coplanar stripline is contacted via a modified microwave probe (GGB Industries, Picoprobe model 50A, loss $< 1\text{ dB}$, DC-50 GHz), which is shown in Fig. 2.7a. For the frequency range 5-20 GHz we cannot use the RF switch, but instead, we use microwave mixers. Two mixers are connected in series in order to suppress the leakage, whereas the extra loss is compensated by an Hittite amplifier (Fig. 2.10c).

2. Device and measurement techniques



SMR40 : Rohde&Schwarz MW source (1-40 GHz)
 SM300: Rohde&Schwarz vector source (9 kHz-3 GHz)
 HP83650A: HP MW source (10 MHz - 50 GHz)
 M90540: Marki microwaves mixer (5-40 GHz)
 SLP1200: Minicircuits low pass filter (DC - 1 GHz)
 ZFRSC-42: Minicircuits splitter (DC-4.2 GHz)
 AWG: Arbitrary waveform generator, Tektronix AWG 520
 PE2064: Pasternack splitter (DC-18 GHz)
 ZASWA-2-50DR: Minicircuits switch (DC-5 MHz)
 DC block: picosecond (3nF outer conductor, 2 nF inner conductor)
 Home-made DC block (1.6 μ F outer conductor, 4.7 μ F inner conductor)

Figure 2.10: (a) Block diagrams depicting the generation of gate voltage pulses of $\sim 1\mu s$ and phase-controlled RF burst sequences for magnetic ESR. (b) Block diagrams depicting the generation of RF bursts for electrically driven ESR (1-5 GHz), combined with the generation of gate pulses of $\sim 1\mu s$. (c) Similar as (b) for the frequency range 5-20 GHz.

Chapter 3

Interaction of a confined electron spin with its environment

Quantum information, stored in a qubit, is very fragile and easily lost due to interactions with the environment. Therefore, understanding the mechanisms that lead to the loss of quantum information and controlling these processes is crucial when developing a qubit. In this chapter, we present the basic theoretical concepts of decoherence and relaxation. In the context of these concepts, we discuss the most important interactions of a confined electron spin with its environment. These are the electron-phonon interaction together with the spin-orbit coupling, and the hyperfine interaction with the nuclear spins in the host semiconductor lattice.

3.1 Relaxation and decoherence

Here, we will briefly discuss a basic theoretical framework to evaluate two types of information loss of a quantum two-level system representing a qubit. The first is energy relaxation where the qubit relaxes from the excited state to the ground state and energy is transferred to the environment. The second is decoherence where the qubit loses phase information but the energy is preserved. This is often denoted as “information leakage into the environment” or “environmental-based measurements” causing an apparent collapse of the wavefunction. It is not clear what a collapse of the wavefunction actually means or whether projective measurements really do exist. And if they do not exist, it is still an open question why we observe the world as classical and not as a quantum mechanical superposition. For these and other reasons, decoherence has been a subject of active research for the last two decades [49].

The theory of qubit relaxation and decoherence we discuss here considers only the most simple case, namely a fluctuating environment that affects the qubit. In general, the dynamics of the qubit-environment interactions can be much more involved and more elaborate studies are required. An example is a single spin coupled to a bath with many spins. In that case, the bath affects the qubit but the qubit also affects the bath. This results in very complex and rich dynamics (see for example [50]), but is beyond the scope of this section. Still, much insight in the basic properties of decoherence and relaxation is provided by analyzing the impact of the fluctuations in the environment on the qubit. The Hamiltonian of the qubit and noise sources can be written as:

$$H = -\frac{1}{2}[h_z\sigma_z + \delta h_z(t)\sigma_z + \delta h_x(t)\sigma_x + \delta h_y(t)\sigma_y], \quad (3.1)$$

where h_z is the energy splitting of the qubit and $\delta h_{x,y,z}(t)$ are fluctuations in the x, y, z -direction that couple to the qubit. These fluctuations can have any source like the electromagnetic environment of an electronic circuit, moving charges in a substrate, magnetic field fluctuations of a superconducting magnet, fluctuations of an electrostatic trap, electric field fluctuations from phonons or magnetic dipole fluctuations of the nuclear spins. As we will see below, it is useful to express these fluctuations in the form of a noise spectral density $S_{x,y,z}(\omega) = \frac{1}{2\pi} \int_{-\infty}^{\infty} e^{i\omega t} C_{\delta h_{x,y,z}}(t) dt$, with $C_x(t)$ the covariance function of $x(t)$.

Energy relaxation is the process where the qubit relaxes from the excited state to the ground state due to a process that couples the two qubit states (Fermi’s golden rule). As can be seen from Eq. (3.1), the x, y -components of δh couple the two qubit states, but for energy conservation arguments, only the h_z/\hbar frequency component of the noise spectrum contributes to relaxation. For example, an

3.1 Relaxation and decoherence

electron spin in a static magnetic field can undergo transitions from spin up to spin down due to magnetic field fluctuations in the x, y -direction at a frequency that matches the Larmor precession. In the case of weak coupling between qubit and environment and for times longer than the bath correlation time (Markov approximation), the qubit relaxes exponentially in time with a typical timescale:

$$1/T_1 = S_x(h_z/\hbar) + S_y(h_z/\hbar) \quad (3.2)$$

This expression has been derived phenomenologically in the context of NMR (see for example [51, 52]) but it has also been derived by integration of the qubit time dynamics over different noise paths [53].

The loss of phase information, also referred to as decoherence, is due to the longitudinal fluctuations h_z . A qubit in a superposition state undergoes due to h_z a precession in the xy -plane of the Bloch-sphere, which can be seen as a loss of phase coherence if the value of h_z is unknown. In contrast to relaxation where only one frequency component of the noise spectrum contributes, a wide range of frequency components of $S_z(\omega)$ can contribute to the loss of phase coherence (see below for a more precise definition).

Experimentally, the coherence decay can be measured via a Ramsey sequence performed on a qubit eigenstate; e.g. $|0\rangle$ (Fig. 3.1). The sequence is given by $U_{\pi/2} - \tau - U_{\pi/2}$, with $U_{\pi/2}$ a qubit rotation, pictured in the Bloch-sphere, over $\pi/2$ around the x or y -axis, and τ the time during which the qubit is allowed to evolve freely. If no decoherence has taken place during τ , we will find state $|1\rangle$ after the sequence. In contrast, if the qubit has rotated in the xy -plane by π , we will find qubit state $|0\rangle$ after the sequence. Altogether, the degree of decoherence is mapped on the decay of the qubit state after the sequence. The coherence decay of a qubit in a superposition of $|0\rangle$ and $|1\rangle$ can also be represented as the decay of the off-diagonal elements of the qubit density matrix ρ_{ij} . If there is no memory in the environment, we can write $C_z(t) = 2\Gamma\delta(t)$ (white noise), and the coherence decays exponentially: $\rho_{12} = e^{-\Gamma t}$ (often referred to as Markovian dynamics). If the noise has predominantly low frequency components, the coherence decay

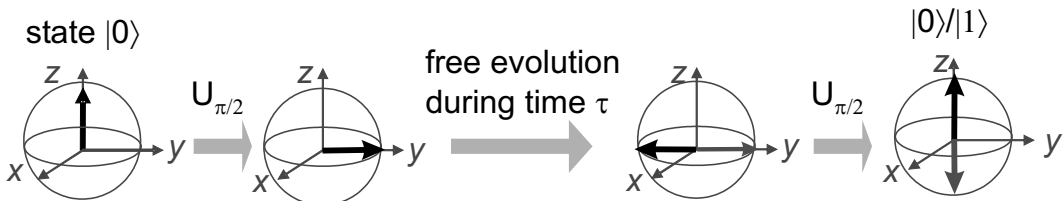


Figure 3.1: Ramsey sequence.

3. Interaction of a confined electron spin with its environment

reads [54]:

$$\rho_{12}(\tau) \propto e^{-(\tau/T_2^*)^2}, \text{ with } (1/T_2^*)^2 = \int S_z(\omega)d\omega = \sigma. \quad (3.3)$$

This is the result of averaging the qubit precession in the xy-plane with rate $h_{x,y}$ over the distribution of δh_z , which we have taken Gaussian in this case with spread σ . This expression for T_2^* is only valid when $S_z(\omega) \cong 0$ for $\omega > 1/T_2^*$. In that case, the time-dependent fluctuations of h_z are quasi-static compared to the precession rate due to h_z . The loss of spin coherence that is caused by the low frequency components of $S_z(\omega)$ is often referred to as dephasing or inhomogeneous broadening, and characterized by the typical timescale T_2^* . These terms were used in traditional NMR experiments on ensembles of spins. Then, each spin experiences a different δh_z and therefore, the coherence decay is an average effect of the δh_z distribution. For single qubit experiments, dephasing can still occur when coherence measurements are averaged over long times. In that case, also the very low frequency components of $S_z(\omega)$ are then considered as a dephasing source.

Dephasing is reversible by a Hahn echo, which is a qubit π -rotation in the xy-plane of the Bloch-sphere (Fig. 3.2). This will reverse completely the dynamics caused by the low frequency components of $S_z(\omega)$, but higher frequency components still contribute to a (echo) coherence decay. The echo coherence decay characteristics depends on the details of the distribution of h_z and the frequency spectrum $S_z(\omega)$. If h_z is Gaussian distributed, an analytical relation can be obtained:

$$\rho_{12}(\tau) = \int_{-\infty}^{\infty} S_z(\omega) \frac{1}{2} \frac{\sin^4(\omega\tau/2)}{(\omega/4)^2} d\omega \quad (3.4)$$

Here, we give one example. If we assume that h_z is Gaussian distributed with spread σ , and that the spectrum $S_z(\omega)$ has a high frequency cutoff (represented here as a Lorentzian spectrum with cutoff time τ_c), the initial Hahn echo coherence decay is given by [55, 54]:

$$\rho_{12} \propto e^{-(\frac{2\tau}{T_{2,\text{echo}}})^3}, \text{ with } T_{2,\text{echo}} = (12T_2^{*2}\tau_c^*)^{1/3}, \quad (3.5)$$

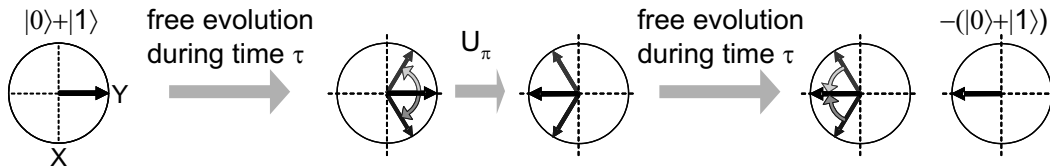


Figure 3.2: Echo sequence.

3.2 Spin-orbit interaction

which is valid for $\tau \ll \tau_c$. From this expression we see that $T_{2,\text{echo}}$ can be much longer than T_2^* when $S_z(\omega)$ contains predominantly low frequency components, i.e. when the correlation time of the environment τ_c is very long. For example a correlation time of $\tau_c = 10^6 T_2^*$ gives a T_2 which is a factor of 100 longer than T_2^* .

It is also possible to reverse the dynamics due to higher frequency components of $S_z(0)$ by using concatenated echo-pulses (also called Carr-Purcell pulses, described in [54]). If the echo-pulses are separated in time much less than τ_c , all the dynamics due to h_z -fluctuations can in principle be reversed [56].

Finally, we remark that the effect of δh_z on the coherence is quite different for a driven qubit. In that case, $S_z(0)$ and the driving frequency ω_d component of the noise power spectrum $S_z(\omega_d)$ contribute to the coherence decay [57]. This implies that driving the qubit faster results in a longer decay time, provided that $S_z(\omega)$ is smaller for larger ω , which is often the case. In chapter 7, we discuss an experiment where $S_z(\omega_d)$ is zero, i.e. $1/\omega_d$ is much shorter than the correlation time of the environment. In that case, the decay of the driven oscillations is only due to $S_z(0)$ and follows a power law instead of the usual exponential decay.

As we will see below, relaxation of an electron spin in a GaAs quantum dot is dominated by electric field fluctuations from phonons which couple to the electron spin via the spin-orbit interaction (SOI). The associated effective field fluctuations point in the transverse direction only (see next section) with a more significant contribution at higher frequencies. Therefore, this mechanism contributes mainly to spin relaxation. In contrast, a fluctuating effective field due to the interaction with the nuclear spins points in all three directions, and contains mostly low-frequency components. Therefore, the contribution from the nuclei to spin relaxation is very small, but instead, the nuclei do cause very rapid spin dephasing (see section 3.3).

3.2 Spin-orbit interaction

An electron moving in a static but non-homogeneous electric field “sees” in its restframe a time-varying electric field, which induces a magnetic field. In turn, this magnetic field acts on the magnetic moment of the electron. This coupling between the electron spin and its orbital momentum in space gives rise to the well-known fine splitting in atomic spectra. Interestingly, the line splitting in the hydrogen spectrum was among one of the first experimental evidences for the existence of the electron spin! The spin-orbit interaction (SOI) was introduced by Dirac as a relativistic correction to the Hamiltonian of the Schrödinger equation: $H_{\text{SO}} = \frac{\hbar}{4m_0^2 c^2} (\nabla V) \times \mathbf{p} \cdot \boldsymbol{\sigma}$, where m_0 is the free electron mass, c is the speed

3. Interaction of a confined electron spin with its environment

of light, V the potential landscape, p the electron momentum, and $\boldsymbol{\sigma}$ the Pauli matrices. For atoms, due to spherical symmetry it is relatively easy to evaluate this perturbation as a term proportional to $\mathbf{l} \cdot \mathbf{s}$ [58, 59], with \mathbf{s} the electron spin and \mathbf{l} the electron angular momentum.

In semiconductors, the SOI is also present because the moving electrons (and holes) experience an internal field from the crystal potential landscape. The SOI is in general characterized by a splitting of the hole bands which experience strong SOI because of their non-zero angular momentum ($l = 1$). This splitting is called the Pauli spin-orbit gap h_z , and separates the $j = l + 1/2 = 3/2$ band from the $j = l - 1/2 = 1/2$ band. The size of this splitting depends both on the crystal properties and the nucleus charge. Due to the latter, Δ scales roughly with Z^4 , with Z the atomic number. The SOI is much weaker for conduction band electrons because they occupy predominantly s-orbitals ($l=0$ and therefore $\mathbf{l} \cdot \mathbf{s}=0$). Still, for semiconductors with a relatively small band gap, the electron SOI can be relatively strong due to $\mathbf{k} \cdot \mathbf{p}$ mixing of the conduction band to the valence band. For example, in GaAs $\Delta = 0.34$ eV and $E_g=1.42$ eV, giving rise to moderately strong SOI, which is for example the origin of the negative g-factor. The SOI is still much stronger for semiconductors with a smaller bandgap like InAs ($E_g=0.35$ eV).

In 2DEGs formed in III-V semiconductors, we can distinguish two sources for the SOI. The first is due to an asymmetric crystal potential. This is present in III-V semiconductors that crystallize in the zinc-blende structure, which does not have inversion symmetry (in contrast to silicon). This effect was investigated theoretically by Dresselhaus [60], and the Hamiltonian in two dimensions reads: $H_D = \beta(-p_x\sigma_x + p_y\sigma_y) + \mathcal{O}(|p^3|)$, with the $|p^3|$ term much smaller than the linear-momentum terms due to strong confinement in the z-direction. Here, β depends on material properties and the confinement in the z-direction, and x, y point along the crystallographic directions [100],[010].

The second source giving rise to SOI is the asymmetry of the confining potential in the z-direction. This type of SOI is known as Rashba SOI [61] with Hamiltonian $H_R = \alpha(-p_y\sigma_x + p_x\sigma_y)$. Although the average electric field acting on the electron is zero, the Rashba SOI is non-zero due to mixing of the conduction band with the valence band. For that reason the strength α of the Rashba SOI depends not only on the shape of the confining potential, but also on the crystal composition in the quantum well, and is largest for narrow gap III-V semiconductors, such as InAs and InGaAs.

From $H_{D,R}$, it can be seen directly that an electron with momentum $p_{x,y}$ experiences an effective magnetic field due to the SOI. This is the origin of spin relaxation and decoherence for electrons in a two-dimensional electron gas, where

3.2 Spin-orbit interaction

the effective internal magnetic fields changes during or in between scattering events [62, 63]. In quantum dots, the average momentum of the electron is zero and for that reason the spin-orbit Hamiltonian H_{SO} does not couple directly the Zeeman-split sublevels of one orbital (in two-dimensions denoted by the two quantum numbers n and l): $\langle nl \downarrow | H_{\text{SO}} | nl \uparrow \rangle = 0$. However, the spin-orbit Hamiltonian does couple states with different orbital and spin: $\langle n'l' \downarrow | H_{\text{SO}} | nl \uparrow \rangle \neq 0$ for $n'l' \neq nl$. For this reason, electric field fluctuations which couple to the electron orbital, also couple to the spin. As we will see below, this can lead to spin relaxation [64, 65, 66, 67], but can also serve as a means to drive spin transitions coherently [68, 69, 70, 34].

A convenient way for studying the effect of the SOI is to perform a spin-dependent canonical transformation of the momentum operator (also called Schrieffer-Wolff transformation [71]), resulting (up to first order in \mathbf{B}) in a position dependent correction to the Zeeman Hamiltonian [65, 68, 67]:

$$\tilde{H} = g\mu_{\text{B}}(\mathbf{B}_{\text{ext}} \times \mathbf{n}) \cdot \boldsymbol{\sigma} + \frac{1}{2}g\mu_{\text{B}}\mathbf{B}_{\text{ext}} \cdot \boldsymbol{\sigma}; \quad (3.6)$$

$$n_x = \frac{2m^*}{\hbar}(-\alpha y - \beta x); \quad n_y = \frac{2m^*}{\hbar}(\alpha x + \beta y). \quad (3.7)$$

From this Hamiltonian it is directly clear that due to this field correction, the spin eigenstates of confined electrons are not aligned with the external field. Furthermore, the field correction is *proportional and perpendicular* to B_{ext} and depends on the electron position, which can be modified by an electric field. In this way, a time-dependent electric field can induce a time-dependent effective magnetic field and therefore induce transitions between spin states. In chapter 9, we demonstrate coherently driven electron spin transitions by electric fields.

Besides externally applied electric fields, several sources of uncontrolled fluctuating electric fields are present in semiconductor quantum dots, like fluctuations of the gate potentials [72], background charge fluctuations [72], noise in an adjacent point contact [73] or lattice phonons [67]. The latter is the dominant source for spin relaxation, which is extensively studied in theory and experiments. Because the Zeeman energy E_z (for fields below 12 T) is much smaller than the typical orbital level spacing $\hbar\omega$, this relaxation time can be extraordinary long, especially when approaching zero field. This can be understood from the fact that virtual transitions to the excited orbital are necessary to flip the spin. An elaborate calculation of the spin relaxation rate includes the phonon density of states ($\sim E_z^2$) [74] and the electric field amplitude of piezo-electric or deformation phonons respectively: $\propto E_z^{\pm 1/2}$. This gives $1/T_1 \propto (N(E_z) + 1)E_z^5/(\hbar\omega_0)^4$ for piezo-electric phonons and $1/T_1 \propto (N(E_z) + 1)E_z^7/(\hbar\omega_0)^6$ for deformation phonons [75, 65]. Here, $N(E_z) = (e^{E_z/kT} - 1)^{-1}$ is the Bose occupation number

3. Interaction of a confined electron spin with its environment

for the phonons. A more detailed and intuitive description of these results can be found in Ref. [76]. Experimentally measured relaxation times between Zeeman sublevels range from 120 μs at 14 T to a value exceeding a second at 1 T [40, 77, 78].

In general, energy relaxation processes will also lead to decoherence, and therefore by definition $T_2 \leq 2T_1$. However, in leading order the field correction due to the SOI given in Eq. 3.7 is always perpendicular to the quantization axis B_{ext} , and therefore, there is no pure phase randomization of the electron spin. In that case T_2 is limited by T_1 giving $T_2 = 2T_1$ [67]. This prediction is correct if other spin-orbit mechanisms such as p^3 -terms in the Dresselhaus Hamiltonian and strain fields produced by phonons [65] are negligible. The SOI-limited decoherence time has so far not been measured because decoherence due to interactions with nuclear spin bath was dominant.

3.3 Interaction with the nuclear spin bath

3.3.1 Hyperfine interaction

In all III-V semiconducting materials such as GaAs, the nuclei have non-zero spin. The magnetic coupling between the electron and nuclear dipole moments μ_n and μ_e is described by the Hamiltonian

$$H = \frac{\mu_e \cdot \mu_n}{r^3} - \frac{3(\mu_e \cdot \mathbf{r})(\mu_n \cdot \mathbf{r})}{r^5}, \quad (3.8)$$

where \mathbf{r} is the vector from the nucleus to the electron. Provided that the magnetic moments are sufficiently far apart (for any state of nonzero angular momentum, like p and d-states), the interaction is evaluated straightforwardly by averaging over the electron wavefunction. However, for s-states (like conduction band electrons), the wavefunction is non-zero at the nucleus and the large electrostatic potential energy requires the evaluation of relativistic theory. Solving the Dirac equation for the s-state results in the so-called Fermi contact hyperfine interaction between the electron spin \mathbf{S} and nuclear spin \mathbf{I} [52]. The contact hyperfine Hamiltonian after averaging over the electron wavefunction $\psi(\mathbf{r})$ is derived in more detail in Ref. [79] and reads:

$$H_F = \frac{8\pi}{3} \frac{\mu_0}{4\pi} g_0 \mu_B \gamma_n \hbar \mathbf{I} \cdot \mathbf{S} |\psi(0)|^2, \quad (3.9)$$

3.3 Interaction with the nuclear spin bath

with μ_B the Bohr magneton, g_0 the free-electron g factor¹, γ_n the nuclear gyro-magnetic ratio, and $|\psi(0)|^2$ the value of the electronic wave function $\psi(\mathbf{r})$ at the position of the nucleus.

When an electron spin interacts with more than one nuclear spin (like in the solid-state environment), we sum over the contributions from the nuclear spins in different unit cells [52, 54]:

$$H_{HF} = \sum A_i \mathbf{I}_i \cdot \mathbf{S}, \quad (3.10)$$

where we introduced the hyperfine constant $A_i = \nu A |\psi(r_i)|^2$, with ν the volume of a crystal unit cell containing one nuclear spin, and A is the average hyperfine coupling constant. In GaAs $A \sim 90 \mu\text{eV}$ [79], which is weighted by the natural abundances of the three isotopes ^{69}Ga , ^{71}Ga and ^{75}As (of respectively 1,0.6 and 0.4). We note that A is independent of N , which implies that the hyperfine energy of one electron interacting with one nucleus is the same as one electron interacting with one million nuclei, provided that they point in the same direction. Furthermore, roughly speaking $A \propto 1/Z^3$ because $|\psi(0)|^2 \sim 1/Z^3$ for hydrogenic s-type wavefunctions and assuming an unscreened potential from the nucleus.

The contact hyperfine interaction is exactly zero for p or d-type orbitals because $\psi(0) = 0$. For these orbitals, the anisotropic hyperfine interaction is important, which is the case for example for confined GaAs hole spins. For s-type orbitals, the anisotropic hyperfine interaction is exactly zero because the angular integral vanishes. In GaAs, the conduction band is not completely s-type and for that reason the anisotropic hyperfine interaction is not exactly zero. Still, it is small relative to the isotropic contact hyperfine interaction.

3.3.2 Spin dephasing due to the nuclear field

The effects of the hyperfine interaction can be very complex, as the nuclear spins can affect the electron spin, giving rise to relaxation and/or decoherence. In turn, the electron spin affects the nuclear spins, giving rise to a so-called Knight field (effective field felt by the nuclei) and electron-mediated interactions between distant nuclear pairs. In this section, we will discuss how the nuclear spins affects the coherence of the electron spin, and in the next section, we will address the nuclear dynamics mediated by the electron.

From the perspective of the electron, it is under certain conditions allowed (when quantum fluctuations of H_{HF} can be neglected [80]) to replace the operator

¹The effective g-factor takes into account the spin interaction of the electron with the crystal field that varies slowly in space. This is different for the hyperfine field created by the nuclei where the free electron g-factor must be used

3. Interaction of a confined electron spin with its environment

$\sum A_i \mathbf{I}_i$ with a classical magnetic field \mathbf{B}_N , also called Overhauser field. When all nuclear spins are fully polarized, $|\mathbf{B}_N| \sim 5$ T, independent of N . However, in thermal equilibrium with typical temperatures (≥ 10 mK) and magnetic fields (≤ 12 T), the thermal energy kT dominates the nuclear Zeeman energy (described by \hat{H}_N) and H_{HF} . In that case, according to the central-limit theorem we can write the diagonal elements of the density matrix of the thermal nuclear spin state as

$$\rho_N \cong e^{-\hat{H}_N/kT} = \sum_J P_J |J\rangle \langle J|, \quad (3.11)$$

where $|J\rangle$ is an eigenstate of \hat{H}_N . The average effective nuclear field of this thermal nuclear spin state is zero, but the distribution is Gaussian in all three direction with spread $\sigma_N = A/\sqrt{N} \sim 5$ mT for $N = 10^6$ [75, 81]. This is a typical number of nuclei overlapping with the wavefunction of the confined electron. The nuclear field distribution is commonly seen as a statistical nuclear field $B_{N,\text{stat}}$ which fluctuates around zero with spread σ . However, this distribution can also been seen as an intrinsic distribution because the nuclear state is in general not an eigenstate of \hat{H}_N [80]. Namely, due to dipole-dipole interactions between the nuclear spins the off-diagonal elements of Eq. 3.11 will have non-zero values. The statistical nuclear field distribution has been measured in both optical [82, 83] and electrical dots [84, 85] (see also chapter 5), and varied between 1 and 28 mT. We remark that this statistical nuclear field is much stronger for electrons localized in dots or bound to impurities than for free electrons in a 2DEG which overlap with a much larger number of nuclei.

The statistical nuclear field is an important dephasing source, because it can point in the direction of the external field and the electron Larmor precession time around a typical nuclear field $1/g\mu_B B_{N,\text{stat}}$ can be quite fast. The coherence decay is reflected in an average precession about a Gaussian distributed nuclear field: $\int_{-\infty}^{\infty} \frac{1}{\sqrt{2\pi}\sigma} e^{(-B_{N,z}^2/2\sigma^2)} \cos(g\mu_b B_{N,z} t/\hbar) dB_{N,z} = e^{-(t/T_2^*)^2}$, with $T_2^* = \hbar/g\mu_b\sigma \sim 5$ ns [81, 86] (assuming $\sigma = 5$ mT).

There are several ways to suppress this dephasing source. First of all, one can perform a Hahn echo, which will be discussed in the next section. Next, polarizing the nuclear system by a fraction of p suppresses the field distribution by a factor $1/\sqrt{N(1-p^2)}$ [87, 50, 86]. However, a very large and therefore difficult to realize, polarization of 99.99% is needed to enhance T_2^* by a factor of 100. Perhaps, a more feasible proposal is to reduce the nuclear field uncertainty by performing measurements of the nuclear field in the z-direction [88, 89, 90, 91].

Finally, we remark that (similar to the SOI) the effective nuclear field depends on the position of the electron. This implies that an applied electric field at the

3.3 Interaction with the nuclear spin bath

frequency of the electron spin splitting together with the transverse nuclear field $B_{N,x,y}$ can induce spin transitions [92]. Similar, uncontrolled field fluctuations, like phonons [93, 94, 95, 96] can lead to spin relaxation, but this process is relatively weak, and the expected relaxation time due to the nuclear field is on the order of a second.

3.3.3 Spin decoherence due to nuclear dynamics

The electron spin dynamics due to the statistical nuclear field can be reversed by a Hahn echo technique (see section 3.1) to the extent the nuclear field is static. However, the spin-echo coherence time $T_{2,\text{echo}}$ can still be limited by fluctuations of the nuclear field due to the hyperfine interaction (as we will see below), and the dipole interaction between neighboring nuclear spins.

In order to study the dynamics of the electron-nuclear system, we write the hyperfine interaction Hamiltonian in the following way:

$$H = \sum_i A_i (\sigma_z I_{z,i} + \sigma_+ I_{i-} + \sigma_- I_{i+}). \quad (3.12)$$

The last two terms represent electron-nuclear flips-flops that cause fluctuations of the nuclear field. However, due to the difference in Zeeman energy between electron and nuclear spin (roughly a factor of 10^3), this process is not energy conserving and therefore very inefficient for $B_{\text{ext}} \gg B_{\text{stat}}$. However, virtual processes such as $A_i A_j I_{i+} I_{j-} \sigma_+ \sigma_- + \dots$ preserve the electron spin polarization and thus have only a small energy cost ($\sim A_i - A_j$). Namely, $A_i \sim 0.09 \mu\text{eV}$ while $E_z \sim 25 \mu\text{eV/T}$. An example of such a process is depicted in Fig. 3.3, which shows the virtual state with a flipped electron. This energy mismatch of the electron Zeeman energy is allowed for a very short time, similar to an electron tunneling process. While the rate of direct electron-nuclear flip-flops is reduced efficiently with $1/B_z^2$, the rate of the first order virtual processes scale with $1/B_z$ and therefore, these are much harder to suppress. The virtual processes will lead

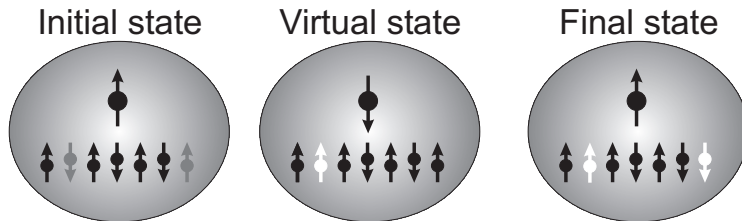


Figure 3.3: Interaction between two distant nuclear spin mediated by the electron.

3. Interaction of a confined electron spin with its environment

to a long-range coupling between the nuclear spins changing the effective nuclear field $\sum A_i I_{i,z}$ and therefore also the electron spin coherence (like discussed in section 3.1). We note that this process is similar to the long-range RKKY interaction between nuclear spins in metals.

Calculating the dynamics due to the hyperfine-mediated nuclear-nuclear flip-flop is a complex many body problem, especially for inhomogeneous A_i which suppresses this process due to the energy cost $A_i - A_j$ of a flip-flop. Furthermore, because the nuclear dynamics are not independent of the electron spin, the coupled electron-nuclear system can lead to coherence decay characteristics different than the usual exponential decay. These so-called non-Markovian dynamics are extensively discussed in [50]. In general, the predicted coherence time due to this process is in the range 1-100 μs [50, 75, 97, 98, 99] for magnetic fields below 3 T. Interestingly, some theories predict that the hyperfine-mediated dynamics are reversible by a Hahn echo at sufficiently high field (>100 mT) [97, 98, 99]. This would imply that a Hahn echo can not only reverse the spin dynamics due to the environment, but that even the dynamics of the spin environment can be reversed via the electron spin itself!

A second process governing the nuclear dynamics is the dipole-dipole interaction between neighboring nuclei, which is given by the secular approximation (valid for Zeeman energies larger than the interaction strength D):

$$H_{i,j} = D(I_i^+ I_j^- + I_i^- I_j^+ - 4I_i^z I_j^z)/2, \quad (3.13)$$

with $D \sim 1/100\mu s$ [100]. The first two terms give rise to flip-flops of nuclear pairs which changes $B_{N,z}$ and therefore affects the electron spin coherence. The timescale of the drift in $B_{N,z}$ is difficult to evaluate due to a combination of complications. First of all, the flip-flop rate is suppressed when $A_i - A_{i+1} > D$, causing an energy mismatch [99]. This so-called Knight gradient is stronger in the z-direction (quantum well confinement ~ 5 nm) than x,y-direction (quantum dot confinement ~ 30 nm). It is expected that the drift in $B_{N,z}$ due to the dipole interaction has a timescale of 1-100 sec, depending sensitively on the dot size. This timescale is much longer than $1/D$ due to the Knight gradient. If we assume the Knight gradient is very small, still long diffusion times are expected because then many neighbor-neighbor interactions are needed to diffuse nuclear spins to the edge of the quantum dot.

The contribution from the dipole-dipole interaction to the electron coherence time is estimated theoretically at ~ 10 -100 μs [101, 102, 98, 103], much faster than the $B_{N,z}$ drift time. This can be understood qualitatively from Eq. 3.5, although the details of the coherence decay can be different. We remark that the nuclear dipole-dipole contribution to T_2 is independent of B_{ext} but depends strongly on

3.3 Interaction with the nuclear spin bath

the size of the dot and thickness of the quantum well [102]. According to Ref. [102], for very small dots (<10 nm) and a thin quantum well, the large Knight gradient leads to a long T_2 . The other extreme, very large dots (>300 nm) and thicker quantum wells result in a more homogeneous A_i leading as well (but for a different reason) to long T_2 because nuclear-nuclear flip-flops do not change $B_{N,z}$. For intermediate dot sizes, T_2 is shortest and both processes are in competition. We remark that the drift of $B_{N,z}$ is governed only by flip-flops from nuclear pairs of the same species. Namely, different species have different gyromagnetic ratios (due to the difference in nuclear mass), resulting in an energy mismatch.

3. Interaction of a confined electron spin with its environment

Chapter 4

Electron spin state detection in a double quantum dot

F. H. L. Koppens, C. Buizert, I. T. Vink, K. C. Nowack,
T. Meunier, L. P. Kouwenhoven & L. M. K. Vandersypen

Recent experiments have demonstrated the coherent evolution of a single electron spin via magnetic resonance, as well as the hybridization of two-electron spin states due to spin dephasing. Spin-dependent transport measurements through a double quantum dot were used to detect these phenomena. In this chapter, we discuss the theory of these transport processes. Specifically, we analyze the two-electron spin states, and the hybridization of these states due to the nuclear spins in the electron spin environment. The effect of spin transitions induced via magnetic resonance on the electron transport is described with a master equation approach. We study the spin detector efficiency for a wide range parameters, via a numerical evaluation of the current flow. The experimental data are compared with the model and we find a reasonable agreement.

Parts of this chapter have been published in *Journal of Applied Physics* **101**, 081706 (2007).

4.1 Introduction

Spin-dependent transport through a double quantum dot is a valuable tool for probing electron spin states and its dynamics. It has been used to detect the coherent oscillations of a single electron spin (see Chapter 6 and Ref. [104]), two-electron spin state hybridization due to a nuclear field gradient (Chapter 5) and to measure the electron dephasing and coherence times (Chapter 8). Briefly, the device can be operated (in a spin blockade regime [105]) such that the electron in the left dot can only move to the right dot if a spin flip in one of the two dots is induced. This is possible via an oscillating magnetic field (electron spin resonance or ESR) or an effective magnetic field due to the interaction with the nuclear spins. From the right dot, the electron exits to the right reservoir and another electron enters the left dot from the left reservoir. A continuous repetition of this transition will result in a net current flow.

Compared to the single dot detection scheme [106], using the double-dot as a detector has two major advantages. First, experiments can be performed at lower and even zero magnetic field. This allows access to the interesting regime of nuclear-spin induced relaxation. Furthermore, for ESR detection it requires lower, technically less demanding, excitation frequencies. Finally, the spin detector is rather insensitive to unwanted electric fields, charge fluctuations in the environment, or temperature broadening of the Fermi energy in the reservoir. This is because the relevant dot levels can be positioned far from the Fermi energies of the leads.

The drawback of the double-dot detector is that spin detection is based on the projection in the two-electron singlet-triplet basis, while for example for ESR detection, one would like to detect the spin state of a single electron. However, this detection is still possible because the electrons in the two dots experience different effective nuclear fields. This is due to the hyperfine interaction of the electron spins with the (roughly 10^6) nuclear spins in the host semiconductor material of each quantum dot [84, 85, 82, 107, 81, 75, 50, 108]. In order to provide more insight in this double-dot ESR detection scheme for single spin rotations, it is necessary to analyze the coherent evolution of the two-electron spin states, together with the transitions in the transport cycle.

In this chapter, we discuss a model that describes the transport cycle in the spin blockade regime, including the coherent coupling between the two dots, and the influence of a static and an oscillating magnetic field together with the effective nuclear fields on the electron spin states. The aim is to understand how effectively single spin resonance will affect the measured quantity in the experiment, namely the current flow in the spin blockade regime. The organization of

4.2 Double dot spin states and Pauli spin blockade

this chapter is as follows. First, we will discuss the two-electron spin states in a double quantum dot, as well as the transport cycle and the mechanism that blocks current flow due to the Pauli principle (Pauli spin blockade). Next, we will briefly discuss the static system Hamiltonian and the mixing of the two-electron spin states by the effective nuclear field. Then we add an oscillating magnetic field to this Hamiltonian, that forms -together with the double dot tunnelling processes- the basis of the rate equations that describe how the density matrix of the two-electron spin states evolves in time. The current flow, calculated from the steady state solution of the density operator, is then analyzed for different coherent coupling values, magnitudes of the oscillating magnetic field, in combination with different effective nuclear fields in the two dots. This provides further insight in the optimal conditions for spin flip detection with a double quantum dot.

4.2 Double dot spin states and Pauli spin blockade

In double quantum dots, interdot charge transitions conserve spin and obey spin selection rules, which can lead to a phenomenon called Pauli spin blockade. Spin blockade occurs in the regime where the occupancy of the double quantum dot can be (0,1), (1,1), or (0,2), with (m,n) the occupations of the left and right dots. In the (1,1) and (0,2) charge state, the four possible spin states are the singlet state ($|S\rangle = |\uparrow\downarrow\rangle - |\downarrow\uparrow\rangle$, normalization omitted for brevity) and the three triplets states $|T^0\rangle = |\uparrow\downarrow\rangle + |\downarrow\uparrow\rangle$, $|T^+\rangle = |\uparrow\uparrow\rangle$, $|T^-\rangle = |\downarrow\downarrow\rangle$. Due to a finite tunnel coupling t between the two dots, the (1,1) and (0,2) singlet states can hybridize close to the degeneracy of these two states. Around this degeneracy, the energy difference between the (0,2) and (1,1) triplet states is much larger than t , and therefore, we can neglect hybridization between these states and charge transitions to the (0,2) triplet state. We calculate the energy of the eigenstates via the system Hamiltonian, which is written in the basis states $|S_{11}\rangle$, $|T_{11}^+\rangle$, $|T_{11}^-\rangle$, $|T_{11}^0\rangle$ and $|S_{02}\rangle$. In the description, we neglect the thermal energy kT , which is justified when the (absolute) energy difference between the eigenstates and the Fermi energy of the left and right reservoir is larger than kT . The Hamiltonian is given by

$$\begin{aligned}
 H_0 = & - \Delta_{\text{LR}} |S_{02}\rangle \langle S_{02}| + \sqrt{2}t \left(|S_{11}\rangle \langle S_{02}| + |S_{02}\rangle \langle S_{11}| \right) \\
 & - g\mu_{\text{B}} B_{\text{ext}} \left(|T_{11}^+\rangle \langle T_{11}^+| - |T_{11}^-\rangle \langle T_{11}^-| \right),
 \end{aligned} \tag{4.1}$$

4. Electron spin state detection in a double quantum dot

where Δ_{LR} is the energy difference between the $|S_{11}\rangle$ and $|S_{02}\rangle$ state (level detuning, see Fig.4.1a), t is the tunnel coupling between the (1,0) and (0,1) orbitals, and B_{ext} is the external magnetic field in the z-direction. The eigenstates of the Hamiltonian (4.1) for finite external field are shown in figure 4.1c. For $|\Delta_{LR}| < t$, the tunnel coupling t causes an anti-crossing of the $|S_{11}\rangle$ and $|S_{02}\rangle$ states.

Using this energy diagram, we can analyze the current-carrying cycle via the charge transitions: $(1, 1) \rightarrow (0, 2) \rightarrow (0, 1) \rightarrow (1, 1)$. For $\Delta_{LR} < 0$, transport is blocked by Coulomb blockade, because the (0,2) state $|S_{02}\rangle$ is at a higher energy than the (1,1) state $|S_{11}\rangle$. For $\Delta_{LR} \geq 0$, two possible situations can occur. First, an electron that enters the left dot can form a double-dot singlet state $|S_{11}\rangle$ with the electron in the right dot. It is then possible for the left electron to move to the right dot because the right dot singlet state $|S_{02}\rangle$ is energetically accessible. Transitions from $|S_{02}\rangle$ to $|S_{11}\rangle$ are governed by coherent coupling between the states (Fig. 4.1b) or inelastic relaxation (Fig. 4.1a). From $|S_{02}\rangle$, one electron tunnels from the right dot to the right lead and another electron can again tunnel into the left dot. The second possibility is that an electron entering the left dot forms a triplet state $|T_{11}\rangle$ with the electron in the right dot. In that case, the left electron cannot move to the right dot, as the right dot triplet state $|T_{02}\rangle$ is much higher in energy (due to the relatively large singlet-triplet splitting

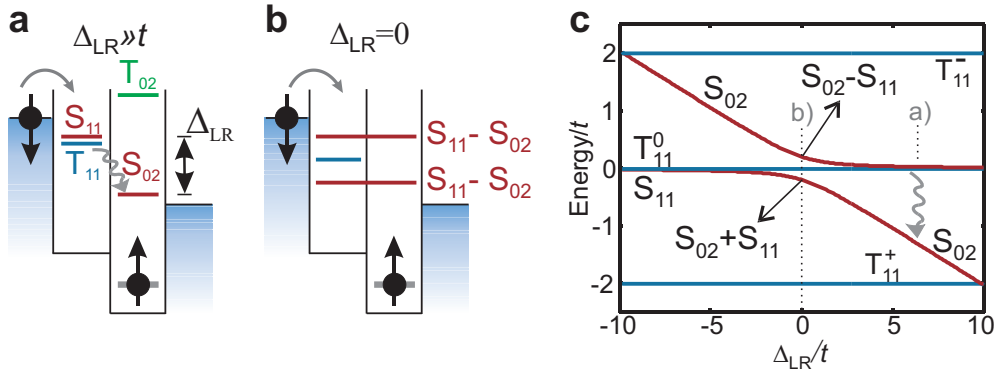


Figure 4.1: (a) A schematic of the double dot and the electro-chemical potentials (energy relative to the (0,1) state) of the relevant two-electron spin states. For $\Delta_{LR} > t$, transitions from the S_{11} state to the S_{02} state are possible via inelastic relaxation with rate Γ_{in} . Spin blockade occurs when one of the T_{11}^i states is occupied. (b) Similar schematic for $\Delta_{LR} = 0$, where the singlet states are hybridized. Also in this case, spin blockade occurs when one of T_{11}^i states is occupied. (c) Energy levels as a function of detuning. At $\Delta_{LR} = 0$, the singlet states hybridize into bonding and anti-bonding states. The splitting between the triplet states corresponds to the Zeeman energy $g\mu_B B_{\text{ext}}$.

4.3 Singlet-triplet mixing by the nuclear spins

in a single dot). The electron can also not move back to the lead due to fast charge relaxation in the reservoir, and therefore, further current flow is blocked as soon as any of the (1,1) triplet states is formed (see schematics in Fig. 4.2a).

The key experimental signature of Pauli spin blockade is the strong dependence of current flow on bias direction. For forward bias, current flow is strongly suppressed because as soon as one the triplet states is occupied, the current-carrying cycle is interrupted (Fig. 4.2a). For reverse bias, only singlet states can be loaded and a current can always flow (Fig. 4.2b).

The second experimental signature of Pauli spin blockade is visible when the voltage bias is larger than the energy splitting Δ_{ST} between the states $|T_{02}\rangle$ and $|S_{02}\rangle$. Spin blockade is lifted when the relative dot alignment is such that the transition from the $|T_{11}\rangle$ state to $|T_{02}\rangle$ state is energetically allowed (Fig. 4.3).

4.3 Singlet-triplet mixing by the nuclear spins

Spin blockade only occurs if at least one of the eigenstates of the system Hamiltonian is a pure triplet state. If processes are present that induce transitions from all the three triplet states $|T_{11}^i\rangle$ to the singlet state $|S_{11}\rangle$, spin blockade is lifted and a current will flow. As we will see below, the presence of the nuclear spins in the host semiconductor can give rise to such transitions.

The effect of the hyperfine interaction with the nuclear spins can be studied [109] by adding a static (frozen) effective nuclear field \mathbf{B}_N^L (\mathbf{B}_N^R) at the left (right) dot to the system Hamiltonian:

$$\begin{aligned}
 H_{\text{nuc}} &= -\frac{g\mu_B}{\hbar}(\mathbf{B}_N^L \cdot \mathbf{S}_L + \mathbf{B}_N^R \cdot \mathbf{S}_R) \\
 &= -\frac{g\mu_B}{\hbar}(\mathbf{B}_N^L - \mathbf{B}_N^R) \cdot (\mathbf{S}_L - \mathbf{S}_R)/2 \\
 &\quad -\frac{g\mu_B}{\hbar}(\mathbf{B}_N^L + \mathbf{B}_N^R) \cdot (\mathbf{S}_L + \mathbf{S}_R)/2,
 \end{aligned} \tag{4.2}$$

with $\mathbf{S}_{L(R)}$ the spin operator for the left (right) electron. For the sake of convenience, we separate the inhomogeneous and homogeneous contribution, for reasons which we will discuss later. Considering the nuclear field as static is justified since the tunneling rates and electron spin dynamics are expected to be much faster than the dynamics of the nuclear system [50, 101, 79]. Therefore, we will treat H_{nuc} as time-independent. The effect of nuclear reorientation will be included later by ensemble averaging.

We will show now that triplet states mix with the $|S_{11}\rangle$ state if the nuclear field is different in the two dots (in all three directions). This mixing will lift spin

4. Electron spin state detection in a double quantum dot

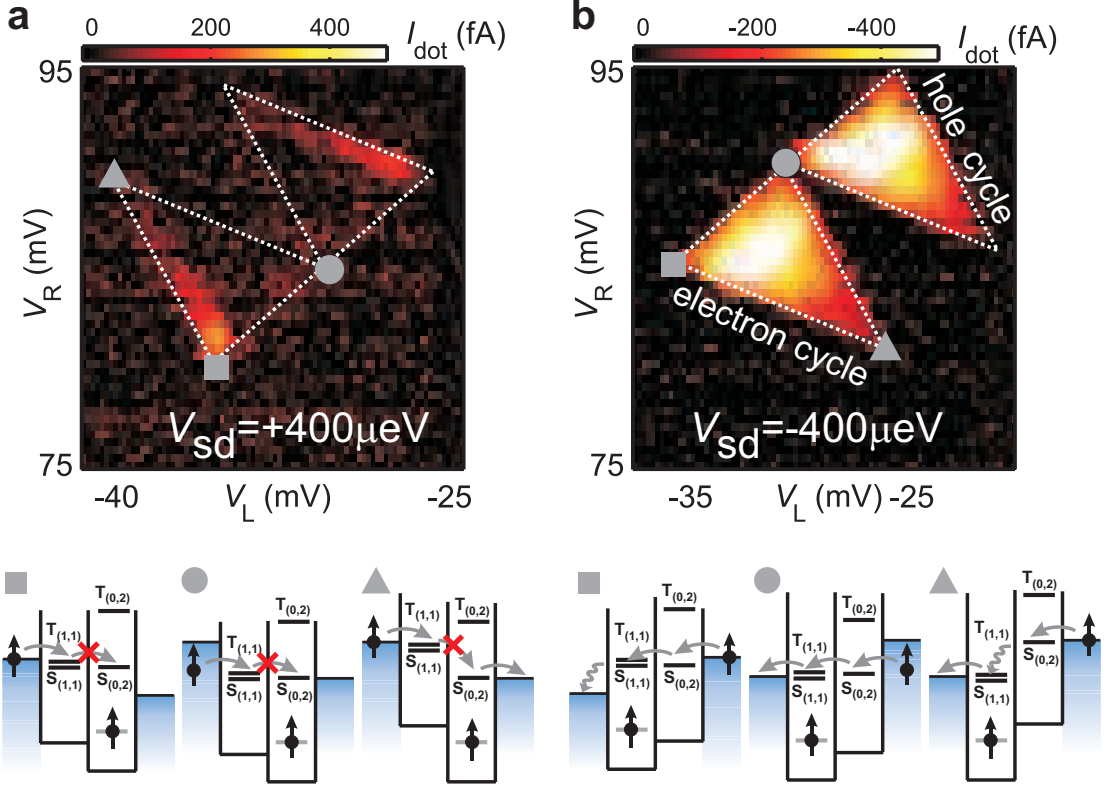


Figure 4.2: Spin blockade observed with forward bias is absent for reverse bias. (a) Color-scale plot of the current through the double quantum dot under forward bias ($400 \mu\text{eV}$) as a function of the gate voltages controlling the left and right dot potential (V_L and V_R) at $B_{\text{ext}} = 100 \text{ mT}$. The white dotted triangles define the region in gate space where transport is energetically allowed, but transport is still suppressed due to spin blockade. Outside these triangle, the number of electrons is fixed by Coulomb blockade. A small leakage current is visible in the area around the gray rectangle. This is due to spin exchange with the lead, a process which is significant when the T_{11} state is close to the Fermi energy of the left reservoir (within $kT \sim 10 \mu\text{eV}$). The two triangles correspond to two different current cycles, commonly known as the electron cycle and hole cycle. The schematics depict transport by the electron cycle, $(1,1) \rightarrow (0,2) \rightarrow (0,1) \rightarrow (1,1)$. The hole cycle $(1,2) \rightarrow (1,1) \rightarrow (0,2) \rightarrow (1,2)$, exhibits features similar to those visible in the electron cycle, although slight differences can exist. The horizontal black line in the schematics depict the electrochemical potential for transitions from the $(0,1)$ state to the $(0,2)$ and $(1,1)$ singlet (S) and triplet (T) states. (b) Similar data for opposite bias ($-400 \mu\text{eV}$). The schematics depict transport by the opposite cycles: $(0,1) \rightarrow (0,2) \rightarrow (1,1) \rightarrow (0,1)$ for the electron cycle and $(1,2) \rightarrow (0,2) \rightarrow (1,1) \rightarrow (1,2)$ for the hole cycle. In these cases the system is in $(0,2)$ before it is in $(1,1)$, so it can never get stuck in T_{11} and Pauli blockade does not occur. Therefore, current flows throughout the area defined by the two white dotted triangles.

4.3 Singlet-triplet mixing by the nuclear spins

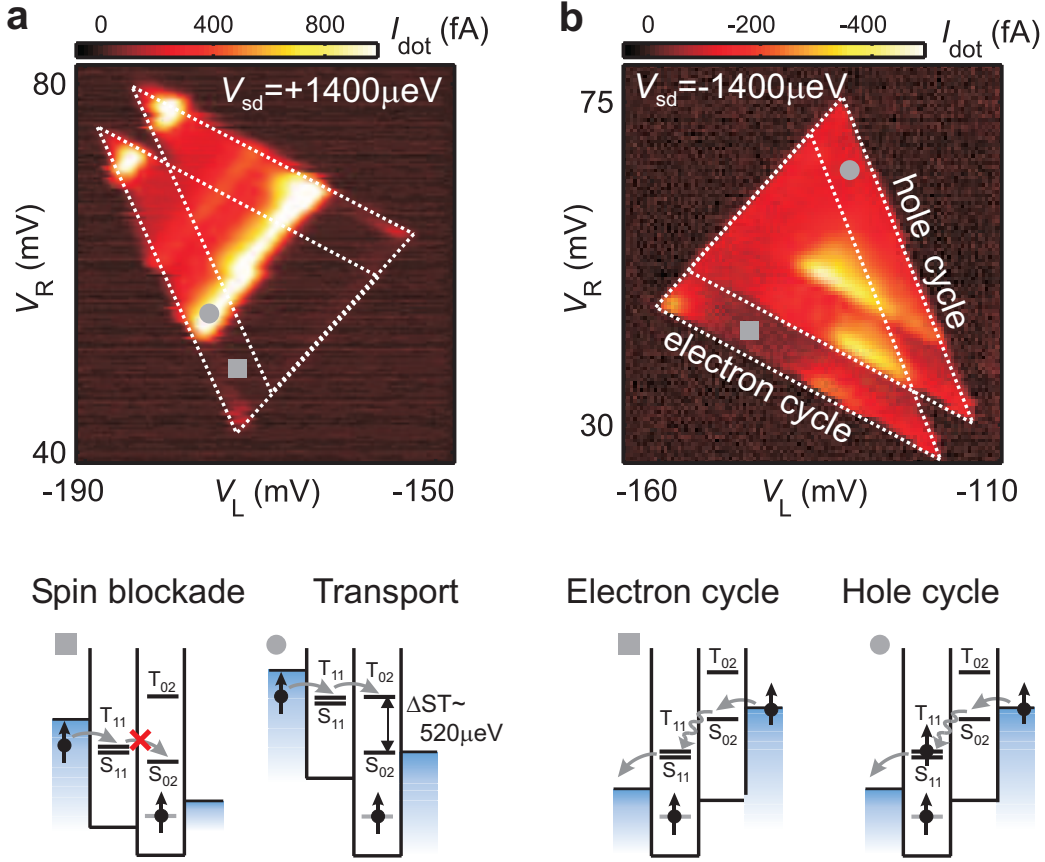


Figure 4.3: High bias transport measurements in the spin blockade regime. (a) Color-scale plot of the current through the double quantum dot under forward bias ($1400 \mu\text{eV}$) as a function of the gate voltages controlling the left and right dot potential (V_L and V_R) at $B_{\text{ext}} = 100 \text{ mT}$. The white dotted triangles define the region in gate space where transport is energetically allowed. Transport is suppressed due to spin blockade in part of the triangles (gray rectangle). Spin blockade is lifted (and transport is allowed) when the T_{02} state becomes energetically accessible from the T_{11} state (depicted by the gray circle). (b) Similar measurement as in (a), but for reverse bias ($-1400 \mu\text{eV}$). Current flows in the entire region in gate space where it is energetically allowed (within the white dotted triangles).

blockade, visible as a finite current running through the dots for $\Delta_{LR} \geq 0$. The effective nuclear field can be decomposed in a homogeneous and an inhomogeneous part (see right-hand side of (4.2)). The homogeneous part simply adds vectorially to the external field B_{ext} , changing slightly the Zeeman splitting and preferred spin orientation of the triplet states. The inhomogeneous part $\Delta \mathbf{B}_N \equiv \mathbf{B}_N^L - \mathbf{B}_N^R$ on the other hand couples the triplet states to the singlet state, as can be seen

4. Electron spin state detection in a double quantum dot

readily by combining the spin operators in the following way

$$\begin{aligned}
 S_L^x - S_R^x &= \frac{\hbar}{\sqrt{2}} \left(|S_{11}\rangle \langle T_{11}^-| - |S_{11}\rangle \langle T_{11}^+| + h.c. \right) \\
 S_L^y - S_R^y &= \frac{\hbar}{\sqrt{2}} \left(i |S_{11}\rangle \langle T_{11}^-| - i |S_{11}\rangle \langle T_{11}^+| + h.c. \right) \\
 S_L^z - S_R^z &= \hbar \left(|S_{11}\rangle \langle T_{11}^0| + |T_{11}^0\rangle \langle S_{11}| \right).
 \end{aligned} \tag{4.3}$$

The first two expressions reveal that the inhomogeneous field in the transverse plane $\Delta B_N^x, \Delta B_N^y$ mixes the $|T_{11}^+\rangle$ and $|T_{11}^-\rangle$ states with $|S_{11}\rangle$. The longitudinal component ΔB_N^z mixes $|T_{11}^0\rangle$ with $|S_{11}\rangle$ (third expression). The degree of mixing between two states will depend strongly on the energy difference between them

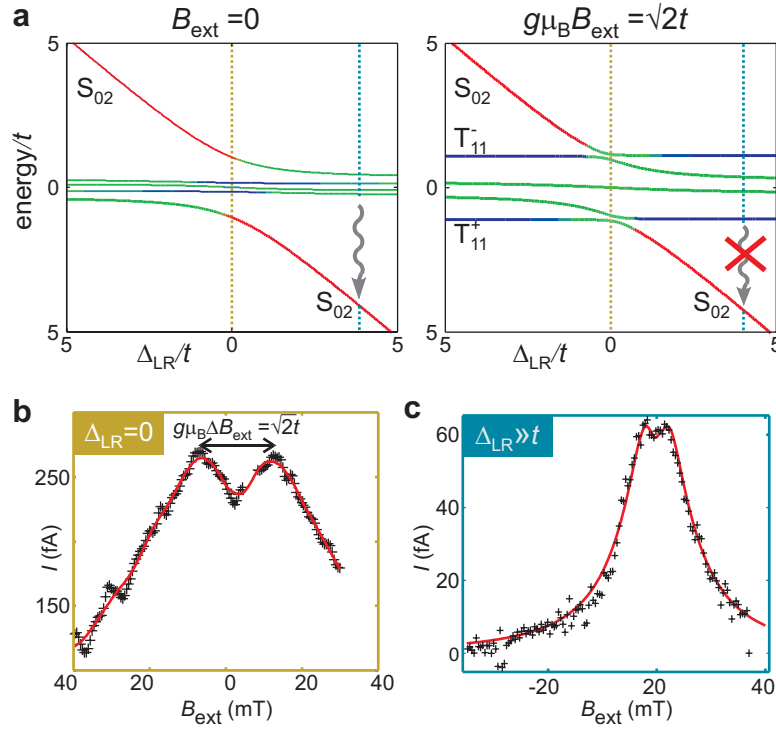


Figure 4.4: (a) Energies corresponding to the eigenstates of $H_0 + H_{\text{nucl}}$ as a function of Δ_{LR} ($t \sim 2\Delta B_{N,z}$). Singlet and triplet eigenstates are denoted by red and blue lines respectively. Hybridized states (of singlet and triplet) are denoted by green lines. For $\Delta_{\text{LR}} \gg t$ and $g\mu_B B_{\text{ext}} \gg g\mu_B \Delta \mathbf{B}_N$, the split-off triplets (T_{11}^+ and T_{11}^-) are hardly perturbed and current flow is blocked when they become occupied. Parameters: $t = 0.2 \mu\text{eV}$, $g\mu_B B_{N,L} = (0.03, 0, -0.03) \mu\text{eV}$, $g\mu_B B_{N,R} = (-0.03, -0.06, -0.06) \mu\text{eV}$ and $g\mu_B B_{\text{ext}} = 0.2 \mu\text{eV}$. (b) Observed current flow in the resonant transport regime ($\Delta_{\text{LR}} \sim 0$ and $t \sim 0.18 \mu\text{eV}$) due to singlet-triplet mixing by the nuclei. See chapter 5 for more details. (c) Observed current flow in the inelastic transport regime ($\Delta_{\text{LR}} \gg t$) due to singlet-triplet mixing by the nuclei.

4.4 Oscillating magnetic field and rate equations

[85].

This is illustrated in Fig. 4.4a where the energies corresponding to the eigenstates of the Hamiltonian $H_0 + H_{\text{nucl}}$ are plotted as a function of Δ_{LR} . We first discuss the case where $\Delta_{\text{LR}} \gg t$. For $g\mu_{\text{B}}B_{\text{ext}} < g\mu_{\text{B}}\sqrt{\langle\Delta B_{\text{N}}^2\rangle}$, the three triplet states are close in energy to the $|S_{11}\rangle$ state. Their intermixing will be strong, lifting spin blockade. For $g\mu_{\text{B}}B_{\text{ext}} \gg g\mu_{\text{B}}\sqrt{\langle\Delta B_{\text{N}}^2\rangle}$ the $|T_{11}^+\rangle$ and $|T_{11}^-\rangle$ states are split off in energy by an amount of $g\mu_{\text{B}}B_{\text{ext}}$. Consequently the perturbation of these states caused by the nuclei will be small. Although the $|T_{11}^0\rangle$ remains mixed with the $|S_{11}\rangle$ state, the occupation of one of the two split-off triplet states can block the current flow through the system. The situation for $\Delta_{\text{LR}} \sim 0$ is more complicated due to a three-way competition between the exchange interaction and nuclear and external magnetic fields. In contrast to the previous case, increasing B_{ext} from 0 to $\sqrt{2}t/g\mu_{\text{B}}$ gives an increase of singlet-triplet mixing, as illustrated in Fig. 4.4a. Two examples of experimental datasets showing the effect of singlet-triplet hybridization by the nuclear fields on the current flow for are displayed in Fig. 4.4b,c (data taken from chapter 5). More details and discussion about hyperfine-mediated singlet-triplet mixing is presented in chapter 5. Theoretical calculations of the nuclear-spin mediated current flow, obtained from a master equation approach, are discussed in [109, 110].

4.4 Oscillating magnetic field and rate equations

So far, we have seen that hybridization of singlet and triplet spin states leads to a small current in the spin blockade regime. We will now discuss how this lifting of spin blockade can also be used to detect single spin rotations, induced via electron spin resonance. The basic idea is the following. If the system is blocked in e.g. $|\uparrow\uparrow\rangle$, and the driving field rotates e.g. the left spin, then transitions are induced to the state $|\downarrow\uparrow\rangle$. This state contains a singlet component and therefore a probability for the electron to move to the right dot and right lead. Inducing single spin rotations can therefore lift spin blockade.

However, together with the driving field, the spin transitions are much more complicated due to the interplay of different processes: spin resonance of the two spins, interaction with the nuclear fields, spin state hybridization by coherent dot coupling and inelastic transitions from the S_{11} state to the S_{02} state. In order to understand the interplay of these processes, we will first model the system with a time-dependent Hamiltonian and a density matrix approach. Next, we will discuss the physical interpretation of the simulation results.

The Hamiltonian now also contains a term with an oscillating magnetic field

4. Electron spin state detection in a double quantum dot

in the x-direction with amplitude B_{ac}

$$H_{ac}(t) = \frac{g\mu_B B_{ac}}{\hbar} \sin(\omega\tau) \cdot (S_L^x + S_R^x). \quad (4.4)$$

We assume that B_{ac} is equal in both dots, which is a reasonable approximation in the experiment (from simulations we find that the difference of B_{ac} is 20% at most [104]). We assume $B_{ext} \gg B_N, B_{ac}$, which allows application of the rotating wave approximation [111]. Therefore, we will define $B_1 \equiv \frac{1}{2}B_{ac}$, which is, due to the rotating-wave approximation, the relevant driving field for the ESR process.

We construct rate equations that include the unitary evolution of the spins in the dots governed by the time-dependent Hamiltonian. This approach is based on the model of reference [109], where the Hamiltonian contained only time-independent terms. Seven states are involved in the transport cycle, namely the three triplets $|T_{11}^i\rangle$, the singlet states $|S_{11}\rangle$ and $|S_{02}\rangle$ and the two (0,1) states $|\uparrow\rangle_{01}$ and $|\downarrow\rangle_{01}$, making the density operator a 7×7 matrix. The rate equations based on the time-independent Hamiltonian are given in [109]. These are constructed from the term that gives the unitary evolution of the system governed by the Hamiltonian ($H = H_0 + H_{ac}$) $d\hat{\rho}_k/d\tau = -\frac{i}{\hbar} \langle k | [H, \hat{\rho}] | k \rangle$, together with terms that account for incoherent tunnelling processes between the states. The rate equations for the diagonal elements are given by

$$\begin{aligned} \frac{d\hat{\rho}_{T_{11}^+}}{d\tau} &= -\frac{i}{\hbar} \langle T_{11}^+ | [H, \hat{\rho}] | T_{11}^+ \rangle + \frac{\Gamma_L}{2} \hat{\rho}_{\uparrow 01} \\ \frac{d\hat{\rho}_{T_{11}^-}}{d\tau} &= -\frac{i}{\hbar} \langle T_{11}^- | [H, \hat{\rho}] | T_{11}^- \rangle + \frac{\Gamma_L}{2} \hat{\rho}_{\downarrow 01} \\ \frac{d\hat{\rho}_{T_{11}^0}}{d\tau} &= -\frac{i}{\hbar} \langle T_{11}^0 | [H, \hat{\rho}] | T_{11}^0 \rangle + \frac{\Gamma_L}{4} (\hat{\rho}_{\uparrow 01} + \hat{\rho}_{\downarrow 01}) \\ \frac{d\hat{\rho}_{S_{11}}}{d\tau} &= -\frac{i}{\hbar} \langle S_{11} | [H, \hat{\rho}] | S_{11} \rangle + \frac{\Gamma_L}{4} (\hat{\rho}_{\uparrow 01} + \hat{\rho}_{\downarrow 01}) - \Gamma_{in} \hat{\rho}_{S_{11}} \\ \frac{d\hat{\rho}_{S_{02}}}{d\tau} &= -\frac{i}{\hbar} \langle S_{02} | [H, \hat{\rho}] | S_{02} \rangle + \Gamma_{in} \hat{\rho}_{S_{11}} - \Gamma_R \hat{\rho}_{S_{02}} \\ \frac{d\hat{\rho}_{\uparrow 01}}{d\tau} &= +\frac{\Gamma_R}{2} \hat{\rho}_{S_{02}} - \Gamma_L \hat{\rho}_{\uparrow 01} \\ \frac{d\hat{\rho}_{\downarrow 01}}{d\tau} &= +\frac{\Gamma_R}{2} \hat{\rho}_{S_{02}} - \Gamma_L \hat{\rho}_{\downarrow 01} \end{aligned} \quad (4.5)$$

The rate equations for the off-diagonal elements are given by

$$\frac{d\hat{\rho}_{jk}}{d\tau} = -\frac{i}{\hbar} \langle j | [H, \hat{\rho}] | k \rangle - \frac{1}{2} (\Gamma^j + \Gamma^k) \hat{\rho}_{jk} \quad (4.6)$$

where the indices $j, k \in \{T_{11}^i, S_{11}, S_{02}, \uparrow_{01}, \downarrow_{01}\}$ label the states available to the system. The tunneling/projection rates Γ^j equal Γ_{in} and Γ_R for the S_{11} and S_{02}

4.4 Oscillating magnetic field and rate equations

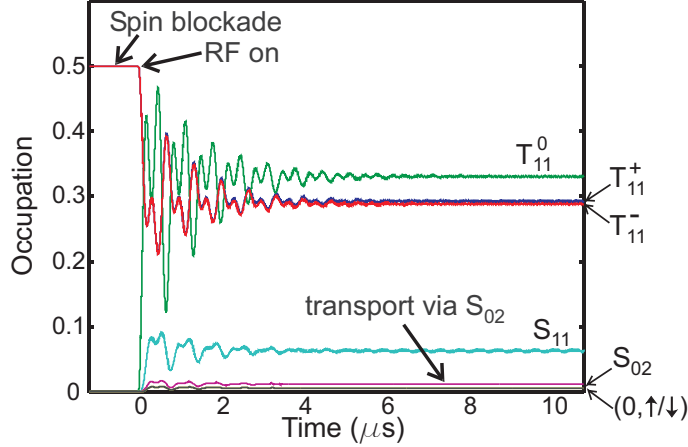


Figure 4.5: Time evolution of the diagonal elements of the density matrix for one particular nuclear configuration. Parameters: $\hbar\omega = g\mu_B 100$ mT, $B_{\text{ext}} = 100$ mT, $B_{N,x,y,z}^L = (0,0,2.2)$ mT, $B_{N,x,y,z}^R = (0,0,0)$, $B_1 = 1.3$ mT, $\Gamma_L = 73$ MHz, $\Gamma_R = 73$ MHz, $\hbar\Gamma_{\text{in}} = g\mu_B B_{N,z}^L$ and $\Delta_{\text{LR}} = 200$ μeV , $t = 0.3$ μeV .

states respectively, and equal zero for the other 5 states. The first term on the right-hand side describes the unitary evolution of the system, while the second term describes a loss of coherence due to the finite lifetime of the singlet states. This is the first source of decoherence in our model. The second one is the inhomogeneous broadening due to the interaction with the nuclear system. We do not consider other sources of decoherence, as they are expected to occur on much larger timescales.

Because we added a time-dependent term to the Hamiltonian (the oscillating field), we numerically calculate the time evolution of $\hat{\rho}(t)$, treating the Hamiltonian as stationary on the timescale $\Delta\tau \ll 2\pi/\omega$. To reduce the simulation time, we use the steady state solution $\hat{\rho}_{\tau \rightarrow \infty}$ in the absence of the oscillating magnetic field as the initial state $\hat{\rho}(\tau = 0)$ for the time evolution. At $\tau = 0$ the oscillating field is turned on and the system evolves towards a dynamic equilibrium on a timescale set by the inverse of the slowest tunnelling rate Γ . This new equilibrium distribution of populations is used to calculate the current flow, which is proportional to the occupation of the $|S_{02}\rangle$ state ($I = e\Gamma_R \hat{\rho}_{S_{02}}$). An example of the time evolution of the density matrix elements is shown in Fig. 4.5. The figure clearly reveals that the blockade is lifted when the oscillating field is applied. This is visible as an increase of the occupation of the S_{02} state.

In order to simulate the measured current flow, we assume that the measurement time of each datapoint is much longer than the typical timescale of the nuclear dynamics. Then, we expect that each datapoint is an integration of the response over many configurations of the nuclei. The effect of the evolving nuclear

4. Electron spin state detection in a double quantum dot

system is included in the calculations by averaging the different values of the (calculated) current flow obtained for each frozen configuration. These configurations are randomly sampled from a gaussian distribution of nuclear fields in the left and right dot (similar as in [109]). Because the electron in the two dots interact with different nuclear spins, the isotropic gaussian distributions in the two dots are uncorrelated, such that $\sqrt{\langle \Delta B_N^2 \rangle} = \sqrt{2} \sqrt{\langle B_N^2 \rangle}$ and $\langle B_{N,x}^2 \rangle = \langle B_{N,y}^2 \rangle = \langle B_{N,z}^2 \rangle$. For the sake of convenience we define

$$\sigma_N = \sqrt{\langle B_N^2 \rangle} \quad \text{and} \quad \sigma_{N,z} = \sqrt{\langle B_{N,z}^2 \rangle} = \sqrt{\frac{1}{3} \langle B_N^2 \rangle}. \quad (4.7)$$

4.5 Simulation results and physical picture

An example of the calculated (average) current flow as a function of B_{ext} (Fig. 4.6a,b) shows a (split) peak around zero magnetic field and two satellite peaks for $B_{\text{ext}} = \pm \hbar\omega / (g\mu_B)$, where the spin resonance condition is satisfied. The response from the induced spin flips via the driving field is visible for both inelastic and resonant transport regime, and the current flow has comparable magnitude as the peak at $B_{\text{ext}} = 0$. The satellite peaks are also visible in the experimental data (Fig. 4.6), although the shape and width of the satellite peaks are different, as we will see in the discussion below.

More specific, for the resonant transport regime, we see that for $t/\sigma_N < 5$ the satellite peaks increase in height when increasing t , simply because the coupling between the two singlet states increases. However, further increasing t reduces the ESR signal, and we see furthermore a split-peak at $B_{\text{ext}} = 0$. This splitting is due to the $S - T^0$ splitting, which is illustrated in Fig. 4.4b. Increasing the $S - T^0$ splitting also reduces the ESR signal, because the mixing between the $|T_{11}^0\rangle$ state with the hybridized singlet state by the nuclear field gradient is reduced. This mixing is a crucial element for detecting the induced rotations of one of the two electron spins. In the inelastic transport regime, this exchange splitting is negligibly small and, therefore, the height of the satellite peak depends only on Γ_{in} and the driving field B_1 . We see that the satellite peaks reduce in amplitude when increasing Γ_{in} beyond $5g\mu_B\sigma_N$. This is because the inelastic transition induces decoherence which suppresses the evolution from a triplet state to the $|S_{11}\rangle$ state.

A study of the height of the satellite peak as a function of B_1 reveals a non-monotonous behaviour, which can be seen in Fig. 4.7a. The physical picture behind this behavior is most easily sketched by distinguishing three regimes:

1. For $B_1 < \sigma_{N,z}$, for most of the nuclear configurations the spin in at most

4.5 Simulation results and physical picture

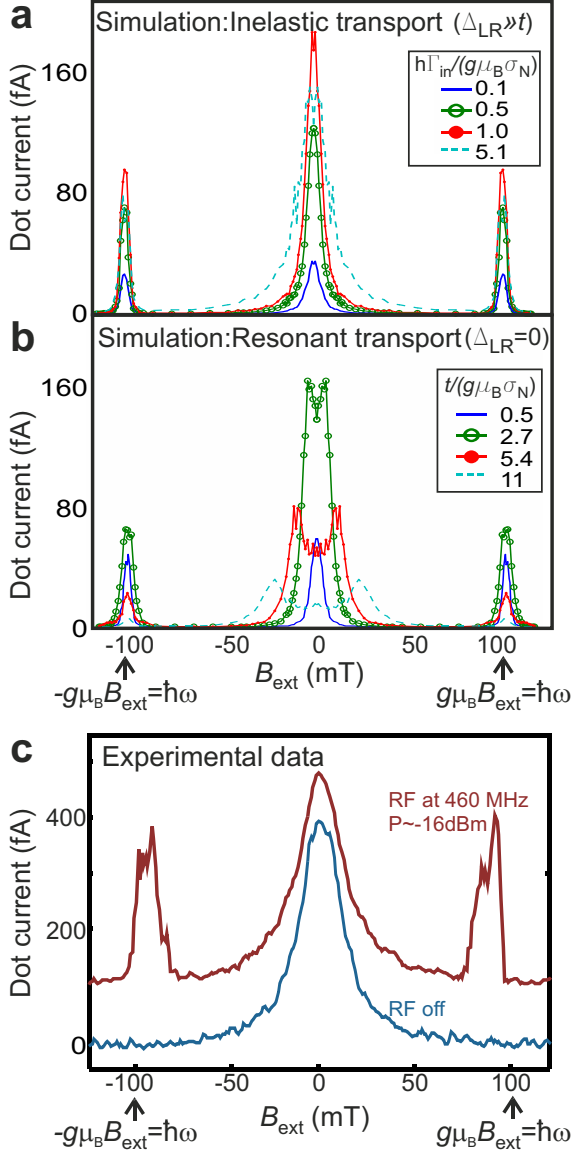


Figure 4.6:

(a). Calculated average current flow in the inelastic transport regime. Parameters: $\hbar\omega = g\mu_B 100$ mT, $B_{\text{ext}} = 100$ mT, $\sigma_N = 2.2$ mT, $B_1 = 1.3$ mT, $\Gamma_{L,R} = 73$ MHz, $t = 0.3$ μeV and $\Delta_{LR} = 200$ μeV . Results are similar for any value for t , provided that $\Delta_{LR} \gg t$.

(b) Calculated average current flow in the resonant transport regime at zero detuning for different values of t . Parameters: $\hbar\omega = g\mu_B 100$ mT, $\sigma_N = 2.2$ mT, $B_1 = 1.3$ mT, $\Gamma_{L,R} = 73$ MHz, $\Gamma_{\text{in}} = 0$ and $\Delta_{LR} = 0$. Averaged over 400 nuclear configurations for $t / (g\mu_B\sigma_N) > 0.5$ and 60 configurations for $t / (g\mu_B\sigma_N) = 0.5$. Simulation carried out for positive magnetic fields only; values shown for negative fields are equal to results obtained for positive field.

(c) Experimental data from ref. [104] with (curve offset by 100 fA for clarity) and without oscillating magnetic field. The frequency of the oscillating magnetic field is 460 MHz and the applied power is -16 dBm.

one of the two dots is on resonance, so spins are flipped in either the left or right dot. In that case transitions are induced from e.g. $|\uparrow\uparrow\rangle$ to $|\uparrow\downarrow\rangle = |S_{11}\rangle + |T_{11}^0\rangle$ or $|\downarrow\uparrow\rangle = |S_{11}\rangle - |T_{11}^0\rangle$. The resulting current flow initially increases quadratically with B_1 , as one would normally expect (Fig. 4.7a).

2. For $B_1 \gg \sigma_{N,z}$, for most of the nuclear configurations two spins are rotated simultaneously due to power broadening of the Rabi resonance. The stronger B_1 , the more the transitions occur only in the triplet subspace (the driving field B_1 that rotates two spins dominates the $S - T_0$ mixing by the nuclear spins). As a result, the current decreases for increasing B_1 .
3. If $B_1 \sim \sigma_{N,z}$ the situation is more complex because both processes (rotation

4. Electron spin state detection in a double quantum dot

of 2 spins simultaneously *and* transitions from $|T_{11}^0\rangle$ to $|S_{11}\rangle$) are effective. We find that if both processes occur with comparable rates, the overall transition rate to the singlet state is highest. This is the reason why the current has a maximum at $B_1 \approx \sigma_{N,z}$ (Fig. 4.7a).

The experimental data of the ESR satellite peak height (normalized by the zero-field current flow) for two different values of Δ_{LR} are shown in Fig. 4.7a. In order to compare the experimental results with the model we have estimated the rate Γ_{in} from the measured current flow at $B_{ext} = 0$ (we found similar values for both curves). The agreement of the experimental data with the model is reasonable, as it shows the expected quadratic increase with B_1 , as well as a comparable peak height. However, we see that variations of the level detuning Δ_{LR} can result in considerable differences of the measured ESR peak height. We have two possible explanations for the deviations of the experimental data with the model. First, we have found experimental signatures of dynamic nuclear polarization when the ESR resonance condition was fulfilled. We expect that this is due to feedback of the electron transport on the nuclear spins (similar to that discussed in [108, 110, 112]), although the exact processes are not (yet) fully understood. Second, unwanted electric fields affect the electron tunnelling processes, but are not taken into account in the model. We expect that these

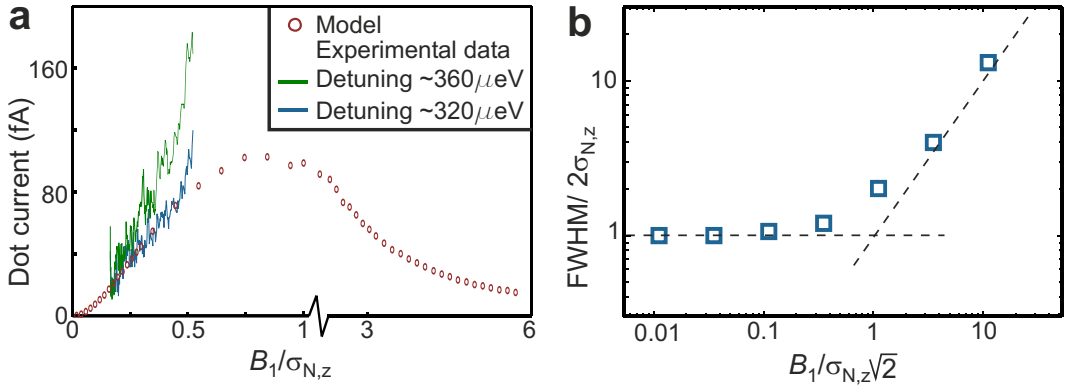


Figure 4.7: Height and width of the ESR satellite peak. (a) Circles: calculated ESR peak height as a function of driving amplitude B_1 . Parameters: $\hbar\omega = g\mu_B 100$ mT, $B_{ext} = 100$ mT, $\sigma_N = 2.2$ mT, $\Gamma_{L,R} = 73$ MHz, $t = 0.3$ μ eV, $\hbar\Gamma_{in} = g\mu_B\sigma_N$ and $\Delta_{LR} = 200$ μ eV. Lines are the current measurements for 2 different values of Δ_{LR} . The measurements show time-dependent (telegraph type) behavior. Therefore, the curves are obtained by repeating sweeps of B_1 and then selecting the largest current value for each value of B_1 . (b) Calculated width of the ESR satellite peaks as a function of B_1 . For small ESR power the peak is broadened by the random nuclear fluctuations, at high powers it is broadened by B_1 .

4.5 Simulation results and physical picture

electric fields will not change the location and width of the ESR satellite peaks because this field does not couple the spin states. It is however possible that the height of the satellite peak is altered by the electric field because it can affect the coupling between the S_{02} and the S_{11} state.

Finally, we discuss the width of the ESR satellite peak (Fig. 4.7b). If the inelastic tunnelling process between the dots (with rate Γ_{in}) and B_1 are both smaller than $\sigma_{N,z}$, the ESR peak (obtained from simulations) is broadened by the statistical fluctuations of the effective nuclear field. For high B_1 , the width approaches asymptotically the line with slope 1 (see Fig. 4.7b). In this regime, the peak is broadened by the RF amplitude B_1 . In the experiment [104], the shape of the satellite peak was different (flat on top with sharp edges) than expected from the model. Furthermore, the FWHM was larger than expected from just $\sigma_{N,z}$. We attribute this to feedback of the ESR-induced current flow on the nuclear spin bath. As a result, a clear FWHM increase with B_1 could not be observed.

It should be noted that in the simulation the central peak is broader than the satellite peaks. From studying the influence of various parameters in the model, we conclude that the greater width of the central peak is caused by the transverse nuclear field fluctuations ($B_{N,x}$ and $B_{N,y}$), which broaden the central peak but not the ESR satellite peaks.

We conclude that the model discussed here qualitatively agrees with the main features that were observed in the double dot transport measurements that aims at detecting (continuous wave) ESR of a single electron spin. The details of the ESR satellite peak height and width do not agree quantitatively with the model. We believe these deviations can be attributed to unwanted electric fields and feedback of the electron transport on the nuclear spin polarization. Improving the understanding of these feedback mechanisms remains interesting for future investigation as it might point towards a direction to mitigate the decoherence of the electron spin [88, 109].

This study was supported by the Dutch Organization for Fundamental Research on Matter (FOM), the Netherlands Organization for Scientific Research (NWO) and the Defense Advanced Research Projects Agency Quantum Information Science and Technology program.

4. Electron spin state detection in a double quantum dot

Chapter 5

Control and detection of singlet-triplet mixing in a random nuclear field

F. H. L. Koppens, J. A. Folk, J. M. Elzerman, R. Hanson, L. H. Willems van Beveren, I. T. Vink, H. P. Tranitz, W. Wegscheider, L. P. Kouwenhoven & L. M. K. Vandersypen

We observe mixing between two-electron singlet and triplet states in a double quantum dot, caused by interactions with nuclear spins in the host semiconductor. This mixing is suppressed by applying a small magnetic field, or by increasing the interdot tunnel coupling and thereby the singlet-triplet splitting. Electron transport involving transitions between triplets and singlets in turn polarizes the nuclei, resulting in striking bistabilities. We extract from the fluctuating nuclear field a limitation on the time-averaged spin coherence time T_2^* of 25 nanoseconds. Control of the electron-nuclear interaction will therefore be crucial for the coherent manipulation of individual electron spins.

This chapter has been published in *Science* **309**, 1346-1350 (2005).

5.1 Introduction

A single electron confined in a GaAs quantum dot is often referred to as artificial hydrogen. One important difference between natural and artificial hydrogen, however, is that in the first, the hyperfine interaction couples the electron to a single nucleus, whereas in artificial hydrogen the electron is coupled to about one million Ga and As nuclei. This creates a subtle interplay between electron spin eigenstates affected by the ensemble of nuclear spins (the Overhauser shift), nuclear spin states affected by time-averaged electron polarization (the Knight shift), and the flip-flop mechanism that trades electron and nuclear spins [113, 114].

The electron-nuclear interaction has important consequences for quantum information processing with confined electron spins [20]. Any randomness in the Overhauser shift introduces errors in a qubit state, if no correcting measures are taken [81, 82, 115]. Even worse, multiple qubit states, like the entangled states of two coupled electron spins, are redefined by different Overhauser fields. Characterization and control of this mechanism will be critical both for identifying the problems and finding potential solutions.

Here, the implications of the hyperfine interaction on entangled spin states are studied in two coupled quantum dots — an artificial hydrogen molecule — in which the molecular states can be controlled electrically. A random polarization of nuclear spins creates an inhomogeneous effective field that couples molecular singlet and triplet states, and leads to new eigenstates that are admixtures of these two. We use transport measurements to determine the degree of mixing over a wide range of tunnel coupling, and observe a subtle dependence of this mixing on magnetic field. We find that we can controllably suppress the mixing by increasing the singlet-triplet splitting. This ability is crucial for reliable two-qubit operations such as the SWAP gate [20].

Furthermore, we find that electron transport itself acts back on the nuclear spins through the hyperfine interaction, and time-domain measurements reveal complex, often bistable, behavior of the nuclear polarization. Understanding the current-induced nuclear polarization is an important step towards electrical control of the nuclear spins. Such control will be critical for electrical generation and detection of entangled nuclear spin states [116], or for transfer of quantum information between electron and nuclear spin systems [19, 117]. Even more appealing will be reducing the nuclear field fluctuations in order to achieve longer electron spin coherence times [87, 75, 50].

5.2 Spin blockade

The coupled electron-nuclear system is studied using electrical transport measurements through two dots in series [118], in a regime where the Pauli exclusion principle blocks current flow [105, 119]. The dots are defined using electrostatic gates on a GaAs/AlGaAs heterostructure¹ (see Fig. 5.1e). The gate voltages are tuned such that one electron always resides in the right dot, and current flows if a second electron tunnels from the left reservoir, through the left and right dots, to the right reservoir (see Fig. 5.1d). This cycle can be described using the occupations (m, n) of the left and right dots: $(0, 1) \rightarrow (1, 1) \rightarrow (0, 2) \rightarrow (0, 1)$. When an electron enters from left dot, the two-electron system forms either a molecular singlet, $S(1,1)$, or a molecular triplet, $T(1,1)$. From $S(1,1)$, the electron in the left dot can move to the right dot to form $S(0,2)$. From $T(1,1)$, however, the transition to $(0,2)$ is forbidden by spin conservation ($T(0,2)$ is much higher in energy than $S(0,2)$). Thus, as soon as $T(1,1)$ is occupied, further current flow is blocked (Pauli blockade).

5.3 Lifting of spin blockade due to the nuclear field

A characteristic measurement of this blockade is shown in Fig. 5.1a. The suppression of current (< 80 fA) in the region defined by dashed lines is a signature of Pauli blockade [105, 119] (see also section 4.2). Fig. 5.1b shows a similar measurement, but with a much weaker interdot tunnel coupling t . Strikingly, a large leakage current now appears in the Pauli blocked region, even though the barrier between the two dots is more opaque. Furthermore, this leakage current is substantially reduced by an external magnetic field of only 100 mT (Fig. 5.1c). Such a strong field dependence is remarkable because the in-plane magnetic field, B_{ext} , couples primarily to spin and the Zeeman energies involved are very small ($E_Z \sim 2.5 \mu\text{eV}$ at $B_{\text{ext}} = 100$ mT compared to the thermal energy, $\sim 15 \mu\text{eV}$ at 150 mK, for example).

Leakage in the Pauli blockade regime occurs when singlet and triplet states are coupled. The $T(1,1)$ state that would block current can then transition to the $S(1,1)$ state and the blockade is lifted (Fig. 5.1d). As we will show, coupling of sin-

¹The electrostatic gates are on the surface of a GaAs/AlGaAs heterostructure. The 2DEG is 90 nm below the surface, with density $1.33 \times 10^{11} \text{ cm}^{-2}$ and mobility $9.71 \times 10^5 \text{ cm}^2/\text{Vs}$. Measurements are performed in a dilution refrigerator at 150 mK, with a magnetic field in the plane of the heterostructure.

5. Control and detection of singlet-triplet mixing in a random nuclear field

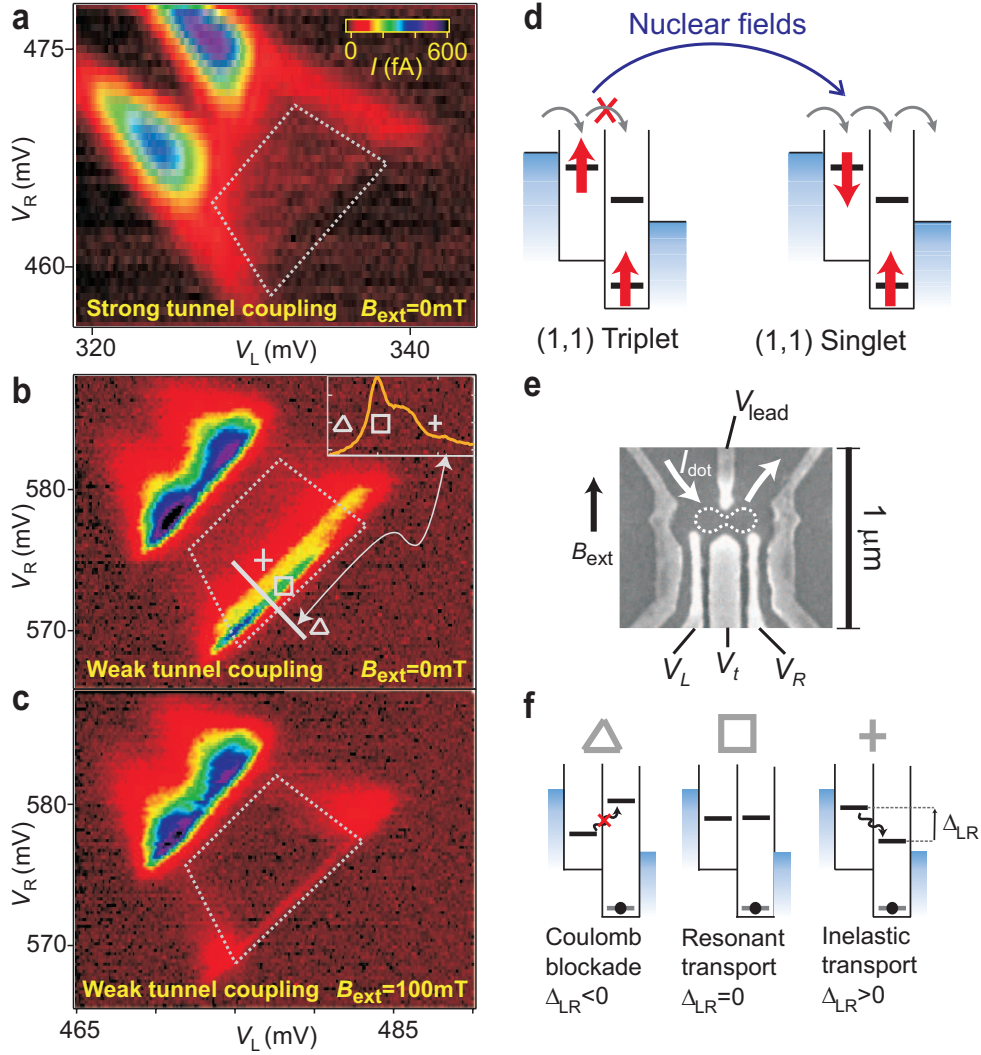


Figure 5.1: Pauli blockade and leakage current. (a) Color-scale plot of the current through two coupled dots as a function of the left and right dot potentials (voltage bias $800 \mu\text{eV}$, $V_t = -108$ mV). The experimental signature of Pauli blockade is low current (< 80 fA) in the area denoted by dotted grey lines. (b) Analogous data for smaller interdot tunnel coupling ($V_t = -181$ mV), with the same color scale as in (a). A dramatic increase of leakage current is seen in the lower part of the Pauli blocked area (green/yellow band). Inset: 1D trace along the solid grey line, with Coulomb blocked, resonant and inelastic transport regimes marked, see also (f). (c) Analogous data for the same tunnel coupling as in (b), but for $B_{\text{ext}} = 100$ mT. The leakage current from (b) is strongly suppressed. (d) Two level diagrams that illustrate Pauli blockade in coupled quantum dots (see text). When the (1,1) triplet is changed into the (1,1) singlet (red arrow), Pauli blockade is lifted. (e) SEM micrograph showing the device geometry. White arrows indicate current flow through the two coupled dots (dotted line). (f) Level diagrams illustrating three transport regimes. Δ : Coulomb blockade; transport would require absorption of energy. \square : Resonant transport; the dot levels are aligned. $+$: Inelastic transport; energy must be transferred to the environment, for instance by emitting a phonon.

5.4 Singlet-triplet splitting

glets and triplets in Figs. 5.1b,c originates from the hyperfine interaction between the electron spins and the Ga and As nuclear spins (other leakage mechanisms can be ruled out, see section 5.9.1).

The hyperfine interaction between an electron with spin \mathbf{S} and a nucleus with spin \mathbf{I} has the form $A\mathbf{I} \cdot \mathbf{S}$, where A characterizes the coupling strength. An electron coupled to an ensemble of n nuclear spins experiences an effective magnetic field $\mathbf{B}_N \sim \frac{1}{g\mu_B} \sum_i^n A_i \mathbf{I}_i$, with g the electron g -factor and μ_B the Bohr magneton [113]. For fully polarized nuclear spins in GaAs, $B_N \sim 5$ T [79]. For unpolarized nuclear spins, statistical fluctuations give rise to an effective field pointing in a random direction with an average magnitude of $5 \text{ T}/\sqrt{n}$ [81, 107, 82]. Quantum dots like those measured here contain $n \sim 10^6$ nuclei, so $\sqrt{\langle |\mathbf{B}_N|^2 \rangle} \sim 5$ mT.

Nuclei in two different dots give rise to effective nuclear fields, \mathbf{B}_{N1} and \mathbf{B}_{N2} , that are uncorrelated. Although the difference in field $\Delta\mathbf{B}_N = \mathbf{B}_{N1} - \mathbf{B}_{N2}$ is small, corresponding to an energy $E_N \equiv g\mu_B \sqrt{\langle \Delta |\mathbf{B}_N|^2 \rangle} \sim 0.1 \mu\text{eV}$, it nevertheless plays a critical role in Pauli blockade. The (1,1) triplet state that blocks current flow consists of one electron on each of the two dots. When these two electrons are subject to different fields, the triplet is mixed with the singlet and Pauli blockade is lifted. For instance, an inhomogeneous field along \hat{z} causes the triplet $|T_0\rangle = \frac{1}{\sqrt{2}}(|\uparrow\downarrow\rangle + |\downarrow\uparrow\rangle)$ to evolve into the singlet $\frac{1}{\sqrt{2}}(|\uparrow\downarrow\rangle - |\downarrow\uparrow\rangle)$. Similarly, the other two triplet states, $|T_+\rangle = |\uparrow\uparrow\rangle$ and $|T_-\rangle = |\downarrow\downarrow\rangle$, evolve into the singlet due to \hat{x} and \hat{y} components of $\Delta\mathbf{B}_N$.

5.4 Singlet-triplet splitting

The degree of mixing by the inhomogeneous field depends on the singlet-triplet energy splitting, E_{ST} . Singlet and triplet states that are close together in energy ($E_{ST} \ll E_N$) are strongly mixed, whereas states far apart in energy ($E_{ST} \gg E_N$) experience only a slight perturbation due to the nuclei.

The singlet-triplet splitting depends on the interdot tunnel coupling t and on the detuning of left and right dot potentials Δ_{LR} . Δ_{LR} and t are controlled experimentally using gate voltages (Fig. 5.1e). V_t controls the interdot tunnel coupling. V_L and V_R set the detuning, and thereby determine whether transport is inelastic (detuned levels), resonant (aligned levels), or blocked by Coulomb blockade (Fig. 5.1f). The coupling of the dots to the leads is held constant with V_{lead} .

The effect of the two tunable parameters t and Δ_{LR} on the singlet and triplet energies is illustrated in Figs. 5.2a,b. For weak tunnel coupling ($t \sim 0$), and in

5. Control and detection of singlet-triplet mixing in a random nuclear field

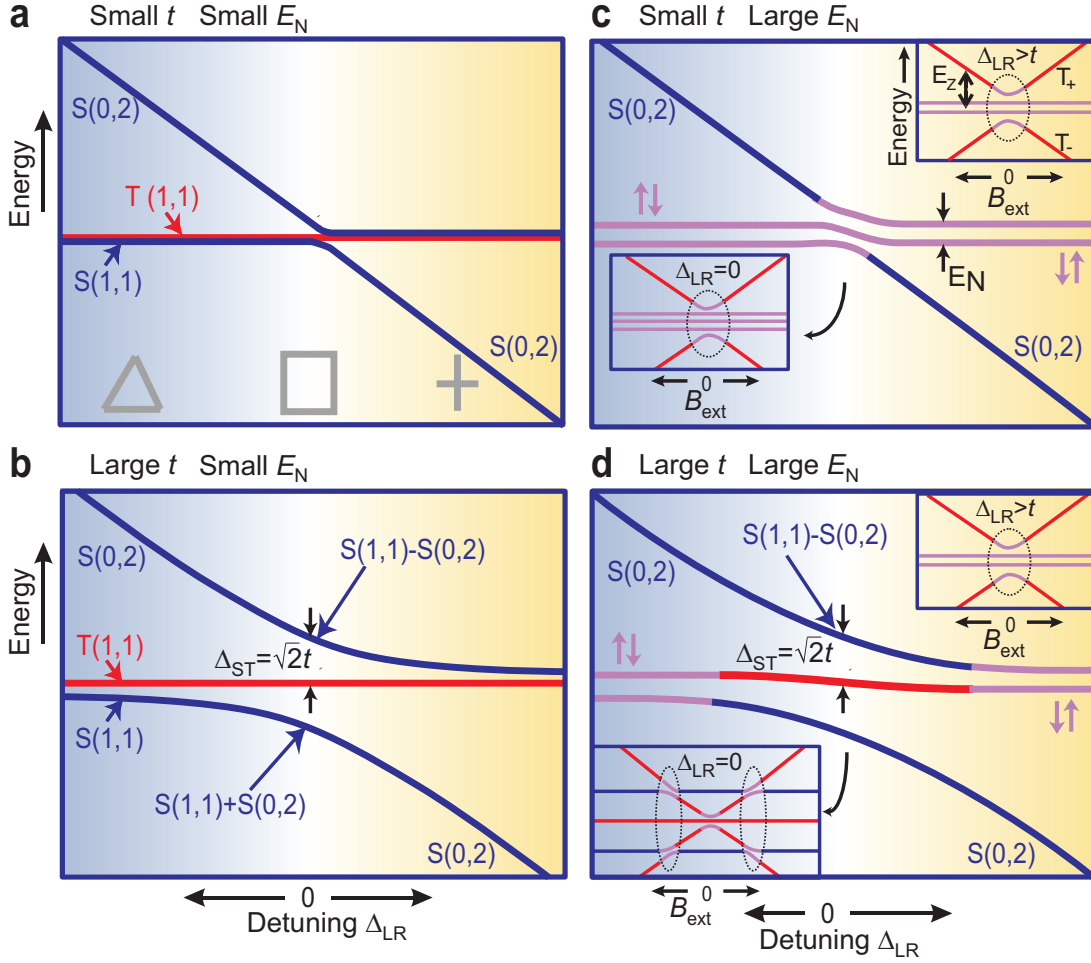


Figure 5.2: Two-electron level diagrams showing energy as a function of detuning Δ_{LR} . Detuning is defined so that the energy of $T(1,1)$ remains constant as Δ_{LR} varies (see also section 4.2). The panels on the left illustrate the effect of t ; the panels on the right include the additional effect of an inhomogeneous magnetic field. Pure singlet and triplet states are drawn in blue and red respectively, strong admixtures in purple. The blue, white and yellow background correspond to the Coulomb blockade, resonant and inelastic transport regime respectively. (a) For small tunnel coupling, $T(1,1)$ and $S(1,1)$ are nearly degenerate. (b) For finite t , level repulsion between the singlet states results in a larger singlet-triplet splitting compared to (a), which depends on detuning. The tunnel coupling does not mix singlet and triplet states. For large Δ_{LR} (but smaller than the single dot S-T splitting) $E_{ST} \sim t^2/\Delta_{LR}$. (c and d) An inhomogeneous field mixes triplet and singlet states that are close in energy (purple lines). For clarity only one triplet state is shown in the main panels. (c) For small t , $T(1,1)$ and $S(1,1)$ mix strongly over the full range of detuning. (d) For large t , $T(1,1)$ mixes only strongly with the singlet for large detuning. The insets to (c) and (d) show the effect of an external magnetic field on the two-electron energy levels. All three triplets are shown now; the triplets $|T_+\rangle$ and $|T_-\rangle$ split off from $|T_0\rangle$ due to B_{ext} . The leakage current is highest in the regions indicated by black dotted ellipses (see text).

5.5 Competition between exchange interaction and nuclear field

the absence of a hyperfine interaction ($E_N \sim 0$), the (1,1) singlet and (1,1) triplet states are nearly degenerate (Fig. 5.2a). A finite interdot tunnel coupling t leads to an anticrossing of S(1, 1) and S(0, 2). The level repulsion results in an increased singlet-triplet splitting that is strongly dependent on detuning (Fig. 5.2b). At the resonant condition ($\Delta_{LR} = 0$, aligned levels), the two new singlet eigenstates are equidistant from the triplet state, both with $E_{ST} = \sqrt{2}t$. For finite detuning (but smaller than the single dot S-T splitting), one singlet state comes closer to the triplet state ($E_{ST} \sim t^2/\Delta_{LR}$), while the other moves away. Both in Figs. 5.2a and 5.2b, singlet and triplet states are pure eigenstates (not mixed) and therefore Pauli blockade would be complete.

The additional effect of the inhomogeneous nuclear field is shown in Figs. 5.2c and 5.2d. For small t ($\sqrt{2}t, t^2/\Delta_{LR} < E_N$), the (1,1) singlet and (1,1) triplet are close together in energy and hence mix strongly (purple lines) over the entire range of detuning. For t such that $t^2/\Delta_{LR} < E_N < \sqrt{2}t$, triplet and singlet states mix strongly only for finite detuning. This is because E_{ST} is larger than E_N for aligned levels but smaller than E_N at finite detuning. For still larger t ($\sqrt{2}t, t^2/\Delta_{LR} > E_N$, not shown in Fig. 5.2), mixing is weak over the entire range of detuning. In the cases where mixing between S and T is strong, as in Figs. 5.2c and D (for large detuning), Pauli blockade is lifted and a leakage current results.

5.5 Competition between exchange interaction and nuclear field

The competition between E_{ST} and E_N can be seen experimentally by comparing 1D traces of leakage current as a function of detuning over a wide range of t (Fig. 5.3a). Resonant current appears as a peak at $\Delta_{LR} = 0$; inelastic leakage as the shoulder at $\Delta_{LR} > 0$ [120]. When the interdot tunnel coupling is small, both resonant and inelastic transport are allowed due to singlet-triplet mixing, and both rise as the middle barrier becomes more transparent. As the tunnel coupling is raised further, the point is reached where E_{ST} becomes larger than the nuclear field and Pauli blockade suppresses the current (see also Fig. 5.1a). The maximum resonant current occurs at a smaller value of t compared to the maximum inelastic current (see Fig. 5.3a, inset). This is consistent with E_{ST} being much smaller for finite detuning than for aligned levels ($t^2/\Delta_{LR} \ll \sqrt{2}t$) (Figs. 5.2b,d).

The experimental knob provided by electrostatic gates is very coarse on the energy scales relevant to the hyperfine interaction. However, the external magnetic field can easily be controlled with a precision of 0.1 mT, corresponding to a

5. Control and detection of singlet-triplet mixing in a random nuclear field

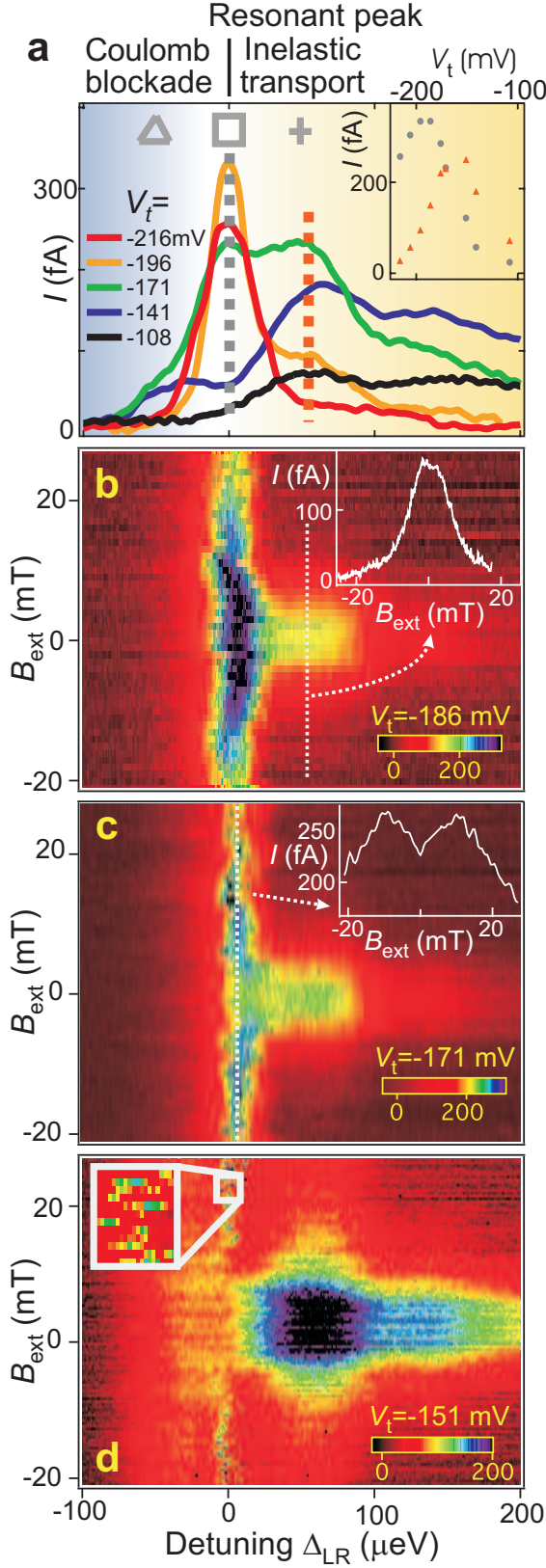


Figure 5.3: The measured leakage current results from a competition between E_N , E_{ST} and E_Z .

(a) 1D traces of the leakage current as a function of detuning at $B_{\text{ext}} = 0$, for a wide range of tunnel couplings (analogous to the inset of Fig. 5.1b). Coulomb blockade, resonant transport and inelastic transport are indicated by colored backgrounds as in Fig. 5.2. Inset: leakage current along the dotted grey and orange lines is shown as a function of V_t . Resonant and inelastic leakage (grey and orange markers) reach a maximum at different tunnel couplings ($V_t = -190$ mV and -150 mV respectively).

(b) For small tunnel coupling ($< E_N$), both the resonant and inelastic leakage currents drop monotonically with B_{ext} . Inset: magnetic field dependence of the inelastic current along the dotted line ($\Delta_{\text{LR}} = 40 \mu\text{eV}$).

(c) For larger t ($> E_N$), the resonant leakage current is maximum at $B_{\text{ext}} \pm 10$ mT. Inset: field dependence of the resonant peak height (dotted line). (d) For still larger t , the resonant current is strongly reduced at low field, then becomes unstable for higher field (see inset).

5.5 Competition between exchange interaction and nuclear field

Zeeman splitting (2 neV) that is 50 times smaller than E_N . For this reason, monitoring the field dependence allows a more detailed examination of the competing energy scales E_{ST} , E_Z and E_N .

The competition between E_Z and E_N is clear for small interdot tunnel coupling (Fig. 5.3b). Leakage current is suppressed monotonically with magnetic field, on a scale of ~ 5 mT and ~ 10 mT for inelastic and resonant transport respectively. The qualitative features of this field dependence are represented in the insets to Fig. 5.2c. At zero field all states are mixed strongly by the inhomogeneous nuclear field, but when E_Z exceeds E_N , the mixing between the singlet and two of the triplet states ($|T_+\rangle$ and $|T_-\rangle$) is suppressed. An electron loaded into either of these blocks further current flow and leakage disappears.

The magnitude of the fluctuating Overhauser field can be extracted from the inelastic peak shape in the limit of small t (as in the inset of Fig. 5.3b). We fit the data to a model that describes the transport cycle using the master equation approach [109] (see Fig. 5.4). From this fit, we find a magnitude of the inhomogeneous field $\sqrt{\langle \Delta B_N^2 \rangle} = 1.73 \pm 0.02$ mT ($E_N = 0.04 \mu\text{eV}$), largely independent of Δ_{LR} over the parameter range studied². The value for the effective nuclear field fluctuations in a single dot is obtained from the relation $\langle B_N^2 \rangle = \frac{1}{2} \langle \Delta B_N^2 \rangle$, giving $\sqrt{\langle B_N^2 \rangle} = 1.22$ mT. This is consistent with the strength of the hyperfine interaction in GaAs and the number of nuclei that are expected in each dot [81, 84].

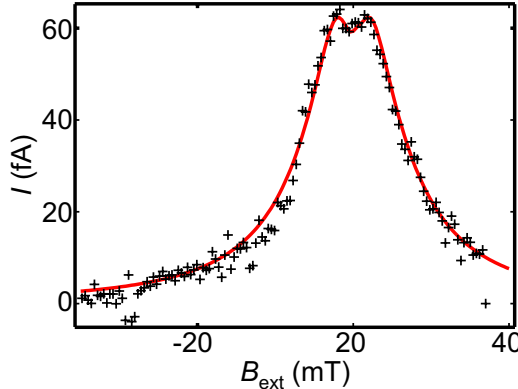


Figure 5.4: The calculated peak shape (solid line) shows excellent agreement with the measured inelastic leakage current (crosses, $V_t = -206$ mV, $\Delta_{LR} = 50 \mu\text{eV}$).

²The difference between the field dependence of the resonant and inelastic current can be explained by the coupling with the leads. The S(0,2) state is lifetime broadened due to coupling with the right lead ($\sim 0.3 \mu\text{eV}$) giving a weaker field dependence for the resonant current. The field dependence of the inelastic leakage is not affected by the lead coupling, because under the high bias conditions of this experiment, there are no available states in the left lead that could broaden S(1,1).

5.6 Competition between exchange interaction, nuclear field and external field

The three-way interplay between E_{ST} , E_Z and E_N is most clearly visible in the resonant current. At an intermediate value of tunnel coupling, $t \gtrsim E_N$ (Fig. 5.3c), the resonant peak is split in magnetic field, with maxima at ± 10 mT (see Fig. 5.3, inset). The lower inset to Fig. 5.2d illustrates this behaviour. At $B_{\text{ext}} = 0$, the current is somewhat suppressed compared to the current in Fig. 5.3b, because $E_{\text{ST}} > E_N$ at that point. Increasing B_{ext} enhances the mixing as the $|T_+\rangle$ and $|T_-\rangle$ states approach the singlet states. The maximum leakage occurs when the states cross, at $E_{\text{ST}} (= \sqrt{2}t) = E_Z$. Here, E_Z is $0.25 \pm 0.03 \mu\text{eV}$ at the current maximum, from which we can extract $t = 0.18 \pm 0.02 \mu\text{eV}$ for this setting of V_t . At still larger B_{ext} , $|T_+\rangle$ and $|T_-\rangle$ move away from the singlet states again, and the leakage current is suppressed.

5.7 Current fluctuations

The system enters into a new regime for still higher tunnel coupling (Figs. 5.2d and 5.5), where it becomes clear that the electron-nuclear system is dynamic. The zero field resonant leakage is further suppressed and above 10 mT prominent current spikes appear (Fig. 5.3d, inset). The spikes are more markedly visible in a three-dimensional surface plot of leakage over a broader range of field (Fig. 5.5a). Even for fixed experimental parameters, the current fluctuates in time as shown in Fig. 5.5b.

We find that time dependent behavior is a consistent feature of resonant transport for $(E_{\text{ST}}, E_Z) \gg E_N$. For some settings the time dependence is fast (for example, the fluctuations in Figs. 5.5a and 5.5b), but for others the leakage changes much more slowly. An example of the slower time dependence is shown in Fig. 5.5c. Starting from an equilibrium situation (bias voltage switched off for 5 minutes), the current is initially very small after the bias is turned on. It builds up and then saturates after a time that ranges from less than a second to several minutes. This timescale depends on Δ_{LR} , t , and B_{ext} . When no voltage bias is applied, the system returns to equilibrium after ~ 80 s at 200 mT. Similar long timescales of the nuclear spin-lattice relaxation times have been reported before in GaAs systems [121] and quantum dots [122]. We thus associate these effects with current-induced dynamic nuclear polarization and relaxation.

Evidence that the fast fluctuations too are related to current induced nuclear polarization (and cannot be explained by fluctuating background charges alone),

5.7 Current fluctuations

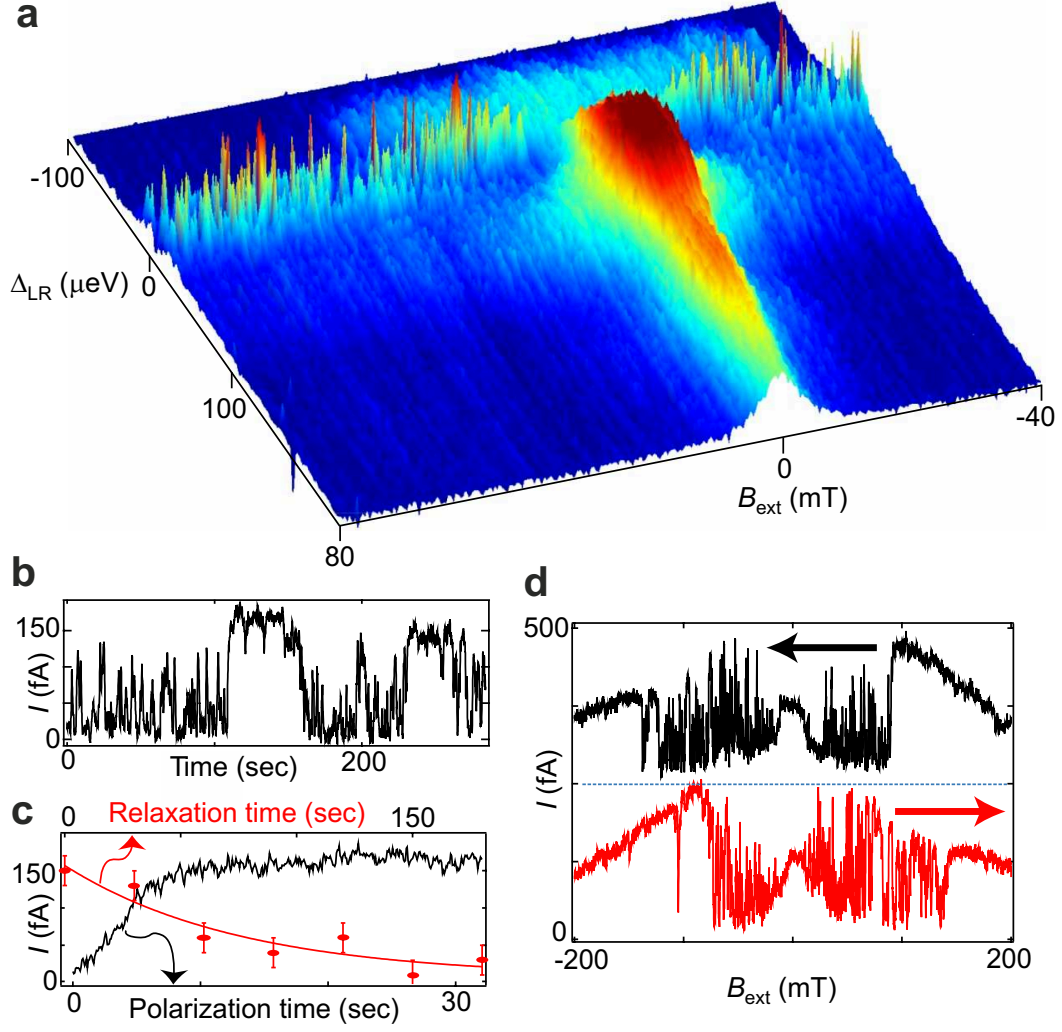


Figure 5.5: Time dependence of the leakage current reveals the dynamics of the electron-nuclear system. This time dependence occurs in the regime corresponding to Fig. 5.2d. (a) Surface plot of electrical transport for $V_t = -151$ mV. Instability on the resonant peak is visible as sharp current spikes. The sweep direction is from $+$ to $-\Delta_{\text{LR}}$, for fields stepped from $-$ to $+B_{\text{ext}}$. (b) Explicit time dependence of the resonant current exhibits bistability ($V_t = -141$ mV, $B_{\text{ext}} = 100$ mT). (c) Lower axis: dynamic nuclear polarization due to electron transport through the device ($V_t = -141$ mV, $\Delta_{\text{LR}} = 0$, $B_{\text{ext}} = 200$ mT), after initialization to zero polarization by waiting for 5 minutes with no voltage applied. Top axis: in order to measure the nuclear spin relaxation time, we wait for the current to saturate, switch off the bias voltage for a time t_{rel} , and then remeasure the leakage current. An exponential fit gives a time constant of 80 ± 40 s (measurements of these long timescales result in large error bars, ± 20 fA due to $1/f$ noise). (d) The field dependence of the resonant current is hysteretic in sweep direction ($V_t = -149$ mV). Each trace takes ~ 7 minutes.

5. Control and detection of singlet-triplet mixing in a random nuclear field

is found in their dependence on sweep direction and sweep rate [121]³. When the magnetic field is swept while maintaining fixed Δ_{LR} , the current shows fluctuations at low field but suddenly becomes stable at high field (Fig. 5.5d). The crossover from unstable to stable behavior occurs at a field that is hysteretic in sweep direction (Fig. 5.5d), and this hysteresis becomes more pronounced at higher sweep rates (faster than ~ 1 mT/s). The connection between the fluctuations and nuclear polarization is also evident from time traces, in which instability develops only after the nuclear polarization is allowed to build for some time (Fig. 5.6).

Unlike the regular oscillations that have been observed in other GaAs structures (see e.g. [108, 113]), the fluctuations in our measurements are random in time, and in many cases suggest bistability with leakage current moving between two stable values. We discuss the origin of such fast bistable fluctuations in section 5.9.2.

5.8 Conclusions

The ensemble of random nuclear spins that gives rise to the mixing of two-electron states as observed in this experiment also gives rise to an uncertainty of $g\mu_B\sqrt{\langle B_N^2 \rangle} = 0.03 \mu\text{eV}$ in the Zeeman energy of one electron. When averaged over a time longer than the correlation time of the nuclear spin bath ($\sim 100 \mu\text{s}$) [102], this implies an upper limit on the dephasing time of $T_2^* = \hbar/g\mu_B\sqrt{\frac{2}{3}\langle B_N^2 \rangle} = 25$ ns (as defined in [81]), comparable to the T_2^* found in recent optical spectroscopy measurements⁴. This value is four orders of magnitude shorter than the theoretical prediction for the electron spin T_2 in the absence of nuclei, which is limited only by spin-orbit interactions [67, 40, 77].

One way to eliminate the uncertainty in Zeeman energy that leads to effective dephasing is to maintain a well-defined nuclear spin polarization [50]. Many of the regimes explored in this paper show leakage current that is stable when current-induced polarization is allowed to settle for some time. These may in fact

³The leakage current is sensitive to magnetic fields of only a few mT, corresponding to 0.1% nuclear polarization. Given that the dot has $\sim 10^6$ nuclei, changes in the nuclear polarization of 0.1% can be caused by 1000 electron-nuclear flip-flop processes. For typical currents (~ 100 fA) 1000 electrons move through the dot in one millisecond, so in principle current fluctuations as fast as 1 kHz are possible.

⁴In Ref. [115], a T_2^* of 16 ns was found in a GaAs quantum dot, slightly shorter than in our experiment, presumably due to a smaller dot size. A considerably shorter timescale, 500 ps, was measured in InAs dots [82], due to a notable difference in dot size, nuclear spin I , and the stronger hyperfine coupling constant in InAs.

5.9 Additional material

be examples of specific nuclear polarizations that are maintained electrically.

The authors are grateful to O.N. Jouravlev and Y. Nazarov for developing a model that helped greatly with the physical interpretation of the data, and to G. Burkard, W.A. Coish, V.N. Golovach, A.C. Johnson, D. Loss and C.M. Marcus for fruitful discussions. We thank R. Schouten, B. van den Enden and M. van Oossanen for technical assistance and J. Caro for supporting infrastructure. This work was supported by the DARPA-QUIST program, the Dutch Organisation for Fundamental Research on Matter (FOM), the Netherlands Organization for Scientific Research (NWO), the ONR, ERATO, and the EU-RTN network on spintronics

5.9 Additional material

5.9.1 Other processes that lead to leakage currents

Spin exchange with the leads allows a blocked $T(1,1)$ state to change into $S(1,1)$, which can then move to $S(0,2)$. Alternatively, a second order virtual tunnelling process can bring $T(1,1)$ through the energetically forbidden $T(0,2)$ state. Both effects were observed, when the dot levels were close to the lead chemical potentials or to the $T(0,2)$ chemical potential respectively (for example outside the dotted lines in Fig. 5.1a). However, the measurements presented in Figs. 5.3 and 5.5 were taken with dot parameters at which these processes were insignificant. As further evidence that these processes are not relevant in our measurements, neither would have a strong dependence on in-plane magnetic field. A spin-orbit interaction may also couple triplet to singlet states, but the rate for this process is very slow for states close together in energy [64].

Instead, the field dependence observed in our measurements is consistent with an inhomogeneous field between the two dots of order 2 mT; the magnitude of this field, combined with field hysteresis and the observation of long relaxation times demonstrate that the origin of the leakage current is the hyperfine interaction with the nuclear spins of the semiconductor lattice.

5.9.2 Bistability of the nuclear polarization

Multiple stable values for the leakage current (see e.g. Fig. 5b) suggest multiple stable configurations of the electron-nuclear spin system. The existence of multiple stable configurations can arise from the competition between several polarization and depolarization processes. Dynamic nuclear polarization close to the $|T_+\rangle - |S\rangle$ transition tends to enhance the external field, while the $|T_-\rangle - |S\rangle$

5. Control and detection of singlet-triplet mixing in a random nuclear field

transition opposes the field. At 150 mK, nuclear spin diffusion and spin-lattice relaxation processes always lead to depolarization.

In contrast to previous reports on bistability of the electron-nuclear system when sweeping field (as in [121, 113]), we observe that the system can fluctuate in time between stable points. We believe that the electron-nuclear system can be kicked out of a stable point for instance by background charge fluctuations or statistical fluctuations in the nuclear field, and reach another stable point through dynamic nuclear polarization. When such processes occur repeatedly, they lead to a randomly fluctuating leakage current. We stress that charge fluctuations alone cannot explain our observations. Such an explanation would be inconsistent with the observations of Figs. 5.5d and 5.6, as explained in section 5.7.

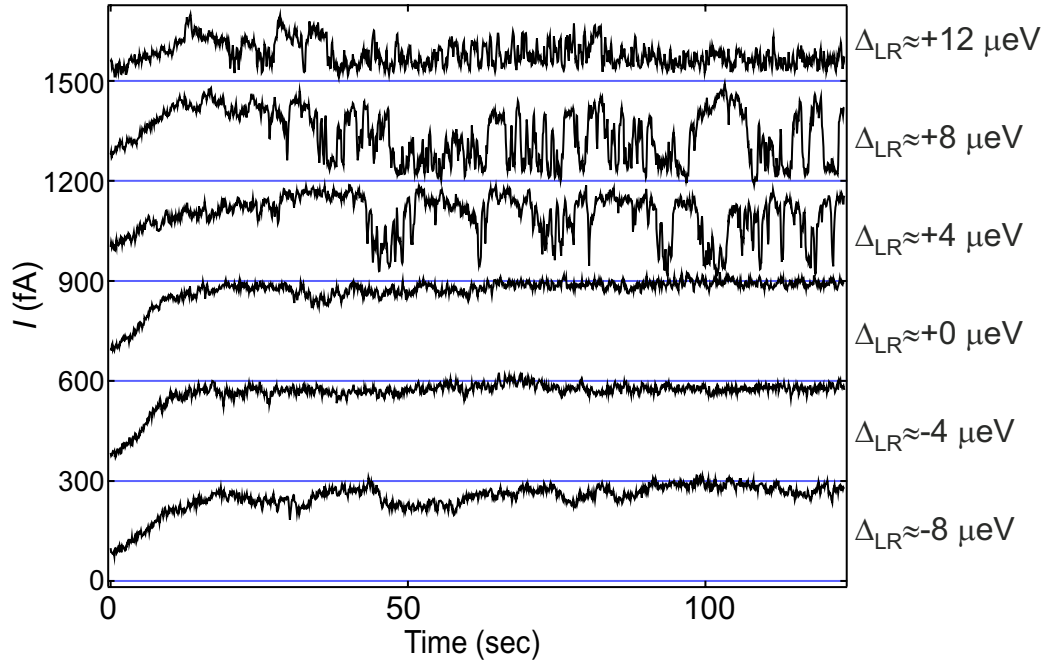


Figure 5.6: Time dependence of the resonant leakage current at several values of Δ_{LR} , with the nuclear system initialized to zero polarization for each trace (the position of $\Delta_{LR} = 0$ is approximate, but the step size is accurate). The fluctuations change character sharply when Δ_{LR} is changed by only $4 \mu\text{eV}$, which corresponds to a change in V_L and V_R of only $50 \mu\text{V}$ ($V_t = -149 \text{ mV}$, $B_{\text{ext}} = 200 \text{ mT}$).

Chapter 6

Driven coherent oscillations of a single electron spin in a quantum dot

F. H. L. Koppens, C. Buizert, K. J. Tielrooij, I. T. Vink, K. C. Nowack, T. Meunier, L. P. Kouwenhoven & L. M. K. Vandersypen

The ability to control the quantum state of a single electron spin in a quantum dot is at the heart of recent developments towards a scalable spin-based quantum computer. In combination with the recently demonstrated exchange gate between two neighbouring spins, driven coherent single spin rotations would permit universal quantum operations. Here, we report the experimental realization of single electron spin rotations in a double quantum dot. First, we apply a continuous-wave oscillating magnetic field, generated on-chip, and observe electron spin resonance in spin-dependent transport measurements through the two dots. Next, we coherently control the quantum state of the electron spin by applying short bursts of the oscillating magnetic field and observe about eight oscillations of the spin state (so-called Rabi oscillations) during a microsecond burst. These results demonstrate the feasibility of operating single-electron spins in a quantum dot as quantum bits.

This chapter has been published in *Nature* **442**, 766-771 (2006).

6.1 Introduction

The use of quantum mechanical superposition states and entanglement in a computer can theoretically solve important mathematical and physical problems much faster than classical computers [9, 8]. However, the realization of such a quantum computer represents a formidable challenge, because it requires fast and precise control of fragile quantum states. The prospects for accurate quantum control in a scalable system are thus being explored in a rich variety of physical systems, ranging from nuclear magnetic resonance and ion traps to superconducting devices [123].

Electron spin states were identified early on as an attractive realization of a quantum bit [12], because they are relatively robust against decoherence (uncontrolled interactions with the environment). Advances in the field of semiconductor quantum dots have made this system very fruitful as a host for the electron spin. Since Loss and DiVincenzo's proposal [20] on electron spin qubits in quantum dots in 1998, many of the elements necessary for quantum computation have been realized experimentally. It is now routine to isolate with certainty a single electron in each of two coupled quantum dots [124, 125, 126, 127]. The spin of this electron can be reliably initialized to the ground state, spin-up, via optical pumping [128] or by thermal equilibration at sufficiently low temperatures and strong static magnetic fields (for example, $T = 100$ mK and $B_{\text{ext}} = 1$ T). The spin states are also very long-lived, with relaxation times of the order of milliseconds [129, 41, 40]. Furthermore, a lower bound on the spin coherence time exceeding 1 s was established, using spin-echo techniques on a two-electron system [42]. These long relaxation and coherence times are possible in part because the magnetic moment of a single electron spin is so weak. On the other hand, this property makes read-out and manipulation of single spins particularly challenging. By combining spin-to-charge conversion with real-time single-charge detection [130, 38, 2], it has nevertheless been possible to accomplish single-shot read-out of spin states in a quantum dot [40, 131].

The next major achievement was the observation of the coherent exchange of two electron spins in a double dot system, controlled by fast electrical switching of the tunnel coupling between the two quantum dots [42]. Finally, free evolution of a single electron spin about a static magnetic field (Larmor precession) has been observed, via optical pump-probe experiments [83, 132]. The only missing ingredient for universal quantum computation with spins in dots remained the demonstration of driven coherent spin rotations (Rabi oscillations) of a single electron spin.

The most commonly used technique for inducing spin flips is electron spin

6.2 Device and ESR detection concept

resonance (ESR) [111]. ESR is the physical process whereby electron spins are rotated by an oscillating magnetic field B_{ac} (with frequency f_{ac}) that is resonant with the spin precession frequency in an external magnetic field B_{ext} , oriented perpendicularly to B_{ac} ($hf_{ac} = g\mu_B B_{ext}$, with μ_B the Bohr magneton and g the electron spin g -factor). Magnetic resonance of a single electron spin in a solid has been reported in a few specific cases [133, 22, 134], but has never been realized in semiconductor quantum dots. Detecting ESR in a single quantum dot is conceptually simple [106], but experimentally difficult to realize, as it requires a strong, high-frequency magnetic field at low temperature, while accompanying alternating electric fields must be minimized. Alternative schemes for driven rotations of a spin in a dot have been proposed, based on optical excitation [31] or electrical control [135, 34, 32] but this is perhaps even more challenging and has not been accomplished either.

Here, we demonstrate the ability to control the spin state of a single electron confined in a double quantum dot via ESR. In a double dot system, spin-flips can be detected through the transition of an electron from one dot to the other [105, 136] rather than between a dot and a reservoir, as would be the case for a single dot. This has the advantage that there is no need for the electron spin Zeeman splitting (used in a single dot for spin-selective tunnelling) to exceed the temperature of the electron reservoirs (~ 100 mK; the phonon temperature was ~ 40 mK). The experiment can thus be performed at a smaller static magnetic field, and consequently with lower, technically less demanding, excitation frequencies. Furthermore, by applying a large bias voltage across the double dot, the spin detection can be made much less sensitive to electric fields than is possible in the single-dot case (electric fields can cause photon-assisted tunnelling; see Section 6.9.1). Finally, in a double dot, single-spin operations can in future experiments be combined with two-qubit operations to realize universal quantum gates [20], and with spin read-out to demonstrate entanglement [137, 138].

6.2 Device and ESR detection concept

Two coupled semiconductor quantum dots are defined by surface gates (Fig. 6.1a) on top of a two-dimensional electron gas. By applying the appropriate negative voltages to the gates the dots can be tuned to the few-electron regime [126]. The oscillating magnetic field that drives the spin transitions is generated by applying a radio-frequency (RF) signal to an on-chip coplanar stripline (CPS) which is terminated in a narrow wire, positioned near the dots and separated from the surface gates by a 100-nm-thick dielectric (Fig. 6.1b). The current through the wire generates an oscillating magnetic field B_{ac} at the dots, perpendicular to the

6. Driven coherent oscillations of a single electron spin in a quantum dot

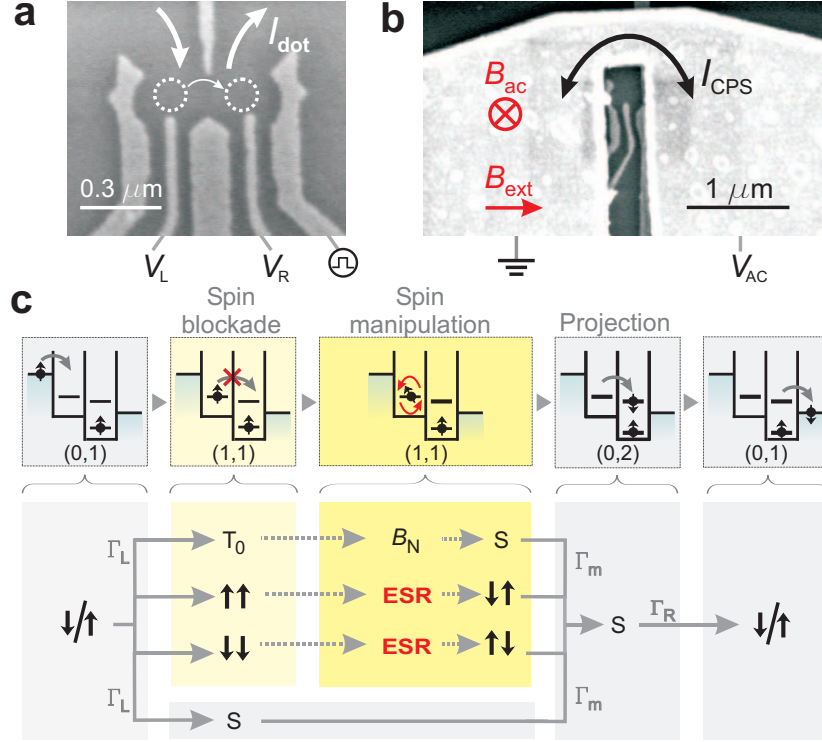


Figure 6.1: Device and ESR detection scheme. (a) Scanning electron microscope (SEM) image of a device with the same gate pattern as used in the experiment. The Ti/Au gates are deposited on top of a GaAs/AlGaAs heterostructure containing a two-dimensional electron gas 90 nm below the surface. White arrows indicate current flow through the two coupled dots (dotted circles). The right side gate is fitted with a homemade bias-tee (rise time 150 ps) to allow fast pulsing of the dot levels. (b) SEM image of a device similar to the one used in the experiment. The termination of the coplanar stripline is visible on top of the gates. The gold stripline has a thickness of 400 nm and is designed to have a 50Ω characteristic impedance, Z_0 , up to the shorted termination. It is separated from the gate electrodes by a 100-nm-thick dielectric (Calixerene) [44]. (c) Diagrams illustrating the transport cycle in the spin blockade regime. This cycle can be described via the occupations (m, n) of the left and right dots as $(0,1)$ $(1,1)$ $(0,2)$ $(0,1)$. When an electron enters the left dot (with rate Γ_L) starting from $(0,1)$, the two-electron system that is formed can be either a singlet $S(1,1)$ or a triplet $T(1,1)$. From $S(1,1)$, further current flow is possible via a transition to $S(0,2)$ (with rate Γ_m). When the system is in $T(1,1)$, current is blocked unless this state is coupled to $S(1,1)$. For T_0 , this coupling is provided by the inhomogeneous nuclear field B_N . For T_+ or T_- , ESR causes a transition to $\uparrow\downarrow$ or $\downarrow\uparrow$, which contains a $S(1,1)$ component and a T_0 component (which is in turn coupled to $S(1,1)$ by the nuclear field).

static external field B_{ext} and slightly stronger in the left dot than in the right dot (see Fig. 2.4). To detect the ESR-induced spin rotations, we use electrical transport measurements through the two dots in series in the spin blockade regime where current flow depends on the relative spin state of the electrons in the two dots [105, 119]. In brief, the device is operated so that current is blocked owing

6.3 Role of the nuclear spin bath for ESR detection

to spin blockade, but this blockade is lifted if the ESR condition ($hf_{ac} = g\mu_B B_{\text{ext}}$) is satisfied.

This spin blockade regime is accessed by tuning the gate voltages such that one electron always resides in the right dot, and a second electron can tunnel from the left reservoir to the left dot (Fig. 6.1c and Section 4.2). If this electron forms a double-dot singlet state with the electron in the right dot ($S = \uparrow\downarrow - \downarrow\uparrow$; normalization omitted for brevity), it is possible for the left electron to move to the right dot, and then to the right lead (leaving behind an electron in the right dot with spin \uparrow or spin \downarrow), since the right dot singlet state is energetically accessible. If, however, the two electrons form a double-dot triplet state, the left electron cannot move to the right dot because the right dot's triplet state is much higher in energy. The electron also cannot move back to the lead and therefore further current flow is blocked as soon as any of the (double-dot) triplet states is formed.

6.3 Role of the nuclear spin bath for ESR detection

In fact, the situation is more complex, because each of the two spins experiences a randomly oriented and fluctuating effective nuclear field of $\sim 1\text{-}3$ mT [84, 85]. This nuclear field, B_N , arises from the hyperfine interaction of the electron spins with the Ga and As nuclear spins in the host material, and is in general different in the two dots, with a difference of δB_N . At zero external field and for sufficiently small double dot singlet-triplet splitting (see chapter 5 and Fig. 6.8a), the inhomogeneous component of the nuclear field causes all three triplet states (T_0 , T_+ and T_-) to be admixed with the singlet S (for example, $T_0 = \uparrow\downarrow + \downarrow\uparrow$ evolves into $S = \uparrow\downarrow - \downarrow\uparrow$ due to $\Delta B_{N,z}$, and $T_+ = \uparrow\uparrow$ and $T_- = \downarrow\downarrow$ evolve into S owing to $B_{N,x,y}$). As a result, spin blockade is lifted. For $B_{\text{ext}} \gg \sqrt{\langle B_N^2 \rangle}$, however, the T_+ and T_- states split off in energy, which makes hyperfine-induced admixing between T_{\pm} and S ineffective (T_0 and S remain admixed; see Fig. 6.2a). Here spin blockade does occur, whenever a state with parallel spins ($\uparrow\uparrow$ or $\downarrow\downarrow$) becomes occupied.

ESR is then detected as follows (see Fig. 6.1c). An oscillating magnetic field resonant with the Zeeman splitting can flip the spin in the left or the right dot. Starting from $\uparrow\uparrow$ or $\downarrow\downarrow$, the spin state then changes to $\uparrow\downarrow$ (or $\downarrow\uparrow$). If both spins are flipped, transitions occur between $\uparrow\uparrow$ and $\downarrow\downarrow$ via the intermediate state $\frac{\uparrow\pm\downarrow}{\sqrt{2}} \frac{\uparrow\pm\downarrow}{\sqrt{2}}$. In both cases, states with anti-parallel spins ($S_z = 0$) are created owing to ESR. Expressed in the singlet-triplet measurement basis, $\uparrow\downarrow$ or $\downarrow\uparrow$ is a superposition of

6. Driven coherent oscillations of a single electron spin in a quantum dot

the T_0 and S state ($\uparrow\downarrow = T_0 + S$). For the singlet component of this state, the left electron can transition immediately to the right dot and from there to the right lead. The T_0 component first evolves into a singlet due to the nuclear field and then the left electron can move to the right dot as well. Thus whenever the spins are anti-parallel, one electron charge moves through the dots. If such transitions from parallel to anti-parallel spins are induced repeatedly at a sufficiently high rate, a measurable current flows through the two dots.

6.4 ESR spectroscopy

The resonant ESR response is clearly observed in the transport measurements as a function of magnetic field (Figs. 6.2a,b and 6.8), where satellite peaks develop at the resonant field $B_{\text{ext}} = \pm hf_{\text{ac}}/g\mu_B$ when the RF source is turned on (the zero-field peak arises from the inhomogeneous nuclear field, which admixes all the triplets with the singlet (see chapter 5 and refs [85, 109])). The key signature of ESR is the linear dependence of the satellite peak location on the RF frequency, which is clearly seen in the data of Fig. 6.2c, where the RF frequency is varied from 10 to 750 MHz. From a linear fit through the top of the peaks we obtain a g -factor with modulus 0.35 ± 0.01 , which lies within the range of reported values for confined electron spins in GaAs quantum dots [129, 139, 140, 141]. We also verified explicitly that the resonance we observe is magnetic in origin and not caused by the electric field that the CPS generates as well; negligible response was observed when RF power is applied to the right side gate, generating mostly a RF electric field (see Fig. 6.2d)¹.

The amplitude of the peaks in Fig. 6.2b increases linearly with RF power ($\sim B_{\text{ac}}^2$) before saturation occurs, as predicted [106] (Fig. 6.2b, inset). The ESR satellite peak is expected to be broadened by either the excitation amplitude B_{ac} or incoherent processes, like cotunnelling, inelastic transitions (to the $S(0,2)$ state) or the statistical fluctuations in the nuclear field, whichever of the four has the largest contribution. No dependence of the width on RF power was found within the experimentally accessible range ($B_{\text{ac}} < 2$ mT). Furthermore, we suspect that

¹A very faint line is still present at the same position as the ESR response in Fig. 6.2c. This response could be due to the small magnetic field generated by the current in the gate, which is capacitively coupled to its environment. It could also be due to the coupling of the electric field to the electron spin, through Rashba or Dresselhaus spin-orbit interaction (see chapter 9 and [34]). A final possibility is that spins are flipped when the electron wave function is moved back-and-forth in the inhomogeneous nuclear field [32]. In any case, it is clear that in our experiment, all these mechanisms are much less efficient than magnetic excitation via the CPS.

6.4 ESR spectroscopy

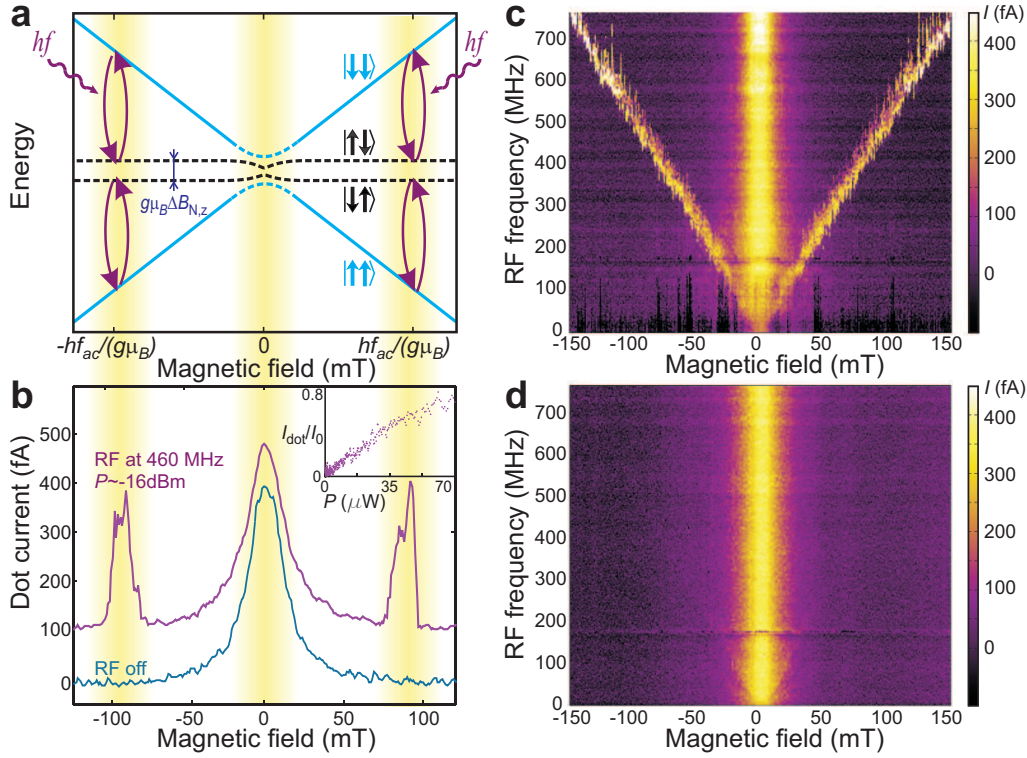


Figure 6.2: ESR spin state spectroscopy. (a) Energy diagram showing the relevant eigenstates of two electron spins in a double-dot, subject to an external magnetic field and nuclear fields. Because $B_{N,z}$ is in general different in the two dots, the energy for $\uparrow\downarrow$ and $\downarrow\uparrow$ is different. ESR turns the spin states $\uparrow\uparrow$ and $\downarrow\downarrow$ into $\uparrow\downarrow$ or $\downarrow\uparrow$, depending on the nuclear fields in the two dots. The yellow bands denote the ranges in B_{ext} where spin blockade is lifted (by the nuclear field or ESR) and current will flow through the dots. (b) Current measured through the double-dot in the spin blockade regime, with (red trace, offset by 100 fA for clarity) and without (blue trace) a RF magnetic field. Satellite peaks appear as the external magnetic field is swept through the spin resonance condition. Each measurement point is averaged for one second, and is therefore expected to represent an average response over many nuclear configurations. The RF power P applied to the CPS is estimated from the power applied to the coax line and the attenuation in the lines. Inset, satellite peak height versus RF power ($f = 408$ MHz, $B_{\text{ext}} = 70$ mT, taken at slightly different gate voltage settings). The current is normalized to the current at $B_{\text{ext}} = 0$ ($=I_0$). Unwanted electric field effects are reduced by applying a compensating signal to the right side gate with opposite phase as the signal on the stripline (see section 6.9.1). This allowed us to obtain this curve up to relatively high RF powers. (c) Current through the dots when sweeping the RF frequency and stepping the magnetic field. The ESR satellite peak is already visible at a small magnetic field of 20 mT and RF excitation of 100 MHz, and its location evolves linearly in field when increasing the frequency. For higher frequencies the satellite peak is broadened asymmetrically for certain sweeps, visible as vertical stripes. This broadening is time dependent, hysteretic in sweep direction, and changes with the dot level alignment. The horizontal line at 180 MHz is due to a resonance in the transmission line inside the dilution refrigerator. (d) Similar data as in (c), but now with the RF signal applied to the right side gate instead of to the ESR stripline. The amplitude of the RF signal (-50 dBm at the gate) was chosen such that the electric field is equally strong as in the ESR measurements of (c) (determined from the measured PAT rate).

6. Driven coherent oscillations of a single electron spin in a quantum dot

the broadening is not dominated by cotunnelling or inelastic transitions because the corresponding rates are smaller than the observed broadening (see Fig. 6.8). The observed ESR peaks are steeper on the flanks and broader than expected from the nuclear field fluctuations. In many cases, the peak width and position are even hysteretic in the sweep direction, suggesting that the resonance condition is shifted during the field sweep. We speculate that dynamic nuclear polarization due to feedback of the electron transport on the nuclear spins plays a central part here [109, 108, 112, 110].

6.5 Coherent Rabi oscillations

Following the observation of magnetically induced spin flips, we next test whether we can also coherently rotate the spin by applying RF bursts with variable length. In contrast to the continuous-wave experiment, where detection and spin rotation occur at the same time, we pulse the system into Coulomb blockade during the spin manipulation. This eliminates decoherence induced by tunnel events from the left to the right dot during the spin rotations. The experiment consists of three stages (Fig. 6.3): initialization through spin blockade in a statistical mixture of $\uparrow\uparrow$ and $\downarrow\downarrow$, manipulation by a RF burst in Coulomb blockade, and detection by pulsing back for projection (onto S(0,2)) and tunnelling to the lead. When one of the electrons is rotated over $(2n + 1)\pi$ (with integer n), the two-electron state evolves to $\uparrow\downarrow$ (or $\downarrow\uparrow$), giving a maximum contribution to the current (as before, when the two spins are anti-parallel, one electron charge moves through the dots). However, no electron flow is expected after rotations of $2n\pi$, where one would find two parallel spins in the two dots after the RF burst.

We observe that the dot current oscillates periodically with the RF burst length (Fig. 6.4). This oscillation indicates that we performed driven, coherent electron spin rotations, or Rabi oscillations. A key characteristic of the Rabi process is a linear dependence of the Rabi frequency on the RF burst amplitude, B_{ac} ($f_{\text{Rabi}} = g\mu_B B_1/h$ with $B_1 = B_{ac}/2$ due to the rotating wave approximation). We verify this by extracting the Rabi frequency from a fit of the current oscillations of Fig. 6.4b with a sinusoid, which gives the expected linear behaviour (Fig. 6.4b, inset). From the fit we obtain $B_{ac}=0.59$ mT for a stripline current I_{CPS} of ~ 1 mA, which agrees well with predictions from numerical finite element simulations (see Fig. 2.4). The maximum B_1 we could reach in the experiment before electric field effects hindered the measurement was 1.9 mT, corresponding to $\pi/2$ rotations of only 27 ns (that is, a Rabi period of 108 ns, see Fig. 6.4b). If the accompanying electric fields from the stripline excitation could be reduced

6.6 Theoretical model

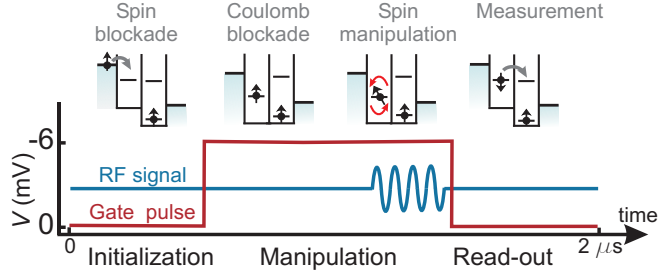


Figure 6.3: The control cycle for coherent manipulation of the electron spin. During the 'initialization' stage the double-dot is tuned in the spin blockade regime. Electrons will move from left to right until the system is blocked with two parallel spins (either $\uparrow\uparrow$ or $\downarrow\downarrow$; in the figure only the $\uparrow\uparrow$ case is shown). For the 'manipulation' stage, the right dot potential is pulsed up so none of the levels in the right dot are accessible (Coulomb blockade), and a RF burst with a variable duration is applied. 'Read-out' of the spin state at the end of the manipulation stage is done by pulsing the right dot potential back; electron tunnelling to the right lead will then take place only if the spins were anti-parallel. The duration of the read-out and initialization stages combined was $1 \mu\text{s}$, long enough ($1 \mu\text{s} \gg 1/\Gamma_L, 1/\Gamma_M, 1/\Gamma_R$) to have parallel spins in the dots at the end of the initialization stage with near certainty (this is checked by signal saturation when the pulse duration is prolonged). The duration of the manipulation stage is also held fixed at $1 \mu\text{s}$ to keep the number of pulses per second constant. The RF burst is applied just before the read-out stage starts.

in future experiments (for example, by improving the impedance matching from coax to CPS), considerably faster Rabi flopping should be attainable.

The oscillations in Fig. 6.4b remain visible throughout the entire measurement range, up to $1 \mu\text{s}$. This is striking, because the Rabi period of $\sim 100 \text{ ns}$ is much longer than the time-averaged coherence time T_2^* of 10-20 ns (refs [42, 83, 84, 85]) caused by the nuclear field fluctuations. The slow damping of the oscillations is only possible because the nuclear field fluctuates very slowly compared to the timescale of spin rotations and because other mechanisms, such as the spin-orbit interaction, disturb the electron spin coherence only on even longer timescales [40, 77, 67]. We also note that the decay is not exponential (grey line in Fig. 6.4a), which is related to the fact that the correlation time of the nuclear bath is longer than the Rabi period (see [50, 142] and chapter 7).

6.6 Theoretical model

To understand better the amplitudes and decay times of the oscillations, we model the time evolution of the spins throughout the burst duration. The model uses a hamiltonian that includes the Zeeman splitting for the two spins and the RF field, which we take to be of equal amplitude in both dots (\mathbf{S}_L and \mathbf{S}_R refer to

6. Driven coherent oscillations of a single electron spin in a quantum dot

the electron spins in the left and right dot respectively):

$$H = g\mu_B(\mathbf{B}_{\text{ext}} + \mathbf{B}_{L,N}) \cdot \mathbf{S}_L + g\mu_B(\mathbf{B}_{\text{ext}} + \mathbf{B}_{R,N}) \cdot \mathbf{S}_R + g\mu_B \cos(\omega t) \mathbf{B}_{\text{ac}} \cdot (\mathbf{S}_L + \mathbf{S}_R) \quad (6.1)$$

where $\mathbf{B}_{L,N}$ and $\mathbf{B}_{R,N}$ correspond to a single frozen configuration of the nuclear field in the left and right dot. This is justified because the electron spin dynamics is much faster than the dynamics of the nuclear system. From the resulting time evolution operator and assuming that the initial state is a statistical mixture of $\uparrow\uparrow$ and $\downarrow\downarrow$, we can numerically obtain the probability for having anti-parallel spins after the RF burst. This is also the probability that the left electron tunnels to the right dot during the read-out stage.

In the current measurements of Fig. 6.4a, each data point is averaged over 15 s, which presumably represents an average over many nuclear configurations. We include this averaging over different nuclear configurations in the model by taking 2,000 samples from a gaussian distribution of nuclear fields (with standard

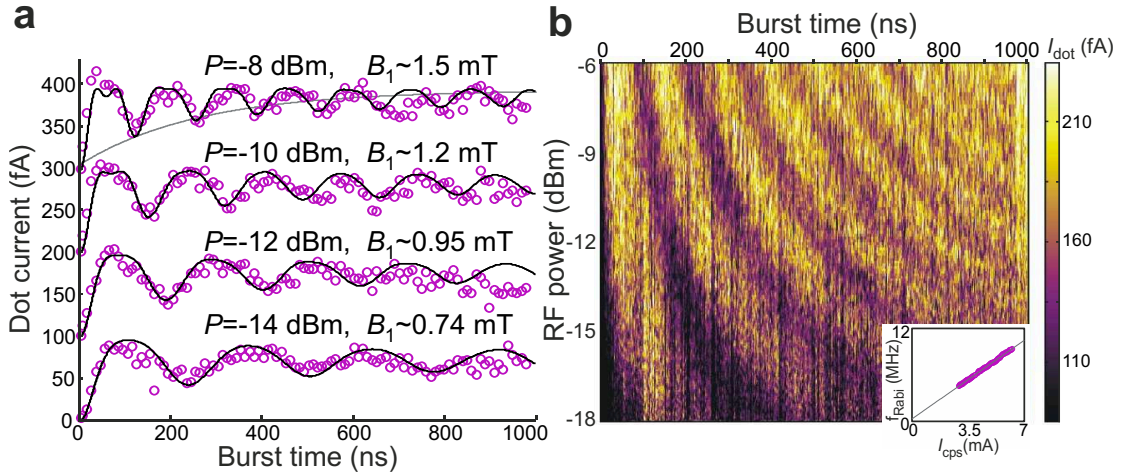


Figure 6.4: Coherent spin rotations. (a) The dot current-reflecting the spin state at the end of the RF burst-oscillates as a function of RF burst length (curves offset by 100 fA for clarity). The frequency of B_{ac} is set at the spin resonance frequency of 200 MHz ($B_{\text{ext}} = 41$ mT). The period of the oscillation increases and is more strongly damped for decreasing RF power. The RF power P applied to the CPS is estimated from the power applied to the coax line and the attenuation in the lines and RF switch. From P , the stripline current is calculated via the relation $P = \frac{1}{2}(I_{\text{CPS}})^2 Z_0$ assuming perfect reflection of the RF wave at the short. Each measurement point is averaged over 15 s. We correct for a current offset which is measured with the RF frequency off-resonance (280 MHz). The solid lines are obtained from numerical computation of the time evolution, as discussed in the text. The grey line corresponds to an exponentially damped envelope. (b) The oscillating dot current (represented in colourscale) is displayed over a wide range of RF powers (the sweep axis) and burst durations. The dependence of the Rabi frequency f_{Rabi} on RF power is shown in the inset. f_{Rabi} is extracted from a sinusoidal fit with the current oscillations from 10 to 500 ns for RF powers ranging from -12.5 dBm up to -6 dBm.

6.7 Time evolution of the spin states during RF bursts

deviation $\sigma = \sqrt{\langle B_N^2 \rangle}$, and computing the probability that an electron tunnels out after the RF burst. When the electron tunnels, one or more additional electrons, say m , may subsequently tunnel through before $\uparrow\uparrow$ or $\downarrow\downarrow$ is formed and the current is blocked again. Taking m and σ as fitting parameters, we find good agreement with the data for $m = 1.5$ and $\sigma = 2.2$ mT (solid black lines in Fig. 6.4a). This value for σ is comparable to that found in refs [84, 85]. The value found for m is different from what we would expect from a simple picture where all four spin states are formed with equal probability during the initialization stage, which would give $m = 1$. We do not understand this discrepancy, but it could be due to different tunnel rates for \uparrow and \downarrow or more subtle details in the transport cycle that we have neglected in the model.

6.7 Time evolution of the spin states during RF bursts

We now discuss in more detail the time evolution of the two spins during a RF burst. The resonance condition in each dot depends on the effective nuclear field, which needs to be added vectorially to B_{ext} . Through their continuous reorientation, the nuclear spins will bring the respective electron spins in the two dots on and off resonance as time progresses. When a RF burst is applied to two spins initially in $\uparrow\uparrow$, and is on-resonance with the right spin only, the spins evolve as:

$$|\uparrow\rangle|\uparrow\rangle \rightarrow |\uparrow\rangle \frac{|\uparrow\rangle + |\downarrow\rangle}{\sqrt{2}} \rightarrow |\downarrow\rangle|\uparrow\rangle \rightarrow \frac{|\uparrow\rangle - |\downarrow\rangle}{\sqrt{2}} \rightarrow |\uparrow\rangle|\uparrow\rangle$$

When the RF burst is on-resonance with both spins, the time evolution is:

$$|\uparrow\rangle|\uparrow\rangle \rightarrow \frac{|\uparrow\rangle + |\downarrow\rangle}{\sqrt{2}} \frac{|\uparrow\rangle + |\downarrow\rangle}{\sqrt{2}} \rightarrow |\downarrow\rangle|\downarrow\rangle \rightarrow \frac{|\uparrow\rangle - |\downarrow\rangle}{\sqrt{2}} \frac{|\uparrow\rangle - |\downarrow\rangle}{\sqrt{2}} \rightarrow |\uparrow\rangle|\uparrow\rangle$$

In both cases, the RF causes transitions between the \uparrow and \downarrow states of single spin-half particles. When the RF is on-resonance with both spins, such single-spin rotations take place for both spins simultaneously. Because the current through the dots is proportional to the $S_z = 0$ probability ($\uparrow\downarrow$ or $\downarrow\uparrow$), we see that when both spins are excited simultaneously, the current through the dots will oscillate twice as fast as when only one spin is excited, but with only half the amplitude.

In the experiment, the excitation is on-resonance with only one spin at a time for most of the frozen nuclear configurations (Fig. 6.5). Only at the highest powers ($B_1/\sqrt{\langle B_N^2 \rangle} > 1$), both spins may be excited simultaneously (but independently) and a small double Rabi frequency contribution is expected, although it could not be observed, owing to the measurement noise.

6. Driven coherent oscillations of a single electron spin in a quantum dot

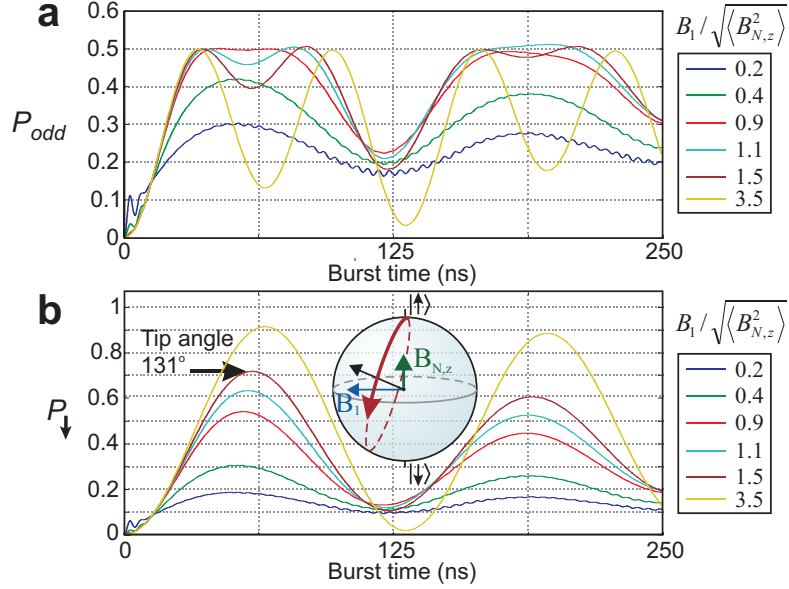


Figure 6.5: Time evolution of the spin states. (a) Probability for the two spins to be in $\uparrow\downarrow$ or $\downarrow\uparrow$ ($S_z=0$) at the end of a RF burst, with initial state $\uparrow\uparrow$, computed using the hamiltonian H of Eq. 6.1, for six different values of $\sigma_{N,z} = \langle B_N^2 \rangle^{1/2}$ (fixed $B_1=1.5$ mT, $B_{\text{ext}}=40$ mT, each of the traces is averaged over 2000 static nuclear configurations). As expected, the oscillation contains a single frequency for B_1 small compared to $\sigma_{N,z}$, corresponding to the Rabi oscillation of a single spin. The oscillation develops a second frequency component, twice as fast as the first, when $B_1/\sigma_{N,z} > 1$. For $B_1/\sigma_{N,z} > 4$ the double frequency component is dominant, reflecting the simultaneous Rabi oscillation of the two spins. (b) Probability for one of the spins to be \downarrow at the end of a RF burst. The spin state evolution is computed as in a. This oscillation represents the Rabi oscillation of one spin by itself. For increasing B_1 , the maximum angle over which the spin is rotated in the Bloch sphere increases as well. In the experiment, this angle could not be measured directly, because the current measurement constitutes a two-spin measurement, not a single-spin measurement. We can, however, extract the tip angle from P_{\downarrow} .

6.8 Quantum gate fidelity

We can estimate the angle over which the electron spins are rotated in the Bloch sphere based on our knowledge of B_1 and the nuclear field fluctuations in the z -direction, again using the hamiltonian H . For the maximum ratio of $\sqrt{\langle B_N^2 \rangle} = B_1/(\sigma/\sqrt{3}) = 1.5$ reached in the present experiment, we achieve an average tip angle of 131° for an intended 180° rotation, corresponding to a fidelity of 73% (Fig.6.5). Apart from using a stronger B_1 , the tip angle can be increased considerably by taking advantage of the long timescale of the nuclear field fluctuations. First, application of composite pulses, widely used in nuclear magnetic resonance to compensate for resonance off-sets [143], can greatly improve the quality of the rotations. A second solution comprises a measurement

6.9 Additional material

of the nuclear field (nuclear state narrowing [88, 91, 89]), so that the uncertainty in the nuclear field is reduced, and accurate rotations can be realized for as long as the nuclear field remains constant.

In future experiments, controllable addressing of the spins in the two dots separately can be achieved through a gradient in either the static or the oscillating magnetic field. Such gradient fields can be created relatively easily using a ferromagnet or an asymmetric stripline. Alternatively, the resonance frequency of the spins can be selectively shifted using local g -factor engineering [144, 145]. The single spin rotations reported here, in combination with single-shot spin read-out [40, 131] and the tunable exchange coupling in double dots [42], offers many new opportunities, such as measuring the violation of Bell's inequalities or the implementation of simple quantum algorithms.

We thank R. Hanson, L. Willems van Beveren, W. Coish, J. Elzerman, D. Klauser, A. Lupascu, D. Loss and in particular J. Folk for discussions; R. Schouten, B. van der Enden and W. den Braver for technical assistance; The International Research Centre for Telecommunication and Radar at the Delft University of Technology for assistance with the stripline simulations. Supported by the Dutch Organization for Fundamental Research on Matter (FOM), the Netherlands Organization for Scientific Research (NWO) and the Defense Advanced Research Projects Agency Quantum Information Science and Technology programme.

6.9 Additional material

6.9.1 Photon assisted tunnelling due to electric fields

The coplanar stripline is designed to maximize the ratio between the RF magnetic field and electric field. Nevertheless, a small RF electric field will unavoidably be generated. High frequency electric fields can excite an electron to higher lying orbitals in the dot or in the reservoir. In this process, one or more photons are absorbed to match the excitation energy. Such so-called photon-assisted tunnelling (PAT) processes [146, 147] can lift spin blockade and overwhelm the ESR signal. In this section we will discuss two different kinds of PAT processes that can lift spin blockade (Figs. 6.6a,b). The first is PAT through the interdot barrier. Electrons blocked in any of the three T(1,1) states can tunnel to the T(0,2) state if the energy difference between these states corresponds to an integer multiple of the photon energy hf . This will lead to sideband resonances running parallel to the T(0,2) line with a spacing hf . In the classical limit, where hf is much smaller than the line width of the states $h\Gamma$ (Γ is the tunnel rate), the individual sidebands cannot be resolved. Instead the T(0,2) line is broadened. We can quantify

6. Driven coherent oscillations of a single electron spin in a quantum dot

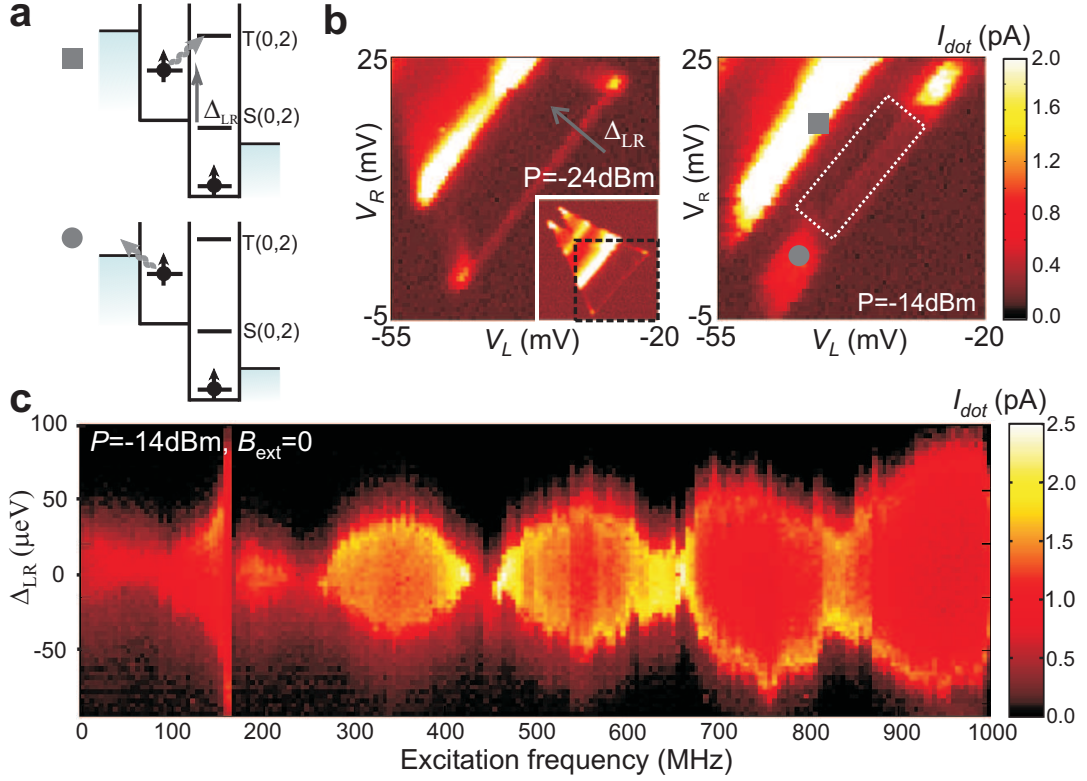


Figure 6.6: (a) Diagrams showing schematically two photon-assisted tunnelling (PAT) processes. Top: excitation from T(1,1) to T(0,2). Bottom: excitation from T(1,1) to the left reservoir. (b) The current measured through the double dot under forward bias is plotted in colorscale, as a function of the gate voltages controlling the left and right dot potential (RF power -24 dBm and -14 dBm applied to the CPS and $B_{ext} = 100$ mT). The effect of the two PAT processes on the measured current is visible as current enhancement in the areas around the yellow circle and blue square. ESR detection in the experiments has been performed in the area enclosed by the white dotted lines where the PAT rates are smaller than the measurement noise (~ 10 -100 fA). (c) Current as a function of CPS excitation frequency and Δ_{LR} (energy difference between S(1,1) and S(0,2) state, see also a and b) with an RF signal applied both to the right side gate (time-delayed and 34 dB attenuated) and the CPS ($B_{ext} = 0$). The amplitude of the total electric field, reflected in the broadening of the current peak along the vertical axis, shows constructive and destructive interference as a function of frequency.

how efficient PAT is in lifting spin blockade using ref. [146]. The basic idea is that an AC voltage drop $V = V_{ac} \cos(2\pi ft)$ across a tunnel barrier modifies the tunnel rate through the barrier as $\Gamma(\tilde{E}) = \sum_{n=-\infty}^{n=\infty} J_n^2 \Gamma(E + nhf)$. Here $\Gamma(E)$ and $\Gamma(\tilde{E})$ are the tunnel rates at energy E with and without an AC voltage, respectively; $J_n^2(\alpha)$ is the square of the n th order Bessel function evaluated at $\alpha = (eV_{ac})/hf$, which describes the probability that an electron absorbs or emits n photons of energy hf ($-e$ is the electron charge). The energy splitting between the S(0,2) and

6.9 Additional material

T(0,2) states is typically ~ 410 eV, and the energy difference between the T(1,1) and the T(0,2) state will be of the same order. Since we can keep the Zeeman splitting small in this double dot measurement, the excitation frequency can be kept small too. Typically, $f = 200$ MHz in the present experiment. The single-photon energy is then $hf = 0.8 \mu\text{eV}$. PAT processes from T(1,1) to T(0,2) thus require $n = 500$ photons, and will therefore be very inefficient. Such 500-photon processes only occur with a reasonable probability, $J_n^2(\alpha) > 0.05$, if $\alpha > n - 1 \sim 500$. So only when the amplitude of the oscillating voltage across the central barrier exceeds roughly $400 \mu\text{V}$, spin blockade is lifted due to PAT from the T(1,1) to the T(0,2) state. In the continuous-wave experiment this occurs for RF powers larger than -12 dBm. The second PAT process occurs through the outer barriers. The electron blocked in the left dot can be excited to the left reservoir if the Fermi level of this reservoir lies within nhf in energy from the T(1,1) electrochemical potential (Fig. 6.6a). Subsequently, another electron with possibly a different spin state can tunnel from the left reservoir into the dot. Effectively this process can thus flip the spin by electron exchange with the reservoir. Similarly, the electron in the right dot can be excited to the right reservoir. The data presented in Figs. 6.2 and 6.4 are taken with a large bias voltage of 1.4 mV applied across the double dot, and with the relevant levels in the left and right dots far separated in energy from the Fermi level in the corresponding reservoir. In this way, PAT processes to the reservoirs were minimized. We point out that a third process, namely photon-assisted tunnelling from the S(1,1) state to the S(0,2) state, does not disturb ESR detection. This process only broadens the ESR peak on the gate axis (defined by Δ_{LR} , see Figs. 6.6a,b and 6.8). Even though PAT can thus be easily recognized and minimized in double dot measurements, PAT rates still became excessive at higher RF powers. This imposed a limitation on the power we could apply to the CPS, and thus on the amplitude of B_{ac} we could produce in the experiment (before heating of the sample or the mixing chamber became a limitation). We therefore developed a method to reduce the PAT rates via interference between two signals. Hereby we split the RF signal at the output of the source, send one branch directly to the CPS and send the other branch to the right side gate of the dot. The latter signal is delayed through an additional coax of length L and properly attenuated such that for specific RF frequencies $f = (n + \frac{1}{2})c/\Delta L$, the electric field generated by the CPS interferes destructively with the electric field created by the side gate (Fig. 6.6c). At the frequencies that correspond to nodes in the interference pattern, it is possible to apply about 6 dB more RF power than is possible without PAT cancellation. Only the data in the inset of Fig. 6.2b are obtained with PAT reduction. For the pulsed experiments, the PAT rate to the T(0,2) state is smaller than in the continuous-wave

6. Driven coherent oscillations of a single electron spin in a quantum dot

experiments, because the right dot levels are pulsed to a higher energy (thereby increasing the energy difference between $T(0,2)$ and $T(1,1)$) when the microwaves are applied.

6.9.2 Additional figures: lifting of spin blockade by nuclear spins or ESR.

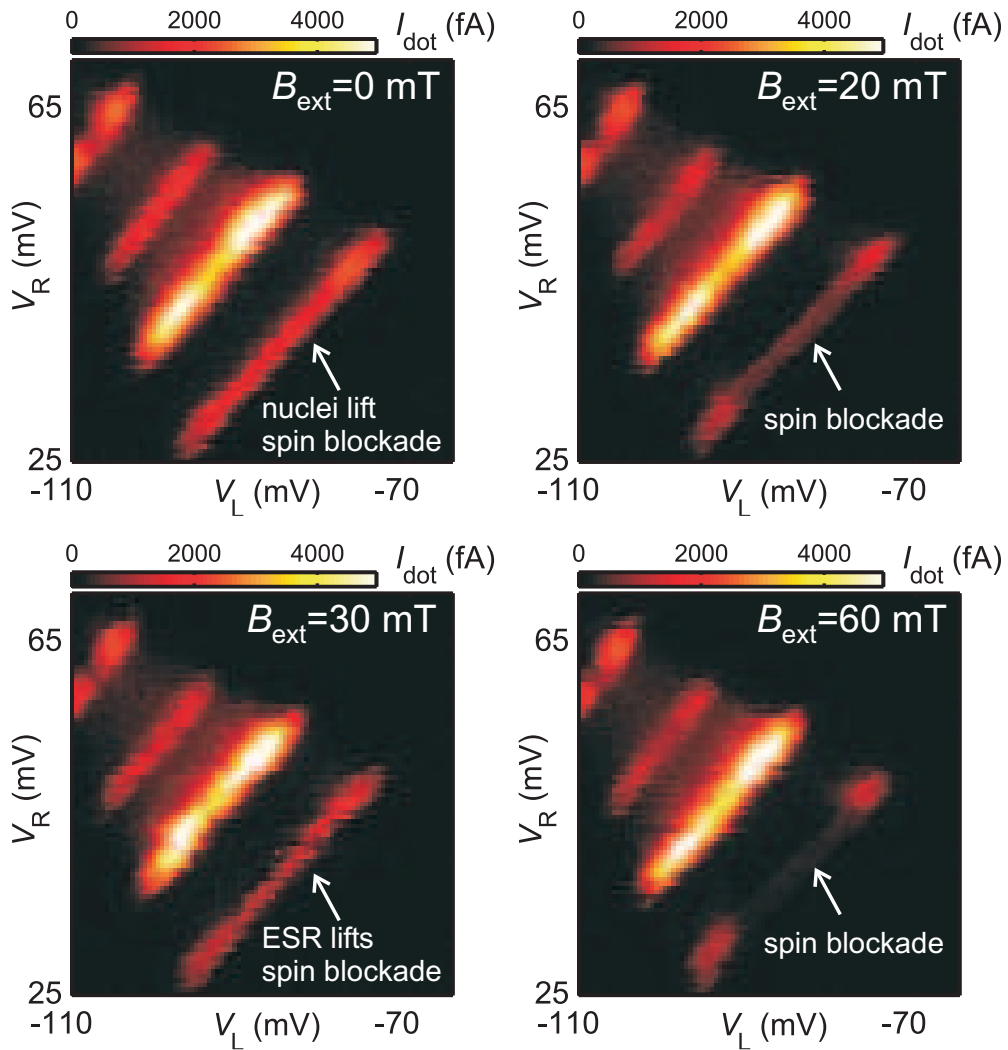


Figure 6.7: Current through the double quantum dot under forward bias ($1400 \mu\text{eV}$) as a function of V_L and V_R with RF power -14 dBm and frequency 200 MHz applied to the CPS. At zero external field, the nuclear field admixes all three triplets with the singlet, and spin blockade is lifted. At $B_{\text{ext}}=20,60$ mT, transport is blocked by spin blockade, but at $B_{\text{ext}}=35$ mT spin blockade is lifted by ESR.

6.9 Additional material

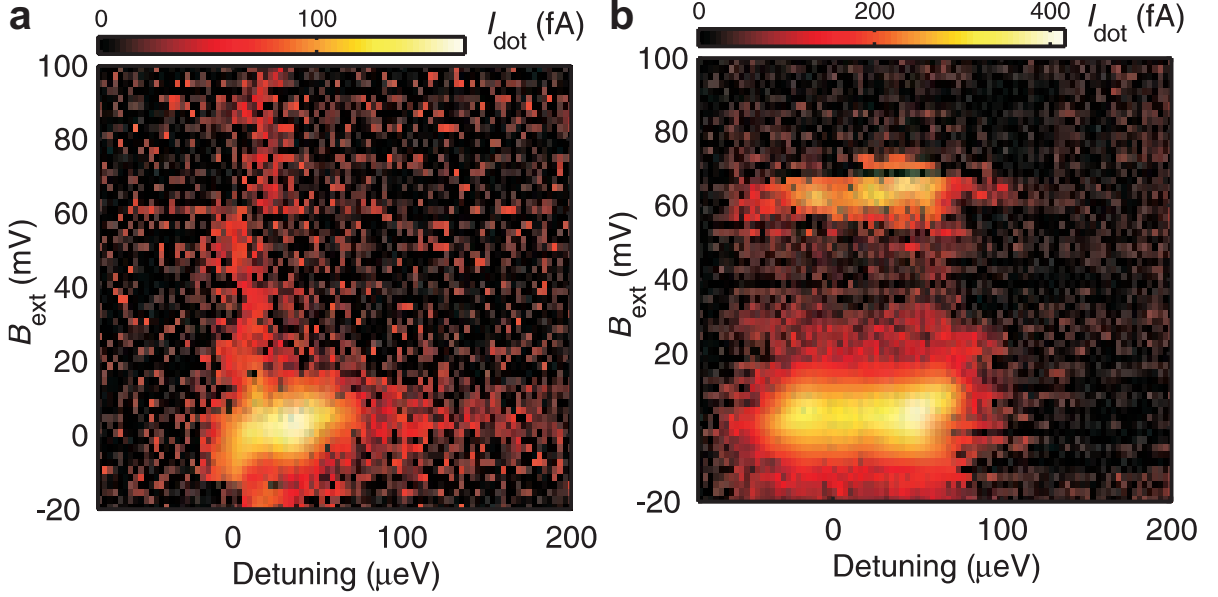


Figure 6.8: (a) Current through the double quantum dot under forward bias (1400 μeV) as a function of field and detuning between the S(1,1) and S(0,2) chemical potential. No splitting of the leakage current peak on the field axis at zero detuning can be observed. This indicates that the energy splitting J between S(1,1) and T(1,1) is smaller than $\langle B_{\text{N}}^2 \rangle^{0.5}$ (like discussed in chapter 5). This gives an upper bound for the tunnel coupling t ($=J/\sqrt{2}$ at zero detuning) and inelastic transitions Γ_{in} from the S(1,1) state to the S(0,2) state: $t, h\Gamma_{\text{in}} < g\mu_{\text{B}}\langle B_{\text{N}}^2 \rangle^{1/2}$. (b) Similar measurement as in (a), but now with RF power -13 dBm and frequency 300 MHz applied to the CPS. Spin blockade is lifted around $B_{\text{ext}} = hf/g\mu_{\text{B}}$, where the resonance condition is matched. The extra broadening of the leakage current peak on the detuning axis is due to the (unwanted) oscillating electric field (see chapter 9 and Fig. 6.6).

6. Driven coherent oscillations of a single electron spin in a quantum dot

Chapter 7

Universal phase shift and non-exponential decay of driven single-spin oscillations

Frank Koppens, Daniel Klauser, Bill Coish, Leo Kouwenhoven,
Daniel Loss, Lieven Vandersypen

We study, both theoretically and experimentally, driven Rabi oscillations of a single electron spin coupled to a nuclear spin bath. Due to the long correlation time of the bath, two unusual features are observed in the oscillations. The decay follows a power law, and the oscillations are shifted in phase by a universal value of $\sim \pi/4$. These properties are well understood from a theoretical expression that we derive here in the static limit for the nuclear bath. This improved understanding of the coupled electron-nuclear system is important for future experiments using the electron spin as a qubit.

7.1 Introduction

A quantum bit is engineered such that its coupling to the disturbing environment is minimized. Understanding and controlling this coupling is therefore a major subject in the field of quantum information processing. It is not solely the coupling strength but also the dynamics of the environment that governs the quantum coherence. In particular, the limit where these dynamics are slow compared to the evolution of the quantum system is interesting. The well-known Markovian Bloch equations that describe the dynamics of a driven system, including the exponential decay of the longitudinal and transverse magnetization [51], then lose their validity. Such deviations from the exponential behavior have been studied theoretically [148, 149] and experimentally, for instance in superconducting qubit systems [150].

An electron spin confined in the solid state is affected predominantly by phonons via the spin-orbit interaction [64, 67, 40, 77, 151], and by nuclear spins in the host material via the hyperfine interaction. At low temperature, coupling to the nuclear spins is the dominant decoherence source [75, 81, 50, 152, 84, 85, 42, 153]. Although this strong coupling leads to an apparent decoherence time T_2^* of the order of 20 ns when time-averaged over experimental runs, the decoherence time T_2 strongly depends on the dynamics in the nuclear spin bath. This typical nuclear spin dynamics is very slow, because the nuclear spins are only weakly coupled with each other and the bath itself is coupled very weakly to its dissipative environment (like phonons). This implies that here, the Markovian Bloch equations are not valid.

Here we study the dynamics and decoherence of an electron spin in a quantum dot that is coherently driven via pulsed magnetic resonance, and is coupled to a nuclear spin bath with a long correlation time. We find experimentally that, remarkably, the electron spin oscillates coherently, even when the Rabi period is much longer than $T_2^* = 10 - 20$ ns. In addition, the characteristics of the driven electron spin dynamics are unusual. The decay of the Rabi oscillations is not exponential but follows a power law and a universal (parameter independent) phase shift emerges. We compare these experimental results with a theoretical expression, derived in the limit of a static nuclear spin bath.

7.2 Theoretical model

We consider a double quantum dot with one electron in each dot and a static external magnetic field in the z -direction, resulting in a Zeeman splitting $\epsilon_z = g\mu_B B_z$. The spin transitions are driven by a burst of a transverse oscillating field

7.2 Theoretical model

along the x -direction with amplitude B_{ac} and frequency ω , which is generated by a current I_s through a microfabricated wire close to the double dot [154]. The interaction between the electron spin and the nuclear bath is described by the Fermi contact hyperfine interaction $\vec{S} \cdot \vec{h}$, where \vec{h} is the field generated by the nuclear spins at the position of the electron. For a large but finite number of nuclear spins ($N \sim 10^6$ for lateral GaAs dots) h_z is Gaussian distributed (due to the central-limit theorem) with mean $h_0 = \overline{h_z}$ and variance $\sigma^2 = \overline{(h_z - h_0)^2}$ [75, 81, 50]. For a sufficiently large external magnetic field ($\epsilon_z \gg \sigma$), we may neglect the transverse terms $S_\perp \cdot h_\perp$ of the hyperfine interaction that give rise to electron-nuclear-spin flip-flops (see below). Furthermore, if the singlet-triplet energy splitting J is much smaller than both ϵ_z and $g\mu_B B_{ac}$, we may treat the spin dynamics of the electrons in each dot independently (valid for times less than $1/J$).

For each dot we thus have the following spin Hamiltonian ($\hbar = 1$):

$$H(t) = \frac{1}{2}(\epsilon_z + h_z)\sigma_z + \frac{b}{2}\cos(\omega t)\sigma_x, \quad (7.1)$$

where σ_i (with $i = x, z$) are the Pauli matrices and $b = g\mu_B B_{ac}$ (taken to be equal in both dots). longitudinal nuclear field h_z . Here, h_z is considered as completely static during the electron spin time evolution. This is justified because the correlation time of the fluctuations in the nuclear-spin system due to dipole-dipole and hyperfine-mediated interaction between the nuclear spins, which is predicted to be $\gtrsim 10 - 100 \mu\text{s}$ [50, 75, 81, 98, 102, 88, 99, 155], is much larger than the timescale for electron spin dynamics considered here (up to $1 \mu\text{s}$).

In the experiment, the electron spin state is detected in a regime where electron transport through the double quantum dot occurs via transitions from spin states with one electron in each dot (denoted as $(1,1)$) to the singlet state $|S(0,2)\rangle$ with two electrons in the right dot. These transitions, governed via the tunnel coupling t_c by the tunneling Hamiltonian $H_{t_c} = t_c |S(1,1)\rangle \langle S(0,2)| + H.c.$, are only possible for anti-parallel spins, because $\langle \uparrow\uparrow | H_{t_c} |S(0,2)\rangle = \langle \downarrow\downarrow | H_{t_c} |S(0,2)\rangle = 0$, while $\langle \downarrow\uparrow | H_{t_c} |S(0,2)\rangle, \langle \uparrow\downarrow | H_{t_c} |S(0,2)\rangle \neq 0$. Therefore, the states with even spin parity (parallel spins) block transport, while the states with odd spin parity (antiparallel spins) allow for transport. If the system is initialized to an even spin-parity state, the oscillating transverse magnetic field (if on resonance) rotates one (or both) of the two spins and thus lifts the blockade [154]. Initializing to $|\uparrow\rangle$ in both dots (the case with $|\downarrow\rangle$ gives the same result), we calculate the probability for an odd spin parity P_{odd} under time evolution for each of the two spins governed by the Hamiltonian in Eq.(7.1).

Introducing the detuning from resonance $\delta_\omega = \epsilon_z + h_z - \omega$, the probability to find spin up for a single value of h_z in the rotating wave approximation (which

7. Universal phase shift and non-exponential decay ...

is valid for $(b/\epsilon_z)^2 \ll 1$) is given by

$$P_{\uparrow, \delta\omega}(t) = \frac{1}{2} \left[1 + \frac{4\delta_\omega^2}{b^2 + 4\delta_\omega^2} + \frac{b^2}{b^2 + 4\delta_\omega^2} \cos \left(\frac{t}{2} \sqrt{b^2 + 4\delta_\omega^2} \right) \right]. \quad (7.2)$$

Assuming that $\omega = h_0 + \epsilon_z$, i.e., $\delta_\omega = h_z - h_0$, we find when averaging over the Gaussian distribution of h_z values (see section 7.5.2)

$$P_{\uparrow}(t) \sim \frac{1}{2} + C + \sqrt{\frac{b}{8\sigma^2 t}} \cos \left(\frac{b}{2} t + \frac{\pi}{4} \right) + \mathcal{O} \left(\frac{1}{t^{3/2}} \right), \quad (7.3)$$

for $t \gg \max(\frac{1}{\sigma}, 1/b, b/2\sigma^2)$, with $C = \frac{1}{2} - \frac{\sqrt{2\pi}b}{8\sigma} \exp\left(\frac{b^2}{8\sigma^2}\right) \operatorname{erfc}\left(\frac{b}{2\sqrt{2}\sigma}\right)$. We can now calculate the probability of finding an odd spin-parity state taking $\omega = h_0 + \epsilon_z$ for both dots and drawing the value of h_z independently from a distribution with width σ in each dot:

$$\begin{aligned} P_{\text{odd}}(t) &= P_{\uparrow,L}(t)(1 - P_{\uparrow,R}(t)) + (1 - P_{\uparrow,L}(t))P_{\uparrow,R}(t) \\ &= \frac{1}{2} - 2C^2 - C \frac{f(t)}{\sqrt{t}} - \frac{g(t)}{t} + \mathcal{O} \left(\frac{1}{t^{3/2}} \right); \end{aligned} \quad (7.4)$$

$$f(t) = \sqrt{\frac{2b}{\sigma^2}} \cos \left(\frac{bt}{2} + \frac{\pi}{4} \right), \quad (7.5)$$

$$g(t) = \frac{b}{8\sigma^2} \left[1 + \cos \left(bt + \frac{\pi}{2} \right) \right]. \quad (7.6)$$

This result is valid for times $t \gtrsim \max(1/\sigma, 1/b, b/2\sigma^2) \sim 20\text{ns}$ for a 1.4 mT nuclear field (see below) and $b \leq 2\sigma$ (accessible experimental regime). The $1/t$ -term oscillates with the double Rabi frequency which is the result of both spins being rotated simultaneously (see also [154]). This term only becomes important for $b > \sigma$, because in that case for both spins most of the nuclear-spin distribution is within the Lorentzian lineshape of the Rabi resonance. The $1/\sqrt{t}$ -term oscillates with the Rabi frequency and originates from only one of the two spins being rotated [154]. This term is important when $b < \sigma$, i.e., when only a small fraction of the nuclear-spin distribution is within the lineshape of the Rabi resonance.

We also give the expression for $P_{\text{odd}}(t)$ for the case where only one of the two spins is on resonance ($\epsilon_z + h_0 - \omega = 0$), while the other is far off-resonance ($|\epsilon_z + h_0 - \omega| \gg \sigma$). In this case the spin in one dot always remains up while the spin in the other dot rotates. This leads to

$$P_{\text{odd}}^{(1)}(t) = 1 - P_{\uparrow}(t) = \frac{1}{2} - C - \frac{f(t)}{4\sqrt{t}} + \mathcal{O} \left(\frac{1}{t^{3/2}} \right), \quad (7.7)$$

with the same range of validity as in Eq.(7.4). We see that the $1/t$ -term, which oscillates with frequency b , is not present in this case.

7.3 Power-law decay

The expressions for $P_{\text{odd}}(t)$ (Eqs. (7.4) and (7.7)) reveal two interesting features: the *power-law decay* and a universal *phase shift* of $\pi/4$ (see Eq. (7.5)) in the oscillations which is independent of all parameters. These features can both only appear if the nuclear field h_z is static during a time much longer than the Rabi period. This is crucial because only then the driven spin coherence for one fixed value of h_z is fully preserved. Because different values of h_z give different oscillation frequencies, the decay is due to averaging over the distribution in h_z .

The phase shift is closely related to the power-law decay because it also finds its origin in the off-resonant contributions. These contributions have a higher Rabi frequency and shift the average oscillation in phase. This universal phase shift therefore also characterizes the spin decay, together with the power law. Interestingly, the specific shape of the distribution in h_z (as long as it is peaked around the resonance) is not crucial for the appearance of both the power-law decay and the phase shift (see section 7.5.2). The values of the decay power and the phase shift are determined by the dependence of the oscillation frequency on h_z (in this case $\sqrt{b^2 + 4\delta_\omega^2}$).

A power-law decay has previously been found theoretically in [75, 50, 156, 157] and both a power-law decay ($1/t^{3/2}$) and a universal phase shift also appear in double dot correlation functions [152, 88]. In [153] a singlet-triplet correlation function was measured, but the amplitude of the oscillations was too small for the phase shift and the power-law decay to be determined. Here, we consider driven Rabi oscillations of a single electron spin with a power-law decay of $1/\sqrt{t}$ that is already valid after a short time $1/\sigma \sim 20$ ns. Therefore, the amplitude of the driven spin oscillations is still high when the power-law behavior sets in, even for small driving fields ($b < 2\sigma$) which are experimentally easier to achieve. The power-law decay and the phase shift thus should be observable in the experiment.

7.3 Power-law decay

We now discuss the observation of the power-law decay in the experimental data of which a selection is shown in Fig. 7.1. The data are obtained with the same device and under the same experimental conditions as in [154]. A fit is carried out to the observed oscillations for four different driving fields B_{ac} (Fig. 7.1), with three different fit functions: the theoretical expressions (Eqs. (7.4) and (7.7) with b and a constant scaling factor as fit parameters) and an exponentially decaying cosine. The width of the nuclear distribution $\sigma = g\mu_B(1.4 \text{ mT})$ is obtained from a fit of the steady state value $\frac{1}{2} - 2C^2$ of $P_{\text{odd}}(t)$ to a dataset obtained at $t = 950$ ns (Fig. 7.2a).

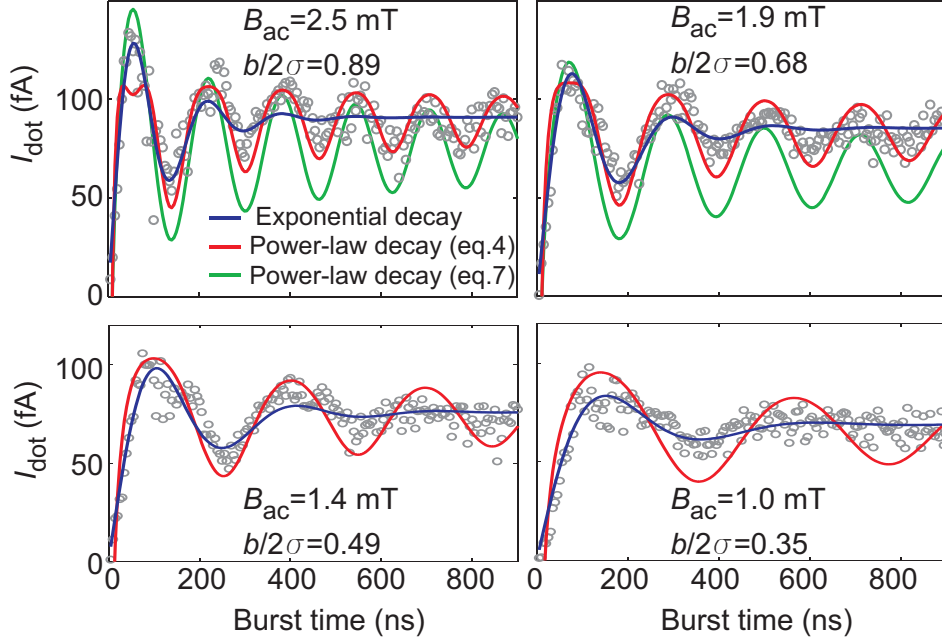


Figure 7.1: Rabi oscillations for four different driving fields B_{ac} ($B_z = 55$ mT, $g=0.355$ and $\sigma = g\mu_B(1.4$ mT)). The gray circles represent the experimentally measured dot current (averaged over 15 s for each value of t), which reflects the probability to find an odd spin-parity state after the RF burst that generates B_{ac} . The dotted, solid and dashed lines represent the best fit to the data of an exponentially decaying cosine function and the derived analytical expressions for $P_{\text{odd}}(t)$ and $P_{\text{odd}}^{(1)}(t)$ (Eqs. (7.4) and (7.7)) respectively. For clarity, the dashed line is shown only for the top two panels. The fit was carried out for the range 60 to 900 ns and the displayed values for B_{ac} were obtained from the fit with $P_{\text{odd}}(t)$ (Eq. (7.4)). We fit the data with an exponentially decaying cosine with a tunable phase shift that is zero at $t = 0$: $a_1 e^{-t/a_2} [\cos(\phi) - \cos(2\pi t/a_3 + \phi)] + a_4 (1 - e^{-t/a_2})$. The last term was added such that the saturation value is a fit parameter as well. We note that the fit is best for $\phi = \pi/4$, as discussed in the text.

For the range $B_{ac} \geq 1.9$ mT, we find good agreement with the model that predicts a power-law decay of $1/\sqrt{t}$ (Eq. (7.4); h_0 equal for both dots), while the fit with an exponentially decaying cosine is poor (Fig. 7.1). The power of the decay is independently verified by means of a fit to the data with $a_1 + a_2 \cos(2\pi t/a_3 + \pi/4)/t^d$ where, besides $a_{1,2,3}$, the power d of the time t is a fit parameter as well. We find values of $d \sim 0.6$ (Fig. 7.2b), close to the predicted $1/\sqrt{t}$ -dependence.

We see much better correspondence of the data with Eq. (7.4) than with Eq. (7.7), from which we can conclude that the mean of the Gaussian distribution h_0 is comparable for both dots (in equilibrium, we expect $h_0 \sim 0$ in both dots). There might however still be a small difference in h_0 between the two dots, which

7.4 Phase shift

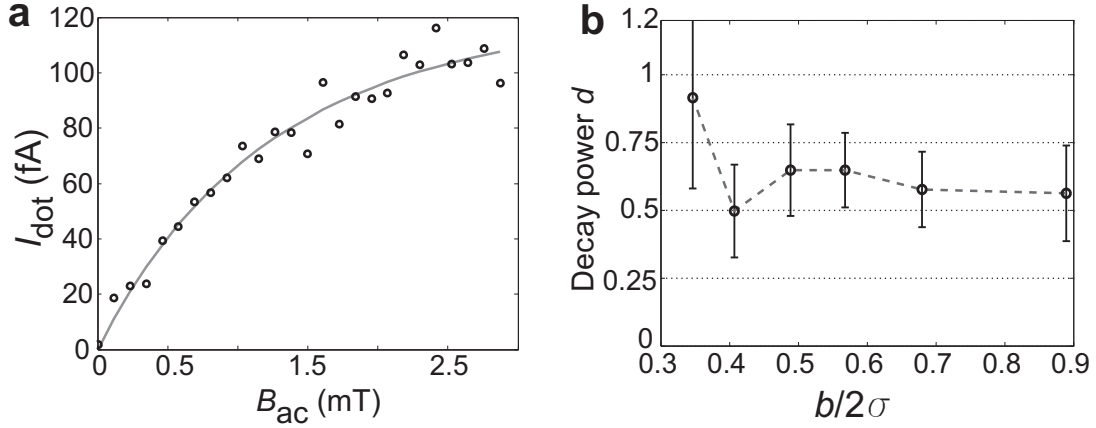


Figure 7.2: **a)** Dot current after an RF burst of 950 ns as a function of B_{ac} , approximately representing the steady-state value. The solid curve is the best fit with $a_1(\frac{1}{2} - 2C^2)$: the steady state expression of Eq. (7.4) with a_1 and σ as fit parameters. We find, for the 95%-confidence interval, $\sigma = g\mu_B(1.0 - 1.7 \text{ mT})$. **b)** Decay power obtained from the best fit of the data (partially shown in Fig. 7.1) with the expression $a_1 + a_2 \cos(2\pi t/a_3 + \pi/4)/t^d$, where $a_{1,2,3}$ and d are fit parameters.

we cannot determine quantitatively because the two models describe only two limiting cases. If present, such a difference in h_0 could help explain the small deviation between data and model at the first oscillation for $B_{\text{ac}} = 2.5 \text{ mT}$. It could originate from asymmetric feedback of the electron spins on the respective nuclear spin baths, e.g. due to unequal dot sizes, leading to different hyperfine coupling constants.

Another observation is that for small driving fields, $B_{\text{ac}} < 1.9 \text{ mT}$, we see that the damping is faster than predicted. Possible explanations for this effect are corrections due to electron-nuclear flip-flops (transverse terms in the hyperfine Hamiltonian) or electric field fluctuations. Electron-nuclear flip-flops may become relevant on a timescale $\sim \epsilon_z/\sigma^2 \sim 1 \mu\text{s}$ in this experiment. Electric field fluctuations can couple to spin states via the spin-orbit interaction [73] or a finite electric-field dependent exchange coupling.

7.4 Phase shift

We continue the discussion with the experimental observation of the second theoretically predicted prominent feature of the Rabi oscillations, i.e., a phase shift of $\pi/4$ in the oscillations, which is independent of all parameters. The value of ϕ can be extracted most accurately from the oscillations measured for a wide range and small steps of B_{ac} , like the data shown in Fig. 7.3a. That is because the Rabi period $T_{\text{Rabi}} = 2\pi/g\mu_B(\frac{1}{2}B_{\text{ac}}) = 2\pi/g\mu_B(\frac{1}{2}KI_s)$ contains only one unknown parameter K (current to oscillating field amplitude B_{ac} conversion factor, in units of

7. Universal phase shift and non-exponential decay ...

T/A) which is independent of the current through the wire I_s that generates B_{ac} [154]. The presence of a phase shift is visible in Fig. 7.3a, where the green and blue lines correspond respectively to the maxima of a cosine with and without a phase shift of $\pi/4$. The green lines match very well the yellow bands representing high data values. In contrast, the blue lines are located on the right side of the yellow bands for small burst times and more and more on the left side of the bands for increasing burst times. Thus, a cosine without a phase shift does not match with the observed Rabi oscillations.

In order to determine ϕ quantitatively, we perform a single two-dimensional fit of the complete dataset in Fig. 7.3a with $P_{odd}(t)$ (Eq. (7.4)), excluding the $1/t$ -term (see section 7.5.1). The fit range is $t = 100 - 900$ ns, such that the contribution from the $1/t$ -term of Eq. (7.4) can be neglected. For the 95% confidence interval we find $\phi = (0.23 \pm 0.01)\pi$, close to the theoretical value. The

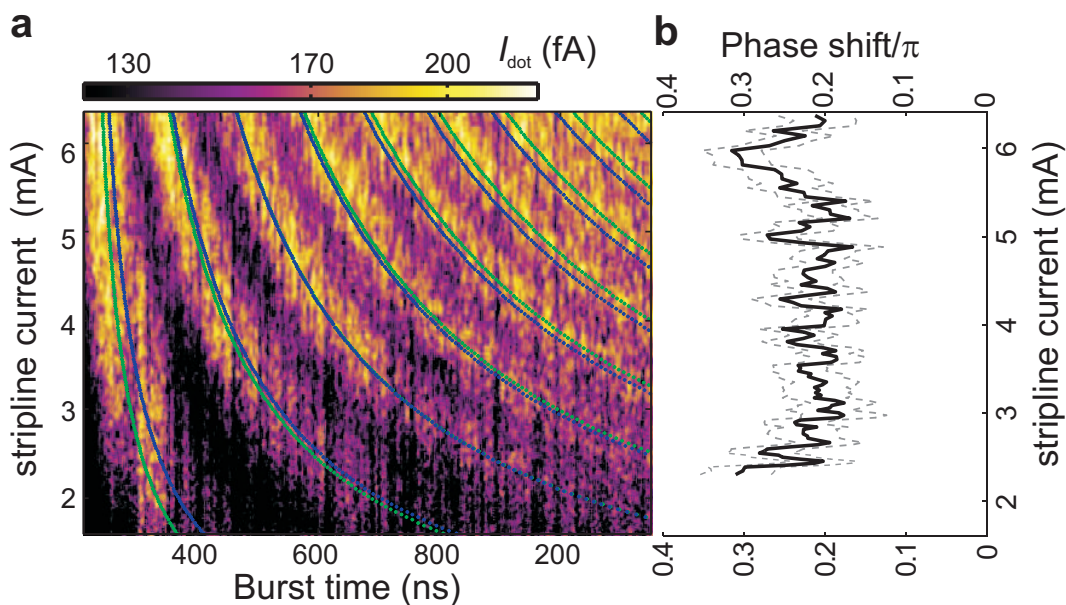


Figure 7.3: **a)** The dot current (represented in colorscale) is displayed over a wide range of B_{ac} (the sweep axis) and burst durations. The green and blue lines correspond respectively to the maxima of a cosine with and without a phase shift of $\pi/4$. The current-to-field conversion factor K is fitted for both cases separately ($K=0.568$ mT/mA and $K=0.60$ mT/mA for respectively with and without phase shift; the fit range is $t = 60 - 500$ ns and $I_s = 3.6 - 6.3$ mA). **b)** Phase shift for a wide range of B_{ac} , displayed as a function of stripline current I_s . Values obtained from a fit of each trace of the data in a) (varying burst time, constant B_{ac}) to a damped cosine $a_1 - a_2 \cos(\frac{1}{2}KI_s g \mu_B t + a_3 \pi) / \sqrt{t}$, where $a_{1,2,3}$ are fit parameters and $K = 0.568$ mT/mA. I_s is a known value in the experiment, extracted from the applied RF power. The grey dashed lines represent the 95% confidence-interval.

7.5 Additional information

relation between ϕ and B_{ac} is visible in Fig. 7.3b, where we find no significant dependence of ϕ as a function of B_{ac} , although the accuracy decreases for smaller B_{ac} (values obtained from fits to single traces, see caption). We have not compensated for the effects of the finite rise time (<2 ns) of the bursts, which leads to a small negative phase shift, on top of the expected positive $\pi/4$ shift.

To conclude, we have experimentally observed a power-law decay and universal phase shift of driven single electron spin oscillations. These features are theoretically understood by taking into account the coupling of the spin to the nuclear spin bath, which is static on the timescale of the electron spin evolution time. Furthermore, the slow power-law decay allows spin manipulation with relatively small driving fields. This improved understanding of the coherence of a driven single electron spin is important for future experiments using the electron spin as a qubit. For future investigation, it remains interesting to obtain more information about the non-static contributions of the nuclear bath or other possible decoherence mechanisms. For that, it is required to measure the driven oscillations at larger external fields, with larger driving powers and longer evolution times than accessible in this work.

We thank T. Meunier, R. Hanson, Y.V. Nazarov and I.T. Vink for discussions; R. Schouten, A. van der Enden, R. Roeleveld and W. den Braver for technical assistance. We acknowledge financial support from the Dutch Organization for Fundamental Research on Matter (FOM), the Netherlands Organization for Scientific Research (NWO), JST ICORP, NCCR Nanoscience, and the Swiss NSF.

7.5 Additional information

7.5.1 Fit procedure

Here, we describe the exact procedure of the two-dimensional fit from which the phase shift $\phi = (0.23 \pm 0.01)$ was obtained. The fit function is a simplification of $P_{\text{odd}}(t)$ (Eq. (4)). The first simplification is the exclusion of the $1/t$ -term because its contribution is negligible within the fit range of $t = 100 - 900$ ns. Second, both expressions for C and $0.5 - 2C^2$ are approximated as being linear in b , which is justified for the regime we consider ($I_s = 3.6 - 6.3$ mA), as can be seen in Fig. 7.4. With these simplifications, we obtain the expression $y_{\text{model}} = a_1 + I_s a_2 + (a_3 + I_s a_4) \cos(\frac{1}{2} K I_s g \mu_B t / \hbar + \phi \pi) / \sqrt{t}$, where $a_{1,2,3,4}$, K and ϕ are fit parameters. The Rabi frequency ω_{Rabi} is given by $\frac{1}{2} K I_s g \mu_B / \hbar$, with I_s the current through the stripline which is known in the experiment. The constant factor $K = B_{ac} / I_s$ is not known in the experiment but can be obtained from the fit. The behavior of $y_{\text{model}} - y_{\text{data}}$ around the optimal values for the fit parameters

7. Universal phase shift and non-exponential decay ...

is seen in Fig. 7.5b.

As a cross-check, we carried out a fit for each trace of the data in Fig. 7.3a of the main text (varying burst time, constant B_{ac}) with a damped cosine $a_1 - a_2 \cos(\frac{1}{2}KI_s g\mu_B t/\hbar + \phi\pi)/\sqrt{t}$, where $a_{1,2}$ and ϕ are fit parameters, and K is kept at a constant value. This fit is carried out for a wide range of values for K and I_s . The best-fit values for ϕ obtained for different I_s are averaged and plotted as a function of K in Fig. 7.5a, together with the spread in ϕ (gray dotted lines) and the fit quality. The figure shows that the best fit is obtained for $\phi = 0.23\pi$, the same value we found from the two-dimensional fit.

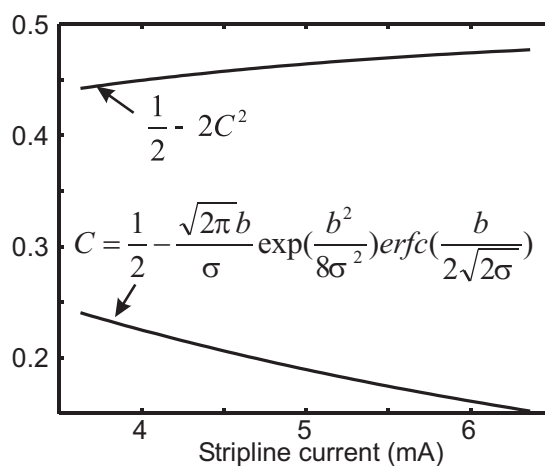


Figure 7.4: C and $0.5 - 2C^2$ as a function of I_s , with $\sigma = g\mu_B(1.4 \text{ mT})$ and $b = g\mu_B K I_s$. $K = 0.56 \text{ mT/mA}$ for the curves shown here, but the curves remain linear as well for $K=0.5-0.6 \text{ mT/mA}$.

7.5 Additional information

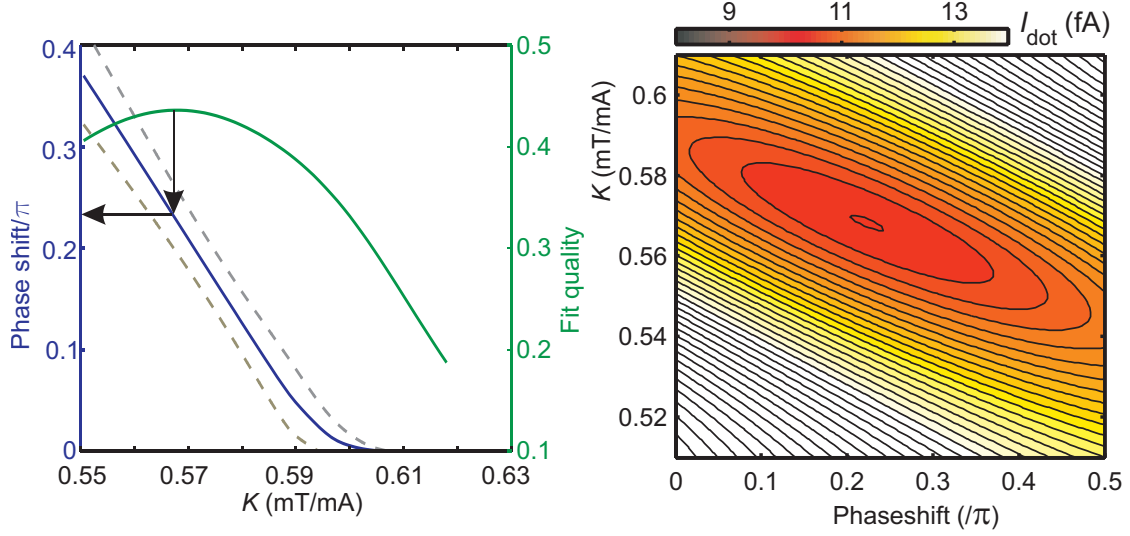


Figure 7.5: (a) Phase shift and fit quality for a range of current-to-field conversion factors K . Values obtained from a fit with a damped cosine to the single traces (constant I_s) of the data set shown in Fig. 3a of the main text, and subsequently averaged over all traces for the range $t = 100 - 900$ ns and $I_s = 3.6-6.3$ mA. The fit-quality R^2 is a measure of the correlation between the observed values y_i and the predicted values \hat{y}_i : $R^2 = \sum_{i=1}^n \frac{(\hat{y}_i - \bar{y}_i)^2}{(y_i - \bar{y}_i)^2}$, with $\bar{y} = \frac{1}{n} \sum y_i$. (b) Root mean square difference between the

measured current y_{data} and the model y_{model} : $\left(\sum_{t, I_s} (y_{t, I_s}^{\text{data}} - y_{t, I_s}^{\text{model}})^2 \right)^{1/2} / N_t N_{I_s}$, for a wide range of K and ϕ . We sum over the range $t = 100 - 900$ ns and $I_s = 3.6-6.3$ mA.

7.5.2 Asymptotic expansion

Here we give steps and additional justification leading to the asymptotic expansion given in Eq. (3) of the main text. We consider averaging Eq. (2) from the main text over a quasicontinuous distribution of h_z values for the case where $\delta_\omega = h_z - h_0$ (with the replacement $\delta_\omega \rightarrow x$):

$$P_\uparrow(t) = \int_{-\infty}^{\infty} dx D(x) P_{\uparrow, x}(t). \quad (7.8)$$

As a consequence of the central-limit theorem, for a large number of nuclear spins in a random unpolarized state, the distribution function $D(x)$ is well-approximated by a Gaussian with standard deviation σ centered at $x = 0$:

$$D(x) = \frac{1}{\sqrt{2\pi}\sigma} e^{-\frac{x^2}{2\sigma^2}}. \quad (7.9)$$

7. Universal phase shift and non-exponential decay ...

Inserting Eq. (7.9) into Eq. (7.8) gives the sum of a time-independent part, which can be evaluated exactly, and a time-dependent interference term $I(t)$:

$$P_{\uparrow}(t) = \frac{1}{2} + C + I(t). \quad (7.10)$$

Here, C is given following Eq. (3) of the main text. With the change of variables $u = (\sqrt{b^2 + 4x^2} - b) / 2\sigma$, and using the fact that the integrand is an even function of x , the interference term becomes $I(t) = \text{Re}\tilde{I}(t)$, where

$$\tilde{I}(t) = \sqrt{\frac{b}{8\pi\sigma}} e^{ibt/2} \int_0^{\infty} du \frac{\exp\left(-\frac{u^2}{2} - \frac{bu}{2\sigma} + i\sigma tu\right)}{\sqrt{u}\sqrt{1 + \frac{\sigma u}{b}}\left(1 + \frac{2\sigma u}{b}\right)}. \quad (7.11)$$

When $\sigma t \gg 1$, the time dependence of $\tilde{I}(t)$ is controlled by the region $u \lesssim 1/\sigma t$. The integrand simplifies considerably for $\sigma u/b \ll 1$, which coincides with $\sigma t \gg 1$ for

$$u \lesssim \frac{1}{\sigma t} \ll \frac{b}{\sigma}, \quad t \gg \frac{1}{\sigma}. \quad (7.12)$$

Equivalently, for

$$t > \max\left(\frac{1}{b}, \frac{1}{\sigma}\right), \quad (7.13)$$

we expand the integrand for $u < \min(1, b/\sigma)$:

$$\tilde{I}(t) = \sqrt{\frac{b}{8\pi\sigma}} e^{ibt/2} \int_0^{\infty} du \frac{\exp(-\lambda u + \mathcal{O}(u^2))}{\sqrt{u}} \left(1 + \mathcal{O}\left(\frac{\sigma u}{b}\right)\right), \quad \lambda = \frac{b}{2\sigma} - i\sigma t. \quad (7.14)$$

Neglecting corrections of order u^2 in the exponential and order $\sigma u/b$ in the integrand prefactor, the remaining integral can be evaluated easily, giving

$$I(t) \sim \frac{\cos[bt/2 + \arctan(t/\tau)/2]}{2[1 + (t/\tau)^2]^{1/4}}, \quad \tau = b/2\sigma^2, \quad (7.15)$$

$$t > \max(1/b, 1/\sigma). \quad (7.16)$$

Eq. (7.15) is valid for the time scale indicated for an arbitrary ratio of $b/2\sigma$. Due to the exponential cutoff at $u \lesssim 2\sigma/b$ in Eq. (7.14), Eq. (7.15) is actually valid for all times in the limit $b/2\sigma \gg 1$. Expanding Eq. (7.15) to leading order for $t/\tau \gg 1$ gives the result in Eq. (3) of the main text. Higher-order contributions to the long-time expansion of Eq. (7.15) and contributions due to corrections of order $\sigma u/b$ in Eq. (7.14) both lead to more rapidly decaying behavior of order

7.5 Additional information

$\sim 1/t^{3/2}$. The reason for the different phase shift here ($\pi/4$) relative to that found in Ref. [152] ($3\pi/4$) is that here the fluctuations are *longitudinal*, while in Ref. [152] the fluctuations are along the transverse direction. This leads to a different integrand in Eq. (S4) and thus to a different value for the phase shift and decay power.

Since the long-time behavior of $I(t)$ is dominated by the form of the integrand near $x = 0$, the same result can be found after replacing the Gaussian distribution function by any other distribution function $\tilde{D}(x)$ which is analytic and has a single peak at $x = 0$. Specifically,

$$\tilde{D}(x) = \tilde{D}(0) \exp\left\{-\frac{x^2}{2\sigma^2} + \mathcal{O}(x^3)\right\}, \quad (7.17)$$

$$\frac{1}{\sigma^2} = - \left. \frac{d^2 \ln \tilde{D}(x)}{dx^2} \right|_{x=0}. \quad (7.18)$$

Thus, the universal form of the long-time power-law decay and phase shift are relatively insensitive to the specific shape of the distribution function.

7. Universal phase shift and non-exponential decay ...

Chapter 8

Spin-echo of a single electron spin in a quantum dot

F. H. L. Koppens, K.C. Nowack & L. M. K. Vandersypen

A spin-echo technique is implemented on a single electron spin confined in a semiconductor quantum dot. When we tip the spin in the transverse plane via a magnetic field burst, it dephases in 37 ns due to the Larmor precession around an effective nuclear field. We reverse this dephasing to a large extent via a spin-echo pulse, and find a coherence time of about 0.5 μ s at 70 mT. These results are in the range of theoretical predictions of the electron spin coherence time governed by the dynamics of the electron-nuclear system.

This chapter is in preparation for submission to *Physical Review Letters*.

8.1 Introduction

An electron spin confined in a solid state device is a natural two-level quantum system which is well protected from uncontrolled interactions with the environment. This is interesting for studying fundamental physical properties and for implementing quantum information processing schemes [20]. Already a long time ago, very long coherence times exceeding hundreds of microseconds were observed for spins weakly bound to phosphorous donors in Si [158], and more recently for a single spin in a nitrogen-vacancy center in diamond [22]. Confining electron spins in gate-defined quantum dots offers the advantage of scalable device fabrication and in-situ tunability of the coherent coupling between the two spins [126, 42]. Long coherence times are expected as well for spins confined in quantum dots [64, 67], but for all III-V semiconductors, the hyperfine interaction with the nuclear spins forms an important dephasing source [75, 81, 84, 85]. Still, the dephasing dynamics, which can be seen as a Larmor precession of the spin around an unknown static effective nuclear field, can be reversed to a large extent by a spin-echo technique. This is required when operating a single spin as a qubit, but also allows a more detailed study on the rich dynamics of the remaining nuclear-induced decoherence processes.

For two coupled electron spins, the implementation of a spin-echo technique was demonstrated by using the exchange interaction [42] to reverse the two-electron dephasing dynamics. An alternative way to overcome dephasing was demonstrated with confined spins in ensembles of optically accessible quantum dots [159], where a train of light pulses was synchronized with the phase of the precessing spins. In order to use the Zeeman spin states as a quantum bit, reversing the dephasing dynamics of a single spin is required. Here, we report the implementation of a spin-echo technique on of a single electron spin confined in a gate-defined quantum dot (shown in Fig. 8.1b), with coherent control realized via electron-spin-resonance (as reported in [104]). We first show with a Ramsey-style experiment that the dephasing time T_2^* is about 37 ns, set by the nuclear field distribution. Via a spin-echo technique we reverse to a large extent the electron-nuclear dynamics, and find a coherence time $T_{2,\text{echo}}$ of about 0.5 μs , which is more than a factor of ten longer than the Ramsey decay time. Furthermore, we demonstrate the ability to rotate the spin about any arbitrary axis in the Bloch-sphere by varying the phase-relation between two ac magnetic field bursts.

The coherent manipulation and read-out scheme is depicted in Fig. 8.1a. The dots are tuned such that one electron always resides in the right dot and a second electron can flow through the two quantum dots only if the spins are anti-parallel. For parallel spins, the electron flow is blocked by the Pauli principle (so-called

8.2 Free-evolution decay

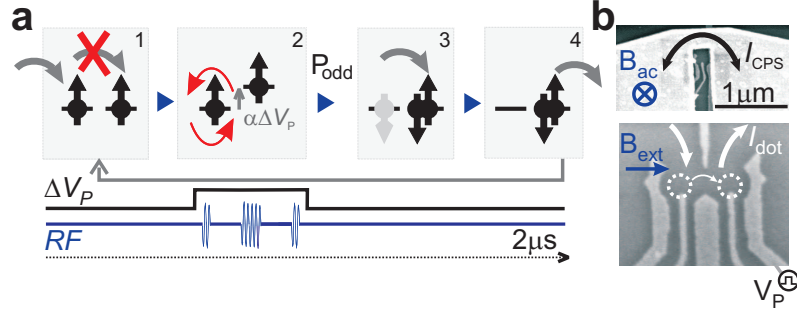


Figure 8.1: (a) Schematic of the electron cycle (time axis not on scale). The voltage ΔV_p (with lever arm α) on the gate detunes the dot levels during the manipulation stage (applied bias is 1.5 mV). In order to generate sequences of RF bursts with controllable phase, we use a vector source (Rohde&Schwarz SM300, 9 kHz to 3 GHz) with RF modulator, controlled by two channels of a Tektronix arbitrary waveform generator (model AWG520). (b) Bottom: Scanning electron microscope (SEM) image of the Ti/Au gates on top of a GaAs/AlGaAs heterostructure containing a two-dimensional electron gas below the surface. White arrows indicate current flow through the two coupled dots (dotted circles). The gate labeled with V_p is connected to a homemade bias-tee (rise time 150 ps) to allow fast pulsing of the dot levels. Top: SEM image of the on-chip coplanar stripline, separated from the surface gates by a 100-nm-thick dielectric.

Pauli blockade)¹, allowing us to initialize the system in a mixed state of $|\uparrow\uparrow\rangle$ or $|\downarrow\downarrow\rangle$ (stage 1). When manipulating one of the electron spins² with a sequence of RF bursts, we also apply a voltage pulse to one of the gates (denoted by ΔV_p in Fig. 8.1a) to avoid decoherence due to tunneling (stage 2). After pulsing back the gate, electron tunneling is allowed, but only for anti-parallel spins (stage 3 and 4). Repeating this cycle results in a current flow reflecting the average probability P_{odd} to find anti-parallel spin.

8.2 Free-evolution decay

We measure the free-evolution decay of the spin coherence via a Ramsey experiment (see inset Fig. 8.2a for the RF pulse sequence). A $\pi/2$ -pulse is applied to

¹Normally, all three triplet states can block current flow. However, due to the difference of nuclear fields in the two dots, one of the triplets T_0 is admixed with the singlet S , which lifts the blockade [85]. Therefore, only $|\uparrow\uparrow\rangle$ or $|\downarrow\downarrow\rangle$ will block the current flow.

²For all experiments discussed here, $B_{ac} < \sigma_N$, and therefore, one electron is on-resonance for most of the nuclear configurations. For that reason, the driven transitions are mostly single spin transitions, although we can not controllably address the spins separately. Furthermore, the tunnel coupling between the two dots is small enough ($\sim 0.05\mu\text{ eV}$) to guarantee (together with the dot alignment) negligible exchange interaction J between the spins compared to the hyperfine interaction with $\sim 10^6$ nuclear spins in the host material.

8. Spin-echo of a single electron spin in a quantum dot

create a coherent superposition between $|\uparrow\rangle$ and $|\downarrow\rangle$, after which the spin dephases during a time τ . Subsequently, a $3\pi/2$ -pulse is applied which rotates the spin component that has not dephased to $|\uparrow\rangle$, while the component that has gained a phase of π is rotated to $|\downarrow\rangle$. Therefore, the degree of dephasing is reflected in the probability to find $|\uparrow\rangle$ after the pulse sequence. The measured signal, proportional to find $|\downarrow\rangle$, is shown as function of τ in Fig. 8.2a. The coherence decays with a typical timescale of $T_2^* \sim 37$ ns, obtained from a Gaussian fit. For these long measurement times, the Ramsey decay can be understood from the interaction Hamiltonian with the nuclei: $H_{\text{hf}} = \mathbf{S} \cdot \mathbf{h} = S_z h_z + S_+ h_- + S_- h_+$; $\mathbf{h} = \sum_i A_i \mathbf{I}_i$, where \mathbf{S} is the spin-1/2 operator for the electron spin, \mathbf{I}_i are the nuclear spin operators and the A_i coupling constants with the electron spin. The $S_z h_z$ term in the Hamiltonian can be seen as a nuclear field $B_{N,z}$ in the z-direction that changes the Larmor precession frequency of the electron spin (other terms are discussed below in the context of spin-echo). This nuclear field fluctuates in time (as discussed further below) with a Gaussian distribution with width σ and a typical correlation time $\sim 100 \mu\text{s} - 1$ s. This is much longer than the cycle time of $2 \mu\text{s}$, but much shorter than the averaging time for each measurement point (~ 20 seconds). Averaging the Larmor precession over a Gaussian distributed nuclear field would result in a Gaussian coherence decay $\int_{-\infty}^{\infty} \frac{1}{\sqrt{2\pi}\sigma} e^{(-B_{N,z}^2/2\sigma^2)} \cos(g\mu_b B_{N,z} t/\hbar) dB_{N,z} = e^{-(t/T_2^*)^2}$, with $T_2^* = \sqrt{2\hbar}/g\mu_b\sigma \sim 30$ ns [81, 86] (assuming $\sigma = 1.5$ mT, extracted from the Rabi oscillations, see [142]). A Gaussian decay with a typical timescale 30 ns is shown in Fig. 8.2a (solid line). However, the observed Ramsey signal cannot be compared directly with this curve because we have to take into account the imperfection of the $\pi/2$ and $3\pi/2$ -pulses due to resonance offsets caused by the nuclear field as well.

To include these effects, we compute the averaged time evolution of the spins in the presence of the nuclear field, not only during the delay time, but also during the pulses. This gives for the spin state at the end of the cycle: $\psi(\tau, B_{L,R}) = U_{3\pi/2}(B_{L,R})U_{\tau}^{\text{free}}(B_{L,R})U_{\pi/2}(B_{L,R})|\uparrow\uparrow\rangle$. Here, $U_x(B_{L,R})$ is the two-spin time-evolution operator corresponding to a Rabi pulse and a static field resonance offset by the value $B_{L,R}$ for the left (right) spin. The time-evolution operator $U_{\tau}^{\text{free}}(B_{L,R})$ represents the two-spin free-evolution in the nuclear field $B_{L,R}$ during a time τ . As we have seen before, the current flow is proportional to the average probability to find anti-parallel spins, P_{odd} . Averaging P_{odd} over two independent Gaussian distributions of nuclear fields in the right and left dot gives

$$P_{\text{odd}}(\tau) = \int \int e^{-(\frac{B_L+B_R}{\sigma})^2} \tilde{P}_{\text{odd}}(B_{L,R}) dB_L dB_R;$$

$$\tilde{P}_{\text{odd}}(\tau, B_{L,R}) = \langle \psi(\tau, B_{L,R}) | \uparrow\downarrow \rangle + \langle \tau, \psi(B_{L,R}) | \downarrow\uparrow \rangle.$$

8.2 Free-evolution decay

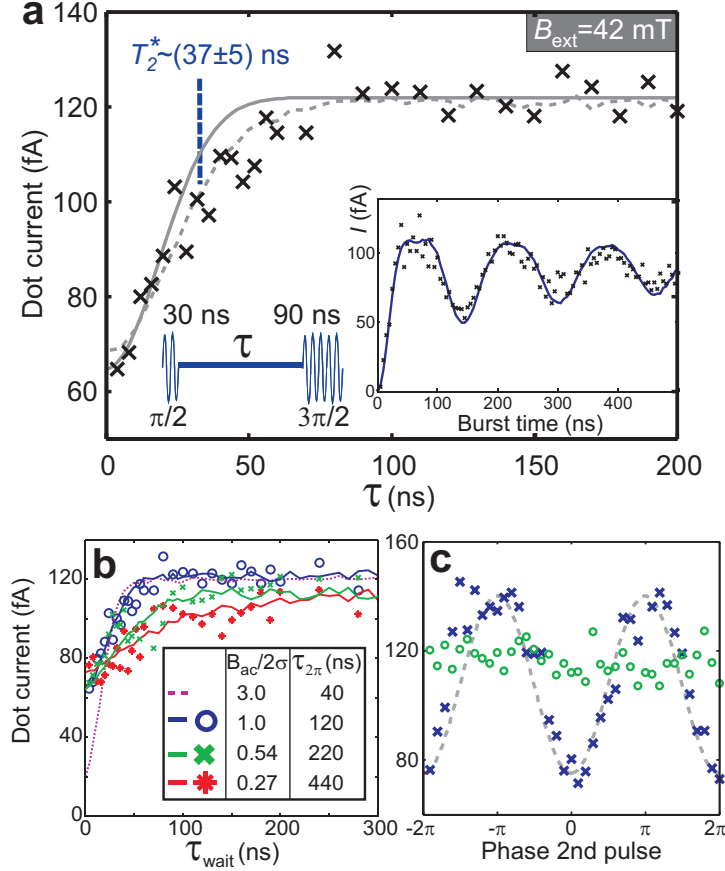


Figure 8.2: a) Ramsey signal as a function of free-evolution time τ . One data point reflects an average over 20 seconds at constant $B_{\text{ext}} = 42$ mT, $f_{\text{ac}} = 210$ MHz, $B_{\text{ac}} = 3$ mT ($\tau_{2\pi} = 120$ ns). In order to optimize the visibility of the decay, the second pulse is a $3\pi/2$ -pulse instead of the usual $\pi/2$ -pulse. This is because we do not measure in the single spin basis, but we measure P_{odd} . If both spins dephase, the signal hardly changes compared to two (imperfect) Rabi $\pi/2$ pulses. Dotted line: numerically calculated dot current $P_{\text{odd}}(m+1)80 + 23$ fA for $\tau_{2\pi} = 40$ -220 ns, and $P_{\text{odd}}(m+1)80 + 43$ fA for $\tau_{2\pi} = 440$ ns. We assume $\sigma = 1.5$ mT in both dots and $m = 1.44$ (see below for definition m). The solid line is a Gaussian decay with a typical timescale of $\sqrt{2}\hbar/g\mu_b\sigma = 30$ ns. Inset: Rabi oscillations with period $\tau_{2\pi} = h/g\mu_b(B_{\text{ac}}/2)$ between parallel and anti-parallel spin states driven by a single RF burst ($B_{\text{ext}} = 42$ mT, $f_{\text{ac}} = 210$ MHz, $B_{\text{ac}} = 3$ mT). $I_{\text{dot}} = P_{\text{odd}}(m+1)80$ fA, with m the additional average number of electrons that tunnels through the dot before a parallel spin state has formed and the current is blocked again ($m = 1.5$ -2 in the experiments discussed here), and 80 fA corresponds to one electron transition per $2 \mu\text{s}$ cycle. b) Numerically calculated (assuming $\sigma = 1.5$ mT) and measured Ramsey signal for a wide range of driving fields. c) Ramsey signal as a function of the relative phase between the two RF bursts for $\tau = 10$ (crosses) and 150 ns (circles). Gray dashed line is a best fit of a cosine to the data.

The numerically calculated $P_{\text{odd}}(\tau)$ (with a scaling factor) is shown in Fig. 8.2a (dotted line). (Simulations with the spin up/down basis gives similar decay times

8. Spin-echo of a single electron spin in a quantum dot

compared to the spin even/odd basis). We find that the decay time is longer when the rotations are imperfect due to resonance offsets. This is more clearly visible in Fig. 8.2b, where the numerical curves are shown together with Ramsey measurements for a wide range of driving fields. For $B_{ac}/2\sigma \lesssim 1$, the experimentally observed Ramsey decay time is longer for smaller B_{ac} , in good agreement with the numerical result. This effect can be understood by realizing that the first RF burst rotates the spin effectively only when the nuclear field lies within the Lorentzian lineshape of power broadened response. For $B_{ac}/2 < \sigma$, this lineshape is narrower than the nuclear spin distribution and therefore the first RF burst ($\pi/2$ -pulse) acts as a filter for far off-resonant contributions, resulting in a longer typical decay time.

Before proceeding, we demonstrate that the variation of I_{dot} seen in Fig. 8.2a really corresponds to a loss of phase coherence. We do this by varying the relative phase ϕ between the two RF bursts. This phase controls the rotation axis of the second pulse compared to the first pulse. As expected, the signal oscillates as a function of ϕ for short free-evolution times τ (see crosses in Fig. 8.2a), and the oscillations disappear when the coherence is lost (circles in Fig. 8.2c). We remark that this also demonstrates our ability to rotate the electron spin on the Bloch-sphere about any arbitrary axis, which provides the necessary universal control when operating the electron spin as a qubit.

8.3 Spin-echo

The dephasing mechanism discussed so far is given by the $S_z h_z$ -term in the Hamiltonian, which is in principle fully time-reversible by a spin-echo pulse (because substitution of $Sz \rightarrow -S_z$ in the Hamiltonian gives $-H$). We will now test to what extent the electron-nuclear dynamics is reversible. The spin-echo sequence we apply is as depicted in the inset of Fig. 8.3a, and the measured signal as a function of the total free-evolution time $\tau_1 + \tau_2$ is shown in Fig. 8.3a. We can see directly from the longer decay time that due to the spin-echo pulse, the coherence is preserved during a time much longer than T_2^* .

To confirm that the echo reverses (a part of) the electron spin dephasing that occurs during the free-evolution time, we measure the echo signal as a function of $\tau_1 - \tau_2$ (Fig. 8.3b). As expected, the echo is optimal for $\tau_1 = \tau_2$, which is visible as a dip in the data. Half of the FWHM is ~ 27 ns, similar to the observed Ramsey decay time. Again, we check whether the coherence is preserved by varying the phase of the second $\pi/2$ -pulse relative to the first two pulses. Now, the oscillations are still clearly visible for a free-evolution time of 150 ns (Fig. 8.3c), while they

8.3 Spin-echo

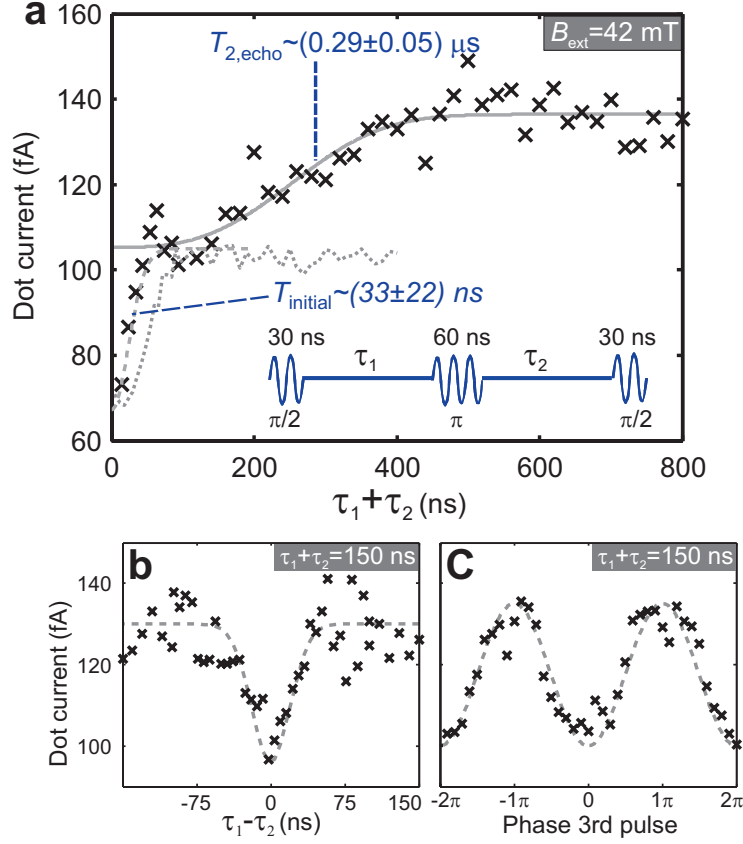


Figure 8.3: (a) Spin-echo signal as a function of total free-evolution time $\tau_1 + \tau_2$. One data point reflects an average over 20 seconds at constant $B_{\text{ext}} = 42$ mT, $f_{\text{ac}} = 210$ MHz, $B_{\text{ac}} = 3$ mT. Solid and dashed lines are best fits of respectively a Gaussian and $e^{-((\tau_1 + \tau_2)/T_{2,\text{echo}})^3}$ to the data for the range $\tau_1 + \tau_2 = 0 - 100$ ns and 100-800 ns. Dotted line: numerically calculated dot current $P_{\text{odd}}(m+1)80 + 25$ fA, assuming $\sigma = 1.5$ mT in both dots and $m = 1.83$. Inset: spin-echo pulse sequence. (b) spin-echo signal as a function of $\tau_1 - \tau_2$. Dashed line is the best fit of a Gaussian to the data. (c) spin-echo signal for $\tau_1 + \tau_2 = 150$ ns as a function of the relative phase between the first two and third pulse. Dashed line is the best fit of a cosine to the data.

were fully suppressed when no echo-pulse was applied (Fig. 8.2b).

The spin-echo signal as function of total free-evolution time $\tau_1 + \tau_2$ (Fig. 8.3a) reveals two types of decay. First, an initial decay with a typical timescale of 33 ns (obtained from a Gaussian fit), comparable to the observed Ramsey decay time (when using the same B_{ac}). This initial decay is due to resonance offsets of the echo-pulse caused by the nuclear field. Therefore, the refocussing is not perfect for part of the nuclear configurations. On average, part of the spin coherence decay is then caused by ensemble averaging similar as in the Ramsey decay. To confirm this, we calculate numerically the echo signal for a static nuclear spin bath with distribution $\sigma = 1.5$ mT (similar as the calculations for the Ramsey

8. Spin-echo of a single electron spin in a quantum dot

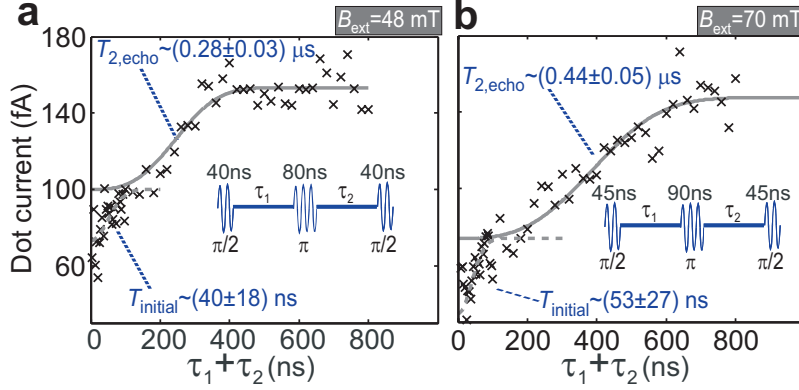


Figure 8.4: Spin-echo signal at $B_{\text{ext}} = 48$ ($f_{\text{ac}} = 280$ MHz) and 70 mT ($f_{\text{ac}} = 380$ MHz). Pulse sequence depicted in the insets. Solid and dashed lines best fits of a Gaussian and $e^{-((\tau_1+\tau_2)/T_{2,\text{echo}})^3}$ to the data for respectively the range $\tau_1 + \tau_2 = 0 - 100$ ns and 100-800 ns.

experiment). We find reasonable agreement of the data with the numerical curve (dotted line in Fig. 8.3a), regarding both the decay time as the amplitude.

Second, the spin-echo data also shows a slower decay, which corresponds to the loss of coherence that cannot be reversed by the echo-pulse (even for a perfect π -pulse). The spin-echo coherence time $T_{2,\text{echo}}$ can be extracted from a best fit of $a + be^{-((\tau_1+\tau_2)/T_{2,\text{echo}})^3}$ [101, 98] to the data ($a, b, T_{2,\text{echo}}$ are fit parameters). We find $T_{2,\text{echo}} = 258$ ns at $B_{\text{ext}}=42$ mT (see Fig. 8.3a). We note that the precise functional form of the decay is hard to extract from the measurement due to noise on the data caused by the slow fluctuations of the nuclear field, but fit functions with powers between 2.5 and 4 in the exponent give similar decay times.

Measurements at higher B_{ext} were only possible by decreasing the driving field and are shown in Fig. 8.4a,b. As expected, we find a longer initial decay time, which is due to the smaller driving field, similar as observed for Ramsey measurements. We see that the longer decay time from which we extracted $T_{2,\text{echo}}$ increases with field, up to $0.44 \mu\text{s}$ at $B_{\text{ext}}=70$ mT. This is about a factor of two smaller than the coherence time observed for two-electron entangled spin states at $B_{\text{ext}}=100$ mT [42]. Possible reasons for the difference could be a smaller applied magnetic field (further discussed below), imperfection of the echo-pulse or the fact that our measurements are sensitive to decoherence of both spins in the two quantum dots.

8.4 Decoherence mechanism

The field-dependent value for $T_{2,\text{echo}}$ we find is more than a factor of 10 longer than T_2^* . This is made possible by the long correlation time of the nuclear spin bath and because the interaction with the nuclei is to a large extent a reversible process. What can limit $T_{2,\text{echo}}$ are processes that can change the nuclear field during one echo sequence, like the flip-flop terms in the hyperfine Hamiltonian H_{hf} ($H_{\text{hf}} = (h_+S_- + h_-S_+)/2$), and the dipole-dipole interaction between neighbouring nuclear spins. The latter is not expected to be field dependent once $B_{\text{ext}} > D/g\mu_B \sim 0.1$ mT, with D the dipole interaction strength between two nuclear spins. The flip-flop terms of H_{hf} are easily suppressed with a magnetic field ($\sim 1/B_{\text{ext}}^2$), but the energy-conserving higher-order contributions can lead to flip-flops between two non-neighboring nuclear spins mediated by the electron spin. This hyperfine-mediated flip-flop rate scales with $1/B_{\text{ext}}$ [152], and is predicted to lead to a coherence decay of about $\sim 1\text{-}100$ μs for $B_{\text{ext}}=1\text{-}5$ T [98, 99]. Therefore, hyperfine-mediated decoherence might limit the observed $T_{2,\text{echo}}$.

Another possible decoherence mechanism other than the interaction with the nuclear spin bath is spin-exchange with the electrons in the reservoir via cotunneling. However, we expect that the typical timescale of this process is very long. That is because the energy difference between the electron orbital and the Fermi energy (> 100 μeV) is much larger than the tunnel rate (< 0.1 μeV). In principle, the Heisenberg coupling with the electron spin in the adjacent quantum dot could also decohere the spin, but during the manipulation stage, we expect that the Heisenberg coupling J is very small due to the large level detuning.

8.5 Conclusion

To conclude, we have measured the free-evolution coherence decay of a single electron spin in a quantum dot and prolong this decay by more than a factor of ten via a spin-echo pulse. We extract a echo decoherence time of 0.28 μs and 0.44 μs at magnetic fields of respectively 48 and 70 mT. Even longer decoherence times are expected at higher magnetic fields, although the observed decay times are already sufficiently long for further exploration of electron spins as qubits. Considerable suppression of the hyperfine-mediated flip-flop rate by a magnetic field is predicted to lead to echo coherence times of $10\text{-}100$ μs [103, 160], limited by the internuclear dipole-dipole interaction. We remark that apart from spin-echo also other possibilities to suppress spin dephasing due to the nuclear field uncertainty have been proposed, such as measurement-based state narrowing of the nuclear spin bath [88] or strong electron-nuclear feedback associated with

8. Spin-echo of a single electron spin in a quantum dot

spin-dependent transport [161]. These opportunities will be investigated in future experiments.

We thank D. Klauser, W. Coish, D. Loss, R. DeSousa, R. Hanson, S. Saikin, I.T. Vink and T. Meunier for discussions; Klaas-Jan Tielrooij for help with device fabrication; R. Schouten, A. van der Enden and R. Roeleveld for technical assistance and L.P. Kouwenhoven for mentorship and support. We acknowledge financial support from the Dutch Organization for Fundamental Research on Matter (FOM) and the Netherlands Organization for Scientific Research (NWO).

Chapter 9

Coherent control of a single spin with electric fields

K. C. Nowack, F. H. L. Koppens, Yu. V. Nazarov & L. M. K. Vandersypen

We experimentally realize coherent control of a single electron spin in a quantum dot using an *ac electric* field generated by a local gate. The electric field induces coherent transitions (Rabi oscillations) between spin-up and spin-down, whereby the rotation angle is controlled by the amplitude and duration of the electric field bursts. We find a strong dependence of the Rabi frequency on the static magnetic field, with 90° rotations as fast as ~ 55 ns at 2.8 T. Our analysis indicates that the electrically-induced spin transitions are mediated by the spin-orbit interaction. These results, together with the recently demonstrated coherent exchange of two neighboring spins, demonstrate the feasibility of fully electrical manipulation of spin qubits.

This chapter has been submitted to Science.

9.1 Introduction

Spintronics and spin-based quantum information processing explore the possibility to add new functionality to today's electronic devices by exploiting the electron spin in addition to the electric charge [162]. In this context, a key element is the ability to induce transitions between the spin-up and spin-down states of a localized electron spin, and to prepare arbitrary superpositions of these two basis states. This is commonly accomplished by magnetic resonance, whereby bursts of a resonant oscillating magnetic field are applied [111]. However, producing strong oscillating magnetic fields in a semiconductor device requires specially designed microwave cavities [163] or microfabricated striplines [104], and has proven very challenging. In comparison, electric fields can be generated much more easily, simply by exciting a local gate electrode. In addition, this allows for greater spatial selectivity, which is important for local addressing of individual spins. It would thus be highly desirable to control the spin by means of electric fields.

Although electric fields do not couple directly to the electron spin, indirect coupling can still be realized by placing the spin in a magnetic field gradient [32] or in a structure with a spatially varying g -tensor, or simply through spin-orbit interaction, present in most semiconductor structures [164, 60]. Several of these mechanisms have been employed to electrically manipulate electron spins in two dimensional electron systems [135, 33, 144, 165], but proposals for coherent electrical control at the level of a single spin [34, 68, 32, 69, 166, 70] have so far remained unrealized.

9.2 Device and measurement technique

Here we demonstrate coherent single spin rotations induced by an oscillating electric field. The electron is confined in a gate-defined quantum dot (see Fig. 9.1a) and we use an adjacent quantum dot, containing one electron as well, for read-out. The ac electric field is generated through excitation of one of the gates that forms the dot, thereby periodically displacing the electron wavefunction around its equilibrium position as sketched in Fig. 9.1b.

The experiment consists of four stages, as depicted in Fig. 9.1c. We initialize the device in a spin-blockade regime where two electrons with parallel spin are held fixed, one in each dot. Next, the two spins are isolated by a dc gate voltage, such that electron tunneling between the dots or to the reservoirs is forbidden.

9.2 Device and measurement technique

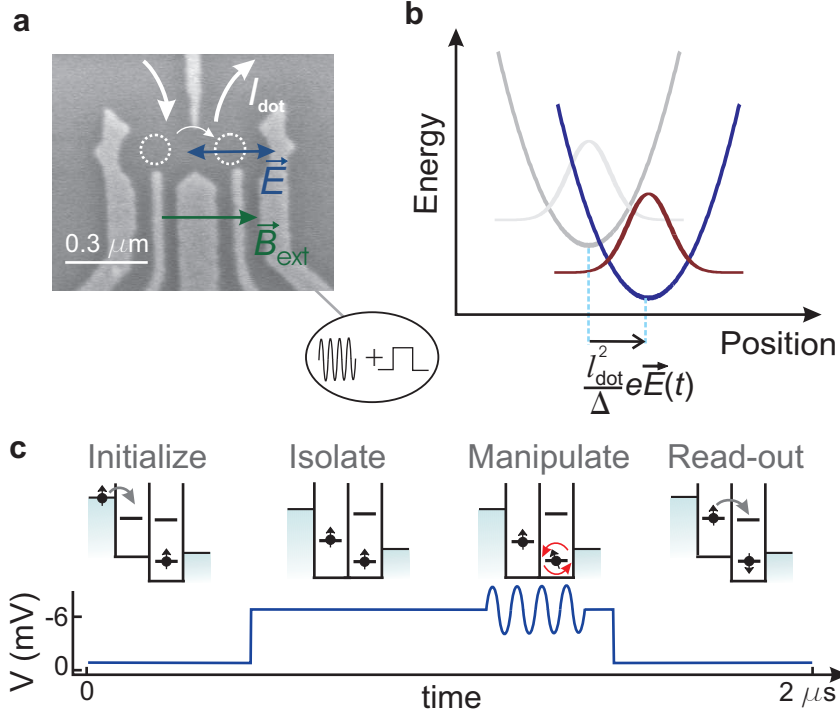


Figure 9.1: (a) Scanning electron microscope image of a device with the same gate structure as the one used in this experiment. Metallic TiAu gates are deposited on top of a GaAs heterostructure which hosts a 2DEG with an electron density $n_s = 4 - 5 \cdot 10^{11} \text{cm}^{-2}$ 90 nm below the surface. Not shown is a coplanar stripline on top of the metallic gates, separated by a dielectric (not used in this experiment, see also [104]). In addition to a dc voltage we can apply fast pulses and microwaves to the right side gate through a home made bias-tee (rise time 150 ps). The orientation of the in plane external magnetic field is as shown. The measurements are performed in a dilution refrigerator at an electron temperature of around 100 mK. (b) The voltage applied to the gate displaces the center of the electron wavefunction along the electric field direction and changes the potential depth. Here, Δ is the orbital splitting, $l_{\text{dot}} = \hbar / \sqrt{m^* \Delta}$ the size of the dot, m^* the effective electron mass, \hbar reduced Planck's constant and $\mathbf{E}(t)$ the electric field. (c) The double dot is initialized into a state with parallel spins due to Pauli spin blockade. Next we apply a pulse on the right side gate which turns off tunneling between the dots. During this pulse a microwaveburst is applied which rotates a spin by an angle that depends on the length of the burst. After manipulation the levels are aligned again and the spin state is projected on the parallel/anti-parallel basis. When the spins are anti-parallel, the left electron tunnels to the right dot, and subsequently, it can tunnel through to the right reservoir. For anti-parallel spins, no tunneling takes place. Repetition of this cycle gives rise to an average current which we monitor (see also [104]).

Then, one of the spins is rotated by an ac voltage burst applied to the gate¹ (most likely the spin in the right dot, where the electric field is expected to be strongest). Finally, the read-out stage allows the left electron to tunnel to the right dot if and only if the spins are anti-parallel. Subsequent tunneling of one electron to the right reservoir gives a contribution to the current². This cycle is continuously repeated, and the current flow through the device is thus proportional to the probability of having anti-parallel spins after excitation.

9.3 Spin spectroscopy

First, we demonstrate that electrical excitation can indeed induce single-electron spin flips. We apply a microwave burst of constant length to the right side gate and monitor the average current flow through the quantum dots as a function of external magnetic field \mathbf{B}_{ext} (Fig. 9.2a). A finite current flow is observed around the single-electron spin resonance condition, i.e. when $|\mathbf{B}_{\text{ext}}| = hf_{\text{ac}}/g\mu_{\text{B}}$, with h Planck's constant, f_{ac} the excitation frequency, and μ_{B} the Bohr magneton. From the position of the resonant peaks measured over a wide magnetic field range (Fig. 9.2b) we determine a g -factor of $|g| = 0.39 \pm 0.01$, which is in agreement with other reported values for electrons in GaAs quantum dots [39].

In addition to the external magnetic field the electron spin feels an effective nuclear field B_{N} , that arises from the hyperfine interaction with nuclear spins in the host material and fluctuates in time [75, 81]. This nuclear field modifies the electron spin resonance condition and is generally different in the left and right dot (by ΔB_{N}). The peaks shown in Fig. 9.2a are averaged over many magnetic field sweeps and have a width of about 10-25 mT. This is much larger than the expected linewidth, which is only 1-2 mT given by the fluctuations of B_{N} [84, 85]. When we look at individual field sweeps measured at constant

¹The microwave bursts were created by sending a microwave signal generated by a Rohde & Schwarz SMR40 source through either a high isolation GaAs RF switch (Minicircuits ZASWA-2-50DR) for frequencies in the range of 10MHz to 4.6GHz or through two mixers in series (Marki Microwave M90540) for frequencies above 5GHz. The switch and the mixers were gated by rectangular pulses from an arbitrary wave form generator (Tektronix AWG520). The microwave bursts and voltage pulses generated by the marker channel of the same waveform generator were combined (splitter Pasternack PE2064) and applied to the right side gate through a home made bias-tee (rise time 150 ps and a RC charging time of $\gg 10$ ms at 77K).

²Normally, all three triplet states can block current flow. However, due to the difference of nuclear fields in the two dots, the triplet T_0 is admixed with the singlet, which lifts the blockade [104]. Therefore, only T_+ or T_- will block the current flow (we note that the exchange interaction between the spins, present due to the tunnel coupling between the dots, can be neglected because it is much weaker than the Zeeman energy due to the nuclear field B_{N}).

9.4 Rabi oscillations

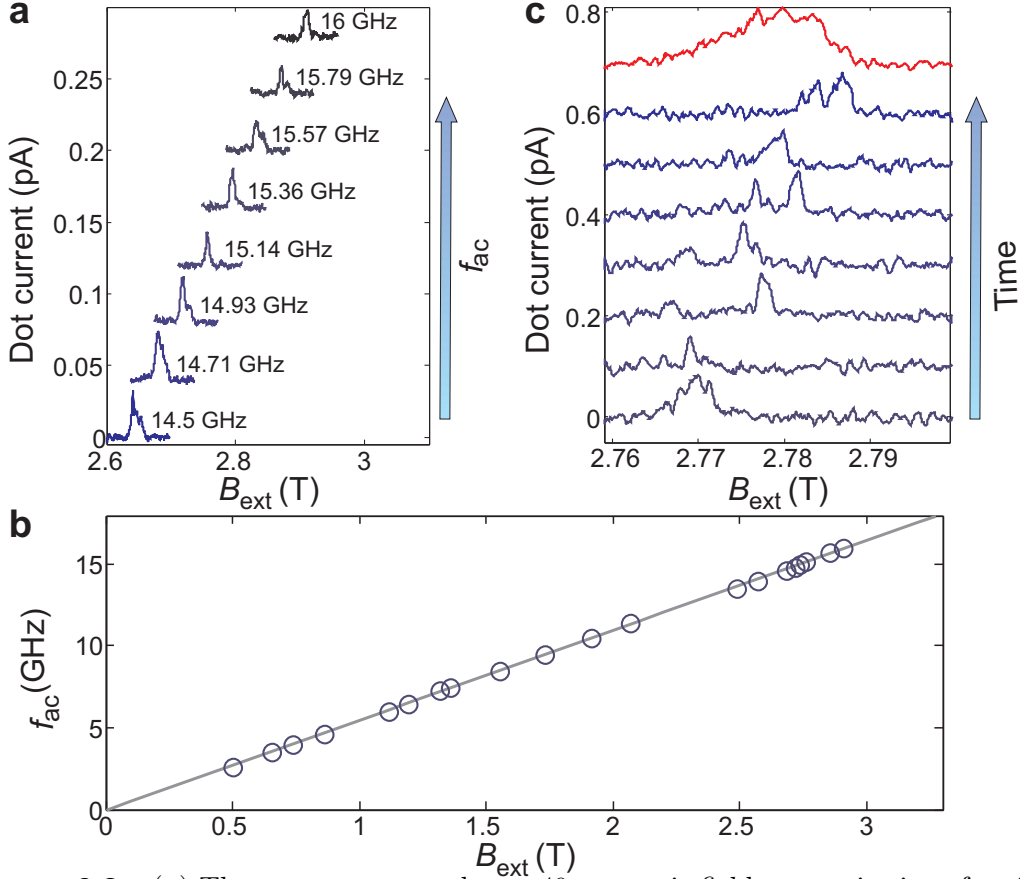


Figure 9.2: (a) The current averaged over 40 magnetic field sweeps is given for eight different excitation frequencies, with a microwave burst length of 150ns. The traces are offset for clarity. The microwave amplitude $V_{\text{mw}} \sim 0.9 - 2.2$ mV depending on the frequency (estimated from the output power of the microwave source and taking into account the attenuation of the coaxial lines and the switching circuit used to create microwave bursts). (b) Position of the resonant response over wider frequency and field ranges ($V_{\text{mw}} \sim 1.2$ mV). Errorbars are smaller than the size of the circles. (c) Individual magnetic field sweeps at $f_{\text{ac}} = 15.2$ GHz measured by sweeping from high to low magnetic field with a rate of 50mT/minute. The traces are offset by 0.1 pA each for clarity. The grey trace is an average over 40 sweeps, including the ones shown and scaled up by a factor of 5.

excitation frequency, we see that the peaks are indeed a few mT wide (see Fig. 9.2c), but the peak positions change in time over a range of ~ 20 mT. Judging from the dependence of the position and shape of the averaged peaks on sweep direction, the origin of this large variation in the nuclear field is most likely feedback of the electron spin on the nuclear spin system [167, 112, 104, 88].

9.4 Rabi oscillations

In order to demonstrate coherent control of the spin, we now vary the length of the microwave bursts, and monitor the current level as a function of burst

9. Coherent control of a single spin with electric fields

duration. In Fig. 9.3a we plot the maximum current per magnetic field sweep as a function of the microwave burst duration, averaged over several sweeps (note that this is a more sensitive method than averaging the traces first and then taking the maximum). The maximum current exhibits clear oscillations as a function of burst length. Fitting with a cosine function reveals a linear scaling of the oscillation frequency with the driving amplitude (Fig. 9.3b). This is the characteristic feature of Rabi oscillations, and proof of coherent control of the electron spin via electric fields.

The highest Rabi frequency we achieved is ~ 4.7 MHz (measured at $f_{ac} = 15.2$ GHz) corresponding to a $\pi/2$ rotation in ~ 55 ns, which is only a factor of two slower than those realized with magnetic driving [104]. Stronger electrical driving was not possible because of photon-assisted-tunneling (a process whereby the electric field excites electrons and lifts spin-blockade, irrespective of whether the spin resonance condition is met). Remarkably small Rabi frequencies could be observed as well. The bottom trace of Fig. 9.3a shows a Rabi oscillation with a period exceeding $1.5\mu s$ (measured at $f_{ac} = 2.6$ GHz). This corresponds to an effective driving field of only about 0.2 mT, ten times smaller than the statistical fluctuations of the nuclear field. The reason the oscillations are nevertheless

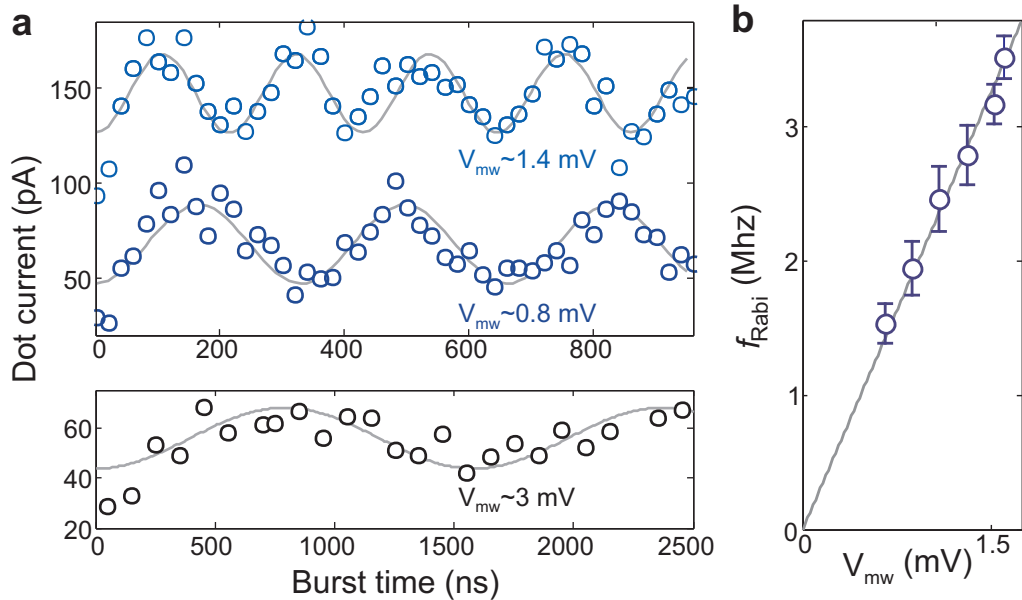


Figure 9.3: (a) Rabi oscillations at 15.2 GHz (blue, average over 5 sweeps) and 2.6 GHz (black, average over 6 sweeps). The two oscillations at 15.2 GHz are measured at different amplitude of the microwaves V_{mw} leading to different Rabi frequencies. The microwave amplitude V_{mw} is estimated from the output power of the microwave source and taking into account the attenuation of the coaxial lines and the switching circuit used to create microwave bursts. (b) Linear dependence of the Rabi frequency on applied microwave amplitude measured at $f_{ac} = 14$ GHz.

9.5 Mechanism

visible is that the dynamics of the nuclear bath is slow compared to the Rabi period, resulting in a slow power law decay of the oscillation amplitude on driving field [142].

9.5 Mechanism

We now turn to the mechanism responsible for resonant transitions between spin states. First, we exclude a magnetic origin since the oscillating magnetic field generated upon excitation of the gate is about more than two orders of magnitude too small to produce the observed response (see section 9.7.2). Next, we have seen that there is in principle a number of ways in which an ac electric field can cause single spin transitions. What is required is that the oscillating electric field give rise to an *effective* magnetic field, $B_{\text{eff}}(t)$, acting on the spin, oscillating in the plane perpendicular to B_{ext} , at frequency $f_{\text{ac}} = g\mu_{\text{B}}|\mathbf{B}_{\text{ext}}|/h$. The g -tensor anisotropy is very small in GaAs so g -tensor modulation can be ruled out as the driving mechanism. Furthermore, in our experiment there is no external magnetic field gradient applied, which could otherwise lead to spin resonance [32]. We are aware of only two remaining possible coupling mechanisms: spin-orbit interaction and the spatial variation of the nuclear field.

In principle, moving the wavefunction in a nuclear field gradient can drive spin transitions [94, 32] as was recently observed [92]. However, the measurement of each Rabi oscillation took more than one hour, much longer than the time during which the nuclear field gradient is constant ($\sim 100\mu\text{s}$ - few s). Because this field gradient and therefore, the corresponding effective driving field slowly fluctuates in time around zero, the oscillations would be strongly damped, regardless of the driving amplitude [92]. Possibly a (nearly) static gradient in the nuclear spin polarization could develop due to electron-nuclear feedback. However, such polarization would be parallel to \mathbf{B}_{ext} and can thus not be responsible for the observed coherent oscillations.

In contrast, spin-orbit mediated driving can induce coherent transitions [34], to be understood as follows. The spin-orbit interaction in a GaAs heterostructure is given by $H_{\text{SO}} = \alpha(p_x\sigma_y - p_y\sigma_x) + \beta(-p_x\sigma_x + p_y\sigma_y)$, where α and β are the Rashba and Dresselhaus spin-orbit coefficient respectively, and $p_{x,y}$ and $\sigma_{x,y}$ are the momentum and spin in the x and y directions (along the [100] and [010] crystal directions respectively). As suggested in [68], the spin-orbit interaction can be conveniently accounted for up to the first order in α, β by applying a (gauge) transformation, resulting in a position-dependent correction to the external magnetic field. This effective magnetic field, acting on the spin, is proportional and

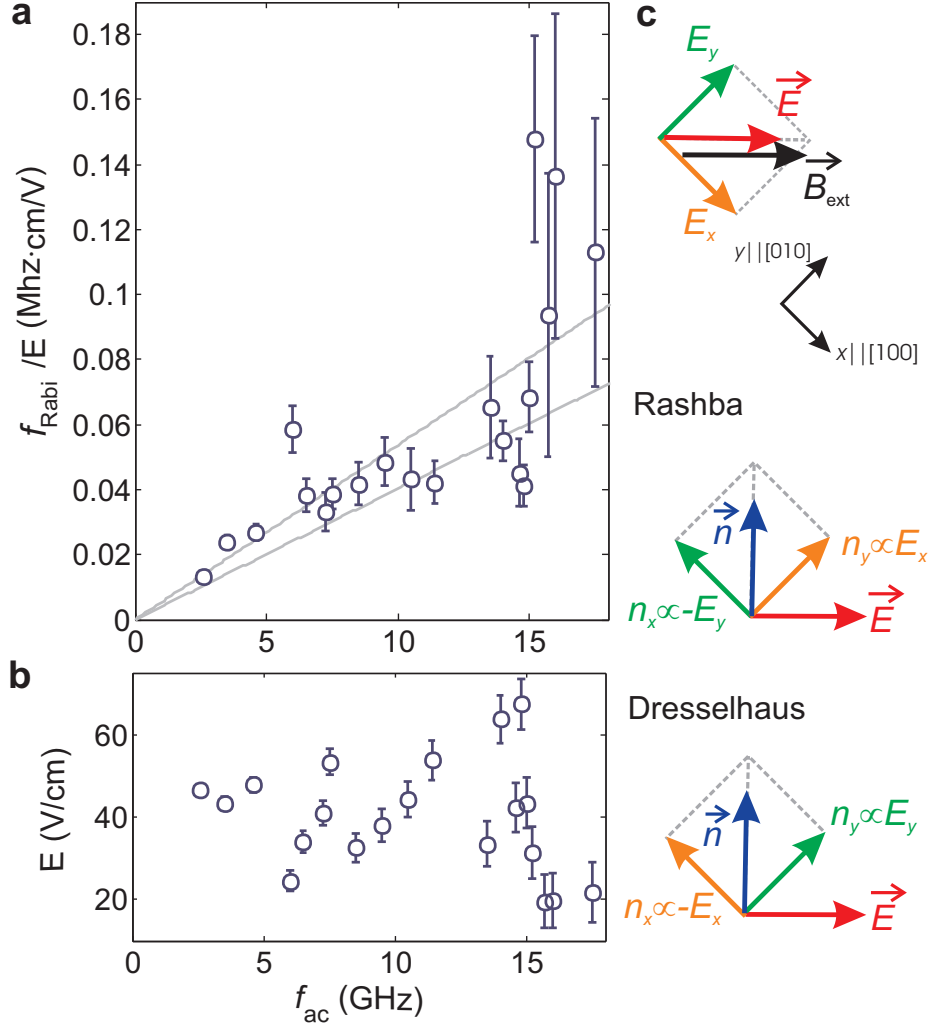


Figure 9.4: (a) Rabi frequency rescaled with the applied electric field for different excitation frequencies. The grey lines are the 95% confidence bounds for a linear fit through the data (weighting the datapoints by the inverse error squared). (b) Estimated electric fields at which the Rabi oscillations of A were measured at the respective excitation frequencies. (c) Construction of the direction of \mathbf{n} resulting from the Rashba and Dresselhaus spin-orbit interaction for an electric field along [110] using equation 1. The coordinate system is set to the crystallographic axis [100] and [010].

orthogonal to the field applied:

$$\mathbf{B}_{\text{eff}}(x, y) = \mathbf{n} \times \mathbf{B}_{\text{ext}}; \quad n_x = \frac{2m^*}{\hbar} (-\alpha y - \beta x); \quad n_y = \frac{2m^*}{\hbar} (\alpha x + \beta y); \quad n_z = 0 \quad (9.1)$$

An electric field $\mathbf{E}(t)$ will periodically and adiabatically displace the electron wave function (see Fig. 9.1b) by $\mathbf{x}(t) = (el_{\text{dot}}^2/\Delta)\mathbf{E}(t)$, so the electron spin will feel an oscillating effective field $\mathbf{B}_{\text{eff}}(t) \perp \mathbf{B}_{\text{ext}}$ through the dependence of \mathbf{B}_{eff} on the

9.5 Mechanism

position. The direction of \mathbf{n} can be constructed from the direction of the electric field as shown in Fig. 9.4c and together with the direction of \mathbf{B}_{ext} determines how effectively the electric field couples to the spin. The Rashba contribution always gives $\mathbf{n} \perp \mathbf{E}$, while for the Dresselhaus contribution this depends on the orientation of the electric field with respect to the crystal axis. Given the gate geometry, we expect the dominant electric field to be along the double dot axis (see Fig. 9.1a) which is here either the $[110]$ or $[\bar{1}\bar{1}0]$ crystallographic direction. For these orientations, the Dresselhaus contribution is also orthogonal to the electric field (see Fig. 9.4c). This is why both contributions will give $\mathbf{B}_{\text{eff}} \neq 0$ and lead to coherent oscillations in the present experimental geometry, where $\mathbf{E} \parallel \mathbf{B}_{\text{ext}}$ (in [92], $\mathbf{E} \perp \mathbf{B}_{\text{ext}}$ and no coherent oscillations were observed which is consistent with the considerations here).

An important characteristic of spin-orbit mediated driving is the linear dependence of the effective driving field on the external magnetic field which follows from Eq. (1) and is predicted in [34, 65]. We aim at verifying this dependence by measuring the Rabi frequency as a function of the resonant excitation frequency (Fig. 9.4a), which is proportional to the external magnetic field. Each point is rescaled by the estimated applied electric field (Fig. 9.4b). Even at fixed output power of the microwave source, the electric field at the dot depends on the microwave frequency due to various resonances in the line between the microwave source and the gate (caused by reflections at the bonding wires and microwave components). However, we use the photon-assisted-tunneling response as a probe for the ac voltage drop across the interdot tunnelbarrier which we convert into an electric field by assuming a typical interdot distance of 100 nm. This allows us to roughly estimate the electric field at the dot for each frequency (see section 9.7.1). Despite the large error bars, which predominantly result from the error made in estimating the electric field, an overall upgoing trend is visible in Fig. 9.4a.

For a quantitative comparison with theory, we extract the spin-orbit strength in GaAs, via the expression of the effective field \mathbf{B}_{eff} perpendicular to \mathbf{B}_{ext} for the geometry of this experiment [34]

$$|\mathbf{B}_{\text{eff}}(t)| = 2|\mathbf{B}_{\text{ext}}| \frac{l_{\text{dot}} e |\mathbf{E}(t)| l_{\text{dot}}}{l_{\text{SO}} \Delta}, \quad (9.2)$$

with l_{SO} the spin-orbit length (for the other definitions see Fig. 9.1b). Here, $l_{\text{SO}}^{-1} = m^*/(\alpha \mp \beta)\hbar$ for the case with the gate symmetry axis along $[\bar{1}\bar{1}0]$ or $[110]$ respectively. Via $f_{\text{Rabi}} = (g\mu_{\text{B}}|\mathbf{B}_{\text{eff}}|)/2\hbar$, the confidence interval of the slope in Fig. 9.4a gives a spin-orbit length of $29 - 39\mu\text{m}$ (with a level splitting Δ in the right dot of 0.9 meV extracted from high bias transport measurements).

Additional uncertainty in l_{SO} is due to the estimate of the interdot distance and the assumption of a homogenous electric field, deformation effects of the dot potential [166] and extra cubic terms in the Hamiltonian [60]. Still, the extracted spin-orbit length is of the same order of magnitude as other reported values for GaAs quantum dots [151, 168, 39].

Both the observed trend of \mathbf{B}_{eff} with f_{ac} and the extracted range for l_{SO} are consistent with our supposition (by elimination of other mechanisms) that spin transitions are mediated by spin-orbit interaction. We note that also for relaxation of single electron spins in which electric field fluctuations from phonons couple to the spin [94, 65, 34], it is by now well established that the spin-orbit interaction is dominant at fields higher than a few 100 mT [40, 77, 151, 168]. It can thus be expected to be dominant for coherent driving as well.

9.6 Conclusions

The electrically driven single spin resonance reported here, combined with the SWAP gate based on the exchange interaction between two neighbouring spins [42], brings all-electrical universal control of electron spins within reach. While the SWAP gate already operates on sub-nanosecond timescales, single-spin rotations still take about one hundred nanoseconds (the main limitation is photon-assisted-tunneling). Faster operations could be achieved by suppressing photon-assisted-tunneling (e.g. by increasing the tunnel barriers or operating deeper into Coulomb blockade), by working at still higher magnetic fields, by using materials with stronger spin-orbit interaction or through optimized gate designs. Furthermore, the electrical control offers the potential for spatially selective addressing of individual spins in a quantum dot array, since the electric field is produced by a local gate. Finally, we note that the spin rotations were realized at magnetic fields high enough to allow for single-shot read-out of a single spin [40], so that both elements can be integrated in a single experiment.

We thank L. P. Kouwenhoven, C. Barthel, E. Laird, I. T. Vink and T. Meunier for discussions; R. Schouten, B. van der Enden and R. Roeleveld for technical assistance. Supported by the Dutch Organization for Fundamental Research on Matter (FOM) and the Netherlands Organization for Scientific Research (NWO).

9.7 Additional material

9.7.1 Estimate of the electric field strength at the dot

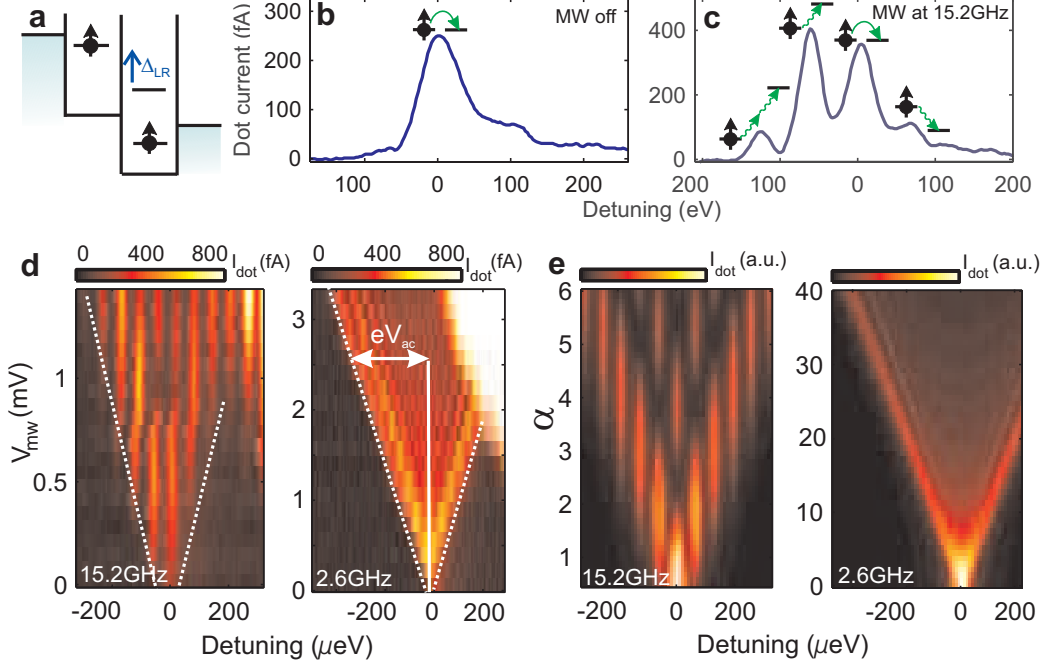


Figure 9.5: (a) Schematic of a double dot with Δ_{LR} (detuning) the difference in the energy the electron needs to access the left or right dot. (b,c) Current through the double dot as a function of detuning with microwaves turned off (b) and on (c). (d) Measured current as a function of detuning Δ_{LR} and microwave amplitude V_{mw} at the gate at $f_{ac} = 15.2$ GHz and 2.6 GHz (applied in continuous wave). The external magnetic field is zero and therefore spin blockade is lifted due to mixing of the spin states through the fluctuating nuclear field[85]. At higher microwave amplitude ($V_{mw} > 0.5$ mV and 1.5 mV respectively), the transition to the right dot triplet state is also visible (in the upper right corner). V_{mw} is determined by the estimated attenuation of the coaxial lines and the switching circuit used to create microwave bursts. (e) Simulated current as a function of detuning and $\alpha = eV_{ac}/(hf_{ac})$ (h Planck's constant) for $f_{ac} = 15.2$ GHz and 2.6 GHz respectively. It reproduces the linear envelope of the measured current as well as, qualitatively, a modulation of the current amplitude in detuning. However the asymmetry with respect to detuning visible in (d) as well as the observed overall increase of the current with V_{mw} is not captured in this model.

The electric field generated at the dot by excitation of a gate is difficult to quantify exactly. While we can estimate the power that arrives at the sample holder from the output power of the microwave source and the measured attenuation in the line, the power that arrives at the gate is generally somewhat less (the coax is connected to the gate via bonding wires). In addition, it is difficult to accurately determine the conversion factor between the voltage modulation of the

9. Coherent control of a single spin with electric fields

gate and the electric field modulation of the dot. We here estimate the voltage drop across the interdot tunnel barrier via photon-assisted-tunneling (PAT) measurements, and extract from this voltage drop a rough indication of the electric field at the dot.

The leakage current through the double quantum dot in the spin blockade regime as a function of the detuning Δ_{LR} (defined in Fig. 9.5a) shows at $B_{\text{ext}} = 0\text{ T}$ a peak at $\Delta_{\text{LR}} = 0$ due to resonant transport and a tail for $\Delta_{\text{LR}} > 0$ due to inelastic transport (emission of phonons) [85]) (Fig. 9.5b). Excitation of the right side gate induces an oscillating voltage drop across the tunnel barrier between the two dots, which leads to side peaks at $\Delta_{\text{LR}} = nhf_{\text{ac}}, n = \pm 1, \pm 2, \dots$ away from the resonant peak (Fig. 9.5c). These side peaks are due to electron tunnelling in combination with absorption or emission of an integer number of photons, a process which is called photon-assisted-tunneling. In the limit where hf_{ac} is much smaller than the linewidth of the states $h\Gamma$ (Γ is the tunnel rate) the individual sidepeaks cannot be resolved, whereas for higher frequencies they are clearly visible (see Fig. 9.5d).

More quantitatively we describe PAT by following reference [146]. An ac voltage drop $V(t) = V_{\text{ac}} \cos 2\pi f_{\text{ac}} t$ across the interdot tunnel barrier modifies the tunnel rate through the barrier as $\tilde{\Gamma}(E) = \sum_{n=-\infty}^{+\infty} J_n^2(\alpha) \Gamma(E + nhf_{\text{ac}})$. Here, $\Gamma(E)$ and $\tilde{\Gamma}(E)$ are the tunnel rates at energy E with and without ac voltage, respectively; $J_n^2(\alpha)$ is the square of the n th order Bessel function of the first kind evaluated at $\alpha = (eV_{\text{ac}})/hf_{\text{ac}}$, which describes the probability that an electron absorbs or emits n photons of energy equal to hf_{ac} (with $-e$ the electron charge). Fig. 9.5e shows the current calculated from this model including a lorentzian broadening of the current peaks. A characteristic of the n -th Bessel function $J_n(\alpha)$, important here, is that it is very small for $\alpha \ll n$ (i.e. when $eV_{\text{ac}} \ll nhf_{\text{ac}}$) and starts to increase around $\alpha \approx n$, implying that the number of side peaks is approximately $eV_{\text{ac}}/hf_{\text{ac}}$. This results in a linear envelope visible in Fig. 9.5e.

We extract eV_{ac} as the width of the region with non-zero current measured at fixed microwave frequency f_{ac} and amplitude V_{mw} . Instead of this width, we can take equivalently the number of side peaks times hf_{ac} (this is possible at frequencies high enough such that individual side peaks are resolved). A reasonable estimate of the error made in determining eV_{ac} is $\pm hf_{\text{ac}}$. Another method to extract V_{ac} is to determine the slope of the envelope (for which a threshold current needs to be chosen) of the PAT response (see Fig. 9.5d). Varying the threshold gives a spread in the slope which defines the error of this method. We note that within the error bars both methods give the same result.

In order to estimate from V_{ac} the amplitude of the oscillating electric field at the dot, $|E|$, we assume that this voltage drops linearly over the distance be-

9.7 Additional material

tween the two dot centers (a rough approximation), which is approximately 100 nm. This estimate is used in Fig. 9.4a, and in the approximate determination of the spin orbit length. Note that the uncertainty in this estimate of the spin-orbit length only affects the overall scaling in Fig. 4a, but not the fact that there is an up-going trend.

9.7.2 Upper bound on the ac magnetic field strength at the dot

The oscillating gate voltage produces an oscillating electric field at the dot. Here we determine an upper bound on the oscillating magnetic field that is unavoidably generated as well. Since the distance from the gate to the dot is much smaller than the wavelength (20 GHz corresponds to 1.5 cm), we do this in the near-field approximation, where magnetic fields can only arise from currents (displacement currents or physical currents).

An oscillating current can flow from the right side gate to ground via the 2DEG, the coplanar stripline [104], or the neighbouring gates (all these elements are capacitively coupled to the right side gate). We first consider the case of the stripline. The right side gate is about 100nm wide and overlaps with the coplanar stripline over a length of about 10 μm , giving an overlap area of $\approx (1\mu\text{m})^2$. The gate and stripline are separated by a 100 nm thick dielectric (calixerene[44], $\epsilon_r = 7.1$), which results in a capacitance of 0.6 fF. For a maximum voltage of 10 mV applied to the right side gate and a microwave frequency of 20 GHz, this gives a maximum displacement current through this capacitor of $\sim 1\mu\text{A}$. This is an upper bound as we neglect all other impedances in the path to ground. Even if this entire current flowed at a distance to the dot of no more than 10 nm (whether in the form of displacement currents or physical currents), it would generate a magnetic field B_{ac} of only $\approx 0.02\text{mT}$, more than two orders of magnitude too small to explain the observed Rabi oscillations. In reality, the displacement current is distributed along the length of the gate, and most of the current through the gate and stripline flows at a distance very much greater than 10 nm from the dot, so B_{ac} is still much smaller than 0.02 mT. The maximum magnetic field resulting from capacitive coupling to the other gates and to the 2DEG is similarly negligible.

It is also instructive to compare the power that was applied to the gate for electric excitation of the spin with the power that was applied to the micro-fabricated stripline for magnetic excitation [104]. For the shortest Rabi periods observed here (220 ns), the power that arrived at the sample holder was less

9. Coherent control of a single spin with electric fields

than ≈ -36 dBm (the output power of the microwave source minus the attenuation of the microwave components in between source and sample holder, measured at 6 GHz – at higher frequencies, the attenuation in the coax lines will be still higher). In order to achieve this Rabi frequency through excitation of the stripline, more than 100 times more power (≈ -14 dBm) was needed directly at the stripline[104].

The upper bounds we find for the oscillating magnetic field generated along with the electric field are thus much smaller than the field needed to obtain the measured Rabi frequencies of a few MHz. We therefore exclude magnetic fields as a possible origin for our observations.

Chapter 10

Conclusions and outlook

In this chapter, we summarize the work presented in this thesis, together with the most important achievements in the research field of spin-qubits in quantum dots. We give suggestions for improving the existing manipulation techniques and coherence properties of single spins confined in quantum dots. These future opportunities will be reviewed in the context of the basic requirements essential to build a scalable quantum computer based on electron spins.

10.1 Current status

The experimental achievements described in this thesis can be summarized as follows:

- We can rotate a single electron spin via magnetic resonance about any arbitrary axis to any predefined superposition state with an accuracy of 75% for a π -rotation with initial state $|\uparrow\rangle$. The fastest π -rotation takes about 60 ns.
- We can rotate a single electron spin with an oscillating electric field to any predefined superposition state. The fastest π -rotation takes about 100 ns.
- When performing time-averaged experiments, the electron spin dephases in ~ 30 ns, which is caused by the statistical fluctuations of the nuclear field.
- Electron spin dephasing due to the nuclear field uncertainty can be largely reversed by a spin-echo pulse. The echo coherence time $T_{2,\text{echo}}$ is about $0.44\mu\text{s}$. The large difference between $T_{2,\text{echo}}$ and T_2^* is due to the long correlation time of the nuclear spin bath.
- The decay of the magnetically induced Rabi oscillations of a single spin follows a power-law instead of the usual exponential decay, and is further shifted in phase by $\pi/4$. This is due to the long correlation time of the nuclear spin bath compared to the duration of a π -rotation.
- At magnetic fields below a few mT, the two-electron singlet and triplet states in a double quantum dot are hybridized and therefore a leakage current flows in the spin-blockade regime. This hybridization is due to the different nuclear fields in the two quantum dots. The hybridization between the singlet S and $m_z = 0$ triplet state T_0 can be suppressed by increasing the tunnel coupling between the two quantum dots. The hybridization between $T_{+/-}$ and the singlet state is suppressed by application of a magnetic field more than a few mT.

We review these results in combination with other achievements in the field of spin qubits in quantum dots, including single-shot read-out of the electron spin and the demonstration of the $\sqrt{\text{SWAP}}$ -gate on two-electron spin states. Altogether, all the proof-of-principle experiments have been demonstrated for the list of basic ingredients necessary for encoding a logical quantum bit in an electron spin [12]. For scalable quantum computation, the demonstrated one and two-electron spin gates do not meet the required accuracy threshold, but there is

10.2 Outlook

sufficient room for improvement, as we will see in the discussion below. With the existing techniques, further progress in the field of spin-based quantum information is already possible like the demonstration of the CNOT-gate or performing simple quantum algorithms. Furthermore, by combining the available techniques, experiments are possible that address fundamental quantum properties of spins in the solid-state environment. These include the demonstration of entanglement [137], performing and reversing weak quantum measurements [169, 170] and the manipulation of the nuclear spin bath via the electron spin [88, 161].

An important question is whether a quantum computer based on electron spins in quantum dots is feasible. In order to make scalable quantum computation with electron spins possible, the error per gate operation p should be smaller than a threshold, which allows for error correction. An error threshold of 10^{-4} [171, 172] is often quoted as the threshold to be achieved in experimental quantum computing. This estimate assumes that classical, local information processing requires only a few time steps of the quantum computer. Furthermore, this threshold is only possible if spins can be shuttled with very low error or if long-distance communication can be performed. It is also possible to transport quantum information via nearest-neighbor interactions, like proposed in [20], but this requires a much lower error threshold of $p = 10^{-6}$ [173]. We note that a higher threshold up to 3% is allowed but this requires many more ancilla qubits and other optimizations [174].

10.2 Outlook

Here, we give suggestions for improving the existing manipulation techniques and coherence properties of single spins confined in quantum dots. These future opportunities will be reviewed in the context of the basic requirements essential to build a scalable quantum computer based on electron spins.

10.2.1 Longer decoherence times

Reducing the nuclear field fluctuations

The dephasing time of ~ 10 -30 ns due to the nuclear field fluctuations can be extended through polarization of the nuclear spins. However, to extend the dephasing time by an order of magnitude, a polarization of above 99% is required, but the best result so far reached is only $\sim 60\%$ in quantum dots [167]. Another and probably more promising approach is to prepare the nuclear spin system in a well-known and well-defined state before performing operations. Namely, if we exactly know the nuclear field in the z -direction h_z , only a known dephasing

will occur. Similar reasoning holds for the two-qubit operations if the difference δh_z of h_z in the two dots is known. In principle, measuring the response when performing ESR on one spin or SWAP on two spins is a measurement of respectively h_z or δh_z [91, 88, 89]. Performing these measurements in a clever way can lead to sufficient reduction of the h_z or δh_z distribution to achieve so-called state narrowing of the nuclear spin bath. Another approach is to exploit feedback from the electron spin to the nuclear spin bath. By tuning the double quantum dot properly close to S/T_+ and S/T_- degeneracies, spin can be transferred to the nuclear spin bath leading to dynamic nuclear polarization. This polarization process can be made self-limiting by balancing the polarization process the two directions. It is predicted that this type of feedback can reduce the fluctuations in the nuclear field significantly [161].

Encoding in a decoherence free subspace

Apart from encoding the qubit in the Zeeman split spin states, it is also possible to encode in the two-electron singlet S and $m_z = 0$ triplet state T_0 [175]. These states are robust against nuclear-spin related dephasing, provided that the qubit splitting J is much larger than the amplitude of the nuclear field fluctuations. This should be combined with a sufficiently high magnetic field to suppresses leakage to the $T_{+/-}$ state. Both requirements can be realized easily. Single qubit rotations can in principle be performed via a magnetic field gradient and a phase-gate via the Heisenberg interaction (the latter has been demonstrated in Ref. [42]). Two-qubit operations can be realized by exploiting the capacitive coupling between two double quantum dots or by coupling the qubit to a resonant cavity mode [176]. The disadvantage of this qubit basis is dephasing due to fluctuations in the qubit splitting J caused by charge fluctuations.

Different materials and systems

Most experiments with electron spins in quantum dots have so far been performed with III-V semiconductor materials such as GaAs, InAs or InP, in which all the atoms have non-zero nuclear magnetic moments. The only semiconductors that have stable isotopes without nuclear magnetic moments are the elemental ones: C, Si, and Ge. The spin decoherence time in these isotopically purified materials is expected to be limited by the spin-orbit interaction (SOI), and could therefore be very long. Namely, theory predicts that in leading order (see also section 3.2) the spin-orbit limited decoherence time is similar as the relaxation time [67], which is in GaAs quantum dots beyond one second at 1 T magnetic field [78]. Furthermore, the SOI is even weaker in Si and C than in GaAs. Experimental progress in developing C and Si quantum dot devices is significant, and includes the re-

10.2 Outlook

alization of gate-defined double quantum dots in carbon nanotubes [177, 178], Si/Ge 2DEGs [179] and Ge/Si nanowires [180]. Another promising host for the electron spin might be a single layer of graphene [181], but it is not yet clear whether gated dots can be defined in this structure. We remark that in Si or C systems, the orbital ground state is two-fold valley degenerate, which can form an important decoherence source [182]. This degeneracy can in principle be broken under certain boundary conditions, which has been demonstrated in Si/SiGe quantum wells [183].

Apart from gate-defined dots, alternatives for confining electrons are donors or impurities like nitrogen-vacancy centers in diamond (N-V centers) or shallow donor states in Si. The coherence properties of these systems are very good. A spin decoherence time of 60 ms was reported in phosphorous donors of isotopically-purified ^{28}Si [184], and the longest decoherence time reported for N-V centers was 0.35-0.5 ms [22, 185]. Disadvantages of these systems are the lack of flexibility in tuning the potential landscape in-situ, and the long distance between the spins making it difficult to couple them. A solution to this is implantation of donors close to each other, and considerable progress is made with the implantation of phosphorous donors in Si [186] as well as N-V centers in diamond [187, 188]. The major advantage of N-V center qubits is the prospect for long-distance spin interactions via photons.

A completely different approach in overcoming spin decoherence is to use the nuclear spins as a storage medium for quantum information [19]. The decoherence time of the nuclear spins are expected to be very long. Coherent oscillations of a single nuclear spin were observed via the electron spin in a N-V center [22] and more recently, quantum information was stored in one N-V center nuclear spin [189].

10.2.2 Improving single spin rotations (one-qubit gate)

The fastest demonstrated single qubit operation has been performed in 27 ns ($\pi/2$ -rotation, see chapter 6) with an estimated accuracy of 75% for a π -rotation with initial state $|\uparrow\rangle$. The accuracy of this gate is limited by spin dephasing due to the nuclear field fluctuations. By reducing this nuclear field uncertainty a factor of ten (see previous section) the gate fidelity can exceed 99%. Faster rotations are required as well in order to achieve the error threshold. If we assume a decoherence time of 10 μs , a spin flip should be performed in 1 ns. It is unlikely that this will be realized via magnetic resonance because an oscillating field of about 75 mT is required. Possibly, faster rotations can be realized via electric resonance if a very strong magnetic field gradient, perpendicular to the

external field, can be applied [32]. An effective field gradient can in principle also be realized by polarizing the nuclear field in one of the two quantum dots and subsequently, rotate this nuclear field via a NMR pulse by π . The effect of NMR excitation signals applied to the nuclear spins in quantum dots has been observed ([108] and Delft, not published) as well as dot-selective polarization (Delft, not published). Furthermore, a nuclear field of 4 T obtained via dynamic nuclear polarization in the spin blockade regime has been reported in Ref. [167]. To estimate the required gradient, we use the numbers from Ref. [92], where hyperfine-mediated (but incoherent) electron spin resonance was observed. For a (random) nuclear field difference between the two dots of ~ 4 mT, the estimated maximum Rabi frequency was about 1.8 MHz. This implies that a π -rotation in 0.5 ns is possible with a 4 T field difference between the two dots. Another promising approach for achieving fast single-spin rotations ($\pi/2$ -rotation in about 1 ns) with a very high precision of $\sim 99.9\%$ is to combine a magnetic field gradient with a switchable Heisenberg interaction with the spin of an ancilla qubit [190].

In dots where besides an electron also holes are confined, in principle very fast optical manipulation of the spin is possible with laser pulses only. Spin $\pi/2$ -rotations in 5.1 ps were demonstrated in GaAs quantum wells [191]. The mechanism for this process relies on the generation of an effective magnetic field by a below-bandgap laser pulse through the optical Stark effect [35]. Finally, we remark that single-spin rotations are not necessarily required for universal quantum computation with spins. In principle, with the Heisenberg interaction alone any quantum computer circuit can be implemented, at the expense of increasing the number of devices and the number of computational steps [192].

10.2.3 Improving the $\sqrt{\text{SWAP}}$ -gate (two-qubit gate)

The two-qubit $\sqrt{\text{SWAP}}$ -gate has been performed in 180 ps [42], allowing for 7000 operations within the reported decoherence time of 1.2 μs . Even shorter gate operation times down to 40 ps are in principle possible because a singlet-triplet splitting of 120 μeV can be achieved. The fidelity of the $\sqrt{\text{SWAP}}$ -gate is limited by nuclear-spin [152] and charge-related dephasing [193]. The latter can be understood from the fact that the singlet-triplet splitting J depends on the level detuning and tunnel coupling between the two dots; both are susceptible to charge noise. In order to achieve higher fidelity for the two-qubit gate, one should use higher J [152] and work in a regime where J is independent of ϵ [194], or by further reducing charge noise (see also section 2.2). We note that the spin-orbit interaction can also lead to gate errors due to a small spin precession when an electron tunnels between the dots. This can be eliminated by using

10.2 Outlook

time-symmetric pulse shapes [195, 196, 197].

10.2.4 Improving spin read-out

Single-shot read-out of the electron spin state has been performed via energy-selective tunneling with a fidelity of 82% [40]. The read-out fidelity can be improved by increasing the measurement bandwidth. This is possible by measuring the signal of the charge detector (QPC) via RF reflection techniques [48] or using a cryogenic pre-amplification stage [47]. A fidelity beyond 99% can be achieved with a 1 MHz measurement bandwidth (assuming $T_1=1$ ms). We remark that the energy-selective read-out technique only works at high magnetic fields (demonstrated so far only for fields larger than 8 T), which makes it difficult to combine with magnetic ESR. At low field, read-out techniques in the singlet-triplet basis are available, like spin-selective tunneling to the reservoir [131] or tunneling to a second quantum dot [136]. As discussed in chapter 4, the latter can be used as well for read-out of spin Zeeman states, provided that a magnetic field gradient over the two dots is present. The disadvantage of this method is the requirement of an extra (ancilla) quantum dot.

10.2.5 Scaling

For near-future experiments, extending the current gate-design to more than two dots is likely to be realized in practice. In fact, tunable GaAs triple quantum dots have been reported [198, 199]. In order to build a quantum computer, consisting of thousands of qubits, it is probably not just sufficient to follow the same strategy. First of all, expanding the quantum dot arrays in a second and maybe even a third dimension will be required. Secondly, communication between distant qubits via the Heisenberg interaction is practically difficult to realize, and also more time-consuming and susceptible to errors. To overcome this, channels or arrays of quantum dots can be developed to shuttle electrons [175]. Also, if spins can be coupled to photons, long-range interactions can be mediated via virtual photons in a cavity (see discussion below). An important practical difficulty in scaling will be the task of tuning all the quantum dots to the few-electron regime, which is very demanding for a large number of gates that do not couple only to one dot or barrier. A solution is to make clusters with only a few coupled gate-defined quantum dots in combination with long-distance communication between these clusters by electron shuttling or photons.

10.2.6 Long-distance communication

Communication between distant qubits in arrays of quantum dots is possible by performing multiple SWAP operations on pairs of electron spins. However, nearest-neighbor communication requires more than a factor 10^2 lower error threshold compared to qubit arrays where long-distance communication is possible [9, 173]. This communication channel could be provided by photons if the qubit can be coupled to photons. This is possible by exploiting the optical selection rules in optically accessible dots (such as dots defined in nanowires, self-assembled dots, or CdSe dots) via polarized laser and cavity fields [31, 200]. However, in gate-defined quantum dots holes are not confined, making optical access difficult. We note that the magnetic moment of the electron spin is coupled magnetically to a cavity photon but this coupling is very weak.

A stronger coupling of the spin to a cavity mode can be achieved electrically, if in some way the electron charge is coupled to its spin. For example, one can use a delocalized state in a double quantum dot in combination with ESR that is resonant only in one dot [201]. Another possibility is to exploit the spin-orbit interaction, present in most semiconductor structures. In GaAs, this coupling is too weak for coupling to a single cavity photon. Namely, an electric field amplitude of 6000 V/m is required to realize a driving frequency of 4.5 MHz at a magnetic field of ~ 3 T (see chapter 9). The one-photon vacuum field of a coplanar waveguide cavity is only 0.2 V/m [202], and higher values up to 25 V/m might be achievable using smaller cavity dimensions [203]. In InAs devices, however, the SOI is expected to be strong enough to couple two quantum dots via a virtual photon in a transmission line [204].

Alternatively, spin-charge coupling can be realized via an applied or nuclear field gradient. An electric field amplitude of ~ 6000 V/m was required for electrically driven spin resonance with driving frequency ~ 1.8 MHz, mediated by a magnetic field difference of 4 mT between the two dots [92]. In order to obtain similar driving frequencies with a vacuum field of 25 V/m, a field difference as large as 1 T is required.

When using the two-electron spin state S/T_0 as a basis, the qubit is very strongly coupled to the electron orbital. This makes capacitive coupling between qubits possible [176, 175], or via a resonant cavity if a field gradient is present [203].

10.3 Conclusion

We can state that the spin-qubit research field has come to a remarkable stage in a relatively short time, and offers a lot of future opportunities in different areas of physics and technology. Current challenges comprise overcoming the practical hurdles when combining existing techniques as well as improving current manipulation schemes and tailoring the disturbing environment like charge noise and the nuclear spins. On the the other hand, one could pursue realizing spin manipulation techniques in different materials and combine systems like quantum dots and cavities to achieve long-distance communication. We expect that all these research efforts will deliver interesting results in the different fields of spin physics, material science and quantum optics. Altogether, by extrapolating the rapid developments in these areas it seems that making a spin-based quantum computer is in principle feasible, but whether it will ever be built remains an open question.

Bibliography

- [1] J. Plantenberg, P. de Groot, C. Harmans, and J. Mooij, “Demonstration of controlled-NOT quantum gates on a pair of superconducting quantum bits”, *Nature*, vol. 447, pp. 836–839, 2007.
- [2] W. Lu, Z. Q. Ji, L. Pfeiffer, K. W. West, and A. J. Rimberg, “Real-time detection of electron tunnelling in a quantum dot”, *Nature*, vol. 423, pp. 422–425, 2003.
- [3] D. Eigler and E. Schweizer, “Positioning single atoms with a scanning tunnelling microscope”, *Nature*, vol. 344, pp. 524–526, 1990.
- [4] L. Hackermüller, K. Hornberger, B. Brezger, A. Zeilinger, and M. Arndt, “Decoherence of matter waves by thermal emission of radiation”, *Nature*, vol. 427, p. 711, 2004.
- [5] W. Marshall, C. Simon, R. Penrose, and D. Bouwmeester, “Towards Quantum Superpositions of a Mirror”, *Phys. Rev. Lett.*, vol. 91, p. 130401, 2003.
- [6] M. Brune, S. Haroche, J. M. Raimond, L. Davidovich, and N. Zagury, “Manipulation of photons in a cavity by dispersive atom-field coupling: Quantum-nondemolition measurements and generation of “schrödinger cat” states”, *Phys. Rev. A*, vol. 45, 1992.
- [7] A. K. Ekert, “Quantum cryptography based on bell’s theorem”, *Phys. Rev. Lett.*, vol. 67, 1991.
- [8] P. Shor, “Algorithms for quantum computation: Discrete logarithms and factoring”, *IEEE Symposium on Foundations of Computer Science*, pp. 124–134, 1994.
- [9] M. A. Nielsen and I. L. Chuang, *Quantum Computation and Quantum Information*, Cambridge Univ. Press, Cambridge, 2000.

- [10] P. Richard, “Feynman. Simulating physics with computers”, *International Journal of Theoretical Physics*, vol. 21, pp. 467–488, 1982.
- [11] S. Lloyd, “Universal Quantum Simulators”, *Science*, vol. 273, pp. 1073–8, 1996.
- [12] D. P. DiVincenzo, “The physical implementation of quantum computation”, *Fortschritte Der Physik-Progress of Physics*, vol. 48, pp. 771–783, 2000.
- [13] Q. A. Turchette, C. J. Hood, W. Lange, H. Mabuchi, and H. J. Kimble, “Measurement of conditional phase shifts for quantum logic”, *Phys. Rev. Lett.*, vol. 75, 1995.
- [14] G. Brennen, C. Caves, P. Jessen, and I. Deutsch, “Quantum Logic Gates in Optical Lattices”, *Phys. Rev. Lett.*, vol. 82, pp. 1060–1063, 1999.
- [15] J. Cirac and P. Zoller, “Quantum Computations with Cold Trapped Ions”, *Phys. Rev. Lett.*, vol. 74, pp. 4091–4094, 1995.
- [16] I. Chuang, N. Gershenfeld, and M. Kubinec, “Experimental Implementation of Fast Quantum Searching”, *Phys. Rev. Lett.*, vol. 80, pp. 3408–3411, 1998.
- [17] J. Mooij, T. Orlando, L. Levitov, L. Tian, C. van der Wal, and S. Lloyd, “Josephson Persistent-Current Qubit”, *Science*, vol. 285, pp. 1036–1039, 1999.
- [18] S. Lyon, “Spin-based quantum computing using electrons on liquid helium”, *Phys. Rev. A*, vol. 74, p. 52338, 2006.
- [19] B. E. Kane, “A silicon-based nuclear spin quantum computer”, *Nature*, vol. 393, p. 133, 1998.
- [20] D. Loss and D. P. DiVincenzo, “Quantum computation with quantum dots”, *Phys. Rev. A*, vol. 57, p. 120, 1998.
- [21] R. Vrijen, E. Yablonovitch, K. Wang, H. W. Jiang, A. Balandin, V. Roychowdhury, T. Mor, and D. DiVincenzo, “Electron-spin-resonance transistors for quantum computing in silicon-germanium heterostructures”, *Phys. Rev. A*, vol. 62, 2000.

BIBLIOGRAPHY

- [22] F. Jelezko, T. Gaebel, I. Popa, A. Gruber, and J. Wrachtrup, “Observation of coherent oscillations in a single electron spin”, *Phys. Rev. Lett.*, vol. 92, p. 076401, 2004.
- [23] L. M. K. Vandersypen, M. Steffen, G. Breyta, C. S. Yannoni, M. H. Sherwood, and I. L. Chuang, “Experimental realization of shor’s quantum factoring algorithm using nuclear magnetic resonance”, *Nature*, vol. 414, p. 883, 2001.
- [24] J. Chiaverini, D. Leibfried, T. Schaetz, M. Barrett, R. Blakestad, J. Britton, W. Itano, J. Jost, E. Knill, C. Langer, *et al.*, “Realization of quantum error correction”, *Nature*, vol. 432, pp. 602–605, 2004.
- [25] H. Haffner, W. Hansel, C. Roos, J. Benhelm, D. Chek-al Kar, M. Chwalla, T. Korber, U. Rapol, M. Riebe, P. Schmidt, *et al.*, “Scalable multiparticle entanglement of trapped ions.”, *Nature*, vol. 438, pp. 643–6, 2005.
- [26] M. Barrett, J. Chiaverini, T. Schaetz, J. Britton, W. Itano, J. Jost, E. Knill, C. Langer, D. Leibfried, R. Ozeri, *et al.*, “Deterministic quantum teleportation of atomic qubits”, *resonance*, vol. 396, pp. 52–55, 1998.
- [27] W. Hensinger, S. Olmschenk, D. Stick, D. Hucul, M. Yeo, M. Acton, L. Deslauriers, C. Monroe, and J. Rabchuk, “T-junction ion trap array for two-dimensional ion shuttling, storage, and manipulation”, *Applied Physics Letters*, vol. 88, p. 034101, 2006.
- [28] D. Stick, W. K. Hensinger, S. Olmschenk, M. J. Madsen, K. Schwab, and C. Monroe, “Ion trap in a semiconductor chip”, *Nature Phys.*, vol. 2, p. 36, 2006.
- [29] S. A. Wolf, D. D. Awschalom, R. A. Buhrman, J. M. Daughton, S. von Molnar, M. L. Roukes, C. A. Y., and D. M. Treger, “Spintronics: A spin-based electronics vision for the future”, *Science*, vol. 294, p. 1488, 2001.
- [30] D. Awschalom and M. Flatté, “Challenges for semiconductor spintronics”, *Nature Physics*, vol. 3, pp. 153–159, 2007.
- [31] A. Imamoglu, D. D. Awschalom, G. Burkard, D. P. DiVincenzo, D. Loss, M. Sherwin, and A. Small, “Quantum information processing using quantum dot spins and cavity qed”, *Phys. Rev. Lett.*, vol. 83, p. 4204, 1999.
- [32] Y. Tokura, W. G. Van der Wiel, T. Obata, and S. Tarucha, “Coherent single electron spin control in a slanting zeeman field”, *Phys. Rev. Lett.*, vol. 96, p. 047202, 2006.

- [33] Y. Kato, R. C. Myers, D. C. Driscoll, A. C. Gossard, J. Levy, and D. D. Awschalom, “Gigahertz Electron Spin Manipulation Using Voltage-Controlled g-Tensor Modulation”, *Science*, vol. 299, p. 1201, 2003.
- [34] V. N. Golovach, M. Borhani, and D. Loss, “Electric-dipole-induced spin resonance in quantum dots”, *Phys. Rev. B*, vol. 74, p. 165319, 2006.
- [35] C. Cohen-Tannoudji and J. Dupont-Roc, “Experimental study of zeeman light shifts in weak magnetic fields”, *Phys. Rev. A*, vol. 5, 1972.
- [36] T. Fujisawa, Y. Tokura, and Y. Hirayama, “Energy relaxation process in a quantum dot studied by DC current and pulse-excited current measurements”, *Physica B*, vol. 298, pp. 573–579, 2001.
- [37] M. Field, C. G. Smith, M. Pepper, D. A. Ritchie, J. E. F. Frost, G. A. C. Jones, and D. G. Hasko, “Measurements of coulomb blockade with a non-invasive voltage probe”, *Phys. Rev. Lett.*, vol. 70, 1993.
- [38] L. M. K. Vandersypen, J. M. Elzerman, R. N. Schouten, L. H. Willems van Beveren, R. Hanson, and L. P. Kouwenhoven, “Real-time detection of single-electron tunneling using a quantum point contact”, *Appl. Phys. Lett.*, vol. 85, p. 4394, 2004.
- [39] R. Hanson and G. Burkard, “Universal set of quantum gates for double-dot spin qubits with fixed interdot coupling”, *Phys. Rev. Lett.*, vol. 98, p. 050502, 2007.
- [40] J. M. Elzerman, R. Hanson, L. H. W. Willems van Beveren, B. Witkamp, L. M. K. Vandersypen, and L. P. Kouwenhoven, “Single-shot read-out of an individual electron spin in a quantum dot”, *Nature*, vol. 430, p. 431, 2004.
- [41] T. Fujisawa, D. G. Austing, Y. Tokura, Y. Hirayama, and S. Tarucha, “Allowed and forbidden transitions in artificial hydrogen and helium atoms”, *Nature*, vol. 419, p. 278, 2002.
- [42] J. R. Petta, A. C. Johnson, J. M. Taylor, E. A. Laird, A. Yacoby, M. D. Lukin, C. M. Marcus, M. P. Hanson, and A. C. Gossard, “Coherent manipulation of coupled electron spins in semiconductor quantum dots”, *Science*, vol. 309, pp. 2180–2184, 2005.
- [43] L. Willems van Beveren, *Electron spins in few-electron lateral quantum dots*. PhD thesis, Delft University of Technology, 2006. Online available from <http://www.library.tudelft.nl/dissertations/>.

BIBLIOGRAPHY

- [44] A. Holleitner, “Fabrication of coupled quantum dots for multiport access”, *Applied Physics Letters*, vol. 82, p. 1887, 2003.
- [45] P. Mooney, “Deep donor levels (DX centers) in III-V semiconductors”, *Journal of Applied Physics*, vol. 67, p. R1, 1990.
- [46] M. Pioro-Ladrière, J. Davies, A. Long, A. Sachrajda, L. Gaudreau, P. Zawadzki, J. Lapointe, J. Gupta, Z. Wasilewski, and S. Studenikin, “Origin of switching noise in GaAs/ Al_xGa_{1-x} As lateral gated devices”, *Phys. Rev. B*, vol. 72, p. 115331, 2005.
- [47] I. T. Vink, T. Nooitgedagt, R. N. Schouten, W. Wegscheider, and L. M. K. Vandersypen, “A cryogenic amplifier for fast real-time detection of single-electron tunneling”, *arXiv preprint cond-mat/0708.0461*, 2007.
- [48] D. J. Reilly, C. M. Marcus, M. P. Hanson, and A. C. Gossard, “Fast single-charge sensing with an rf quantum point contact”, *arXiv preprint cond-mat/0707.2946*, 2007.
- [49] W. Zurek, “Decoherence, einselection, and the quantum origins of the classical”, *Reviews of Modern Physics*, vol. 75, pp. 715–775, 2003.
- [50] W. A. Coish and D. Loss, “Hyperfine interaction in a quantum dot: Non-markovian electron spin dynamics”, *Phys. Rev. B*, vol. 70, p. 195340, 2004.
- [51] F. Bloch, “Nuclear induction”, *Phys. Rev.*, vol. 70, 1946.
- [52] A. Abragam, *The Principles of Nuclear Magnetism*, Clarendon, Oxford, 1961.
- [53] H. Breuer and F. Petruccione, *The Theory of Open Quantum Systems*, Oxford University Press, 2002.
- [54] C. P. Slichter, *Principles of Magnetic Resonance, 3rd ed.*, Springer-Verlag, Berlin, 1990.
- [55] J. R. Klauder and P. W. Anderson, “Spectral Diffusion Decay in Spin Resonance Experiments”, *Phys. Rev.*, vol. 125, p. 912, 1962.
- [56] L. Viola and S. Lloyd, “Dynamical suppression of decoherence in two-state quantum systems”, *Physical Review A*, vol. 58, pp. 2733–2744, 1998.
- [57] E. Geva, “On the relaxation of a two-level system driven by a strong electromagnetic field”, *The Journal of Chemical Physics*, vol. 102, p. 8541, 1995.

- [58] E. Condon, *The Theory of Atomic Spectra*, Cambridge University Press, 1935.
- [59] D. Griffiths, *Introduction to Quantum Mechanics*, Prentice Hall, New Jersey, 2005.
- [60] G. Dresselhaus, “Spin-Orbit Coupling Effects in Zinc Blende Structures”, *Phys. Rev.*, vol. 100, pp. 580–586, 1955.
- [61] E. I. Rashba, “Properties of semiconductors with an extremum loop. 1. Cyclotron and combinational resonance in a magnetic field perpendicular to the plane of the loop”, *Sov. Phys. Solid State*, vol. 2, pp. 1109–1122, 1960.
- [62] M. I. Dyakonov and V. I. Perel, “Spin relaxation of conduction electrons in noncentrosymmetric semiconductors”, *Sov. Phys. Solid State*, vol. 13, pp. 3023–3026, 1972.
- [63] R. J. Elliott, “Theory of the Effect of Spin-Orbit Coupling on Magnetic Resonance in Some Semiconductors”, *Phys. Rev.*, vol. 96, pp. 266–279, 1954.
- [64] A. V. Khaetskii and Y. V. Nazarov, “Spin relaxation in semiconductor quantum dots”, *Phys. Rev. B*, vol. 61, pp. 12639–12642, 2000.
- [65] A. V. Khaetskii and Y. V. Nazarov, “Spin-flip transitions between Zeeman sublevels in semiconductor quantum dots”, *Phys. Rev. B*, vol. 64, p. 125316, 2001.
- [66] L. M. Woods, T. L. Reinecke, and Y. Lyanda-Geller, “Spin relaxation in quantum dots”, *Phys. Rev. B*, vol. 66, p. 161318, 2002.
- [67] V. N. Golovach, A. Khaetskii, and D. Loss, “Phonon-induced decay of the electron spin in quantum dots”, *Phys. Rev. Lett.*, vol. 93, p. 016601, 2004.
- [68] L. Levitov and E. Rashba, “Dynamical spin-electric coupling in a quantum dot”, *Phys. Rev. B*, vol. 67, p. 115324, 2003.
- [69] S. Dehdal and C. Emary, “Spin-Orbit-Driven Coherent Oscillations in a Few-Electron Quantum Dot”, *Phys. Rev. Lett.*, vol. 94, p. 226803, 2005.
- [70] C. Flindt, A. S. Sorensen, and K. Flensberg, “Spin-Orbit Mediated Control of Spin Qubits”, *Phys. Rev. Lett.*, vol. 97, p. 240501, 2006.

BIBLIOGRAPHY

- [71] J. Schrieffer, “Relation between the Anderson and Kondo Hamiltonians”, *Physical Review*, vol. 149, pp. 491–492, 1966.
- [72] F. Marquardt and V. A. Abalmassov, “Spin relaxation in a quantum dot due to Nyquist noise”, *Phys. Rev. B*, vol. 71, p. 165325, 2005.
- [73] M. Borhani, V. N. Golovach, and D. Loss, “Spin decay in a quantum dot coupled to a quantum point contact”, *Phys. Rev. B*, vol. 73, p. 155311, 2006.
- [74] N. W. Ashcroft and N. D. Mermin, *Solid State Physics*, Saunders, New York, 1974.
- [75] A. V. Khaetskii, D. Loss, and L. Glazman, “Electron Spin Decoherence in Quantum Dots due to Interaction with Nuclei”, *Phys. Rev. Lett.*, vol. 88, p. 186802, 2002.
- [76] R. Hanson, L. Kouwenhoven, J. Petta, S. Tarucha, and L. Vandersypen, “Spins in few-electron quantum dots”, *arXiv preprint cond-mat/0610433*, to appear in *Rev. Mod. Phys.*, 2006.
- [77] M. Kroutvar, Y. Ducommun, D. Heiss, M. Bichler, D. Schuh, G. Abstreiter, and J. J. Finley, “Optically programmable electron spin memory using semiconductor quantum dots”, *Nature*, vol. 432, p. 81, 2004.
- [78] S. Amasha, K. MacLean, I. P. Radu, D. M. Zumbuhl, M. A. Kastner, M. P. Hanson, and A. C. Gossard, “Electrical control of spin relaxation in a quantum dot”, *arXiv preprint cond-mat/0707.1656*, 2007.
- [79] D. Paget, G. Lampel, B. Sapoval, and V. I. Safarov, “Low field electron-nuclear spin coupling in gallium arsenide under optical pumping conditions”, *Phys. Rev. B*, vol. 15, p. 5780, 1977.
- [80] W. A. Coish, D. Loss, E. A. Yuzbashyan, and B. L. Altshuler, “Quantum versus classical hyperfine-induced dynamics in a quantum dot”, *Journal of Applied Physics*, vol. 101, p. 081715, 2007.
- [81] I. A. Merkulov, A. L. Efros, and M. Rosen, “Electron spin relaxation by nuclei in semiconductor quantum dots”, *Phys. Rev. B*, vol. 65, p. 205309, 2002.
- [82] P. F. Braun, X. Marie, L. Lombez, B. Urbaszek, T. Amand, P. Renucci, V. K. Kalevich, K. V. Kavokin, O. Krebs, P. Voisin, and Y. Masumoto,

- “Direct Observation of the Electron Spin Relaxation Induced by Nuclei in Quantum Dots”, *Phys. Rev. Lett.*, vol. 94, p. 116601, 2005.
- [83] M. V. G. Dutt, J. Cheng, B. Li, X. D. Xu, X. Q. Li, P. R. Berman, D. G. Steel, A. S. Bracker, D. Gammon, S. E. Economou, R. B. Liu, and L. J. Sham, “Stimulated and spontaneous optical generation of electron spin coherence in charged gas quantum dots”, *Phys. Rev. Lett.*, vol. 94, p. 227403, 2005.
- [84] A. C. Johnson, J. R. Petta, J. M. Taylor, A. Yacoby, M. D. Lukin, C. M. Marcus, M. P. Hanson, and A. C. Gossard, “Triplet-singlet spin relaxation via nuclei in a double quantum dot”, *Nature*, vol. 435, p. 925, 2005.
- [85] F. H. L. Koppens, J. A. Folk, J. M. Elzerman, R. Hanson, L. H. W. van Beveren, I. T. Vink, H. P. Tranitz, W. Wegscheider, L. P. Kouwenhoven, and L. M. K. Vandersypen, “Control and detection of singlet-triplet mixing in a random nuclear field”, *Science*, vol. 309, pp. 1346–1350, 2005.
- [86] A. V. Khaetskii, D. Loss, and L. Glazman, “Electron spin evolution induced by interaction with nuclei in a quantum dot”, *Phys. Rev. B*, vol. 67, p. 195329, 2003.
- [87] J. Schliemann, A. V. Khaetskii, and D. Loss, “Spin decay and quantum parallelism”, *Phys. Rev. B*, vol. 66, p. 245303, 2002.
- [88] D. Klauser, W. A. Coish, and D. Loss, “Nuclear spin state narrowing via gate-controlled Rabi oscillations in a double quantum dot”, *Phys. Rev. B*, vol. 73, p. 205302, 2006.
- [89] D. Stepanenko, G. Burkard, G. Giedke, and A. Imamoglu, “Enhancement of Electron Spin Coherence by Optical Preparation of Nuclear Spins”, *Phys. Rev. Lett.*, vol. 96, p. 136401, 2006.
- [90] O. Cakir and T. Takagahara, “Quantum Dynamics of Electron-Nuclei Coupled System in a Double Quantum Dot”, *arXiv preprint cond-mat/0609217*, 2006.
- [91] G. Giedke, J. M. Taylor, D. DAlessandro, M. D. Lukin, and A. Imamoglu, “Quantum measurement of a mesoscopic spin ensemble”, *Phys. Rev. A*, vol. 74, p. 32316, 2006.
- [92] E. Laird, C. Barthel, E. Rashba, C. Marcus, M. Hanson, and A. Gossard, “Hyperfine-mediated gate-driven electron spin resonance”, *arXiv preprint cond-mat/0707.0557*, 2007.

BIBLIOGRAPHY

- [93] S. I. Erlingsson, Y. V. Nazarov, and V. I. Falko, “Nucleus-mediated spin-flip transitions in GaAs quantum dots”, *Phys. Rev. B*, vol. 64, p. 195306, 2001.
- [94] S. I. Erlingsson and Y. V. Nazarov, “Hyperfine-mediated transitions between a Zeeman split doublet in GaAs quantum dots: The role of the internal field”, *Phys. Rev. B*, vol. 66, p. 155327, 2002.
- [95] S. I. Erlingsson and Y. V. Nazarov, “Evolution of localized electron spin in a nuclear spin environment”, *Phys. Rev. B*, vol. 70, p. 205327, 2004.
- [96] V. A. Abalmassov and F. Marquardt, “Electron-nuclei spin relaxation through phonon-assisted hyperfine interaction in a quantum dot”, *Phys. Rev. B*, vol. 70, p. 75313, 2004.
- [97] N. Shenvi and K. Rogerio de Sousa, “Universal Scaling of Hyperfine-Induced Electron Spin Echo Decay”, *Phys. Rev. B*, vol. 71, p. 224411, 2005.
- [98] W. Yao, R. B. Liu, and L. J. Sham, “Theory of electron spin decoherence by interacting nuclear spins in a quantum dot”, *Phys. Rev. B*, vol. 74, p. 195301, 2006.
- [99] C. Deng and X. Hu, “Analytical solution of electron spin decoherence through hyperfine interaction in a quantum dot”, *Phys. Rev. B*, vol. 73, p. 241303(R), 2006.
- [100] R. G. Shulman, B. J. Wyluda, and H. J. Hrostowski, “Nuclear Magnetic Resonance in Semiconductors. III. Exchange Broadening in GaAs and InAs”, *Phys. Rev.*, vol. 109, p. 808, 1958.
- [101] R. de Sousa and S. Das Sarma, “Theory of nuclear-induced spectral diffusion: Spin decoherence of phosphorus donors in Si and GaAs quantum dots”, *Phys. Rev. B*, vol. 68, p. 115322, 2003.
- [102] R. de Sousa and S. Das Sarma, “Electron spin coherence in semiconductors: Considerations for a spin-based solid-state quantum computer architecture”, *Phys. Rev. B*, vol. 67, p. 33301, 2003.
- [103] W. Witzel and S. Das Sarma, “Quantum theory for electron spin decoherence induced by nuclear spin dynamics in semiconductor quantum computer architectures: Spectral diffusion of localized electron spins in the nuclear solid-state environment”, *Phys. Rev. B*, vol. 74, p. 35322, 2006.

- [104] F. H. L. Koppens, C. Buizert, K.-J. Tielrooij, I. T. Vink, K. C. Nowack, T. Meunier, L. P. Kouwenhoven, and L. M. K. Vandersypen, “Driven coherent oscillations of a single electron spin in a quantum dot”, *Nature*, vol. 442, p. 766, 2006.
- [105] K. Ono, D. G. Austing, Y. Tokura, and S. Tarucha, “Current rectification by pauli exclusion in a weakly coupled double quantum dot system”, *Science*, vol. 297, p. 1313, 2002.
- [106] H.-A. Engel and D. Loss, “Detection of single spin decoherence in a quantum dot via charge currents”, *Phys. Rev. Lett.*, vol. 86, p. 4648, 2001.
- [107] D. Gammon, A. Efros, T. Kennedy, M. Rosen, D. Katzer, D. Park, S. Brown, V. Korenev, and I. Merkulov, “Electron and Nuclear Spin Interactions in the Optical Spectra of Single GaAs Quantum Dots”, *Phys. Rev. Lett.*, vol. 86, pp. 5176–5179, 2001.
- [108] K. Ono and S. Tarucha, “Nuclear-Spin-Induced Oscillatory Current in Spin-Blockaded Quantum Dots”, *Phys. Rev. Lett.*, vol. 92, p. 256803, 2004.
- [109] O. N. Jouravlev and Y. V. Nazarov, “Electron transport in a double quantum dot governed by a nuclear magnetic field”, *Phys. Rev. Lett.*, vol. 96, p. 176804, 2006.
- [110] J. Inarrea, G. Platero, and A. MacDonald, “Double-dot transport in the spin blockade regime”, *arXiv preprint cond-mat/0609323*, 2006.
- [111] C. Poole, *Electron Spin Resonance, 2nd ed.*, Wiley, New York, 1983.
- [112] M. Rudner and L. Levitov, “Self-Polarization and Cooling of Spins in Quantum Dots”, *arXiv preprint cond-mat/0609409*, 2006.
- [113] F. Meier and B. P. Zakharchenya, *Optical orientation. Modern problems in condensed matter sciences*, North-Holland, 1984.
- [114] D. Gammon, S. Brown, E. Snow, T. Kennedy, D. Katzer, and D. Park, “Nuclear spectroscopy in single quantum dots: Nanoscopic Raman scattering and nuclear magnetic resonance”, *Science*, vol. 277, pp. 85–88, 1997.
- [115] A. S. Bracker, E. A. Stinaff, D. Gammon, M. E. Ware, J. G. Tischler, A. Shabaev, A. L. Efros, D. Park, D. Gershoni, V. L. Korenev, and I. A. Merkulov, “Optical Pumping of the Electronic and Nuclear Spin of Single Charge-Tunable Quantum Dots”, *Phys. Rev. Lett.*, vol. 94, p. 47402, 2005.

BIBLIOGRAPHY

- [116] M. Eto, T. Ashiwa, and M. Murata, “Entanglement of nuclear spins in spin-blocked quantum dots”, *Physica E: Low-dimensional Systems and Nanostructures*, vol. 22, pp. 426–429, 2004.
- [117] J. Taylor, A. Imamoglu, and M. Lukin, “Controlling a Mesoscopic Spin Environment by Quantum Bit Manipulation”, *Phys. Rev. Lett.*, vol. 91, p. 246802, 2003.
- [118] W. G. Van der Wiel, S. De Franceschi, J. M. Elzerman, T. Fujisawa, S. Tarucha, and L. P. Kouwenhoven, “Electron transport through double quantum dots”, *Rev. Mod. Phys.*, vol. 75, p. 1, 2003.
- [119] A. C. Johnson, J. R. Petta, C. M. Marcus, M. P. Hanson, and A. C. Gossard, “Singlet-triplet spin blockade and charge sensing in a few-electron double quantum dot”, *Phys. Rev. B*, vol. 72, p. 165308, 2005.
- [120] T. Fujisawa, T. H. Oosterkamp, W. G. van der Wiel, B. W. Broer, R. Aguado, S. Tarucha, and L. P. Kouwenhoven, “Spontaneous Emission Spectrum in Double Quantum Dot Devices”, *Science*, vol. 282, p. 932, 1998.
- [121] M. Dobers, K. Klitzing, and G. Weimann, “Electron-spin resonance in the two-dimensional electron gas of GaAs – Al_xGa_{1-x}As heterostructures”, *Phys. Rev. B*, vol. 38, pp. 5453–5456, 1988.
- [122] A. K. Hüttel, J. Weber, A. W. Holleitner, D. Weinmann, K. Eberl, and R. H. Blick, “Nuclear spin relaxation probed by a single quantum dot”, *Phys. Rev. B*, vol. 69, p. 73302, 2004.
- [123] P. Zoller, T. Beth, D. Binosi, R. Blatt, H. Briegel, D. Bruss, T. Calarco, J. Cirac, D. Deutsch, J. Eisert, *et al.*, “Quantum information processing and communication”, *The European Physical Journal D-Atomic, Molecular and Optical Physics*, vol. 36, pp. 203–228, 2005.
- [124] D. Austing, T. Honda, K. Muraki, Y. Tokura, and S. Tarucha, “Quantum dot molecules”, *Physica B*, vol. 249, pp. 206–209, 1998.
- [125] M. Ciorga, A. S. Sachrajda, P. Hawrylak, C. Gould, P. Zawadzki, S. Julian, Y. Feng, and Z. Wasilewski, “Addition spectrum of a lateral dot from coulomb and spin-blockade spectroscopy”, *Phys. Rev. B*, vol. 61, p. R16315, 2000.

- [126] J. M. Elzerman, R. Hanson, J. S. Greidanus, L. H. Willems van Beveren, S. De Franceschi, L. M. K. Vandersypen, S. Tarucha, and L. P. Kouwenhoven, “Few-electron quantum dot circuit with integrated charge read out”, *Phys. Rev. B*, vol. 67, p. 161308, 2003.
- [127] M. Bayer, P. Hawrylak, K. Hinzer, S. Fafard, M. Korkusinski, Z. Wasilewski, O. Stern, and A. Forchel, “Coupling and Entangling of Quantum States in Quantum Dot Molecules”, 2001.
- [128] M. Atature, J. Dreiser, A. Badolato, A. Hogege, K. Karrai, and A. Imamoglu, “Quantum-dot spin-state preparation with near-unity fidelity”, *Science*, vol. 312, pp. 551–553, 2006.
- [129] R. Hanson, B. Witkamp, L. M. K. Vandersypen, L. H. Willems van Beveren, J. M. Elzerman, and L. P. Kouwenhoven, “Zeeman energy and spin relaxation in a one-electron quantum dot”, *Phys. Rev. Lett.*, vol. 91, p. 196802, 2003.
- [130] R. Schleser, E. Ruh, T. Ihn, K. Ensslin, D. C. Driscoll, and A. C. Gossard, “Time-Resolved Detection of Individual Electrons in a Quantum Dot”, *Appl. Phys. Lett.*, vol. 85, p. 2005, 2004.
- [131] R. Hanson, L. H. Willems van Beveren, I. T. Vink, J. M. Elzerman, W. J. M. Naber, F. H. L. Koppens, L. P. Kouwenhoven, and L. M. K. Vandersypen, “Single-shot readout of electron spin states in a quantum dot using spin-dependent tunnel rates”, *Phys. Rev. Lett.*, vol. 94, p. 196802, 2005.
- [132] A. Greilich, R. Oulton, E. A. Zhukov, I. A. Yugova, D. R. Yakovlev, M. Bayer, A. Shabaev, L. E. Al, I. A. Merkulov, V. Stavarache, D. Reuter, and A. Wieck, “Optical control of spin coherence in singly charged (In, Ga)As/GaAs quantum dots”, *Phys. Rev. Lett.*, vol. 96, p. 227401, 2006.
- [133] M. Xiao, I. Martin, E. Yablonovitch, and H. W. Jiang, “Electrical detection of the spin resonance of a single electron in a silicon field-effect transistor”, *Nature*, vol. 430, p. 435, 2004.
- [134] D. Rugar, R. Budakian, H. J. Mamin, and B. W. Chui, “Single spin detection by magnetic resonance force microscopy”, *Nature*, vol. 430, p. 329, 2004.
- [135] Y. Kato, R. C. Myers, A. C. Gossard, and D. D. Awschalom, “Coherent spin manipulation without magnetic fields in strained semiconductors”, *Nature*, vol. 427, p. 50, 2003.

BIBLIOGRAPHY

- [136] H.-A. Engel, V. N. Golovach, D. Loss, L. M. K. Vandersypen, J. M. Elzerman, R. Hanson, and L. P. Kouwenhoven, “Measurement efficiency and n-shot readout of spin qubits”, *Phys. Rev. Lett.*, vol. 93, p. 106804, 2004.
- [137] M. Blaauboer and D. P. DiVincenzo, “Detecting entanglement using a double quantum dot turnstile”, *Phys. Rev. Lett.*, vol. 95, p. 160402, 2005.
- [138] H.-A. Engel and D. Loss, “Fermionic bell-state analyzer for spin qubits”, *Science*, vol. 309, pp. 586–588, 2005.
- [139] R. M. Potok, J. A. Folk, C. M. Marcus, V. Umansky, M. Hanson, and A. C. Gossard, “Spin and Polarized Current from Coulomb Blockaded Quantum Dots”, *Phys. Rev. Lett.*, vol. 91, p. 16802, 2003.
- [140] L. H. Willems van Beveren, R. Hanson, I. T. Vink, F. H. L. Koppens, L. P. Kouwenhoven, and L. M. K. Vandersypen, “Spin filling of a quantum dot derived from excited-state spectroscopy”, *New Journal of Physics*, vol. 7, p. 182, 2005.
- [141] A. Kogan, S. Amasha, D. Goldhaber-Gordon, G. Granger, M. A. Kastner, and H. Shtrikman, “Measurements of Kondo and Spin Splitting in Single-Electron Transistors”, *Phys. Rev. Lett.*, vol. 93, p. 166602, 2004.
- [142] F. H. L. Koppens, D. Klauser, W. A. Coish, K. C. Nowack, L. P. Kouwenhoven, D. Loss, and L. M. K. Vandersypen, “Universal phase shift and non-exponential decay of driven single-spin oscillations”, *arXiv preprint cond-mat/0703640*, 2007.
- [143] L. M. K. Vandersypen and I. L. Chuang, “Nmr techniques for quantum control and computation”, *Rev. Mod. Phys.*, vol. 76, p. 1037, 2004.
- [144] G. Salis, Y. Kato, K. Ensslin, D. C. Driscoll, A. C. Gossard, and D. D. Awschalom, “Electrical control of spin coherence in semiconductor nanostructures”, *Nature*, vol. 414, p. 619, 2001.
- [145] H. W. Jiang and E. Yablonovitch, “Gate-controlled electron spin resonance in GaAs/Al_xGa_{1-x}As heterostructures”, *Phys. Rev. B*, vol. 64, p. 041307, 2001.
- [146] T. H. Stoof and Y. V. Nazarov, “Time-dependent resonant tunneling via two discrete states”, *Phys. Rev. B*, vol. 53, pp. 1050–1053, 1996.

- [147] T. H. Oosterkamp, T. Fujisawa, W. G. van der Wiel, K. Ishibashi, R. V. Hijman, S. Tarucha, and L. P. Kouwenhoven, “Microwave spectroscopy of a quantum-dot molecule”, *Nature*, 1998.
- [148] D. DiVincenzo and D. Loss, “Rigorous Born approximation and beyond for the spin-boson model”, *Phys. Rev. B*, vol. 71, p. 35318, 2005.
- [149] J. M. Taylor and M. D. Lukin, “Dephasing of quantum bits by a quasi-static mesoscopic environment”, *Quantum Information Processing*, vol. 5, p. 503, 2006.
- [150] G. Ithier, E. Collin, P. Joyez, P. Meeson, D. Vion, D. Esteve, F. Chiarello, A. Shnirman, Y. Makhlin, J. Schrieffer, *et al.*, “Decoherence in a superconducting quantum bit circuit”, *Phys. Rev. B*, vol. 72, p. 134519, 2005.
- [151] S. Amasha, K. MacLean, I. Radu, D. M. Zumbuhl, M. A. Kastner, M. P. Hanson, and A. C. Gossard, “Measurements of the spin relaxation rate at low magnetic fields in a quantum dot”, *arXiv preprint cond-mat/0607110*, 2006.
- [152] W. Coish and D. Loss, “Singlet-triplet decoherence due to nuclear spins in a double quantum dot”, *Phys. Rev. B*, vol. 72, p. 125337, 2005.
- [153] E. A. Laird, J. R. Petta, A. C. Johnson, C. M. Marcus, A. Yacoby, M. P. Hanson, and A. C. Gossard, “Effect of exchange interaction on spin dephasing in a double quantum dot”, *Phys. Rev. Lett.*, vol. 97, 2006.
- [154] F. H. L. Koppens, C. Buizert, K. J. Tielrooij, I. T. Vink, K. C. Nowack, T. Meunier, L. P. Kouwenhoven, and L. M. K. Vandersypen, “Driven coherent oscillations of a single electron spin in a quantum dot”, *Nature*, vol. 442, p. 766, 2006.
- [155] C. Deng and X. Hu, “Erratum: Analytical solution of electron spin decoherence through hyperfine interaction in a quantum dot [phys. rev. b 73, 241303(r) (2006)]”, *Phys. Rev. B*, vol. 74, 2006.
- [156] V. V. Dobrovitski, H. A. De Raedt, M. I. Katsnelson, and B. N. Harmon, “Quantum oscillations without quantum coherence”, *Phys. Rev. Lett.*, vol. 90, 2003.
- [157] R.-S. Huang, V. Dobrovitski, and B. Harmon, “Single Qubit Rabi Oscillation Decohered by Many Two-Level Systems”, 2005.

BIBLIOGRAPHY

- [158] J. P. Gordon and K. D. Bowers, “Microwave spin echoes from donor electrons in silicon”, *Phys. Rev. Lett.*, vol. 1, 1958.
- [159] A. Greilich, D. R. Yakovlev, A. Shabaev, A. L. Efros, I. A. Yugova, R. Oulton, V. Stavarache, D. Reuter, A. Wieck, and M. Bayer, “Mode Locking of Electron Spin Coherences in Singly Charged Quantum Dots”, *Science*, vol. 313, pp. 341–345, 2006.
- [160] W. Yao, R. Liu, and L. Sham, “Restoring Coherence Lost to a Slow Interacting Mesoscopic Spin Bath”, *Phys. Rev. Lett.*, vol. 98, p. 77602, 2007.
- [161] M. Rudner and L. Levitov, “Resonant Cooling of Nuclear Spins in Quantum Dots”, *arXiv preprint cond-mat/0705.2177*, 2007.
- [162] D. Awschalom, D. Loss, and N. Samarth, *Semiconductor Spintronics and Quantum Computation*, Springer, 2002.
- [163] B. Simovič, P. Studerus, S. Gustavsson, R. Leturcq, K. Ensslin, R. Schumann, J. Forrer, and A. Schweiger, “Design of Q-band loop-gap resonators at frequencies of 34–36 GHz for single electron spin spectroscopy in semiconductor nanostructures”, *Review of Scientific Instruments*, vol. 77, p. 064702, 2006.
- [164] Y. A. Bychkov and E. I. Rashba, “Properties of a 2D electron-gas with lifted spectral degeneracy”, *JETP Lett.*, vol. 39, p. 78, 1984.
- [165] M. Schulte, J. G. S. Lok, G. Denninger, and W. Dietsche, “Electron Spin Resonance on a Two-Dimensional Electron Gas in a Single AlAs Quantum Well”, *Phys. Rev. Lett.*, vol. 94, p. 137601, 2005.
- [166] J. Walls, “Parametric spin excitations in lateral quantum dots”, *arXiv preprint cond-mat/0705.4231*, 2007.
- [167] J. Baugh, Y. Kitamura, K. Ono, and S. Tarucha, “Large nuclear Overhauser fields detected in vertically-coupled double quantum dots”, *arXiv preprint cond-mat/0705.1104*, 2007.
- [168] T. Meunier, I. T. Vink, L. H. Willems van Beveren, K. J. Tielrooij, R. Hanson, F. H. L. Koppens, H. P. Tranitz, W. Wegscheider, L. P. Kouwenhoven, and L. Vandersypen, “Experimental Signature of Phonon-Mediated Spin Relaxation in a Two-Electron Quantum Dot”, *Phys. Rev. Lett.*, vol. 98, p. 126601, 2007.

- [169] A. N. Jordan, B. Trauzettel, and G. Burkard, “Weak measurement of quantum dot spin qubits”, *arXiv preprint cond-mat/0706.0180*, 2007.
- [170] A. Romito, Y. Gefen, and Y. M. Blanter, “Weak values of electron spin in a double quantum dot”, *arXiv preprint cond-mat/0707.3695*, 2007.
- [171] D. Gottesman, “Stabilizer Codes and Quantum Error Correction”, *PhD thesis, arXiv preprint quant-ph/9705052*, 1997.
- [172] A. Steane, “Overhead and noise threshold of fault-tolerant quantum error correction”, *Phys. Rev. A*, vol. 68, p. 42322, 2003.
- [173] T. Szkopek, P. O. Boykin, H. Fan, V. Roychowdhury, E. Yablonovitch, G. Simms, M. Gyure, and B. Fong, “Threshold error penalty for fault tolerant computation with nearest neighbour communication”, *IEEE Trans.Nano.*, vol. 5, p. 42, 2006.
- [174] E. Knill, “Quantum computing with realistically noisy devices”, *Nature*, vol. 434, pp. 39–44, 2005.
- [175] J. M. Taylor, H. A. Engel, W. Dur, A. Yacoby, C. M. Marcus, P. Zoller, and M. D. Lukin, “Fault-tolerant architecture for quantum computation using electrically controlled semiconductor spins”, *Nature Physics*, vol. 1, 2005.
- [176] D. Stepanenko and G. Burkard, “Quantum gates between capacitively coupled double quantum dot two-spin qubits”, *Phys. Rev. B*, vol. 75, p. 085324, 2007.
- [177] N. Mason, M. Biercuk, and C. Marcus, “Local Gate Control of a Carbon Nanotube Double Quantum Dot”, *Science*, vol. 303, pp. 655–658, 2004.
- [178] S. Sapmaz, C. Meyer, P. Beliczynski, P. Jarillo-Herrero, and L. P. Kouwenhoven, “Excited state spectroscopy in carbon nanotube double quantum dots”, *Nano Letters*, vol. 6, p. 1350, 2006.
- [179] N. Shaji, C. B. Simmons, M. Thalukulam, L. J. Klein, H. Qin, H. Luo, D. E. Savage, M. G. Lagally, A. J. Rumberg, R. Joynt, M. Friesen, R. H. Blick, S. N. Coppersmith, and M. A. Eriksson, “Spin blockade and coherence-enhanced transport in a few-electron Si/SiGe double quantum dot”, *arXiv preprint cond-mat/0708.0794*, 2007.
- [180] Y. Hu, H. H. O. Churchill, D. J. Reilly, J. Xiang, C. M. Lieber, and C. M. Marcus, “Double quantum dot with integrated charge sensor based

BIBLIOGRAPHY

- on Ge/Si heterostructure nanowires”, *arXiv preprint cond-mat/0706.2271*, 2007.
- [181] B. Trauzettel, D. Bulaev, D. Loss, and G. Burkard, “Spin qubits in graphene quantum dots”, *Nature Physics*, vol. 3, pp. 192–196, 2007.
- [182] B. Koiller, X. Hu, and S. Das Sarma, “Strain effects on silicon donor exchange: Quantum computer architecture considerations”, *Phys. Rev. B*, vol. 66, p. 115201, 2002.
- [183] S. Goswami, K. A. Slinker, M. Friesen, L. M. McGuire, J. L. Truitt, C. Tahan, L. J. Klein, J. O. Chu, P. M. Mooney, D. W. van der Weide, R. Joynt, S. N. Coppersmith, and M. A. Eriksson, “Controllable valley splitting in silicon quantum devices”, *Nature Physics*, vol. 3, pp. 41–45, 2007.
- [184] A. Tyryshkin, S. Lyon, A. Astashkin, and A. Raitsimring, “Electron spin relaxation times of phosphorus donors in silicon”, *Phys. Rev. B*, vol. 68, p. 193207, 2003.
- [185] L. Childress, G. Dutt, J. Taylor, A. Zibrov, F. Jelezko, J. Wrachtrup, P. Hemmer, and M. Lukin, “Coherent Dynamics of Coupled Electron and Nuclear Spin Qubits in Diamond”, *Science*, vol. 314, p. 281, 2006.
- [186] V. Chan, T. Buehler, A. Ferguson, D. McCamey, D. Reilly, A. Dzurak, R. Clark, C. Yang, and D. Jamieson, “Ion implanted Si: P double dot with gate tunable interdot coupling”, *Journal of Applied Physics*, vol. 100, p. 106104, 2006.
- [187] J. Meijer, B. Burchard, M. Domhan, C. Wittmann, T. Gaebel, I. Popa, F. Jelezko, and J. Wrachtrup, “Generation of single color centers by focused nitrogen implantation”, *Applied Physics Letters*, vol. 87, p. 261909, 2005.
- [188] T. Gaebel, M. Domhan, I. Popa, C. Wittmann, P. Neumann, F. Jelezko, J. R. Rabreau, N. Stavrias, A. D. Greentree, S. Prawer, J. Meijer, J. Twamley, P. R. Hemmer, and J. Wrachtrup, “Room-temperature coherent coupling of single spins in diamond”, *Nature Physics*, vol. 2, pp. 408–413, 2006.
- [189] M. Dutt, L. Childress, L. Jiang, E. Togan, J. Maze, F. Jelezko, A. Zibrov, P. Hemmer, and M. Lukin, “Quantum Register Based on Individual Electronic and Nuclear Spin Qubits in Diamond”, *Science*, vol. 316, p. 1312, 2007.

- [190] W. A. Coish and D. Loss, “Exchange-controlled single-electron-spin rotations in quantum dots”, *Phys. Rev. B*, vol. 75, p. 161302, 2007.
- [191] J. Gupta, R. Knobel, N. Samarth, and D. Awschalom, “Ultrafast Manipulation of Electron Spin Coherence”, *Science*, vol. 292, p. 2458, 2001.
- [192] D. P. DiVincenzo, D. Bacon, J. Kempe, G. Burkard, and K. B. Whaley, “Universal quantum computation with the exchange interaction”, *Nature*, vol. 408, p. 339, 2000.
- [193] X. Hu and S. Das Sarma, “Charge-Fluctuation-Induced Dephasing of Exchange-Coupled Spin Qubits”, *Phys. Rev. Lett.*, vol. 96, p. 100501, 2006.
- [194] M. Stopa and C. M. Marcus, “Magnetic field control of exchange and noise immunity in double quantum dots”, *arXiv preprint cond-mat/0604008*, 2006.
- [195] N. Bonesteel, D. Stepanenko, and D. DiVincenzo, “Anisotropic Spin Exchange in Pulsed Quantum Gates”, *Phys. Rev. Lett.*, vol. 87, p. 207901, 2001.
- [196] G. Burkard and D. Loss, “Cancellation of Spin-Orbit Effects in Quantum Gates Based on the Exchange Coupling in Quantum Dots”, *Phys. Rev. Lett.*, vol. 88, p. 47903, 2002.
- [197] D. Stepanenko, N. E. Bonesteel, D. P. DiVincenzo, G. Burkard, and D. Loss, “Spin-orbit coupling and time-reversal symmetry in quantum gates”, *Phys. Rev. B*, vol. 68, 2003.
- [198] L. Gaudreau, S. Studenikin, A. Sachrajda, P. Zawadzki, A. Kam, J. Lapointe, M. Korkusinski, and P. Hawrylak, “Stability Diagram of a Few-Electron Triple Dot”, *Phys. Rev. Lett.*, vol. 97, p. 36807, 2006.
- [199] D. Schröer, A. D. Greentree, L. Gaudreau, K. Eberl, L. C. L. Hollenberg, J. P. Kotthaus, and S. Ludwig, “Electrostatically defined serial triple quantum dot charged with few electrons”, *Phys. Rev. B*, vol. 76, p. 075306, 2007.
- [200] O. Gywat, F. Meier, D. Loss, and D. Awschalom, “Dynamics of coupled qubits interacting with an off-resonant cavity”, *Phys. Rev. B*, vol. 73, p. 125336, 2006.
- [201] L. Childress, A. S. S. rensen, and M. D. Lukin, “Mesoscopic cavity quantum electrodynamics with quantum dots”, *Phys. Rev. A*, vol. 69, p. 042302, 2004.

BIBLIOGRAPHY

- [202] A. Blais, R. Huang, A. Wallraff, S. Girvin, and R. Schoelkopf, “Cavity quantum electrodynamics for superconducting electrical circuits: An architecture for quantum computation”, *Phys. Rev. A*, vol. 69, p. 62320, 2004.
- [203] G. Burkard and A. Imamoglu, “Ultra-long-distance interaction between spin qubits”, *Phys. Rev. B*, vol. 74, p. 41307, 2006.
- [204] M. Trif, V. Golovach, and D. Loss, “Spin dynamics in InAs-nanowire quantum-dots coupled to a transmission line”, *arXiv preprint cond-mat/07082091*, 2007.

Summary

Coherence and control of a single electron spin in a quantum dot

An electron does not only have an electric charge, but also a small magnetic moment, called spin. In a magnetic field, the spin can point in the same direction as the field (spin-up) or in the opposite direction (spin-down). However, the laws of quantum mechanics also allow the spin to exist in both states at the same time (so-called superposition state). The experiments described in this thesis aim at controlling the quantum state of a single electron spin. Using the level of control achieved in these experiments, we investigated the properties of one and two-electron spin states, for example by measuring how the environment affects the superposition states. In addition to unraveling these fundamental properties, this research also aims at the development of a so-called quantum bit. This is an important building block for the future quantum computer, that is for a certain class of calculations in principle much more powerful than an ordinary computer. A quantum bit, or “qubit”, can be “0” or “1” like in a conventional computer, but can also exist in both states at the same time. The spin is expected to be a good representation of a qubit because its ultrasmall magnetic moment is relatively well protected against uncontrolled interactions with the environment.

We trap a single electron in a so-called “quantum dot”, an electrical trap for the electron in a semiconductor. The quantum dot devices studied in this work are defined in a two-dimensional electron gas (2DEG) of a GaAs/AlGaAs heterostructure by applying negative voltages to metallic gate electrodes fabricated on top of the heterostructure.

Manipulation of a single spin has been performed in two different ways. The first is the traditional technique of electron spin resonance (ESR), where a small oscillating magnetic field is combined with a perpendicular larger static field. When the frequency of the oscillating field matches the (Larmor) precession frequency of the spin in the static field, the spin direction will spiral from spin-up to spin-down and again back to spin-up. By applying bursts of the oscillating field, we rotate the spin to any pre-defined superposition state and subsequently

read it out. A very robust read-out was realized by trapping another electron next to the first electron, and use this for read-out of the spin direction of the first electron. This is done by detecting whether the electron in the first quantum dot can move to the neighboring quantum dot which is occupied by the other electron. Due to the Pauli exclusion principle this is only possible if the two electrons have opposite spin directions. This processes is repeated many times resulting in a current flow which is in this case a measure of the relative spin direction of the two electrons. In this way, we have measured the spin-rotation from up to a superposition of up and down and then further to spin-down.

The second method for manipulation the spin exploits the spin-orbit interaction: an electron moving in an electric field also feels an effective magnetic field. In a semiconductor this magnetic field is related to the crystal structure as well as the trapping potential in the semiconductor. For an electron trapped in a quantum dot, this effective field depends on the location of the electron. Via an oscillating electric field, generated with a local gate electrode, the electron's position oscillates and in this way it experiences an oscillating magnetic field. In combination with a static field and a similar read-out method as before, we demonstrated control of a single electron spin states via oscillating electric fields. The advantage of this method is that electric fields can be generated much more easily, simply by exciting a local gate electrode. In addition, this method allows for greater spatial selectivity, which is important for local addressing of individual spins.

When operating the spin as a qubit it is important to minimize errors in the fragile quantum information, stored in the spin. These errors are due to uncontrolled interactions with the environment, processes called decoherence. We studied the effect of the environment on two-electron spin states using spin-dependent transport through two coupled quantum dots. Normally, transport is blocked in this regime due to the long lifetime of the two-electron spin states. However, when the applied static magnetic field is smaller than a few milliTesla, transport becomes possible because the lifetime of the two-electron spin states is then very short. This is due to the interaction of the electron spin with the nuclear spins in the semiconductor material, resulting in a random effective field of ~ 2 milliTesla. We demonstrate that the two-electron spin states are significantly less perturbed by bringing the electrons closer together in combination with the application of a magnetic field.

The decoherence properties of a single spin have been measured via a so-called Ramsey experiment. This involves a rotation of the spin from, for example, spin-up to a superposition state, and after a short waiting time, rotating back to spin-up. However, this is only the possible if the phase-information of the quan-

tum state has been preserved. If this is not the case, we find spin-down instead of spin-up after the second rotation. The phase-information of the quantum state is already lost after about 30 nanoseconds, caused by the precession of the spin around the field from the nuclear spins. This precession can be reversed to a large extent via a spin-echo technique, which implies, after some interaction time with the nuclear spins, a rotation of the spin by 180° . Using this technique, the decoherence time is extended to about 500 nanoseconds. This is more than a factor of 15 longer than the decoherence time without corrections. The decoherence time is long enough for further exploration of the electron spin as a quantum bit.

Frank Koppens
August 2007

Samenvatting

Coherentie en controle van een enkele elektronspin in een quantum dot

Een elektron bezit niet alleen elektrische lading, maar heeft ook een klein magnetisch moment, genaamd spin. In een magneetveld kan de spin in dezelfde richting als het veld wijzen (spin-op) of in omgekeerde richting (spin-neer). Echter, de wetten van de quantummechanica laten de spin ook toe om in beide toestanden tegelijkertijd te bestaan (de zogenaamde superpositie). De experimenten beschreven in dit proefschrift hebben als doel om de quantummechanische toestand van één enkele elektronspin te controleren. Bovendien hebben we de eigenschappen van één en twee-elektron spintoestanden onderzocht, bijvoorbeeld door het effect van verstoringen uit de omgeving op de superpositietoestanden te meten. Naast het blootleggen van deze fundamentele eigenschappen werken we in dit onderzoek ook aan de ontwikkeling van een zogenaamde quantumbit. Dit is een belangrijke bouwsteen voor de quantumcomputer, die voor de uitvoering van een bepaald soort berekeningen in potentie veel krachtiger is dan een conventionele computer. Een quantumbit of “qubit” kan niet alleen “0” of “1” zijn zoals in conventionele computers, maar kan ook in beide toestanden tegelijkertijd bestaan. De verwachting is dat de spin een goede kandidaat is voor een qubit doordat zijn extreem kleine magnetisch moment relatief ongevoelig is voor verstoringen uit de omgeving.

Eén enkel elektron kunnen we opsluiten in een zogenaamde “quantum dot”, een elektrische val voor elektronen in een halfgeleidermateriaal. De in dit werk bestudeerde quantum dots zijn gedefinieerd in een tweedimensionaal elektronengas (2DEG) van een GaAs/AlGaAs heterostructuur, door negatieve spanningen aan te brengen op metalen elektroden bovenop de heterostructuur.

We manipuleren een enkele spin met behulp van twee verschillende mechanismen. De eerste manier is via de techniek van elektronspin resonantie (ESR) waarbij een zwak wisselend magneetveld loodrecht wordt aangelegd op een sterker statisch magneetveld. Als de frequentie van het wisselende veld gelijk is aan de (Larmor) precessiefrequentie van de spin in het statische veld, zal de spinrichting

in een spiraalbeweging van spin-op naar spin-neer en weer terug naar spin-op bewegen. Door het wisselende magneetveld gedurende korte tijd aan te schakelen kan de spin in iedere gewenste superpositie toestand worden gebracht en vervolgens worden uitgelezen. Een robuuste uitleesmethode wordt gerealiseerd door naast het elektron nog een tweede elektron op te sluiten en dit te gebruiken voor de uitlezing van de spinrichting van het eerste elektron. Daarbij wordt nagegaan of het elektron in de ene quantum dot al dan niet kan overspringen naar de naburige quantum dot met het tweede elektron. Door het Pauli-uitsluitingsprincipe is dat alleen mogelijk als de twee elektronen verschillende gerichte spins hebben. In het experiment vertaalt het herhaaldelijk overspringen van een elektron door de dots zich in een meetbare stroom, welke een maat is voor de relatieve spinrichting van de twee elektronen. Hiermee hebben we de aangedreven draaiing van de spin, van spin-op naar een superpositie van op en neer en weer verder naar spin-neer, in beeld gebracht.

Bij de tweede methode om een enkele spin te manipuleren hebben we gebruik gemaakt van de spin-baan wisselwerking: een elektron dat beweegt in een elektrisch veld “voelt” een effectief magneetveld. In de halfgeleider is dit effectieve magneetveld gerelateerd aan de kristalstructuur alsmede de potentiaal die het tweedimensionale elektrongas definieert. Voor het elektron in de quantum dot geldt dat dit effectieve magneetveld afhangt van zijn positie. Door een aangelegd wisselend elektrisch veld, gerealiseerd met een wisselspanning op een nabijgelegen elektrode, oscilleert de positie van het elektron en ervaart het elektron zo dus ook een oscillerend effectief magneetveld. In combinatie met een statisch extern magneetveld hebben we op deze wijze met alleen wisselende elektrische velden controle over de spin gedemonstreerd. Het voordeel van deze methode is dat sterke wisselende elektrische velden in de praktijk eenvoudiger te realiseren zijn dan sterke wisselende magnetische velden en dat deze methode het ook mogelijk maakt een spin lokaal aan te sturen.

Voor het gebruiken van de spin als qubit is het belangrijk dat er zo weinig mogelijk fouten optreden in de zeer fragile quantum informatie, opgeslagen in de spin. Deze fouten kunnen worden veroorzaakt door verstoringen uit de omgeving, processen die decoherentie worden genoemd. De verstoringen van twee-elektron toestanden hebben we bestudeerd met behulp van het, hiervoor beschreven, spin-afhankelijke transport door twee gekoppelde quantum dots. Normaal gesproken wordt dit elektronentransport onderdrukt door de lange levensduur van de twee-elektron spintoestanden. Echter, als het externe magneetveld kleiner is dan enkele milliTesla blijkt transport mogelijk te zijn, doordat de levensduur van de twee-elektron spintoestanden dan veel korter is. Dit komt door de interactie van de elektronspins met de spins van de atoomkernen in het halfgeleidermateriaal, wat

resulteert in een willekeurig gericht magnetisch achtergrondveld ter grootte van ongeveer 2 milliTesla. We hebben aangetoond dat de twee-elektron spintoestanden significant minder verstoord worden wanneer de elektronen dicht bij elkaar worden gebracht, waardoor hun koppeling wordt vergroot.

De decoherentie van een enkele spin hebben we bepaald met een zogenaamd Ramsey experiment. Daarbij wordt de spin van bijvoorbeeld spin-op in een superpositie gebracht en na een korte wachttijd weer teruggeroteerd naar spin-op. Dit is echter alleen mogelijk als de fase-informatie van de quantumtoestand behouden is gebleven. Als dat niet het geval is vinden we soms ook spin-neer na de tweede rotatie. De fase-informatie van de quantum toestand blijkt al na zo'n 30 nanoseconden verloren te gaan, veroorzaakt door de precessie van de spin rond het veld van de kernspins. Deze precessie hebben we voor een groot deel ongedaan gemaakt met een spin-echo techniek, waarbij de spin na enige interactietijd met de atoomkernen 180° gedraaid wordt. Hiermee kan de decoherentie van de spin worden uitgesteld tot een tijdsduur van ongeveer 500 nanoseconden. Deze decoherentietijd is voldoende lang om de elektronspin verder te onderzoeken als mogelijke quantumbit. Bovendien kunnen nu de methodes die zijn beschreven in dit proefschrift worden gecombineerd met al bestaande technieken. Daarmee is het in principe mogelijk om eenvoudige quantumberekeningen met elektronspins uit te voeren of juist om de meer fundamentele quantummechanische eigenschappen van enkele spins te onderzoeken.

Frank Koppens
Augustus 2007

Curriculum Vitae

Frank Henricus Louis Koppens

27-06-1976 Born in Deurne, The Netherlands.

1988-1994 Grammar school, College Asten-Someren, Asten.

1994-2001 M.Sc. Applied Physics (cum laude), Eindhoven University of Technology.

2002-2003 Nuon management traineeship.

2003-2007 Ph.D. research at Delft University of Technology
under supervision of prof.dr.ir. L. P. Kouwenhoven &
dr.ir. L.M.K. Vandersypen.
Subject: Coherence and control of a single electron spin in a quantum dot.

List of publications

1. *Spin-echo of a single electron spin in a quantum dot*
F.H.L. Koppens, K.C. Nowack and L.M.K. Vandersypen
In preparation for submission to Physical Review Letters (2007).
2. *Coherent control of a single spin with electric fields*
K.C. Nowack, F.H.L. Koppens, Yu. V. Nazarov and L.M.K. Vandersypen
Submitted to Science (2007).
3. *Universal phase shift and non-exponential decay of driven single-spin oscillations*
F.H.L.Koppens, D. Klauser, W.A. Coish, K.C. Nowack, D. Loss and
L.M.K. Vandersypen
To be published in Physical Review Letters (2007).
4. *Detection of single electron spin resonance in a double quantum dot*
F.H.L. Koppens, C. Buizert, I.T. Vink, K.C. Nowack, T. Meunier,
L.P. Kouwenhoven and L.M.K. Vandersypen
Journal of Applied Physics **101**, 081706 (2007).
5. *Driven coherent oscillations of a single electron spin in a quantum dot*
F.H.L. Koppens, C. Buizert, K.-J. Tielrooij, I.T. Vink, K.C. Nowack,
T. Meunier, L.P. Kouwenhoven and L.M.K. Vandersypen
Nature **442**, 766 (2006).
6. *Control and Detection of Singlet-Triplet Mixing in a Random Nuclear Field*
F.H.L. Koppens, J.A. Folk, J.M. Elzerman, R. Hanson,
L.H. Willems van Beveren, I.T. Vink, H.P. Tranitz, W. Wegscheider,
L.P. Kouwenhoven and L.M.K. Vandersypen
Science **309**, 1346-1350 (2005).

-
7. *Grip op de spin van één enkel electron*
F.H.L. Koppens, L.P. Kouwenhoven and L.M.K. Vandersypen
Nederlands tijdschrift voor natuurkunde, januari 2007.

 8. *Experimental signature of phonon-mediated spin relaxation in a two-electron quantum dot*
T. Meunier, I.T. Vink, L.H. Willems van Beveren, K.-J. Tielrooij, R. Hanson, F.H.L. Koppens, H.P. Tranitz, W. Wegscheider, L.P. Kouwenhoven, and L.M.K. Vandersypen,
Physical Review Letters **98**, 126601 (2007).

 9. *Nondestructive measurement of electron spins in a quantum dot*
T. Meunier, I. T. Vink, L. H. Willems van Beveren, F. H. L. Koppens, H. P. Tranitz, W. Wegscheider, L. P. Kouwenhoven and L. M. K. Vandersypen
Physical Review B **74**, 195303 (2006).

 10. *Single-shot readout of electron spins in a semiconductor quantum dot*
R. Hanson, L.H. Willems van Beveren, I.T. Vink, J.M. Elzerman, F.H.L. Koppens, L.P. Kouwenhoven and L.M.K. Vandersypen
Physica E **34**, 1-5, (2006).

 11. *Single-shot readout of electron spins in a semiconductor quantum dot*
R. Hanson, J.M. Elzerman, L.H. Willems van Beveren, I.T. Vink, F.H.L. Koppens, L.P. Kouwenhoven, and L.M.K. Vandersypen
AIP Conference Proceedings **850**, 1427 (2006).

 12. *High fidelity measurement of singlet-triplet states in a quantum dot*
T.A.Y. Meunier, K.-J. Tielrooij, I.T. Vink, F.H.L. Koppens, H.P. Tranitz, W. Wegscheider, L.P. Kouwenhoven and L.M.K. Vandersypen
Physica status solidi (b) **243**, 3855-3858 (2006).

 13. *Single-Shot Readout of Electron Spin States in a Quantum Dot Using Spin-Dependent Tunnel Rates*
R. Hanson, L.H. Willems van Beveren, I.T. Vink, J.M. Elzerman, W.J.M. Naber, F.H.L. Koppens, L.P. Kouwenhoven and L.M.K. Vandersypen
Physical Review Letters **94**, 196802 (2005).

-
14. *Spin filling of a quantum dot derived from excited-state spectroscopy*
L.H. Willems van Beveren, R. Hanson, I.T. Vink, J.M. Elzerman,
F.H.L. Koppens, L.P. Kouwenhoven and L.M.K. Vandersypen
New Journal of Physics **7**, Solid State Quantum Information (2005).